

https://dspace.org/

An inquiry into magnesium aluminate spinel as an advanced engineering ceramic

Marais, Francois Pierre

2021
https://hdl.handle.net/10539/32950

Downloaded from a DSpace repository. https://dspace.org/

An Inquiry into Magnesium Aluminate Spinel as an Advanced Engineering Ceramic



UNIVERSITY OF THE
WITWATERSRAND,
JOHANNESBURG

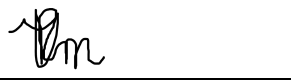
Francois Pierre Marais

A dissertation submitted to the Faculty of Engineering and the Built Environment, University of the Witwatersrand, Johannesburg, in fulfilment of the requirements for the degree of Master of Science in Engineering

2020

Declaration

I declare that this dissertation is my own unaided work. It is being submitted for the Degree of Master of Science in Engineering at the University of the Witwatersrand, Johannesburg. It has not been submitted before for any degree or examination in any other University.



(Signature of candidate)

14th day of April 2021

Abstract

Magnesium aluminate spinel has been investigated as a potential candidate for both optical applications and refractory applications. Transparent polycrystalline magnesium aluminate spinel is a potential candidate for the replacement of fused silica glass used in transparent armour and windows of space craft. A single stage spark plasma sintering process has been used, in conjunction with the sintering aid LiF, to fabricate transparent magnesium aluminate spinel. The spark plasma sintering process used resulted in a spinel disk with a relatively high transmission for a single stage sintering process (the average in the visible spectrum was ≈72%), but relatively poor mechanical properties. Of particular concern was the low Weibull modulus. Independently, an investigation into the effect of the addition of tetragonal-ZrO_2 into the spinel matrix was investigated. Spinel materials' generally poor mechanical properties prevent its utilisation in many refractory applications even though it has excellent chemical and thermal stability. The addition of tetragonal-ZrO_2 was observed to improve the hardness, fracture toughness and biaxial flexural strength of the spinel. Furthermore, the addition of 3mol% Y_2O_3 – ZrO_2 resulted in a reduction of the grain size. The results also indicated that the addition of ZrO_2 improved spinel's high temperature resistance.

Acknowledgements

Firstly, I would like to thank my supervisor, Dr David Whitefield, and my co-supervisor Prof. Iakovos Sigalas. Their guidance was invaluable, and their help greatly appreciated.

Then I would like to thank all those who helped train me in the use the lab equipment: Ben-Louis van der Walt, Dr. Nthabiseng Ntholeng, Thuli Mkhaliphi, Petra Dinham, Brayner Nelwalani, and Lukas Janse Van Rensburg.

And I would like to thank Nthabeleng Tsotetsi, my partner, and my parents, Anne and Pierre Marais, for their welcomed criticisms and emotional support.

Also, I would like to thank the Centre of Excellence in Strong Materials for funding this work.

Lastly, I would like to thank the scientific community at large, without which such endeavours would be futile.

"If I have seen further it is by standing on the shoulders of Giants."

-Sir Isaac Newton

Contents

Declaration i

Abstract iii

Acknowledgements iv

List of Figures ix

List of Tables xvii

Chapter 1: Introduction 1

1.1. Background 1

1.1.1. Transparent spinel 2

1.1.2. Spinel as a refractory material 3

1.2. Research Motivation 5

1.2.1. Transparent spinel 5

1.2.2. Refractory spinel 5

1.3. Aims and Objectives 6

1.4. Hypotheses 7

1.5. Scope 7

Chapter 2: Literature Review 8

2.1. Transparent Spinel 8

2.1.1. The $MgO - Al_2O_3$ System 10

2.1.2. Spinel Crystallography 11

2.1.3. Transparency 15

2.1.4. The Role of LiF 21

2.1.5. Mechanical Properties 28

2.1.6. Production Insights Summary 31

2.2. Zirconia Toughened Spinel 33

2.2.1. ZrO_2 Crystallography 33
2.2.2. Phase Transformations 37
2.2.3. The $ZrO_2 – Al_2O_3 – MgO$ System. 40
2.2.4. Transformation Toughening 42
2.2.5. The Effect on Fracture Toughness 51
2.2.6. Production of Spinel-ZrO_2 composites 54
2.2.7. Production Insights Summary 58
Chapter 3: Methodology 59
3.1. Powder Preparation 59
3.1.1. Transparent Samples 59
3.1.2. Dispersed Zirconia Ceramic (DZC) Samples 59
3.1.3. Mixing, Sieving and Drying 60
3.2. Sample Preparation 60
3.2.1. Sintering 60
3.2.2. Polishing and Grinding 65
3.3. Sample Analysis 65
3.3.1. Particle Size Analyser 65
3.3.2. Density Measurements 66
3.3.3. Spectrophotometry 66
3.3.4. XRD Analysis 66
3.3.5. Scanning Electron Microscopy 67
3.3.6. Optical Microscopy 67
3.3.7. Mechanical Properties 67
Chapter 4: Results 72
4.1. Transparent Spinel 72
4.1.1. Powder Analysis 72

4.1.2. Sintering Results 77
4.1.3. XRD Analysis 80
4.1.4. Transparency 80
4.1.5. Density 84
4.1.6. Grain Structure 87
4.1.7. Mechanical Properties 92
4.2. Zirconia Dispersed Ceramics 105
4.2.1. Powder Analysis 105
4.2.2. Sintering Data 110
4.2.3. Density 112
4.2.4. XRD Analysis 113
4.2.5. EDS Analysis 115
4.2.6. Grain Structure 118
4.2.7. Mechanical Properties 128
Chapter 5: Discussion 142
5.1. Transparent Spinel 142
5.1.1. Powder Analysis 142
5.1.2. Sintering Cycle Analysis 144
5.1.3. Sintered Sample Analysis 146
5.1.4. Sintered Samples Microstructure 151
5.1.5. Hardness and Fracture Toughness 153
5.1.6. Fracture Analysis 156
5.1.7. Biaxial Flexural Strength 158
5.1.8. Comparison to Glass 163
5.2. Dispersed Zirconia Ceramics 165
5.2.1. Powder Analysis 165

5.2.2. Sintering Cycle Analysis.....166
5.2.3. Sintered Sample Analysis.....168
5.2.4. Microstructure.....169
Chapter 6: Conclusions.....179
6.1. Transparent Spinel.....179
6.2. Dispersed Zirconia Ceramics.....179
Chapter 7: Future Work.....181
7.1. Transparent Spinel:.....181
7.2. Dispersed Zirconia Ceramic Composites.....182
References.....183
Appendix.....194

List of Figures

Figure 2.1: Required areal density to stop a given projectile as a function of ceramic thickness. The red line indicates the areal density required for a glass strike-face (Straßburger, 2009)....8

Figure 2.2: Phase diagram for the MgO (halite) - Al_2O_3 (corundum) system (Hallstedt, 1992). 10

Figure 2.3: Conventional FCC unit cell of $MgAl_2O_4$ spinel. (The oxygen is the red sphere, the aluminium is the blue sphere and the magnesium is the orange sphere. This convention is kept throughout.).....11

Figure 2.4: Mg atoms in the $MgAl_2O_4$ spinel structure and carbon atoms in diamond. The Mg^{2+} cations form a diamond cubic sublattice (The CIF for the diamond structure was COD ID: 9012290). 12

Figure 2.5: Two Type I octants and two Type II octants.....13

Figure 2.6: Primitive unit cell of spinel. 13

Figure 2.7: Depiction of how the primitive unit cell combines to form the conventional unit cell.....14

Figure 2.8: Polyhedra formed in the spinel structure, (**a**) highlighting the edge and corner sharing, (**b**) showing the oxygen anions dilation. 14

Figure 2.9: The refractive index (*n*) as a function of wavelength and the resultant effect on the theoretical transmission. 17

Figure 2.10: Depiction of the interaction of light with polycrystalline spinel. Adapted from Krell, et al. (2009). 19

Figure 2.11: Transmission spectra from Frage, et al. (2007), Wang & Zhao, (2009), Bonnefont, et al. (2012), Esposito, et al. (2013), and Cohen, et al. (2018) 20

Figure 2.12: Relative amount of spinel formed at a given temperature (Meir, et al., 2008). .22

Figure 2.13: Area percent distribution of spinel grains obtained by Rothman, et al. (2014). 26

Figure 2.14: Effect of sintering temperature on grain size in the presence and absence of LiF (Rothman, et al., 2014). 26

Figure 2.15: Transmittance as a function of grains size (Rothman, et al., 2014). Sample thickness 1.5mm at a wavelength of 1000nm. 29

Figure 2.16: Photographs of the (**a**) SPSed sample and (**b**) after the HIP post-treatment (Cohen, et al., 2018). 30

Figure 2.17: Unit cells of the ZrO_2 polymorphs. (The oxygen is the red sphere, and the zirconium is the green sphere. This convention is kept throughout) 34
Figure 2.18: Nearest neighbour bonding for the (**a**) O_{II} ions, (**b**) the Zr^{4+} ions, and (**c**) the O_I ions. 35
Figure 2.19: Alternating layers of O_{II} and O_I. The monoclinic unit cell is also shown as the black parallelepiped. 35
Figure 2.20: Tetragonal unit cell showing the coordination of the central zirconium atom...36
Figure 2.21: Tetragonal unit cell showing the (**a**) flattened tetrahedron and (**b**) the elongated tetrahedron. 36
Figure 2.22: Face Centred Cubic (FCC) unit cell of ZrO_2.....37
Figure 2.23: Face-centred unit cells of the polymorphs of ZrO_2. 37
Figure 2.24: Hysteresis formed by the monoclinic to tetragonal transformation (heating) and the tetragonal to monoclinic transformation (cooling) (Ruh, et al., 1968). 38
Figure 2.25: ZO_8 polyhedron in the (**a**) tetragonal phase and (**b**) the cubic phase. 39
Figure 2.26: Liquidus projection of the ZrO_2 – MgO – Al_2O_3 system (McKittrick & Kalonji, 1997). 40
Figure 2.27: ZrO_2 – $MgAl_2O_4$ isopleth (**a**) calculated by Pavlyuchkov, et al. (2014) and (**b**) experimentally determined by Shevchenko, et al. (1993).....41
Figure 2.28: Microstructure of zirconia toughened alumina (Hannink, et al., 2000). 42
Figure 2.29: Schematic illustration of the stress induced transformation around the crack tip. The arrows indicate the compressive stress caused by the transformation (Basu, 2005). 43
Figure 2.30: The ZrO_2 – Y_2O_3 phase diagram depicting the ZrO_2 rich side (Scott, 1975).....45
Figure 2.31: Constrained transformation where the initial state (**a**) is stress-free and (**b**) under a residual stress of σr (Lange, 1982). 48
Figure 2.32: R-curve behaviour of a dispersed zirconia ceramic. Adapted from Kelly & Denry (2008). 53
Figure 2.33: Retained tetragonal ZrO_2 as a function of grain size. Data from Quenard, et al. (2000). 57

Figure 3.1: Schematic diagram of the die set's (**a**) cross section and (**b**) 3D projection. Credited to Rensburg (2018). 61
Figure 3.2: Heating profile (**a**) adapted from Esposito et al. (2013), (**b**) with a cooling rate of 40°C/min and, (**c**) with a cooling rate of 10°C/min. 62
Figure 3.3: Heating profile (**a**) where pressure is released before cooling and (**b**) where the sintering time is 1 hour. 63
Figure 3.4: Heating profile for the dispersed zirconia samples. 64
Figure 3.5: Schematic of an indent with the associated dimension measurements. 68
Figure 3.6: (**a**) Diagram of the B3B test set up and, (**b**) process to begin test. 69

Figure 4.1: Particle size distribution for the MgO powder. 72
Figure 4.2: Particle size distribution for the Al_2O_3 powder. 73
Figure 4.3: Secondary electron SEM image of a large Al_2O_3 agglomerate. 73
Figure 4.4: secondary electron SEM image of the MgO powder prior to milling. 74
Figure 4.5: XRD spectra of the MgO powder. 74
Figure 4.6: XRD spectra of the Al_2O_3 powder. 75
Figure 4.7: A Gaussian curve fitted to the XRD data of the MgO powder. 76
Figure 4.8: Secondary electron SEM image of the mixed Al_2O_3 and MgO after milling. 77
Figure 4.9: Piston movement during the sintering Run 4 with and without LiF additions. ...78
Figure 4.10: Densification curves of Run 4 for the first 1.5 hours. 79
Figure 4.11: Densification curves of Run 4 from 1.5 to 3 hours. 79
Figure 4.12: XRD spectra of the sintered sample (Run 4) showing peaks corresponding to $MgAl_2O_4$ spinel. 80
Figure 4.13: Images taken of the samples which were suspended 2cm above the paper showing the run number. The red circles in Run 1 enclose the locations at which surfaces cracks appeared. 81
Figure 4.14: Images of the suspended samples taken 1cm above the paper showing the run number. 82
Figure 4.15: Images of the samples sintered using Run 4, with and without LiF. 82
Figure 4.16: Transmission spectra normalized to 3cm thick and the theoretical maximum transmission (calculated in Section 2.1.3. Transparency, pp. 17). 83

Figure 4.17: Average measured density of the sintered samples (**a**) with a standard y-axis (**b**) with a reduced y-axis range. The red line indicates the theoretical maximum density. 85
Figure 4.18: Densities of the sintered samples for Run 4 (with LiF). 86
Figure 4.19: Etched image from an $MgAl_2O_4$ sample made using sintering Run 4 (with LiF). 87
Figure 4.20: Measured grain size distribution of this work and that of (Cohen, et al., 2018). 88
Figure 4.21: Normal distribution obtained by taking the natural logarithm of the natural logarithm of the grain size, lnlndi. 89
Figure 4.22: Plot of the cumulative density function and cumulative frequency data. 90
Figure 4.23: "Area Percent" distribution of the measured grains. 91
Figure 4.24: Fracture toughness as a function of grain size. Data from this work and that of other authors (Salem, 2013). 93
Figure 4.25: Characteristic indent of the transparent samples. 94
Figure 4.26: Sample fractured using the ball on 3 balls test. 95
Figure 4.27: Secondary electron micrograph of the fracture origin. 95
Figure 4.28: Secondary electron micrograph of the fracture origin. 96
Figure 4.29: Secondary electron micrograph of the fracture origin. 96
Figure 4.30: Stress as a function of extension for the ball on 3 balls test. 97
Figure 4.31: Experimental data fitted to Equation 4.8. 99
Figure 4.32: Low magnification SEM micrograph of the spinel's fracture surface. 100
Figure 4.33: Medium magnification SEM micrograph of the spinel's fracture surface. 100
Figure 4.34: SEM micrograph of non-uniform areas found at a triple point and grain boundary. 101
Figure 4.35: SEM micrograph of a non-uniform area found at a triple point. 102
Figure 4.36: SEM micrograph of a non-uniform are found at a grain boundary. 102
Figure 4.37: SEM micrograph of an occluded pore. 103
Figure 4.38*:* SEM micrograph of numerous pores on the surface of a grain. 104
Figure 4.39: High magnification SEM micrograph of a pore. 104
Figure 4.40: Particle size distribution for the spinel powder. 105
Figure 4.41: Particle size distribution for the ZrO_2 powder. 106
Figure 4.42: XRD spectra of the $MgAl_2O_4$ spinel powder. 106

Figure 4. 43: XRD spectra of the tetragonal – ZrO_2 powder. 107
Figure 4.44: Immersion-lens SEM micrograph of the ZrO_2 powder. 108
Figure 4.45: Immersion-lens SEM micrograph of the spinel powder. 108
Figure 4.46: Secondary and backscattered electron micrograph of the 30wt.% ZrO_2 mixed powder 109
Figure 4.47: Secondary electron image of the 30wt.% ZrO_2 powder mixture. 109
Figure 4.48: Total piston movement and linear shrinkage as a function of composition. 110
Figure 4.49: Relative piston speed during the SPS runs for each composition (**a**) for the entire run and (**b**) between 5 and 15 minutes (arrows show the change caused by increasing ZrO_2 weight percent) 111
Figure 4.50: Average absolute density for each composition. 112
Figure 4.51: Average relative density for each composition. 113
Figure 4.52: XRD spectra for the sintered composites. 114
Figure 4.53: SEM micrographs of the etched surfaces using the backscatter detector (images taken at 5K magnification) 115
Figure 4.54: SEM micrographs of the etched surfaces using the backscatter detector (images taken at 20K magnification) 118
Figure 4.55: SEM micrographs of the etched surfaces using the backscatter detector (images taken at 50K magnification) 119
Figure 4.56: SEM micrographs of the etched surfaces using the backscatter detector (images taken at 100K magnification) 120
Figure 4.57: Grain Size distribution for the 0wt.% ZrO_2 sample. 121
Figure 4.58: Grain Size distribution for the 2wt.% ZrO_2 sample. 122
Figure 4.59: Grain Size distribution for the 5wt.% ZrO_2 sample. 122
Figure 4.60: Grain Size distribution for the 10wt.% ZrO_2 sample. 123
Figure 4.61: Grain Size distribution for the 20wt.% ZrO_2 sample. 123
Figure 4.62: Plot of the best fit lognormal distributions at different ZrO_2 weight percent. 124
Figure 4.63: Distribution of the natural logarithm of the grain size for the 0wt.% ZrO_2 sample. 125
Figure 4.64: Distribution of the natural logarithm of the grain size for the 2wt.% ZrO_2 sample. 126

Figure 4.65: Distribution of the natural logarithm of the grain size for the 5wt.% ZrO_2 sample. 126
Figure 4.66: Distribution of the natural logarithm of the grain size for the 10wt.% ZrO_2 sample. 127
Figure 4.67: Distribution of the natural logarithm of the grain size for the 20wt.% ZrO_2 sample. 127
Figure 4.68: Mean grain size as a function of weight percent ZrO_2. Linear Intercept Method (LIM), Grain size Distribution (GD), Best Fit pdf (BF). 128
Figure 4.69: Characteristic Vickers indent on the 0wt.% ZrO_2 sample. 129
Figure 4.70: Characteristic Vickers indent on the 30wt.% ZrO_2 sample. 130
Figure 4.71: Hardness and fracture toughness as a function of the nominal ZrO_2 wt.%. 130
Figure 4.72: Secondary electron micrograph for the fracture origin for the 30wt.% ZrO_2 sample. 131
Figure 4.73: Fracture test results for the 0wt.% ZrO_2 samples. 133
Figure 4.74: Weibull analysis for the 0wt.% ZrO_2 samples. 133
Figure 4.75: Fracture test results for the 2wt.% ZrO_2 samples. 134
Figure 4.76: Weibull analysis for the 2wt.% ZrO_2 samples. 134
Figure 4.77: Fracture test results for the 5wt.% ZrO_2 samples. 135
Figure 4.78: Weibull analysis for the 5wt.% ZrO_2 samples. 135
Figure 4.79: Fracture test results for the 10wt.% ZrO_2 samples. 136
Figure 4.80: Weibull analysis for the 10wt.% ZrO_2 samples. 136
Figure 4.81: Fracture test results for the 20wt.% ZrO_2 samples. 137
Figure 4.82: Weibull analysis for the 20wt.% ZrO_2 samples. 137
Figure 4.83: Fracture test results for the 30wt.% ZrO_2 samples. 138
Figure 4.84: Weibull analysis for the 30wt.% ZrO_2 samples. 138
Figure 4.85: Strength of the composites as a function of ZrO_2 wt.%. 139
Figure 4.86: Immersion-lens SEM micrographs of the fracture surfaces. 141

Figure 5.1: SEM micrograph of the mixed Al_2O_3 and MgO powder. 143
Figure 5.2: Reaction geometry of the spinel formation reaction (Aksel, 2004). 144
Figure 5.3: Average transmission as a function of density. 149

Figure 5.4: Arbitary lognormal distributions that have the same mean.....153
Figure 5.5: Microstructure of a Run 4 (with LiF) sample with diamond shapes representing hardness indents from Figure 4.25 (the diamonds are to scale).....154
Figure 5.6: Average transmission for Run 4 and 5 compared to those found in literature for single-stage sintering. (Frage, et al., 2007), (Wang & Zhao, 2009), (Bonnefont, et al., 2012), (Esposito, et al., 2013), and (Cohen, et al., 2018).....155
Figure 5.7: Finite element analysis depiciting the normalised tensile stress (Borger, et al., 2002). 156
Figure 5.8: SEM micrographs of fracture surfaces of samples produced by Esposito, et al. (2015) and this work. 157
Figure 5.9: Schematic of the packing of crystallites (circles) in a powdered compact (**a**) the ideal case, (**b**) realistic goal and (**c**) poorly process powder (Goldstein, 2012).....160
Figure 5 10: Schematic representation of the microstructure showing grains (squares) and pores (circles), (**a**) in the ideal case and (**b**) the case where full attainment of density is not posible (Goldstein, 2012).....162
Figure 5.11: Average transmission for the samples produced using Run 4 (with LiF). The shaded region is one standard deviation above and below the average. 162
Figure 5.12: Initial increase in densification at different ZrO_2 weight percent. 166
Figure 5.13: Relative piston speed during the SPS sintering cycle for the 30 wt.% ZrO_2. Both the measured speed and the calculated weighted sum speed are shown.....167
Figure 5.14: Vickers indent on spinel samples. 171
Figure 5.15: Fracture toughness as a function of ZrO_2 wt.% including data from Quenard, et al. (2000) and Ganesh & Ferreira, (2009).....172
Figure 5.16: Hardness as a function of ZrO_2 wt. % including data from Quenard, et al. (2000) and Ganesh & Ferreira, (2009). 172
Figure 5.17: Fracture toughness as a function of $d^{-0.5}$, showing the fit to the Hall-Petch relation. 173
Figure 5.18: Hardness as a function of $d^{-0.5}$, showing the linear fit to the Hall-Petch relation. 175
Figure 5.19: Hardness as a function of $d^{-0.5}$, showing a quadratic fit. 176

Figure 5.20: Strength as a function of $d^{-0.5}$, showing the linear fit to the Hall-Petch relation. 176

Figure 7.1: Potential sintering profile for transparent spinel for a spark plasma sintering furnace.....181

List of Tables

Table 1.1: List of ceramic materials and their applications. 2
Table 1.2: Zirconia Toughened Alumina Producers and its maximum working temperature. . 4

Table 2.1: Typical properties of $MgAl_2O_4$ spinel (Harris & Turri, 2013). 9
Table 2.2: Spinel unit cell parameters. 12
Table 2.3: Crystallographic data for ZrO_2 34
Table 2.4: Unit cell parameters of the face-centred unit cells of the zirconia polymorphs. ... 37
Table 2.5: Composition and temperature of the ternary eutectics (McKittrick & Kalonji, 1997). 40
Table 2.6: Mechanical properties of sintered $MgAl_2O_4 – ZrO_2$ composites (Ganesh & Ferreira, 2009). 54
Table 2.7: The mechanical properties of the samples fabricated by Quenard, et al. (2000). . . 56

Table 3.1: Impurities within the Al_2O_3 powder. 59
Table 3.2: Impurities within the $MgAl_2O_4$ powder. 60
Table 3.3: Composition of the mixtures. 60
Table 3.4: Naming convention for the sintering profiles used for the transparent samples. .. 64
Table 3.5: Sintering cycle for the dispersed zirconia ceramic samples. 65
Table 3.6: Calculated values for the constants ci used in Equation 3.6 for three different Poisson's ratios (Borger, et al., 2002). 71
Table 3.7: Ranges determined by Borger, et al. (2002) to be valid for Equation 3.6. 71

Table 4.1: Characteristic particle sizes for the MgO and Al_2O_3 powders. 72
Table 4.2: Average transmission in the visible range. 83
Table 4.3: The average, minimum, and maximum densities of samples made using Run 4 (with LiF) (Figure 4.18). 86
Table 4.4:The d_{10}, d_{50}, and d_{90} of the fitted normal curve. 90
Table 4.5: Measured hardness of this work and of other authors. 94
Table 4.6: Experimental and allowable ranges for the parameters needed to calculate the stress for the B3B test. 97

Table 4.7: EDS measurement on the fracture surface. The values contained in brackets indicate the theoretical value. 101
Table 4.8: EDS analysis of the non-uniform area. The theoretical weight and atomic percent for spinel is shown in brackets. 103
Table 4.9: Characteristic sizes for the raw powders, the suppliers values are given in brackets. 105
Table 4.10: Theoretical weight percentages based on the nominal composition 116
Table 4.11: Weight percent measured by the EDS. 116
Table 4.12: Calculated ZrO_2 weight percent. 117
Table 4.13: Average grain size for each method used to determine grain size 124
Table 4.14: Calculated upper and lower bounds of the Young's moduli for the composites. 129
Table 4.15: The measured hardness and fracture toughness for the dispersed zirconia ceramics. 131
Table 4.16: Calculated Poisson's ratio for the dispersed zirconia ceramics. 132
Table 4.17: Experimental and allowable ranges for the parameters needed to calculate the stress for the B3B test for the $ZrO_2 – MgAl_2O_4$ composites. 132
Table 4.18: Weibull modulus and the nominal strength for the composite samples. 139

Table 5.1: Particle size given by the suppliers and measured by the particle size analyser. 142
Table 5.2: Mechanical properties of Glass (Hand & Tadjiev, 2010) 163
Table 5.3: Mean particle size for the spinel powder. 165

“The known is finite, the unknown infinite; intellectually we stand on an islet in the midst of an illimitable ocean of inexplicability. Our business in every generation is to reclaim a little more land.”

-Thomas Henry Huxley

Chapter 1: Introduction

1.1. Background

The 1993 Versailles Project on Advanced Materials and Standards (VAMAS) defined an advanced ceramic as:

"*an inorganic, non-metallic (ceramic), basically crystalline material of rigorously controlled composition and manufactured with detailed regulation from highly refined and/or characterized raw materials giving precisely specified attributes*", (VAMAS, 1993).

Advanced ceramics generally have unique combinations of properties that conventional materials do not. Moreover, the raw materials used in the manufacture of advanced ceramics are abundant, in contrast to the dwindling metal reserves. Thus, they have become an integral part of modern technology (Matizamhuka, 2018). It can therefore be expected that the use of advanced ceramics will grow. **Table 1.1** lists several applications of advanced ceramics and the industry that the ceramic is commonly found. The list is not exhaustive, rather it serves to indicate the range of applications for advanced ceramics.

Table 1.1 shows that advanced ceramics have made inroads in several critical applications over the previous decades, but there are still obstacles hindering greater development. Such an obstacle is the high fabrication costs, which are exacerbated by the lack of suitable processes for large scale production. Other problems include the reluctance of engineers to switch from materials they are more familiar with, and the redesigns that would be required if the usual material were replaced with an advanced ceramic. Furthermore, there is a lack of empirical data associated with advanced ceramics as compared to more commonly used materials. Design, process technology, and machining technology still need to develop to reduce the costs of components to economical levels (Matizamhuka, 2018).

An advanced ceramic that has generated a great deal of interest is magnesium aluminate spinel, $MgAl_2O_4$. Spinel[*] is a cubic material with a unique combination of chemical, mechanical, optical and thermal properties (Ganesh, 2013). Spinel has been identified as a potential

[*] Any mention of "spinel" throughout this work is referring specifically to $MgAl_2O_4$ spinel unless stated otherwise.

candidate for use in certain refractory applications and for optically transparent windows, domes and armours (Ganesh, 2013).

Table 1.1: List of ceramic materials and their applications.

Industry	**Application**
Manufacturing	• Si_3N_4 cutting inserts (Vleugels, 2006) • Al_2O_3 refractories (Maschio, et al., 1988) (Sarkar, 2010) • TiO_2/mullite thermal barrier coatings (Cao, et al., 2004)
Energy	• Mg_2Si radiation shielding (Akman, et al., 2019) • Yttrium stabilised zirconia in solid oxide fuel cells (Huijsmans, 2001) • $(La,Li)TiO_3$ electrolytes in Li-ion batteries (Fergus, 2010)
Transport	• γ-Al_2O_3 washcoat material in catalytic converters (Santos & Costa, 2008) • Al_2O_3 clutches (Albers, et al., 2005)
Healthcare	• Al_2O_3 bone prosthesis (Sedel, 2000) • Partially stabilised zirconia dental replacements (Denry & Holloway, 2010)
Military	• $MgAl_2O_4$/AlON transparent armour (Straßburger, 2009) (Gallo, et al., 2019) • Al_2O_3/SiC armour (Gooch, 2004)
Information technology	• $YBa_2Cu_3O_7$ superconductors (Yan, et al., 1988) • MnZn ferrite permanent magnets (Petrescu, et al., 2019)

1.1.1.Transparent spinel

The idea to use a hard, transparent front layer of single crystal alumina (sapphire) as a component of transparent armour was introduced about four decades ago (Straßburger, 2009). The function of such a front layer would be to damage a projectile's core by erosion and fragmentation thus lowering the chance of successful penetration (Straßburger, 2009). Progress in material technology has led to the development of alternatives to single crystal

alumina, which include polycrystalline magnesium aluminate spinel ($MgAl_2O_4$), aluminium oxynitride (AlON), and submicron grain size polycrystalline α-Al_2O_3.

When fabricated to an extremely low porosity and a high purity, $MgAl_2O_4$ achieves transparency levels high enough for it to be suitable for armour window strike-faces and protective windows for sensors (Goldstein, 2012). Spinel's superior mechanical and ballistic properties compared to traditional glass, enable a 30 – 60% weight reduction in armour window laminates (Benitez, et al., 2017). The protective strength of spinel is only slightly less than polycrystalline α-Al_2O_3, and significantly higher than that of single crystal alumina (Straßburger, 2009). Since spinel has a cubic crystalline structure, it can theoretically be made into very thick parts, unlike sintered polycrystalline α-Al_2O_3. Also, it is expected that transparent spinel would be cheaper to fabricate than transparent AlON (Benitez, et al., 2017).

Another area of interest for transparent spinel is the windows used in spacecraft. This is because of its thermal and chemical stability coupled with its relatively superior mechanical properties and good transparency (Salem, 2013).

The conventional process for fabricating transparent spinel requires a two-stage sintering approach. Spinel powder is sintered in a furnace at ambient pressure for a prolonged period, followed by Hot Isostatic Pressing (HIP) at high pressures (~200MPa) (Ganesh, 2013). However, attention has been given to a one-stage Spark Plasma Sintering (SPS) process utilising LiF as a sintering aid as this is less time consuming and potentially cheaper.

The high processing costs of dense $MgAl_2O_4$ ceramics have hindered its utilisation despite the excellent initial results regarding its performance in transparent applications. Existing literature seems to suggest that the processing costs of $MgAl_2O_4$ can be reduced by improvements in powder processing and densification parameters, and by gaining a more comprehensive understanding of the mechanisms of $MgAl_2O_4$ formation and densification (Ganesh, 2013).

1.1.2. Spinel as a refractory material

Ceramic materials generally possess a high hardness, chemical inertness, wear resistance, and high strength retention at elevated temperatures. However, a major limitation for ceramic materials is their low fracture toughness (Basu, 2005). This impediment prevents the full utilisation of spinel as a refectory material. Spinel is currently used as a refractory material in cement rotary kilns, the lining of steel ladles, the checker bricks of glass furnace regenerators,

and in converters of copper smelting plants (Sarkar, 2010). However, it is not used in other refractory applications, such as molten metal filtrations (with services temperatures of ~1100°C (McAllister Mills, 2020)), because of its relatively poor mechanical properties (particularly its fracture toughness) at room and high temperatures (Quenard, et al., 2000) (Ganesh & Ferreira, 2009).

An approach to improve the mechanical properties of spinel for refractory applications that has been investigated is the incorporation of metastable tetragonal zirconia into the spinel matrix (Ganesh & Ferreira, 2009) (Mohan & Sarkar, 2016). The incorporation of dispersed ZrO_2 particles in a ceramic's matrix can toughen a ceramic material by multiple toughening mechanisms, including stress-induced transformation toughening, microcrack toughening, and crack deflection (Hannink, et al., 2000). While the research for zirconia toughening in ceramic composites is abundant, most of it is focused on zirconia toughened alumina. There is unfortunately not a significant amount of work that has been completed on zirconia toughened spinel (Quenard, et al., 2000).

Zirconia toughened alumina has been successfully used in high temperature applications. There are multiple producers of zirconia toughened alumina for refractory applications, such as crucibles. Producers of zirconia toughened alumina and its respective maximum working temperature are given in **Table 1.2**. Thus, there is a good indication that the addition of zirconia could be used to improve the mechanical properties of spinel for refractory applications.

Table 1.2: Zirconia Toughened Alumina Producers and its maximum working temperature.

Producer	**Maximum Working Temperature (°C)**
Insaco Inc. (2020)	1650
Superior Technical Ceramics (2020)	1500
Astro Met Inc (n.d)	1650
Thermansys (2017)	1650

1.2. Research Motivation

1.2.1. Transparent spinel

There has been extensive research done regarding the optical applications of spinel since Louis Navias created transparent spinel for the General Electric Company in 1961. Recently, it has been stated that spinel could be a "game changing technology" for upcoming armour development (Benitez, et al., 2017). Also, the manufacturing technologies for transparent spinel have reached a "state-of-the-art", thus it is expected that the development of transparent ceramics for armour applications are feasible in the medium-term (Straßburger, 2009).

The top 100 combat armament producing, and military services companies' earnings give an indication of the potential commercial benefits of developing transparent spinel. In 2016 (excluding China) the armament industry earned approximately 375 billion dollars, a 38% increase from 2002 (Gallo, et al., 2019). It has been estimated that the ballistic protection segment on its own will be valued at 11 billion dollars in 2020[*] (Gallo, et al., 2019).

The research and development of transparent spinel done by the armaments industry has piqued the interest of the National Aeronautics and Space Administration (NASA). NASA has begun testing spinel as a potential replacement for the fused-silica used in space-craft window systems (Salem, 2013).

The development of a spinel replacement for space-craft window systems could be financially lucrative particularly due to what has been deemed "NewSpace". NewSpace is essentially the privatisation and commercialisation of space exploration. This has been driven by the development of privately owned space exploration companies, particularly: SpaceX, Blue Origin, and Virgin Galactic/Virgin Orbit (A more comprehensive list is given in **Table A.1.** in the **Appendix pp. 191**). Thus, the industries concerned with manufacturing transparent spinel have shown massive growth.

1.2.2. Refractory spinel

Principle manufacturing processes that consume refractory materials are iron and steelmaking, non-ferrous metal production, cement production, and glass production (McEwan, et al., 2011).

[*] The earnings estimate was calculated prior to the COVID-19 pandemic. Thus, the actual 2020 earnings are likely to be lower.

As the products of these processes are ubiquitous throughout any modern city, it is vital that the production of these materials is as efficient and as safe as possible. There is concern over the use of MgO-chrome refractories used in some of these processes due to the generation of Cr^{6+} ions. Inhalation of compounds containing Cr^{6+} have been found to lead to airway irritation, airway obstruction, and lung, nasal, or sinus cancer (Agency for Toxic Substances & Disease Registry, 2013). This has generated the need for no-chromium containing alternative refractories (Ceylantekin & Aksel, 2012). Spinel could be a suitable safe replacement for the conventional magnesia-chrome refractories. Also, $MgAl_2O_4$ spinel refractories have shown to possess greater life expectancy than magnesia-chrome refractories (Mohan & Sarkar, 2016).

Over the previous 30 years, zirconia toughened ceramics have begun penetrating the market due to their improved mechanical properties (Basu, 2005). While it is known that the incorporation of ZrO_2 into a ceramic matrix improves the mechanical properties, most studies have dealt with $ZrO_2 – Al_2O_3$ composites, only a few studies have focused $ZrO_2 – MgAl_2O_4$ composites (Quenard, et al., 2000). Therefore, there is a need to investigate the zirconia strengthening phenomenon in spinel with the hopes that it will lead to the development of superior and safer $MgAl_2O_4$ spinel refractories.

1.3.Aims and Objectives

There are two aims for this research. The first aim is to fabricate a spinel disk with a thickness of 3mm and a transmission of 70% using a single stage sintering process with the sintering aid LiF and measure its mechanical properties. The second aim is to fabricate a $ZrO_2 – MgAl_2O_4$ composite and investigate any improvements to its mechanical properties.

The objectives associated with aim one are:

- Fabricate a 20mm transparent spinel disk using the sintering curve developed by Esposito, et al. (2013).
- Adjust the sintering pressure, sintering time, or sintering temperature to maximize the transmission of visible light.
- Fabricate at least 10 samples using the sintering cycle that produced the highest transmission.
- Analyse these samples' composition, microstructure, and density.

- Analyse these samples' hardness, fracture toughness and strength.
- Determine the quality of this fabrication process by comparing the mechanical properties and transmission to the values found in literature.

The objectives associated with aim two are:

- Produce disks 20mm in diameter with a range of ZrO_2 compositions.
- Analyse the composites' composition, microstructure, and density.
- Determine the hardness, fracture toughness and strength of the ZrO_2 composites.
- Determine the effectiveness of the zirconia toughening.

1.4.Hypotheses

Sintering by the SPS process with the aid of LiF will result in a transparent ceramic with a transmission of visible light of at least 65%.

The addition of ZrO_2 will result in an improvement of mechanical properties, in a similar fashion to the $ZrO_2 – Al_2O_3$ composites.

1.5.Scope

This research is centred on the materials rather than the process design of a transparent window or a refractory brick. Therefore, attention will be given to how the fabrication parameters, such as temperature and pressure, affect the end material. This research does not include the development of an economically viable process that would produce an armoured window or a refractory component. Rather it focuses on what is required to achieve the desired material and what certain process parameters have on the properties of the final material. Therefore, this research is done to expand the body of knowledge with regard to spinel and its zirconia composite such that a commercially viable processes can be developed.

The research conducted focuses on the two materials, transparent spinel and refractory spinel, separately. This is because the addition of ZrO_2 to spinel to strengthen it causes the spinel part to lose its transparency. Therefore, the Literature Review, Results, Discussion, Conclusions and Future Work chapters are each separated into two parts, one part focuses on the transparent spinel, the other part on the ZrO_2 strengthen spinel.

Chapter 2: Literature Review

2.1. Transparent Spinel

Over the last 60 years, research has been conducted concerning the development of fabrication technologies that can produce commercially viable transparent spinel parts. A commercially viable part would simultaneously have reasonable mechanical properties, the desired shape and size, a high transmission and be available in sufficient amounts at an acceptable price (Goldstein, 2012). Obtaining transparent spinel which exhibits only one or two of the required properties is moderately difficult (Goldstein, 2012). Thus, research is still needed to develop a process which can produce transparent spinel parts with all the required properties.

Polycrystalline $MgAl_2O_4$ spinel exhibits optical transparency when fabricated to a high relative density and purity. It has the potential to replace glass in armoured windows as the strike-face due to its superior mechanical and ballistic properties. **Figure 2.1** shows the areal density of an armoured window required to stop a given projectile as a function of ceramic thickness.

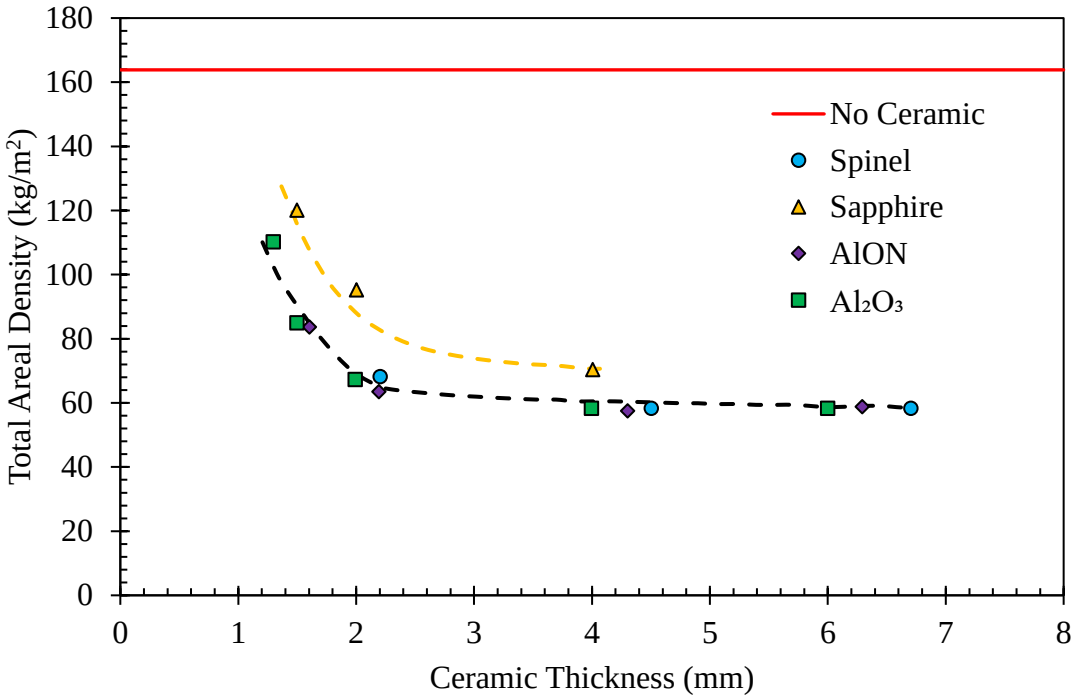


Figure 2.1: Required areal density to stop a given projectile as a function of ceramic thickness. The red line indicates the areal density required for a glass strike-face (Straßburger, 2009).

When the ceramic strike face is 3mm thick, the armoured window is ≈60% lighter in weight than a window made using soda-lime float glass. The weight reduction benefits diminish after ≈3mm. The performance of the polycrystalline materials, $MgAl_2O_4$ spinel, Al_2O_3 and AlON are all similar. The polycrystalline materials perform slightly better than the single crystal alumina (sapphire) (Straßburger, 2009).

Spinel is also being investigated to replace the fused silica windows used in spacecraft (Salem, 2013). Fused silica windows are regularly taken out of service due to various forms of damage. The interest generated by the armament industry in spinel has prompted NASA to begin researching transparent spinel as a potential replacement for the fused silica. It is expected that because spinel's mechanical properties are superior to those of glass, spinel could have an improved lifetime and lighten the window systems of the spacecraft (Salem, 2013).

Transparent polycrystalline spinel can also be used in the fabrication of sensors operating in the mid infrared (MIR) range, windows for barcode readers, tuneable laser hosts, high index optics for ultraviolet (UV) microlithography, high pressure arc lamps, watch casings, optical heat exchangers, night-vision systems, and laser ignitions (Goldstein, 2012) (Esposito, et al., 2015) (Cohen, et al., 2018). **Table 2.1** gives typical properties of $MgAl_2O_4$ spinel.

Table 2.1: Typical properties of $MgAl_2O_4$ spinel (Harris & Turri, 2013).

Property	**Value**
Theoretical density (g/cm^3)	3.5767*
Hardness (GPa) {for a single crystal}	13
Specific Heat Capacity (J/g.K) {at 25°C}	0.820
Poisson's Ratio	0.27
Coefficient of Thermal Expansion (K^{-1})	5.667×10^{-6}
Thermal Conductivity (W/m.K)	17.9
Optical Transmittance (%) {average for the visible spectrum}	86†
Melting Point (°C) {for stoichiometric spinel}	2105‡
Young's Modulus (GPa)	272

*From **Section 2.1.2. Spinel Crystallography pp. 12**, †Calculated in **Section 2.1.3. Transparency pp. 16-17**, ‡From Hallstedt (1992).

2.1.1. The MgO – Al_2O_3 System

Magnesium aluminate spinel is an intermediate phase in the MgO – Al_2O_3 system. The MgO – Al_2O_3 system has been studied and used to understand metallurgical slags, refractories, ceramic materials, and geological systems (Hallstedt, 1992). The MgO – Al_2O_3 binary phase diagram is shown in **Figure 2.2** (Hallstedt, 1992). It consists of a eutectic (1996°C) MgO – $MgAl_2O_4$ reaction and a peritectic (1994°C) $MgAl_2O_4$ – Al_2O_3 reaction. Stoichiometric spinel melts congruently at 2105°C (the congruent maximum) and Al_2O_3-rich spinel melts at 1990°C (the congruent minimum). The lowest temperature at which liquid exists in this system is ~1990°C. Because of this high temperature, the liquid phase of this system has not been thoroughly studied (Hallstedt, 1992). The system has very low terminal solubilities, the solid solubility of MgO (halite) in Al_2O_3 (corundum) is only about 0.012mol.% at 1800°C. But the solubility in spinel of MgO and especially Al_2O_3 is high. When spinel is expressed as $MgO.nAl_2O_3$, the values of *n* can range from $0.6 < n < 7$ at ~1900°C. The spinel phase can even exist as a metastable form of pure Al_2O_3 called γ – Al_2O_3 (Hallstedt, 1992).

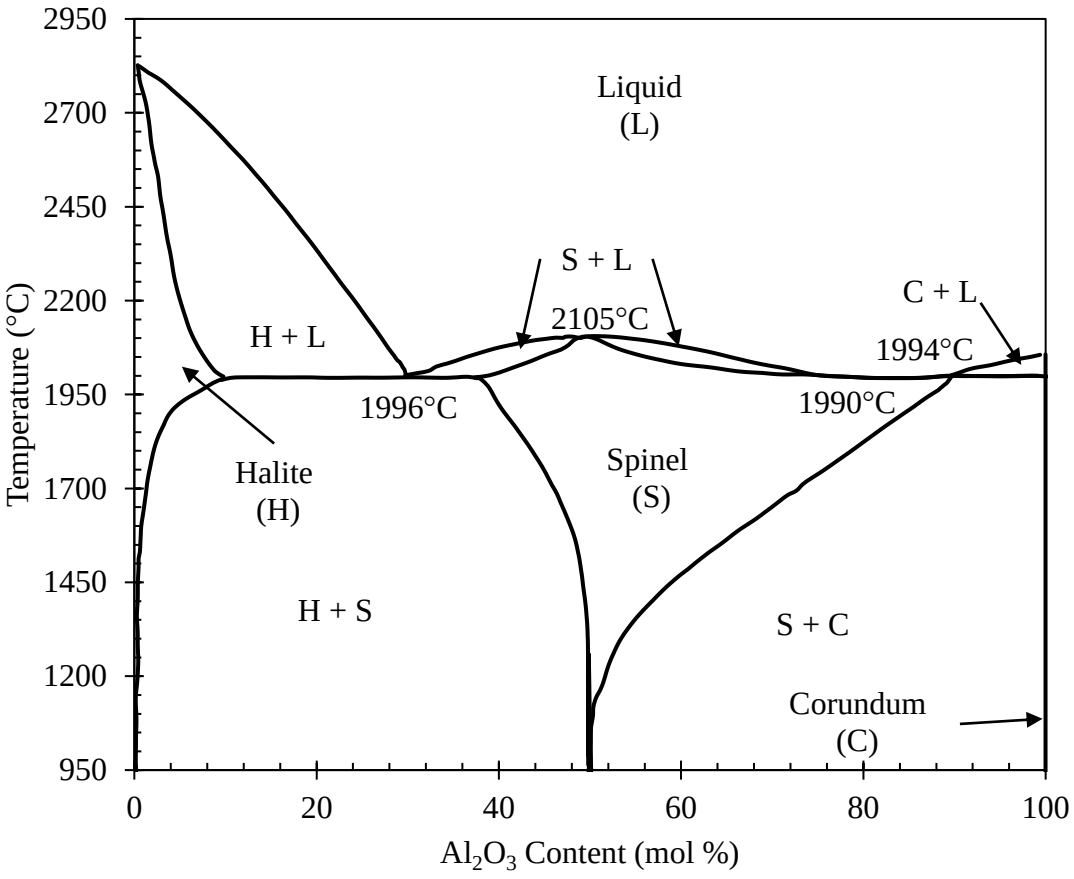


Figure 2.2: Phase diagram for the MgO – Al_2O_3 system (Hallstedt, 1992).

2.1.2. Spinel Crystallography

The mineral "spinel" ($MgAl_2O_4$) is the eponym for the structure spinel (AB_2X_4) (Hosseini, 2008). A list of minerals with the spinel structure are given in **Table A.2.** in the **Appendix pp. 191**. The spinel crystal structure was determined independently by Bragg and Nishikawa in 1915 (Sickafus & Wills, 1999). The "A" is a divalent cation, "B" is a trivalent cation, and "X" is a divalent anion, usually oxygen (Smart & Moore, 2005). In the ideal structure the anion sublattice is arranged in a pseudo-cubic close packed spatial arrangement (Ganesh, 2013) with A-cations (Mg^{2+}) occupying the tetrahedral holes and the B-cations (Al^{3+}) occupying the octahedral holes (Smart & Moore, 2005).

The conventional unit cell of spinel is a Face-Centred Cube (FCC), with a basis of two formula units. Thus, there are 8 Mg^{2+} cations, 16 Al^{3+} cations and 32 O^{2-} anions, for a total of 56 ions per unit cell (Sickafus & Wills, 1999). **Figure 2.3** depicts the conventional spinel unit cell and **Table 2.2** gives the unit cell parameters for the ideal structure. The Crystallographic Information File (CIF) was taken from the Crystallography Open Database (COD), and the data for the CIF was from Ishii, et al. (1982) COD ID: 9005767. The CIF and the VESTA 3 software were used to generate the images of the spinel structure.

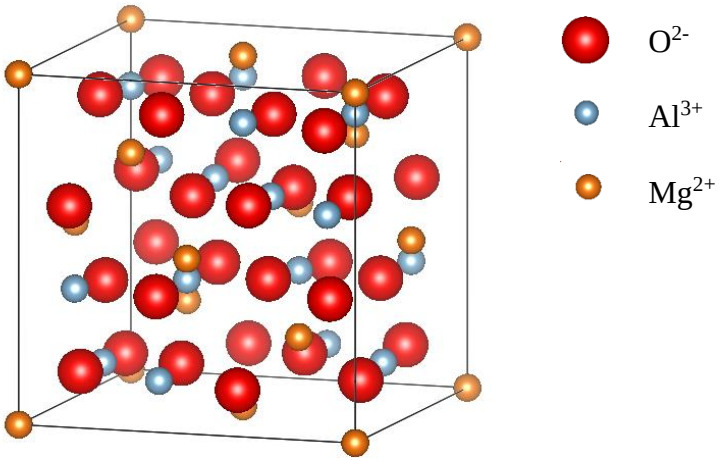


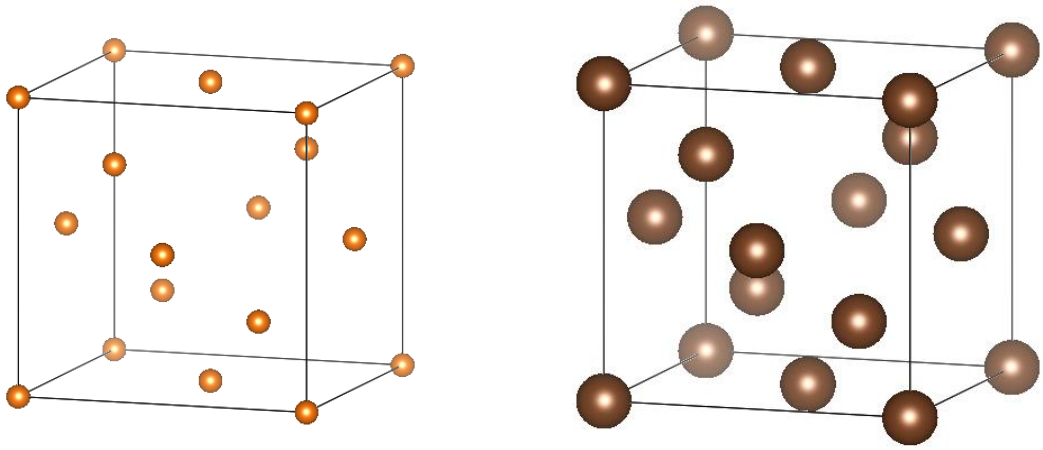
Figure 2.3: Conventional FCC unit cell of $MgAl_2O_4$ spinel. (The oxygen is the red sphere, the aluminium is the blue sphere and the magnesium is the orange sphere. This convention is kept throughout.)

Table 2.2: Spinel unit cell parameters.

Unit Cell	Cubic
Formula Units Per Unit Cell	8
Space Group	Fd3m (227)
a, b, c (Å)	8.08443*
α, β, γ (°)	90
V ($Å^3$)	528.38
Theoretical density (g/cm^3)	3.5767†

*From Navrotsky, et al. (1986), †Calculated from the unit cell parameters. The value corresponds with Harris & Turri (2013) of 3.576g/cm^3.

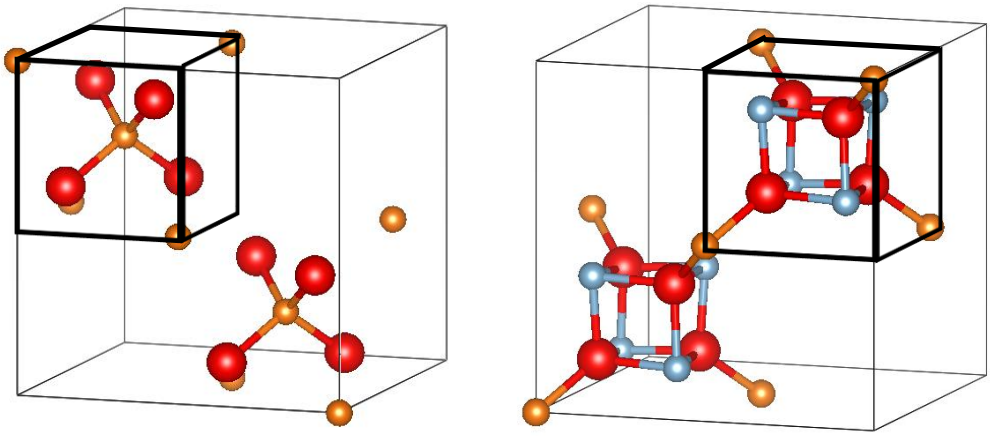
Within a unit cell, the close packed array of O^{2-} ions forms 64 tetrahedrally coordinated cation sites and 32 octahedrally coordinated cation sites (Ganesh, 2013). Of the 64 tetrahedral sites, 8 are occupied by the Mg^{2+} cations. Sixteen of the 32 octahedral sites are occupied by the Al^{3+} cations. The other tetrahedral and octahedral sites remain unoccupied in the ideal structure (Ganesh, 2013). The Mg^{2+} cations are in the same relative positions as the carbon atoms in diamond (Hosseini, 2008), **Figure 2.4**.



Mg^{2+} cations in $MgAl_2O_4$ spinel. Carbon atoms in diamond.

Figure 2.4: Mg atoms in the $MgAl_2O_4$ spinel structure and carbon atoms in diamond. The Mg^{2+} cations form a diamond cubic sublattice (The CIF for the diamond structure was COD ID: 9012290).

The conventional unit cell can also be described by 8 octants of two types. Type I contains Mg^{2+} cations tetrahedrally coordinated to O^{2-} anions and type II contains the Al^{3+} cations in octahedral coordination (Hosseini, 2008). **Figure 2.5** depicts two octants of the same type in the conventional unit cell.



Type I Type II

Figure 2.5: Two Type I octants and two Type II octants.

The primitive unit cell of spinel is tetragonal and consists of two octants, one of type I and one of type II, **Figure 2.6**. The primitive unit cell consists of two $MgAl_2O_4$ formula units (Sickafus & Wills, 1999). Four primitive unit cells combine to form the conventional unit cell, **Figure 2.7**.

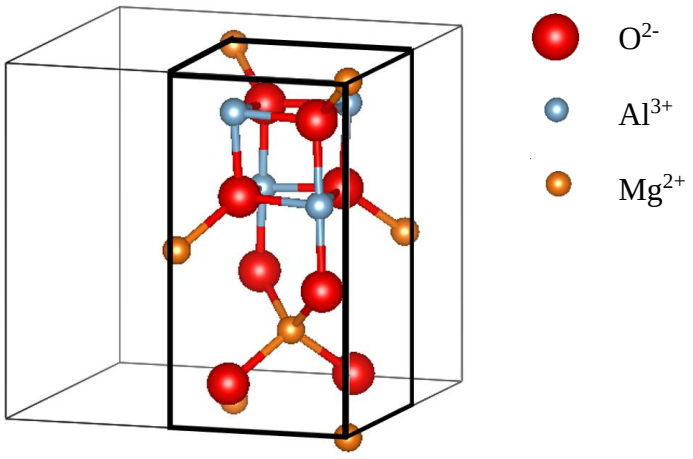
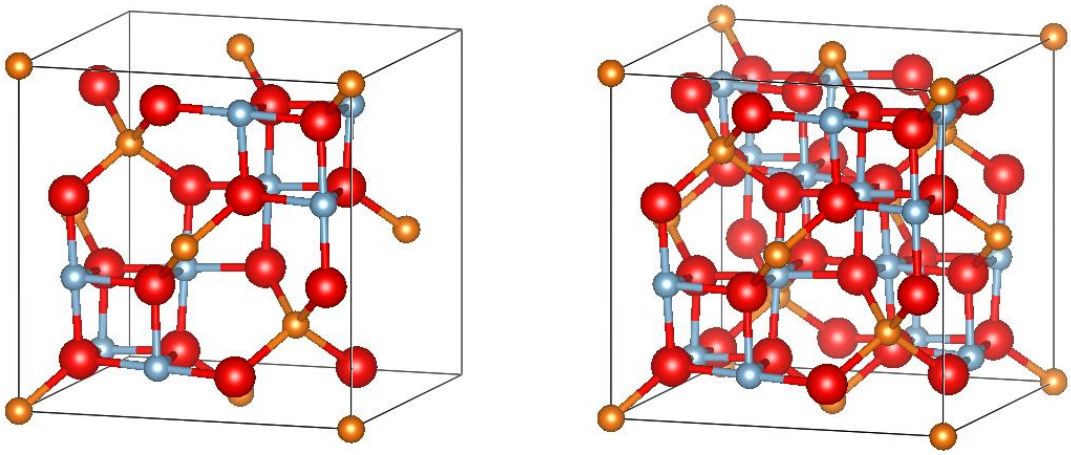


Figure 2.6: Primitive unit cell of spinel.



Conventional unit cell with half the atoms. Fully populated conventional unit cell.

Figure 2.7: Depiction of how the primitive unit cell combines to form the conventional unit cell.

Figure 2.8 shows the octahedra formed by the Al^{3+} ions (the blue octahedra are AlO_6) and the tetrahedra formed by the Mg^{2+} ions (the orange tetrahedra are MgO_4). The tetrahedra are isolated from each other and are corner sharing with the octahedra, **Figure 2.8.a**. No edge sharing occurs for the tetrahedra. The octahedra share 6 of their 12 edges with the nearest Al^{3+} octahedra. The other six edges are shared with octahedra that surround a vacancy (Sickafus & Wills, 1999). **Figure 2.8.b** shows that the oxygen ions are slightly dilated out of their ideal positions (Ganesh, 2013).

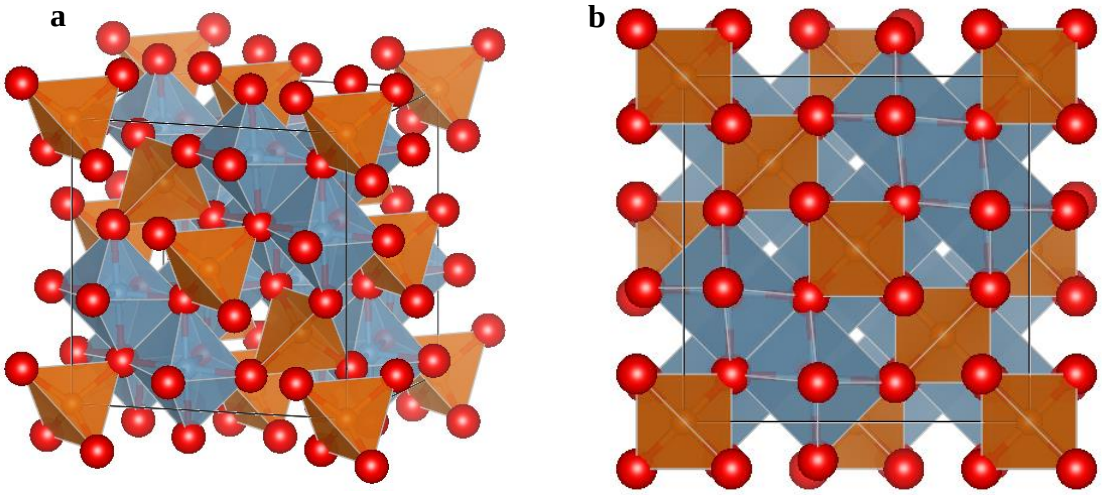


Figure 2.8: Polyhedra formed in the spinel structure, (**a**) highlighting the edge and corner sharing, (**b**) showing the oxygen anions dilation.

The spinel structure has three degrees of freedom which are used to define the most thermodynamically stable configuration. These are the lattice parameter *a*, the anion parameter *u* (the repeat unit of the anion sublattice, which describes the degree of dilation) and the cation inversion parameter *i* (Goldstein, 2012). The spinel structure has the ability to incorporate many cation species of different valance states into its octahedral and tetrahedral sites (Kashii, et al., 1999). Because of this, spinel is known to show cation mixing between tetrahedral and octahedral sites, **Equation 2.1**.

$$Al^{[VI]} + Mg^{[IV]} \leftrightarrow Al^{[IV]} + Mg^{[VI]} \qquad \textbf{Equation 2.1}$$

Where the IV and VI represent the tetrahedral and octahedral coordination, respectively. The extent to which the cations swap positions is described by the inversion parameter, *i*. The general formula for spinel can then be written as **Equation 2.2**.

$$(Mg_{1-i}, Al_i)^{IV}(Mg_i, Al_{2-i})^{VI}O_4 \qquad \textbf{Equation 2.2}$$

Spinel with $i = 0$ is normal spinel, $(Mg)^{IV}(Al_2)^{VI}O_4$, whereas $i = 1$ indicates that the spinel is an inverse spinel, $(Al)^{IV}(AlMg)^{VI}O_4$ (Kashii, et al., 1999). Between these two extremes lies most spinels. Natural spinel has an inversion parameter very close to one. It has been demonstrated that synthetic $MgAl_2O_4$ is always partially inverse, with inversion parameters between ~0.1 – 0.6 generally observed (Sickafus & Wills, 1999).

The unoccupied tetragonal and octahedral sites can accommodate cation species within a stable structure, even at high temperature and pressure (Ganesh, 2013). Due to the number of unoccupied sites, spinel is considered a host cell capable of holding divalent and trivalent cations in solid solution (Ganesh, 2013). The permissible range of radii for these cations is 0.044 – 0.1nm and because of this the lattice parameter of spinel ranges from 0.80 to 0.84 nm, depending on the foreign cations that occupy the vacant sites (Ganesh, 2013). Foreign cation species lower transmission by acting as colour centres. It is important to be cognizant of this during the fabrication of transparent spinel parts. The open structure of spinel also partially explains why MgO and Al_2O_3 have relatively high solubilities within spinel, **Figure 2.2**.

2.1.3. Transparency

Goldstein and Krell (2016) provided an informal definition of transparency, “a material may be considered transparent if it allows the formation of an undistorted image of a target scene in a sensor”. For a material to be transparent, the interaction between the material and the incident

electromagnetic waves (light) must be minimized. The ways in which materials interact with light can be summarised by four phenomena: absorption, reflection, refraction, and scatter. Materials selection for transparent components starts by determining the degree of absorption of light by the material (Krell, et al., 2009).

For transparent ceramics there is a range in which light is not absorbed by the atoms (Goldstein & Krell, 2016). At short wavelengths, light can excite valence electrons to a higher energy state. This occurs when the energy of the light is equivalent to the difference in energy between the valence band and conduction band (Krell, et al., 2009). For pure spinel, the band gap has an energy of ~8eV which corresponds to a wavelength cut-off of ~170nm (Goldstein, 2012). This cut-off lies in the ultra-violet spectrum. Light with a shorter wavelength than 170nm will be absorbed by the electrons of the spinel atoms. At longer wavelengths, the low energy infra-red light cannot excite electrons to higher energy states. However, it can change the vibrational states of the lattice. The low energy light will be absorbed by the highest energy phonons. The energy of these phonons corresponds to a wavelength of ~6200nm which is found in the infrared spectrum (Goldstein & Krell, 2016). Light with a wavelength greater than 6200nm will be absorbed by the spinel lattice. Between these two limits, 170 – 6200nm, light can potentially pass through the material without being wholly absorbed. No strategies are known to extend this range for a given ceramic material. Even within this range, point defects (such as oxygen vacancies and impurity atoms) can engender absorption (Krell, et al., 2009).

Within this range, and assuming no impurity atoms or oxygen vacancies, the theoretical transmission of light is still not 100%. This is because of reflection. The theoretical maximum transmission of the ceramic part is 100% minus the reflection of both surfaces. For a defect free surface, at normal incidence the reflection, R_1, on one surface is given by **Equation 2.3** (Krell, et al., 2009).

$$R_1 = \left(\frac{n-1}{n+1}\right)^2 \qquad \textbf{Equation 2.3}$$

Where n is the refractive index of the material. The total loss due to both surfaces, R_2, is calculated by **Equation 2.4**.

$$R_2 = \frac{2R_1}{1 + R_1} \qquad \textbf{Equation 2.4}$$

Thus, the theoretical transmittance limit (T_{th}) is given by **Equation 2.5**.

$$T_{th} = (1 - R_2) = \frac{2n}{n^2 + 1} \qquad \textbf{Equation 2.5}$$

While the nett effect is small within the range of visible light, the refractive index is a function of wavelength ($n = f(\lambda)$). It increases as the wavelength decreases. For spinel, the refractive index is approximated by the Sellmeier equation (**Equation 2.6**) (Harris & Turri, 2013):

$$n^2 - 1 = \frac{1.8938(\lambda^2)}{\lambda^2 - (0.09942)^2} + \frac{3.0755(\lambda^2)}{\lambda^2 - (15.826)^2} \qquad \textbf{Equation 2.6}$$

$$\{200nm < \lambda < 3500nm\}$$

The refractive index as a function of wavelength is given in **Figure 2.9**. The theoretical transmittance calculated from **Equation 2.5** using the resultant refractive index from **Equation 2.6** is also given in **Figure 2.9**. Within the visible spectrum, the average theoretical transmittance is 86.8% and the minimum (86.18%) and maximum (87.18%) transmissions occur at the limits of the visible spectrum, 380nm and 740nm, respectively.

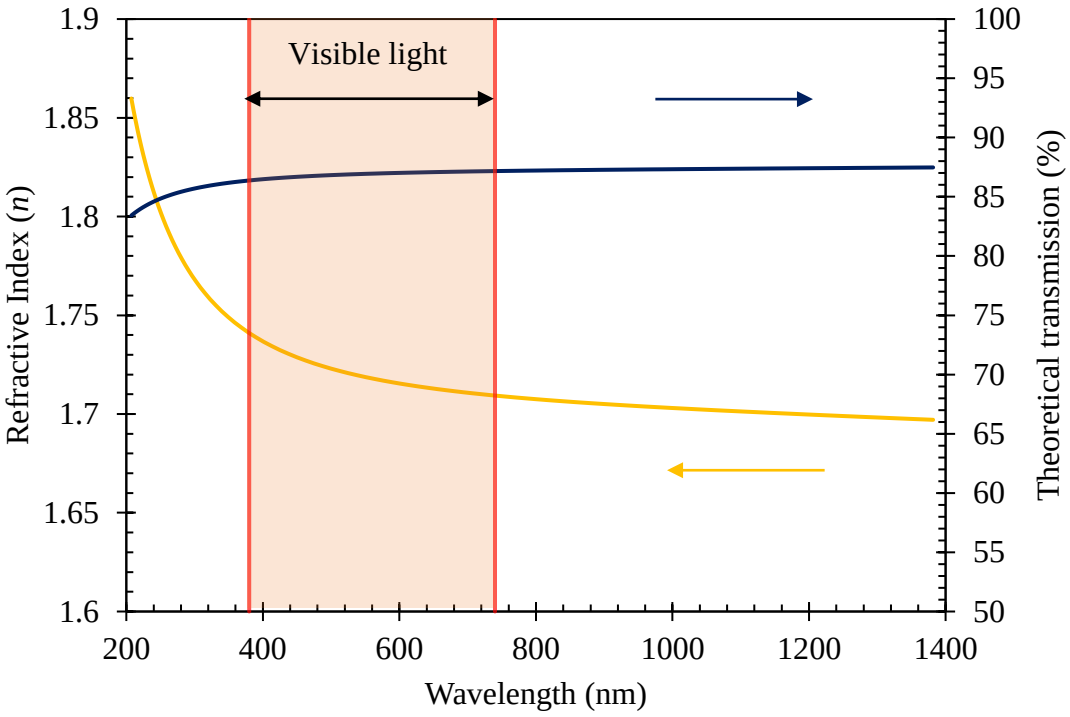


Figure 2.9: The refractive index (n) as a function of wavelength and the resultant effect on the theoretical transmission.

In addition to low absorption and high transmittance, transparency requires a high in-line transmission. An emphasis on high in-line transmittance is important as a high transmittance with a low in-line transmittance will result a translucent component not a transparent one. A high in-line transmission is achieved when the scattering losses are low. The scattering of incident beams occurs in optically inhomogeneous materials by secondary phases with different refractive indices and in anisotropic crystals by birefringence (Krell, et al., 2009). As spinel has a cubic crystal structure, it is optically isotropic therefore birefringence is not an issue at longer wavelengths. However, for single crystals inherent birefringence becomes significant at λ<200nm, but for polycrystals it is ≈0nm/cm (Goldstein, 2012). Thus, the effect of birefringence can be ignored for polycrystalline spinel components. However, scatter caused by secondary phases still poses a significant challenge.

The relative transmission, T_{rel}, is the percent transmission relative to the theoretical maximum transmission. A relative in-line transmission of 70%, implies that 30% of the light is lost to due to scattering and/or the absorption from point defects. When $T_{measured} < T_{th}$, increasing the thickness of the sample decreases the in-line transmission because of the greater number of defects the light interacts with (Goldstein, 2012). This is expressed mathematically in **Equation 2.7** (Krell, et al., 2009).

$$T_{rel} = \frac{T_{measured}}{T_{th}} = e^{(-kt)} \qquad \textbf{Equation 2.7}$$

Where k is the extinction coefficient and t is the thickness of the component. For components which have the same extinction coefficient, their relative transmissions are related by **Equation 2.8**.

$$T_{rel,2} = \left(T_{rel,1}\right)^{\frac{t_2}{t_1}} \qquad \textbf{Equation 2.8}$$

When $T_{measured} = T_{th}$, the thickness of a component does not affect its in-line transmission. Reaching this theoretical transmission limit is difficult, as it would require a completely defect free sample. The major contributors to scattering are pores and secondary phases. The porosity needs to be <0.01% for transmission to become significant (Benitez, et al., 2017), and for an in-line transmission of >80%, the porosity must be <0.002% (Esposito, et al., 2015). The composition must also be extremely pure to prevent the formation of secondary phases which

scatter light. This poses a significant production challenge. **Figure 2.10** shows the interaction of an incident beam of light traveling through a transparent polycrystalline spinel sample.

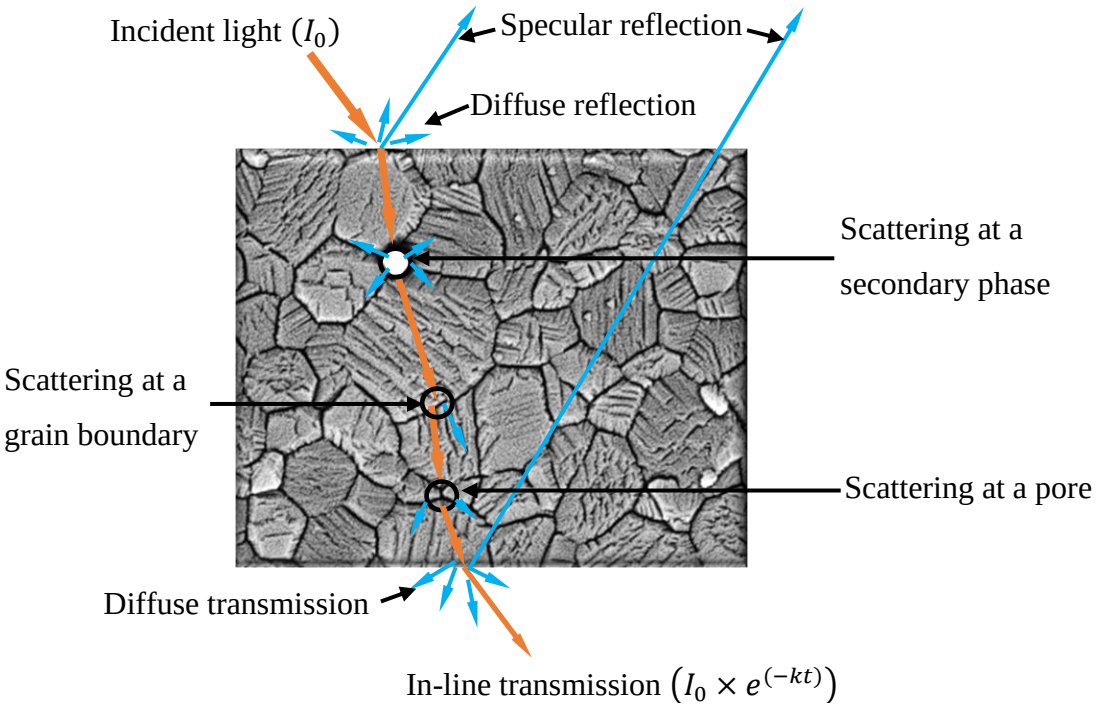


Figure 2.10: Depiction of the interaction of light with polycrystalline spinel. Adapted from Krell, et al. (2009).

Unfortunately, a balance is required between the transmittance and the mechanical properties of the component. For polycrystalline ceramics, when the average grain size increases above 0.5µm, the strength and hardness rapidly deteriorate (Rothman, et al., 2014). However, grain boundaries are defects which cause scatter; thus, transmittance increases with increasing grain size (for optically isotropic ceramics). Also, porosity generally decreases with increasing sintering time but so does grain size. Therefore, in-order to decrease porosity thereby increasing transmittance, grain size increases, sacrificing mechanical properties. Thus, an optimal compromise between the two must be determined (Rothman, et al., 2014).

Over the previous decade, attention has been given to the one-stage SPS process for the fabrication of fully dense $MgAl_2O_4$ in lieu of the conventional two stage approach. The two-stage approach generally consists of prolonged sintering at atmospheric pressures followed by Hot Isostatic Pressing (HIP). This is time consuming and expensive, thus there is potential economic benefit in a simplified one-stage process. However, the transparency of the SPSed components are generally lower than the two-stage approach. The addition of sintering aids has

helped increase the transparency, but this came at the expense of inferior mechanical properties (Cohen, et al., 2018).

An additional issue with the SPS process is scaling up to larger sizes. Due to the nature of the SPS process, there are inhomogeneous temperature and stress distributions which become more pronounced as the sintered part becomes larger, particularly for non-conducting samples. These inhomogeneities cause a mechanical property and transparency gradient from the periphery to the centre of the sintered part (Cohen, et al., 2018). Moreover, carbon contamination tends to increase as the sample diameter increases. Therefore, sintered disks which have diameters that are greater than 25mm and are thicker than 3mm commonly display discoloration and non-uniform transparency (Cohen, et al., 2018).

Figure 2.11 shows the transmission spectra from several authors, including both one-stage sintering processes and two stage sintering processes. The spectra have been normalized using **Equation 2.8** to a thickness of 3mm. Cohen, et al.'s (2018) two stage sintering process produced a ceramic part with a transmission near the theoretical maximum. However, it included a 10-hour HIP post treatment. The other spectra are from single stage processes.

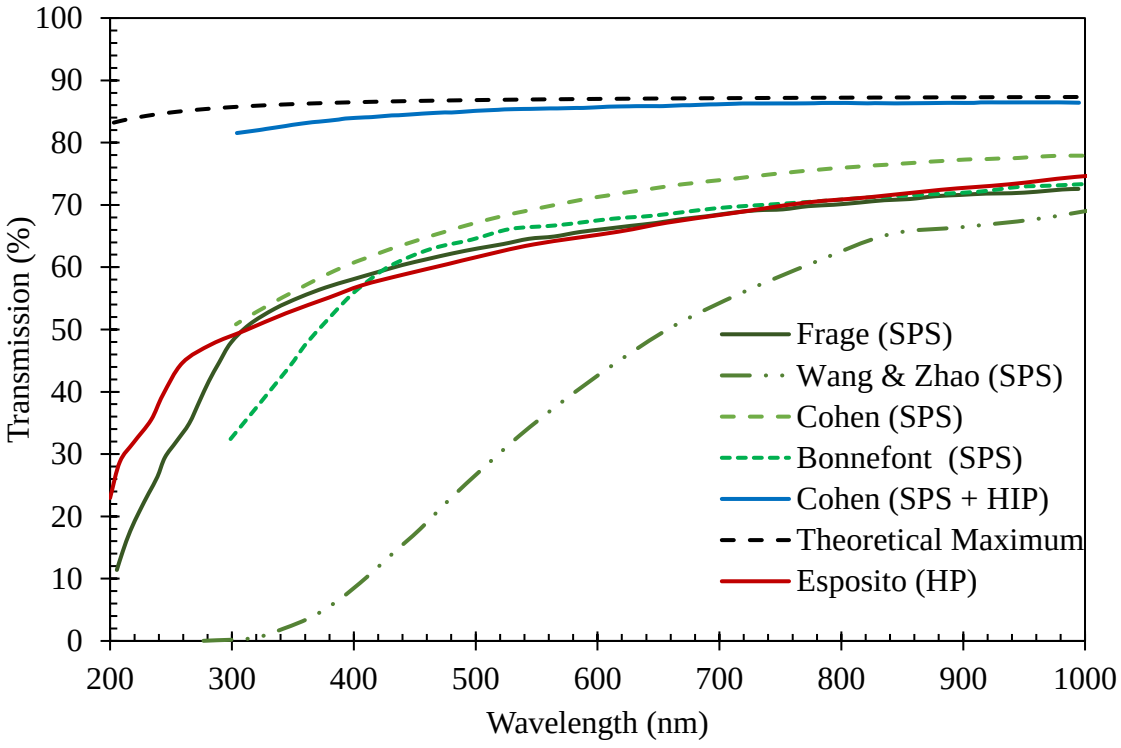


Figure 2.11: Transmission spectra from Frage, et al. (2007), Wang & Zhao, (2009), Bonnefont, et al. (2012), Esposito, et al. (2013), and Cohen, et al. (2018)

2.1.4. The Role of LiF

Multiple additives have been used to enhance the sintering of polycrystalline $MgAl_2O_4$ spinel. They include $CaCO_3$, CaO, LiF, B_2O_3, $AlCl_3$, AlF_3, $NaAlF_6$ (Meir, et al., 2008). Of these, LiF is commonly used when transparency is of importance. LiF has also been used to enhance the sintering kinetics of $SrTiO_3$, $BaTiO_3$, and MgO (Rozenburg, et al., 2007). Lithium fluoride is added in amounts of ~ 0.5 – 1.5wt.%, more than this can lead to a reduction in transmission as LiF remains trapped in the system (Esposito, et al., 2015). The LiF is added to the starting powders, which are either $MgAl_2O_4$ powder (Reimanis & Kleebe, 2007) or a mixture of the oxides Al_2O_3 and MgO (Meir, et al., 2008) (Esposito, et al., 2013).

The advantage of using a mixture of Al_2O_3 and MgO powders is that they are commercially available with low mean particle sizes (d_{50}s), have narrow particle size distributions, and have a high purity. Also, the formation of spinel from its oxides is accompanied by a volume expansion of 7.67%. This expansion is expected to aid in densification when there is an external pressure applied to the component as the expansion will be forced to close pores (Esposito, et al., 2013).

The beneficial effects of LiF addition to both spinel and separate oxide powders are widely discussed in literature, however, a consensus on the exact mechanism on how it aids sintering has not been agreed upon (Esposito, et al., 2015). The addition of LiF has been observed to promote the $Al_2O_3 + MgO \rightarrow MgAl_2O_4$ reaction, the densification of spinel and a reduction in carbon contamination (Meir, et al., 2008). Also, it has been reported that the use of LiF as a sintering aid results in spinel which has a substantially higher Al content (Huang & Sun, 1997) (Rozenburg, et al., 2007).

2.1.4.1. Promoting the reaction

Meir et al. (2008) compared the formation of spinel from the oxide powders with and without the addition of LiF. They heated samples to a given temperature in an air furnace. Once the specified temperature was reached the samples were cooled and analysed. They repeated this procedure using an SPS furnace. They also heated samples and held them for 60 minutes at a specified temperature in an SPS furnace. The results unambiguously show that the addition of LiF assists in the spinel formation reaction, **Figure 2.12**.

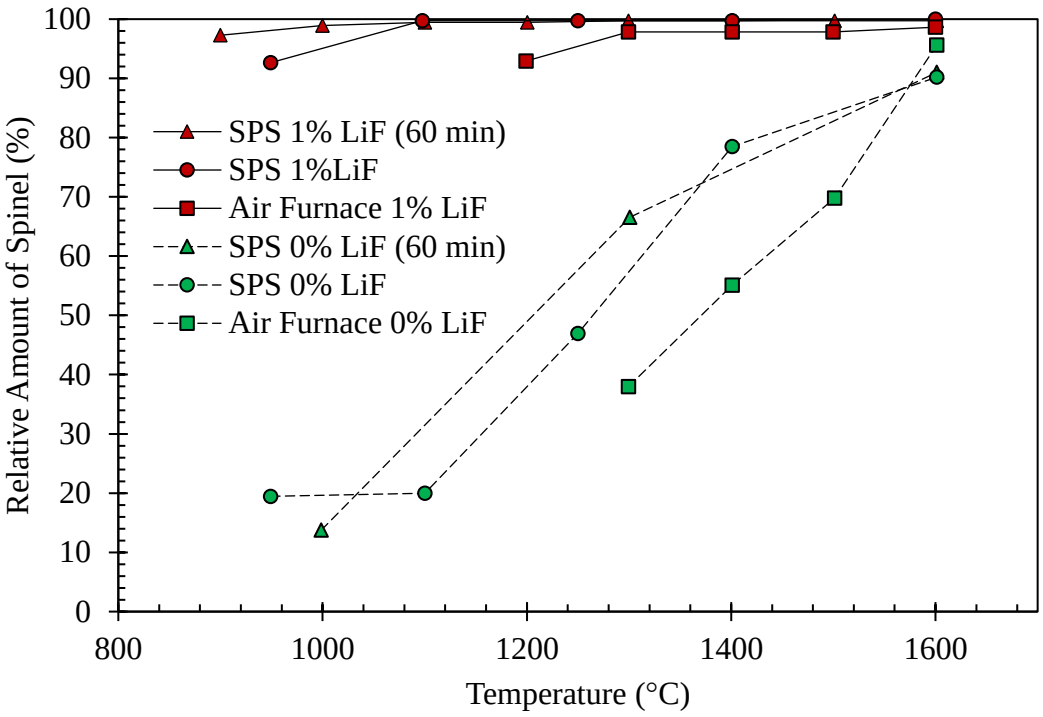


Figure 2.12: Relative amount of spinel formed at a given temperature (Meir, et al., 2008).

For all experiments the addition of 1wt.% LiF decreased the temperature at which the spinel formation reaction was complete regardless of the furnace used. The samples containing LiF, sintered by an SPS furnace completed the reaction at a temperature ~ 500°C lower than the samples without LiF in the same furnace (Meir, et al., 2008).

Esposito et al. (2015) analysed a powder mixture containing 1wt.% LiF and equal molar amounts of MgO and Al_2O_3 using high temperature X-ray diffractometry. They found that the onset of the reaction leading to spinel formation occurred between 900° – 1000°C and that the reaction was complete by 1400°C (Esposito, et al., 2013), which corroborates the results of Meir, et al. (2008).

Huang & Sun (1997) analysed an alumina rich mixture of Al_2O_3 and MgO with 2wt.% LiF using in-situ high-temperature X-ray diffractometry. They observed that when the LiF was not present, the spinel phase only started forming at 1000°C, and that the addition of LiF reduced this temperature.

Esposito et al. (2013) attempted to elucidate the reaction mechanism by analysing the effect of LiF using the Themocalc software. They found that the addition of LiF caused the endothermic spinel formation reaction between MgO and Al_2O_3 to become exothermic between 400° –

1000°C. The reaction proposed by Esposito, et al. (2013) between LiF and the oxides at ≈900°C can be written as:

$$3LiF_{(l)} + MgO_{(s)} + Al_2O_{3\,(s)} \rightarrow LiF{:}MgF_{2\,(l)} + 2LiAlO_{2\,(s)} \quad \textbf{Equation 2.9}$$

The presence of the liquid phase is expected to assist in the spinel formation reaction as mass transport is considerably more rapid than solid-state diffusion (Huang & Sun, 1997). And the presence of $LiAlO_2$ is expected to enhance atomic diffusion due to the formation of oxygen vacancies (Rozenburg, et al., 2007), thus increasing the rate of the reaction.

Upon increasing the temperature to ~1050°C, both the LiF and the MgF_2 are converted to vapour phases (Rozenburg, et al., 2007). The MgF_2 vapour can react with $LiAlO_2$ precipitating spinel and releasing LiF vapours via the reaction shown in **Equation 2.10** (Esposito, et al., 2013):

$$2LiAlO_{2\,(s)} + MgF_{2\,(g)} \rightarrow 2LiF_{(g)} + MgAl_2O_{4\,(s)} \quad \textbf{Equation 2.10}$$

The reformation of spinel, **Equation 2.10**, would be expected to occur at high-energy areas, such as small pores, triple points and the necks between sintering grains (Rozenburg, et al., 2007). However, the presence of $LiAlO_2$ has not yet been detected in samples containing <10wt.% LiF. Reimanis & Kleebe (2007) analysed samples containing 1 and 5wt.% LiF sintered at temperatures of 800°C, 900°C, 1000°C and 1550°C using high-resolution TEM and EDS. They could not confirm the presence of any $LiAlO_2$. In a later paper Esposito, et al. (2015) found that the carbon environment in a hot press discourages the formation of $LiAlO_2$ and concluded that its formation is unlikely in the presence of carbon.

Al_2O_3 and LiF may also react to form $LiAl_4FO_6$. This $LiAl_4FO_6$ has the same symmetry as $MgAl_2O_4$, Fd3m, and has a similar lattice parameter, 7.925Å. This makes the phase nearly invisible when analysing samples made predominantly of $MgAl_2O_4$ using X-ray diffractometry (Rozenburg, et al., 2007).

Therefore, it has been established that the LiF aids in the spinel formation reaction, however a satisfactory mechanism, at low LiF concentrations, has yet to be determined or confirmed.

2.1.4.2. Promoting Densification

In addition to aiding in spinel formation, LiF has been observed to aid in the densification process. Meir, et al. (2008) found that SPS sintered spinel samples with LiF attained full density

at 1400°C, while samples without LiF reached the same density only when the temperature had increased to 1600°C. The term ‘full density’ is often used in literature, however, in the context of transparent spinel the term is ambiguous. The transmission of a spinel component can vary substantially when the density differs by fractions of a percent. Therefore, it would be beneficial if authors would include the measured relative density, rather than stating that the component was fully dense.

By measuring the piston displacement during SPS sintering, Meir, et al. (2008) detected a sudden increase in the densification of the samples containing LiF at ~870°C. This temperature corresponds to the melting temperature of the LiF (847°C) which indicates that the addition of LiF may improve the densification rate by liquid phase sintering at relatively low temperatures (Meir, et al., 2008). This mechanism was further verified by several sessile drop tests. The sessile drop tests were done to determine the extent to which liquid LiF wets the spinel once it melts. They found that once the LiF melts, its wetting angle drops close to 0°. Thus, Meir, et al. (2008) concluded that after the LiF melts, it easily infiltrates the pores of the spinel preform with the assistance of capillary forces and aids the initial densification of the porous body. Esposito, et al. (2015) similarly concluded that that LiF promotes densification though liquid phase sintering, facilitating particle sliding and aiding in the release of jamming.

The addition of LiF has been found to result in more intergranular fracture than transgranular fracture (Reimanis & Kleebe, 2007). It is also known that most of the spinel lattice impurities tend to segregate towards surfaces, including grain boundaries (Goldstein, 2012) and that LiF is active at the interface between the spinel grains (Rozenburg, et al., 2007). Therefore, it could be expected that the LiF would be found at grain boundaries, as is common when species aid by liquid phase sintering. This would also explain the preference for intergranular fracture. However, through their HR-TEM analysis Reimanis & Kleebe (2007) detected no amorphous phase at the grain boundaries, rather the amorphous phase was only observed in relatively large pockets such as triple junctions. They concluded that the liquid phase sintering does not proceed by the classical mechanism and suspected that the densification occurred by another mechanism at elevated temperatures.

In a set of densification experiments Rozenburg, et al. (2007) calculated the activation energy for densification of spinel with varying amounts of LiF and at different pressures, using the Master Sintering Curve (MSC) theory (Su & Johnson, 1996). They calculated that the

specimens with no LiF had the highest activation energies (~480kJ/mol), and that the value of the calculated activation energy was similar to that for the diffusion of oxygen in spinel (430 to 490kJ/mol). The addition of LiF lowered the activation energy for densification significantly to <300kJ/mol (Rozenburg, et al., 2007). From this, it was been inferred that the rate-determining mechanism in spinel densification is oxygen lattice diffusion (Rozenburg, et al., 2008).

At elevated temperatures small spinel grains are expected to dissolve in the liquid phase, and then reprecipitate. This causes the incorporation of Li^+ cations and F^- anions in the spinel matrix, forming a distorted structure with excess oxygen vacancies (Rozenburg, et al., 2008):

$$3LiF \xrightarrow{Spinel} Li'_{Mg} + 2Li''_{Al} + 3F_O^{\cdot} + V_O^{\cdot\cdot} \qquad \textbf{Equation 2.11}$$

The generation of the oxygen vacancies lowers the energy required for oxygen lattice diffusion, therefore enhancing spinel densification (Rozenburg, et al., 2008). The grains that form through the reprecipitation process contain more oxygen vacancies and are expected to grow at an enhanced rate. This has been used as an explanation for the observation that the grain size distribution of spinel sintered in the presence of LiF is bimodal (Reimanis & Kleebe, 2007) (Rozenburg, et al., 2008). The grains that contain the oxygen vacancies grow at an enhanced rate relative to the grains that do not.

Rothman, et al. (2014) consolidated $MgAl_2O_4$ powders using an SPS furnace in which they varied the heating rate, sintering time, LiF content, and applied pressure. They also observed the bimodal grain size distribution (**Figure 2.13**), but they attributed it to the inhomogeneous spread of LiF throughout the powder.

The bimodal grain size distribution was observed for the sample in which the sintering temperature was 1400°C and had a sintering time of 60 minutes. When the temperature was increased to 1500°C and the sintering time increased to 120 minutes, the small particle fraction nearly entirely disappeared, and thus resulted in a wide but single mode grain size distribution.

Figure 2.14 shows the effect increasing the sintering temperature with and without the addition of LiF has on the average grain size. The average grain size of the LiF-doped specimens increased from 5 – 6 µm to about 35 – 45µm when the temperature increased from 1300°C to 1500°C. The standard deviation of the grain size is larger for the LiF doped samples compared to the undoped samples (comparing the length of the error bars). This could be because of the

bimodal microstructure caused by LiF, which would result in a greater spread of the grain sizes. Also, the effect of grain coarsening caused by the addition of LiF becomes significant when the sintering temperature is high (≥1500°C), at lower temperatures it is less pronounced.

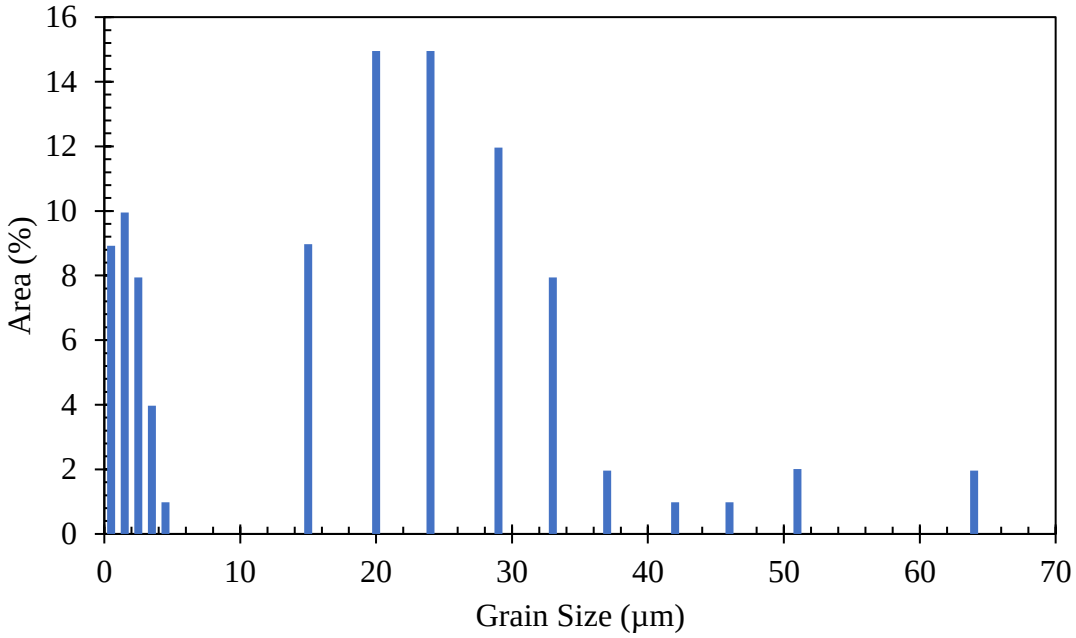


Figure 2.13: Area percent distribution of spinel grains obtained by Rothman, et al. (2014).

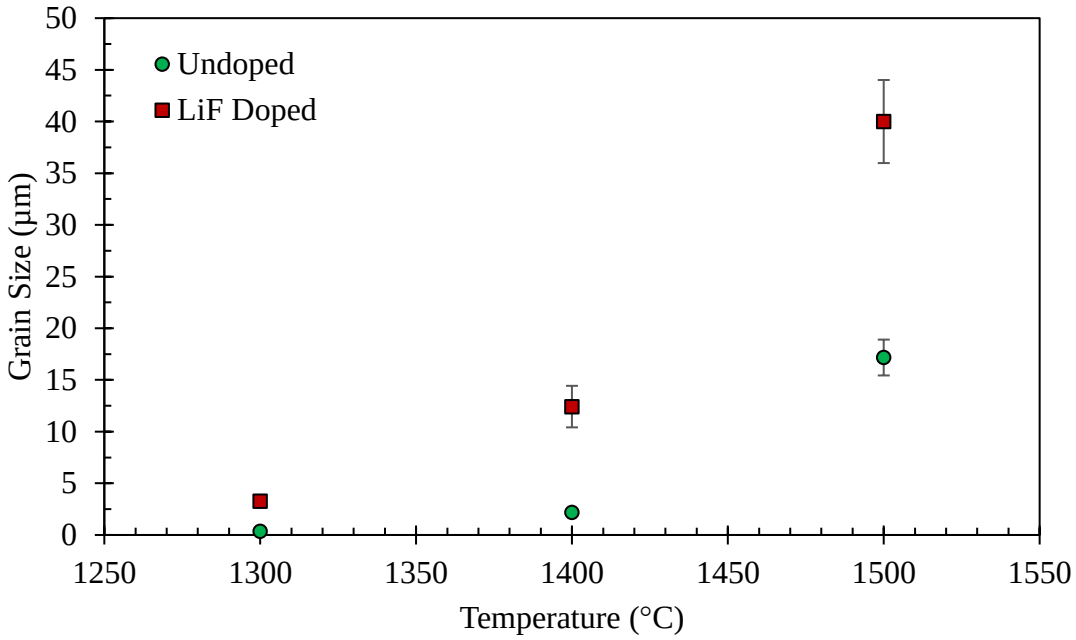


Figure 2.14: Effect of sintering temperature on grain size in the presence and absence of LiF (Rothman, et al., 2014).

Rothman et al. (2014) also noticed that the heating rate was significant when the LiF was added. Slower heating rates led to extensive grain growth. This is to be expected as the slower the heating rate, the more time the LiF has to incorporate into the $MgAl_2O_4$ structure thus enabling enhanced grain growth. When LiF was not added, the heating rate did not significantly affect the grain size under the same conditions (Rothman, et al., 2014). This corroborates the hypothesis put forward by Rozenburg et al. (2008), that including a lengthy step at low pressure at ~900°C increases grain coarsening significantly as there is prolonged contact of the fluoride melt with the spinel.

2.1.4.3. Promoting Carbon Cleaning

The LiF also aids in the purity of spinel as it acts as a carbon "cleaner". In an SPS furnace the powder is in direct contact with carbon dies, which also act as the heating elements. A common problem when sintering with these furnaces is that the samples have a grey hue and contain dark spots within their body (Goldstein, 2012). Meir, et al (2008) initially expected that residual oxygen within the furnace chamber would react with the graphite dies forming carbon oxides. The gaseous carbon oxides would then be trapped in pores that close during densification. Then, via the reversible endothermic reaction, **Equation 2.12**, carbon would be deposited within the spinel.

$$2CO \leftrightarrow C + CO_2 \qquad \textbf{Equation 2.12}$$

However, after further analysis, Meir, et al (2008) determined that this would not result in the large amount of carbon contamination found within the samples. Thus, the contamination was attributed to plasma induced carbon deposition originating from the graphitic dies. However, this is a dubious explanation as the presence of a plasma has yet to be confirmed during the SPS process (Munir, et al., 2006).

The addition of LiF has been observed to reduce the degree of carbon contamination, resulting in an increase in transmission. The carbon cleansing effects of the LiF were demonstrated in an experiment conducted by Meir, et al. (2008) where a powder with no LiF was placed atop graphite foil with a 1mm diameter hole in its centre. Underneath this graphite foil some LiF was placed. This system was then sintered in the SPS furnace. The area accessible to the LiF vapour was more transparent than the rim of the sample which had a grey/brown hue. Therefore, it was expected that it was the LiF vapour which caused the carbon cleaning. The interaction between the LiF vapour and the residual carbon is given by **Equation 2.13**.

$$nLiF + nC \rightarrow nLi + (CF)n \uparrow \qquad \textbf{Equation 2.13}$$

This implies that the F^- ions are removed from the system while the Li^+ ions remain. This is difficult to verify as EDS cannot detect lithium. Meir, et al. (2008) adapted the equation put forward by Reimanis & Kleebe (2007) (**Equation 2.11**) as only Li^+ ions would be incorporated into the spinel lattice as the F^- anions would leave the system with the carbon as gaseous carbon mono-fluoride.

$$3Li \xrightarrow{Spinel} 2Li'_{Mg} + Li''_{Al} + 2V_O^{\cdot\cdot} \qquad \textbf{Equation 2.14}$$

As the reaction shown in **Equation 2.14** still results in the formation of oxygen vacancies the results are still consistent with those of Reimanis & Kleebe (2007).

However, Esposito, et al. (2015) argue against the LiF vapour mechanism. Instead they state that the LiF liquid protects against carbon contamination rather than acting as a carbon cleanser. Esposito, et al. (2015) modelled the Al_2O_3 – MgO – LiF system using the Thermocalc software and determined that the CF_x compounds are unlikely to cause the cleansing effect. The calculated partial pressure of CF_x compounds was too low to result in the substantial cleaning. They postulate that the molten LiF forms a thin film that is effective at shielding the carbon contamination and state that the low wetting angle of LiF on spinel further justifies this explanation (Esposito, et al., 2015). Then by the time the LiF is incorporated into the spinel lattice, enough densification has occurred to prevent extensive carbon contamination in the body of the spinel.

2.1.5. Mechanical Properties

When measuring the mechanical properties of the spinel samples, the detrimental effect of the grain coarsening caused by LiF becomes apparent. Materials with sub-micrometre grains had hardness values up to 1600 ± 28Hv, while samples with grain sizes between 5 to 50µm had an average hardness of 1450Hv (Rothman, et al., 2014). The bending strength also decreased as the grain size increased, and the data fit the Hall-Petch relation with a correlation coefficient of R^2 =0.81. The elastic modulus was not affected by the grain size and had a value of ~280GPa for all samples (Rothman, et al., 2014). Rothman, et al. (2014) claim that the transmittance was strongly affected by the average grain size and gave **Figure 2.15** as proof.

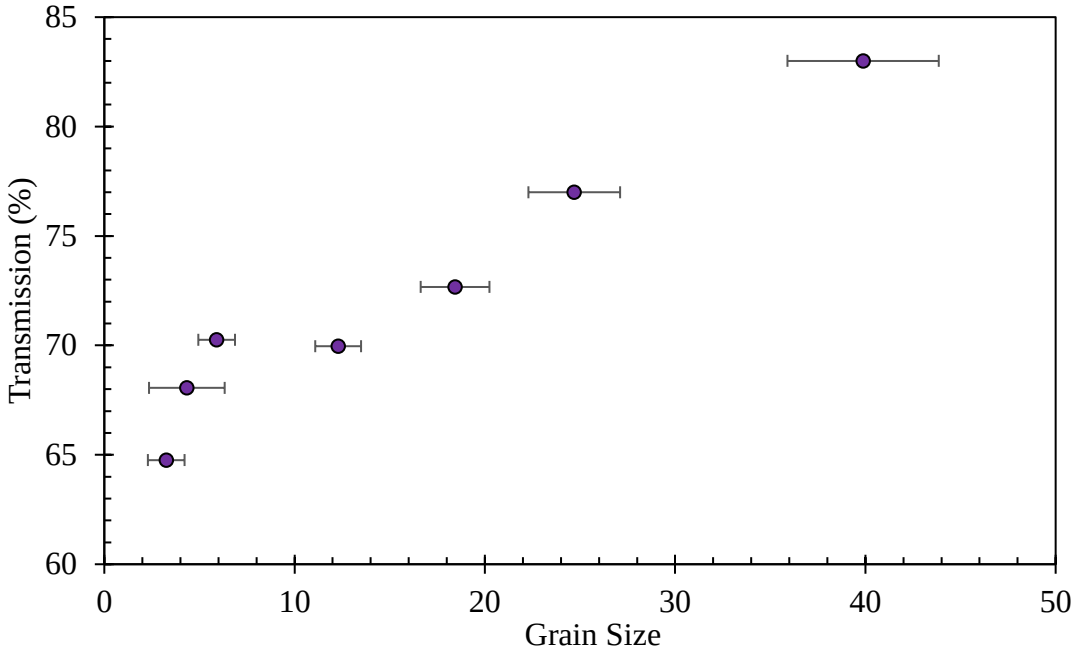


Figure 2.15: Transmittance as a function of grains size (Rothman, et al., 2014). Sample thickness 1.5mm at a wavelength of 1000nm.

It is the opinion of this author that this conclusion was questionable. The reason being that the average grain size can be increased by the addition of LiF, longer sintering times, and higher sintering temperatures. These three factors are also known to increase densification, and thus reduce porosity. As there was no data given showing that the samples with different grain sizes had the same density, it would be incorrect to conclude from **Figure 2.15** that the average grain size was responsible for the change in transmittance. The samples with the larger grains are likely denser. Therefore, it cannot be concluded that the transmittance is strongly affected by the average grain size. It seems more likely that the cause of the increase in grain size also increased the extent of densification. It follows that the increase in densification then increased transmission. Therefore, until grain size can be decoupled from porosity, quantitating the effect of grain size on transmission is questionable.

What is apparent from the results of LiF experiments is that LiF plays a substantial and crucial role in the densification of spinel. In-order to achieve maximal transparency, the initial stage of sintering, where pressure and temperature are increasing to the maximum, needs to be tailored to the conditions ideal for the LiF. If the pressure is increased early and rapidly, the diffusion paths for the LiF are reduced, trapping residual LiF and any gaseous products of

chemical reactions in the ceramic body. This has deleterious effects on transmission (Rozenburg, et al., 2008). Therefore, in-order to ensure the gaseous LiF can leave the system it is important to maintain an open pore system while the partial pressure of LiF is high. Meir, et al. (2008) suggest that application of high external pressure should only occur once high temperatures (>1200°C) have been reached. For Meir, et al. (2008) maximal transparency was achieved when a progressively increasing pressure was applied at 1600°C at a rate of approximately 8MPa/min up to 64MPa.

As shown in **Figure 2.11** (**pp. 20**) Cohen, et al. (2018) achieved very high transmission for their two-stage approach and relatively high transmission for their single-stage approach. Cohen et al. (2018) consolidated spinel powder, with the aid of 0.6wt.% LiF, using the SPS furnace. The relatively thick sample (4mm) sintered at 1400^{o}C at 50MPa for 2 hours exhibited a non-homogenous cloudiness. The periphery had a higher transmission than the centre of the sample, **Figure 2.16.a**. This was attributed to the thermal gradient which exists in non-conductive samples consolidated by the SPS (Cohen, et al., 2018). The cloudiness was removed by a 10h HIP post-treatment at 1500^{o}C **Figure 2.16.b**.

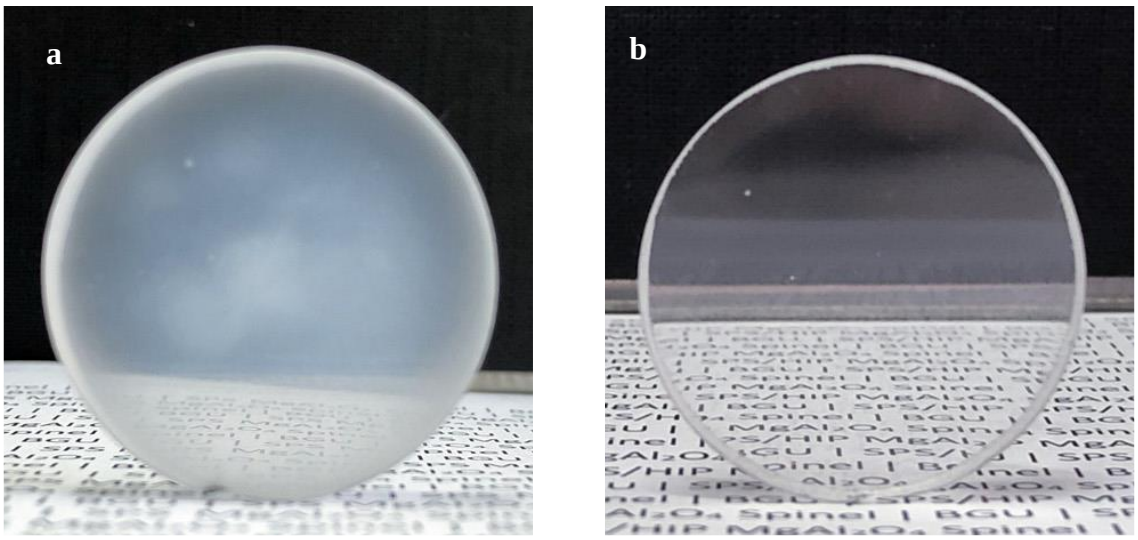


Figure 2.16: Photographs of the (**a**) SPSed sample and (**b**) after the HIP post-treatment (Cohen, et al., 2018).

The SPSed samples contained both small pores 100 – 200nm and large pores 300 – 500nm. The pores were concluded to be the cause for the cloudiness and reduced transparency of the samples prior to the HIP treatment. After the HIP treatment, there was a reduction in the number of pores, however, the remaining pores were much larger, 500 – 1000nm, which was likely the

result of pore coalescence at triple points (Cohen, et al., 2018). Thus, the scatter caused by Rayleigh scattering would have been reduced. As the samples did not have the theoretical maximum transmittance it is likely that the remaining scatter was caused by Mie scattering (Cohen, et al., 2018).

High heating rates (50 and 100^{o}C/min) resulted in grey discoloration of the samples. Cohen, et al. (2018) postulate that this grey discoloration was caused by carbon contamination originating from the graphitic components of the SPS furnace, which agrees with the opinion of Meir, et al. (2008). Cohen, et al. (2018) therefore conclude that increasing the heating rate, increases carbon contamination, which is in agreement to the work done by Morita, et al (2008). Unexpectedly, they found that the transparency was once again higher at the periphery than the centre of the sample. This is counterintuitive as the periphery was in direct contact with the source of carbon, whereas the centre was not. The HIP post treatment did not remove the grey discoloration, like it did with the cloudiness shown in **Figure 2.16**.

The HIP post treatment led to extensive grain growth, especially at 1800^{o}C. The grains grew from an average of ~ 50µm to ~140µm. When the HIP post treatment occurred at 1500^{o}C, the grains only grew to ~70µm (Cohen, et al., 2018). The SPSed samples had a transmission of 66.6% at 600nm and a substantially lower transmission at lower wavelengths, 42.3% at 300nm. While the HIP treated samples had a transmission of 81.7 to 85.2% at 600nm and maintained the transmission at lower wavelengths as well (Cohen, et al., 2018), **Figure 2.11**, **pp 20**.

2.1.6. Production Insights Summary

To achieve a high level of transparency with a single stage sintering cycle, long sintering times are unavoidable. This is because of the extremely low porosity that is required to achieve a high in-line transmission. However, due to the graphitic tooling of the SPS, long sintering times necessitate the addition of LiF. Without LiF carbon contamination is extensive. Also, one of the key benefits of the SPS furnace is the high heating rate that it can achieve. High heating rates have been found to increase carbon contamination when sintering spinel. This further justifies the need for LiF. Thus, it is essential to develop a sintering cycle that caters to the reactions that the LiF induces with either the oxide powders, MgO and Al_2O_3, or $MgAl_2O_4$ powder.

Initial high heating rates will be used as this would reduce the time liquid LiF has in contact with the spinel. This should reduce the extent of grain coarsening. Following this, an

intermediate step at which the temperature is held for a prolonged period should ensure that the LiF is given time to escape the system as a gaseous species. This should be done prior to the application of pressure to ensure the maximum level of open porosity. After this, the temperature and pressure should increase to a maximum to eliminate any residual porosity.

2.2. Zirconia Toughened Spinel

Besides the transparency of spinel, the strengthening of spinel by the addition of ZrO_2 was also investigated. Two developments have increased the applicability of ZrO_2 from a relatively niche field to a much more versatile one. The first development was that of the $ZrO_2 – Y_2O_3$ system. Ruff and Ebert (1929) first investigated the effect of yttria on the transformation of zirconia from the high temperature tetragonal phase to the room temperature monoclinic phase. Then in 1951 Duwez, et al. began attempts to develop a phase diagram for the $ZrO_2 – Y_2O_3$ system. In 1972 the ceramic engineering community began learning that Y_2O_3 (and other dopants) favoured either the metastable tetragonal or cubic phase over the monoclinic phase at room temperature (Kelly & Denry, 2008).

However, zirconia was still of very limited interest as a structural ceramic until 1975. Garvie, et al. (1975) discovered that the tetragonal to monoclinic transformation could be controlled by appropriate materials processing to induce transformation toughening. In their publication "Ceramic Steel?" a comparison highlighting the similarities between the transformation of zirconia and austenite-martensite strengthening of TRIP steels was made. The stress-induced martensitic transformation of ZrO_2 can considerably increase the fracture toughness of zirconia containing ceramics (Becher & Swain, 1992). This discovery led to a dramatic increase in ZrO_2 industrial applicability (Hannink, et al., 2000), which fuelled a great deal of research into the transformations of zirconia and the mechanisms which bring about transformation toughening.

Currently the commercial applications of ZrO_2-based materials include: femoral ball heads, dental restoratives, thrust bearings, extrusion dies and cutting tool inserts, milling media, seals, bearings in seal-less pumps, and knives and scissors used in paper industries (Basu, 2005).

2.2.1. ZrO_2 Crystallography

Zirconium dioxide (ZrO_2) is a binary oxide. The polymorphs of ZrO_2 are monoclinic, tetragonal, cubic, and orthorhombic phases. The monoclinic phase is thermodynamically stable at ambient pressures and temperatures. When heated it transforms to the tetragonal phase, if heating continues, the tetragonal phase will transform to the cubic phase. When the monoclinic phase is subjected to high pressures (above 3.5GPa) it can transform into multiple orthorhombic phases depending on the magnitude of the pressure (Graeve, 2008). **Table 2.3** gives the crystallographic data for the principal polymorphs (the monoclinic, tetragonal, and cubic phases) and **Figure 2.17** shows their unit cells. The Crystallographic Information Files

(CIFs) were taken from the Crystallography Open Database (COD), and the data for the CIFs for the monoclinic, tetragonal, and the cubic phases are referenced from Smith & Newkirk (1965) (COD ID: 9007485), Lutterotti & Scardi (1990) (COD ID: 2300612) and Martin, et al. (1993) (COD ID: 5000038), respectively. The CIFs and the VESTA 3 software were used to generate the images of the crystallographic structures.

Table 2.3: Crystallographic data for ZrO_2

Unit Cell	Monoclinic*	Tetragonal†	Cubic‡
Formula Units Per Unit Cell	4	2	4
Space Group	$P2_1/c$	$P4_2/nmc$	Fm3m
a (Å)	5.1454	3.5961	5.1290
b (Å)	5.2075	3.5961	5.1290
c (Å)	5.3107	5.1770	5.1290
β (°)	99.23	90.00	90.00
V ($Å^3$)	140.5	66.95	134.9
Theoretical Density (g/cm^3) §	5.83	6.11	6.07

* From Smith & Newkirk (1965); † From Lutterotti & Scardi (1990); ‡ From Martin, et al. (1993); § Densities were calculated using the corresponding crystallographic data.

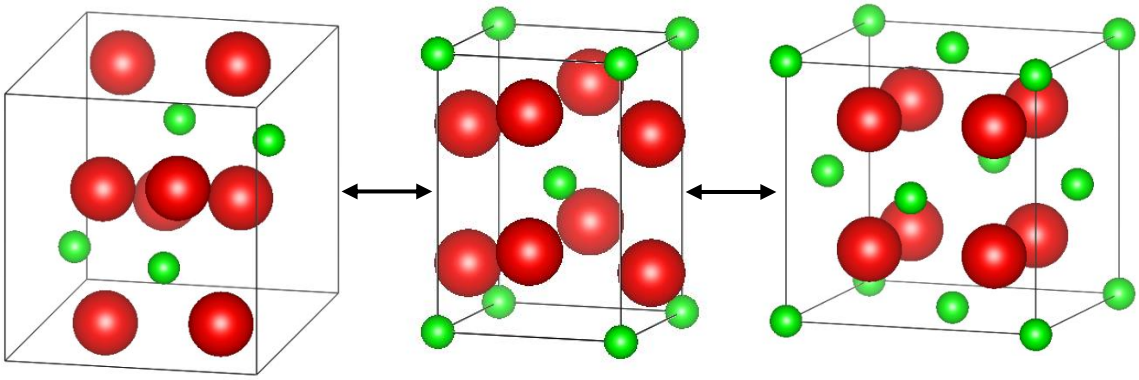


Figure 2.17: Unit cells of the ZrO_2 polymorphs. (The oxygen is the red sphere, and the zirconium is the green sphere. This convention is kept throughout).

2.2.1.1. Monoclinic Structure

In the monoclinic structure, the distances between the Zr^{4+} ion and the O^{2-} ions ranges from 2.04 to 2.26Å for the seven nearest neighbours. The distance of the next nearest neighbour is

3.77Å. Thus, the coordination number of the Zr^{4+} ion in the monoclinic phase is 7 (**Figure 2.18.a**). The structure consists of alternating layers of tetrahedrally coordinated oxide ions (denoted O_{II}, **Figure 2.18.b**) and layers of oxide ions in triangular planar coordination (denoted O_I, **Figure 2.18.c**) (Trueblood & McCullough, 1959). The extended structure is shown in **Figure 2.19**.

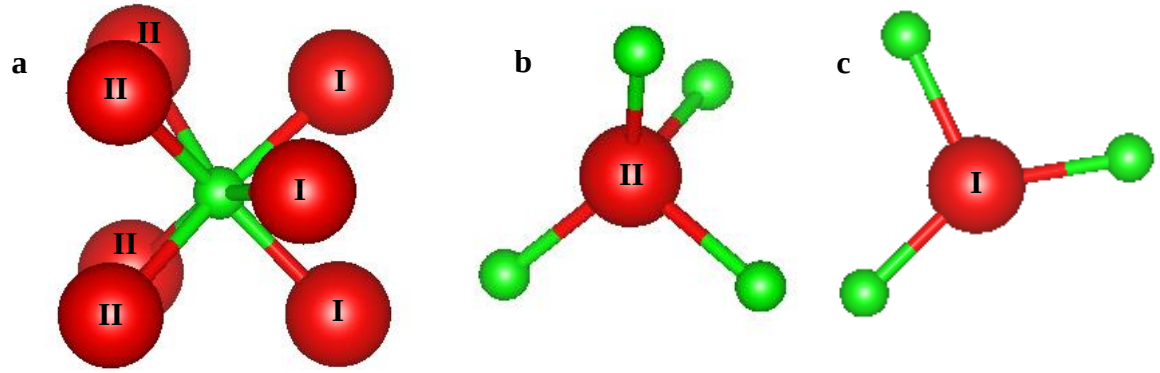


Figure 2.18: Nearest neighbour bonding for (**a**) the Zr^{4+} ions, (**b**) the O_{II} ions, and (**c**) the O_I ions.

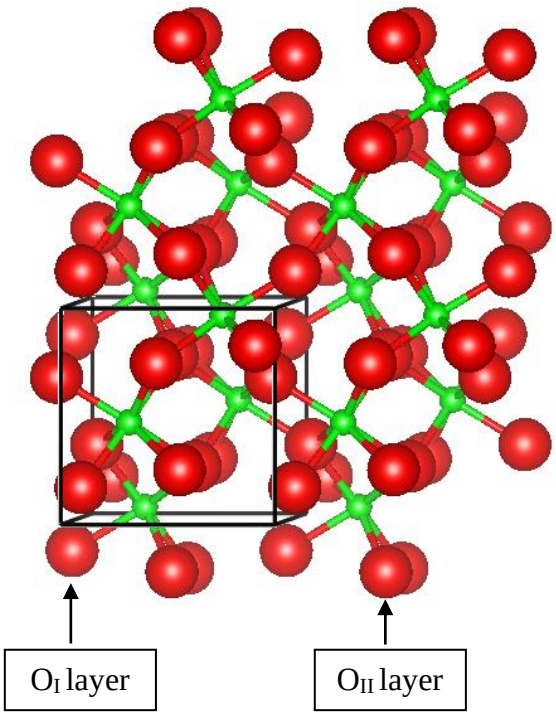


Figure 2.19: Alternating layers of O_{II} and O_I. The monoclinic unit cell is also shown as the black parallelepiped.

2.2.1.2. Tetragonal Structure

The Zr^{4+} ions in the tetragonal phase have a coordination number of eight, **Figure 2.20**.

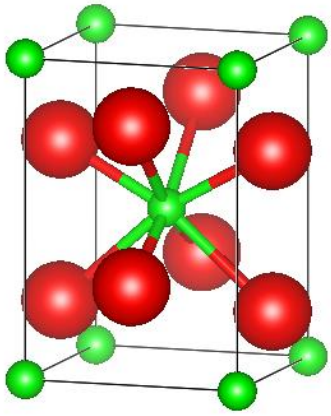
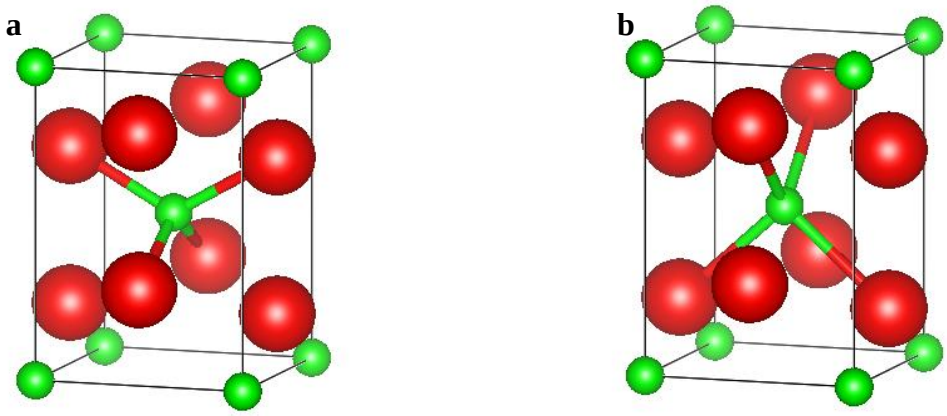


Figure 2.20: Tetragonal unit cell showing the coordination of the central zirconium atom.

Four oxygen ions are 2.065Å from the Zr^{4+} ion in a flattened tetrahedron (**Figure 2.21.a**), the other four are at a distance of 2.455Å and form an elongated tetrahedron which is rotated 90° relative to the former one **Figure 2.21.b** (Teufer, 1962).



Flattened Tetrahedron Elongated Tetrahedron

Figure 2.21: Tetragonal unit cell showing the (**a**) flattened tetrahedron and (**b**) the elongated tetrahedron.

2.2.1.3. Cubic Structure

Cubic zirconia has the fluorite structure, **Figure 2.22**. The Zr^{4+} ions occupy the lattice positions of a Face-Centred Cube (FCC) and the eight tetrahedral holes are occupied by the O^{2-} ions. The Zr^{4+} ions have a coordination number of 8 and the O^{2-} ions, 4 (Graeve, 2008).

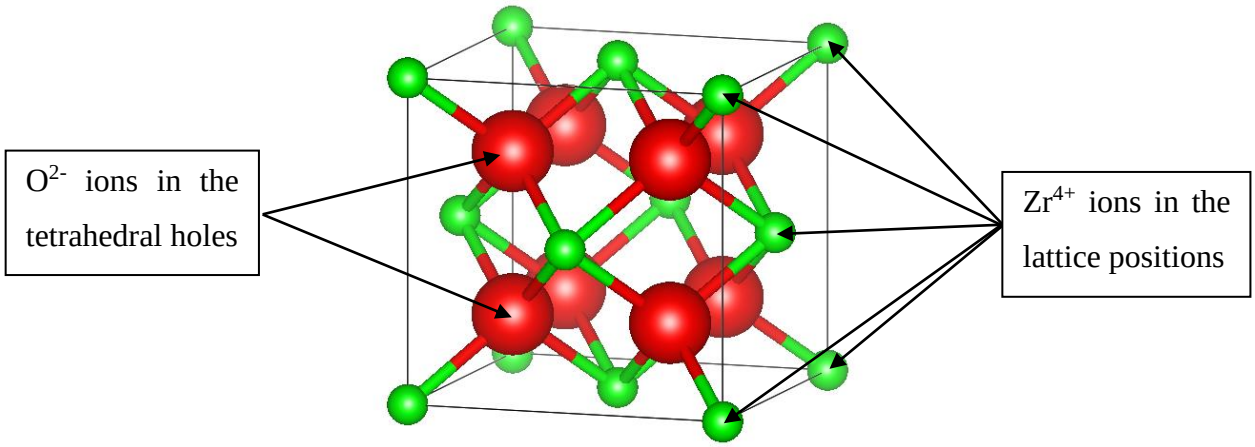


Figure 2.22: Face Centred Cubic (FCC) unit cell of ZrO_2.

2.2.2. Phase Transformations

The transformations between the principle polymorphs are martensitic in nature (Kelly & Denry, 2008). The transformations are diffusionless, occur athermally and involve both a shear strain and a volume change (Lange, 1982). The phases can also be represented in face-centred unit cells to highlight the changes that are made during the transformations, **Figure 2.23.** The corresponding unit cell parameters for the face-centred unit cells are given in **Table 2.4**.

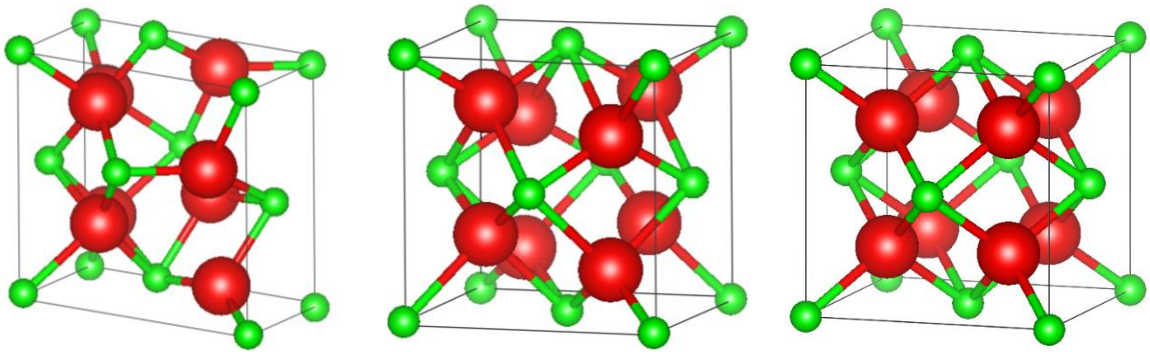


Figure 2.23: Face-centred unit cells of the polymorphs of ZrO_2.

Table 2.4: Unit cell parameters of the face-centred unit cells of the zirconia polymorphs.

Unit Cell	Monoclinic	Tetragonal	Cubic
a (Å)	5.1454	5.0860	5.1290
b (Å)	5.2075	5.0860	5.1290
c (Å)	5.3107	5.1770	5.1290
β (º)	99.23	90.00	90.00

2.2.2.1. Monoclinic to Tetragonal Transformation

The monoclinic to tetragonal transformation is generally destructive for pure zirconium oxide components (Ruh & Corfield, 1970). Sintered structures composed entirely of pure ZrO_2 undergo spallation with fragments disintegrating into multi-grained powders (Kelly & Denry, 2008). The damage arises from the shear strain and volume change accompanying the transformation (Shin, et al., 2018). This renders pure oxides useless for most structural applications. The monoclinic-tetragonal transformation follows a hysteresis (**Figure 2.24**).

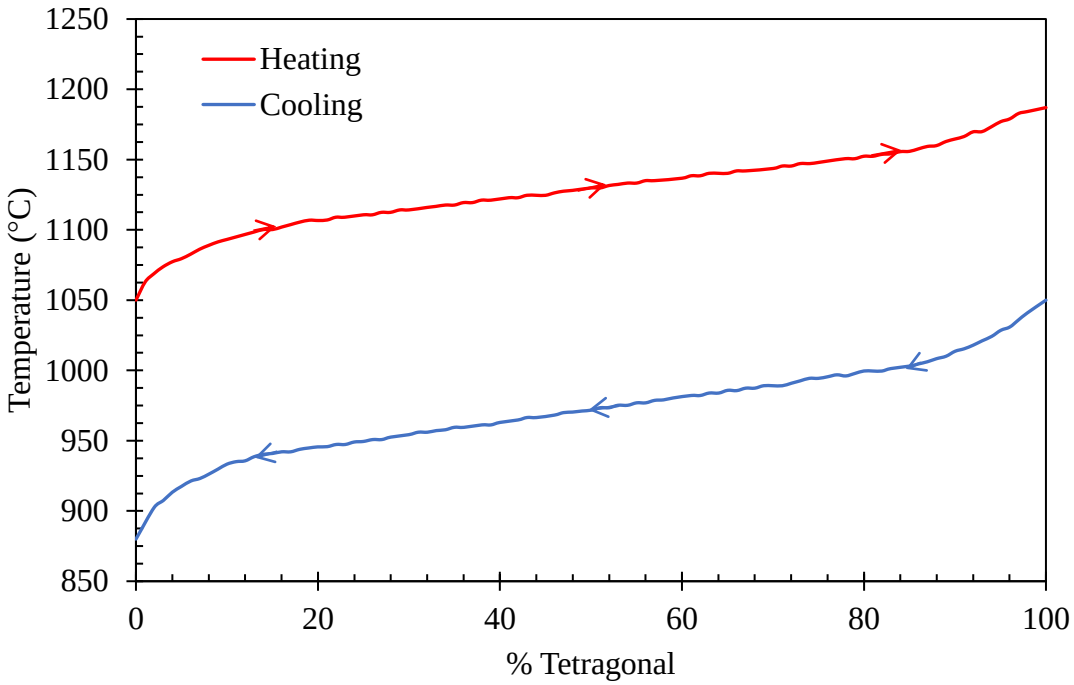


Figure 2.24: Hysteresis formed by the monoclinic to tetragonal transformation (heating) and the tetragonal to monoclinic transformation (cooling) (Ruh, et al., 1968).

The monoclinic-tetragonal transformation typically occurs from 1050ºC to 1187ºC, and the tetragonal-monoclinic transformation from 1050ºC to 880ºC. These values are sensitive to heat-treatment and transformation history (Ruh, et al., 1968). Aside from cooling, the tetragonal to monoclinic transformation can also be induced by an applied external pressure under isothermal conditions (Basu, 2005).

The large hysteresis observed (~200°C) is an indication of the semi-reconstructive transformation that occurs between the two phases. A significant difference between the two structures is the change in coordination number of the Zr^{4+} ion (from 7 to 8) and an O^{2-} ion (the

O_I^{2-} ion's coordination increases from 3 to 4). This change necessitates that some bonds be broken during the transformation (Smith & Newkirk, 1965).

Another change is that of the Zr^{4+} ions lattice positions. The crystallographic orientation relation between the monoclinic and tetragonal face centred unit cells (**Figure 2.23**) is given by $(110)_m \parallel (100)_t$ and $[100]_m \parallel [001]_t$ (Lange, 1982). This can be represented by an unconstrained strain tensor matrix, **Equation 2.15**.

$$\varepsilon^t = \begin{pmatrix} \dfrac{a_m \cos\left(\dfrac{90-\beta}{2}\right) - a_t}{a_t} & 0 & \tan\left(\dfrac{90-\beta}{2}\right) \\ 0 & \dfrac{b_m - a_t}{a_t} & 0 \\ \tan\left(\dfrac{90-\beta}{2}\right) & 0 & \dfrac{c_m \cos\left(\dfrac{90-\beta}{2}\right) - c_t}{c_t} \end{pmatrix} \quad \textbf{Equation 2.15}$$

Where $a, b,$ and c are the unit cell dimensions for either the tetragonal (t) or the monoclinic (m) phases and β is the monoclinic angle. **Equation 2.15** can be used to calculate the shear strain and volume increase associated with the transformation using the crystallographic data from **Table 2.4**. The calculation shows that the transformation involves a volume increase of ~5% and a shear strain of ~8% (Lange, 1982).

2.2.2.2. Tetragonal to Cubic Transformation

The tetragonal to cubic transformation occurs at 2285°C with a maximum hysteresis of 30°C. The small hysteresis implies a displacive transformation. The oxygen ions shift their positions but no change in bond configuration is required (Smith & Newkirk, 1965). The change in atomic positions is shown between **Figure 2.25.a** and **2.25.b**.

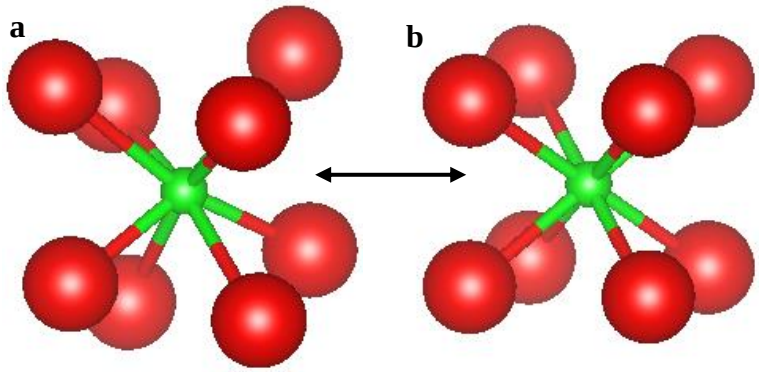


Figure 2.25: ZO_8 polyhedron in the (**a**) tetragonal phase and (**b**) the cubic phase.

2.2.3. The ZrO_2 – Al_2O_3 – MgO System.

In 1964, Bierezhnoi and Kordyuk first attempted to construct the ZrO_2 – MgO – Al_2O_3 phase diagram (Pavlyuchkov, et al., 2014). **Figure 2.26** shows the liquidus projection of the system. The projection consists of four phase fields: ZrO_2 (cubic), MgO, $MgAl_2O_4$, and Al_2O_3 (Pavlyuchkov, et al., 2014). The system shows the existence of two ternary eutectics as well as one eutectic maximum. **Table 2.5** provides the composition and temperature of the ternary eutectic reactions.

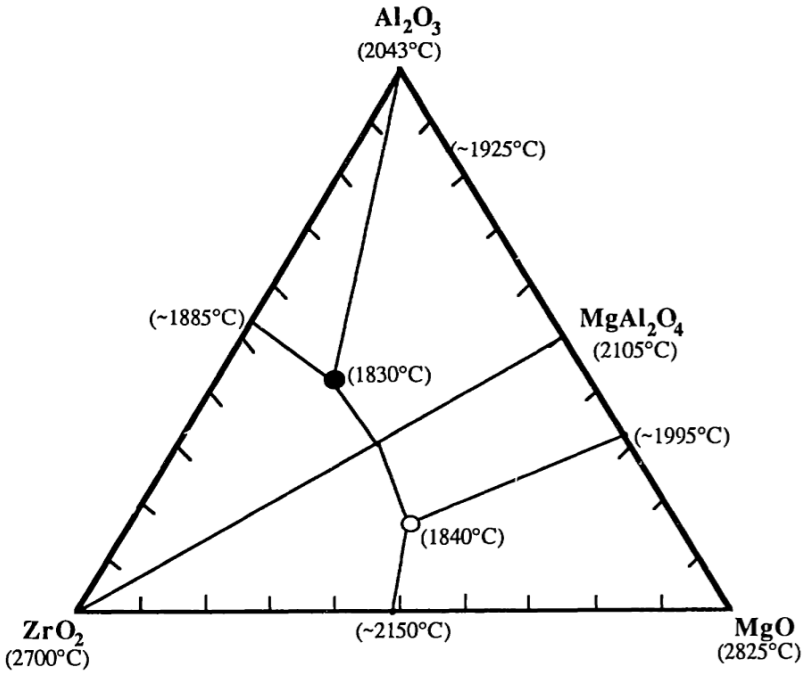


Figure 2.26: Liquidus projection of the ZrO_2 – MgO – Al_2O_3 system (McKittrick & Kalonji, 1997).

Table 2.5: Composition and temperature of the ternary eutectics (McKittrick & Kalonji, 1997).

Eutectic	Composition (mol %)			Temperature (°C)
	Al_2O_3	MgO	ZrO_2	
Al_2O_3 rich region	42.1	17.4	40.5	1830
MgO rich region	16.6	42.1	41.3	1840

Pavlyuchkov, et al. (2014) calculated the ZrO_2 – $MgAl_2O_4$ isopleth and compared it to the experimentally determined isopleth done by Shevchenko, et al. (1993). Both vertical sections are given in **Figure 2.27**.

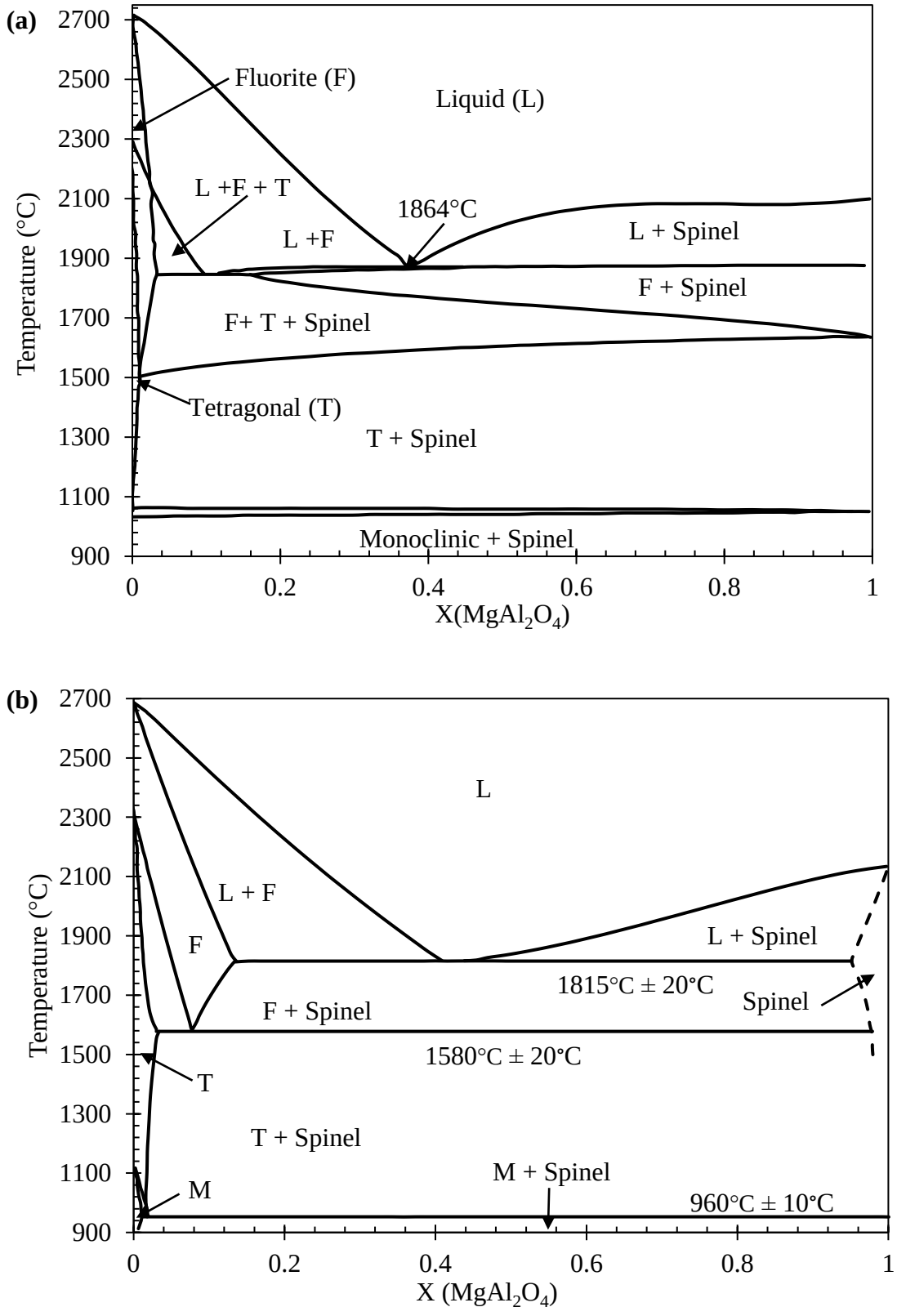


Figure 2.27: ZrO_2 – $MgAl_2O_4$ isopleth (**a**) calculated by Pavlyuchkov, et al. (2014) and (**b**) experimentally determined by Shevchenko, et al. (1993).

There is not a consensus on the whole system, especially at higher temperatures. However, in both phase diagrams there is phase field between ≈1000°C to 1500°C where both the tetragonal phase and the spinel phase are thermodynamically stable. This region is of importance as it indicates that a component can theoretically be made with the two separate phases present, as one phase will not wholly dissolve into the other.

2.2.4. Transformation Toughening

It has been observed that the stress-induced phase transformation of ZrO_2 can be utilised to increase the fracture toughness of a brittle material (Lange, 1982). The incorporation of metastable tetragonal-ZrO_2 into a ceramic's microstructure can engender transformation toughening (Hannink, et al., 2000). When the tetragonal zirconia is dispersed in a ceramic matrix, such as spinel, the material is classified as Dispersed Zirconia Ceramic (DZC). The most commercially developed DZC is zirconia-toughened alumina, **Figure 2.28** (Hannink, et al., 2000). The increase in toughness caused by transformation toughening has been found to be greater than the increase caused by particle or whisker reinforcement (Basu, 2005).

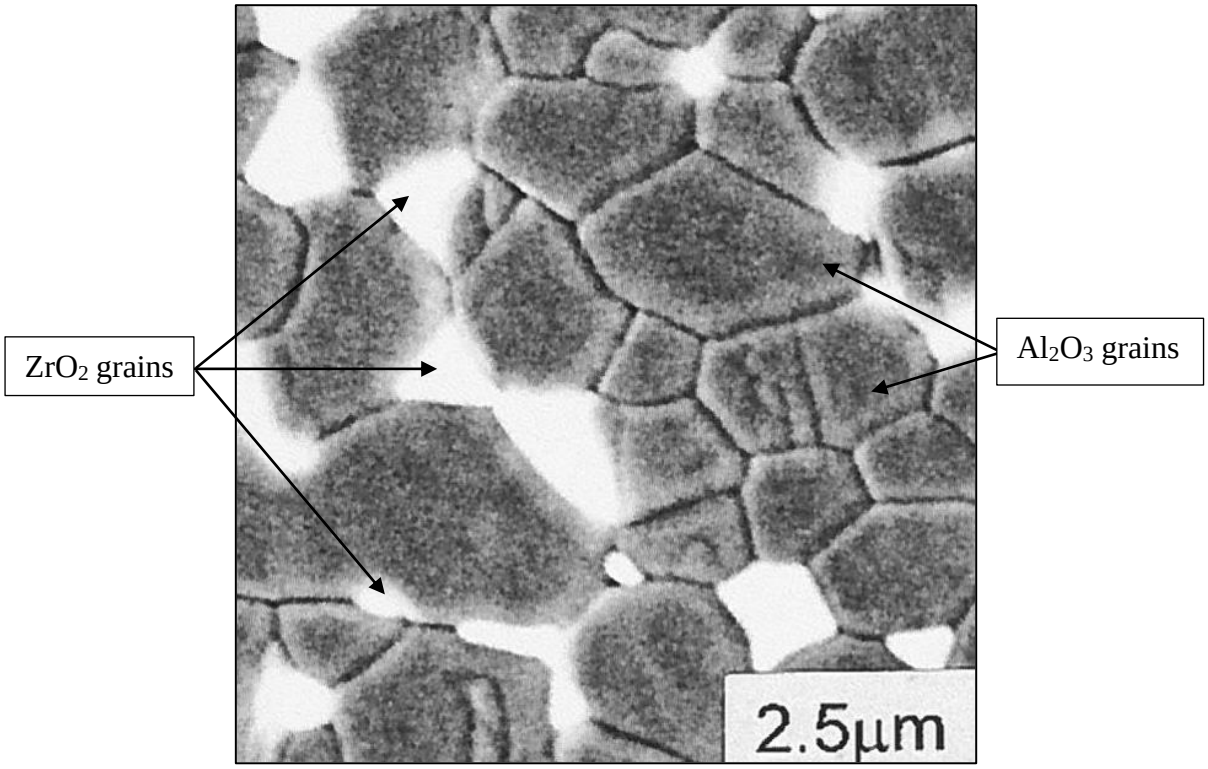


Figure 2.28: Microstructure of zirconia toughened alumina (Hannink, et al., 2000).

Transformation toughening is the process in which metastable tetragonal-ZrO_2 transforms to the stable monoclinic-ZrO_2 phase due to the tensile stress around a propagating crack, **Figure 2.29** (Basu, 2005). The volume change associated with the transformation creates a compressive stress field near the crack tip. The compressive stress opposes the tensile stress, thus lowering the driving force for crack propagation. This increases the effective toughness of the material (Basu, 2005). Also, strain energy associated with any net shear component of the transformation strain within the transformation zone contributes to the energy of fracture (Hannink, et al., 2000). Other contributions to the toughness could result from microcracking to accommodate the transformation shape strain and from crack deflection within the transformation zone ahead of the crack (Hannink, et al., 2000).

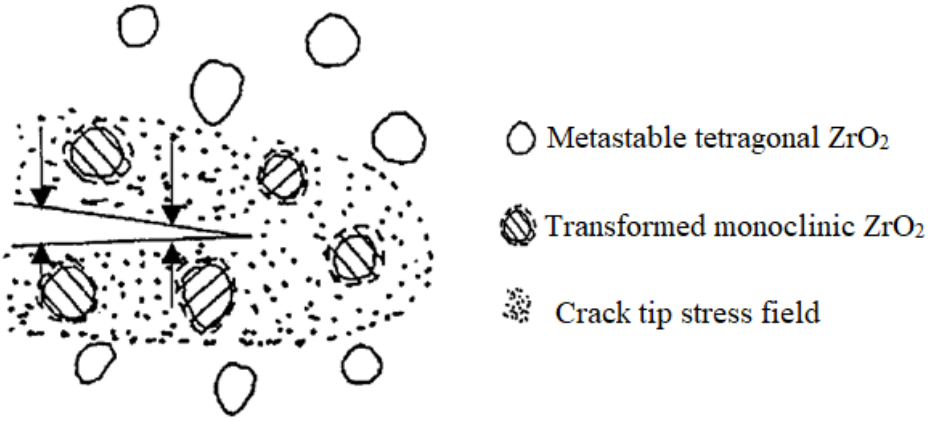


Figure 2.29: Schematic illustration of the stress induced transformation around the crack tip. The arrows indicate the compressive stress caused by the transformation (Basu, 2005).

The dispersed tetragonal grains' ability to transform to the monoclinic phase is central to the efficacy of transformation toughening. As such the "transformability" of the grains significantly affects the materials mechanical properties, especially the fracture toughness (Basu, 2005).

2.2.4.1. The Effect of Temperature

Lange (1982) developed a thermodynamic model for the transformation phenomenon. A state of stress arises in both the tetragonal inclusion and matrix when the tetragonal phase transforms to the monoclinic phase. This stress develops as a result of the constrained volume and shape changes. The differential free energy, $\Delta G_{t\rightarrow m}$, between the two states per unit volume of transformed material can be expressed by **Equation 2.16** or **2.17** (Lange, 1982).

$$\Delta G_{t\to m} = G_m^c - G_t^c + U_{se}^m - U_{se}^t + U_S^m - U_S^t \qquad \textbf{Equation 2.16}$$

Or

$$\Delta G_{t\to m} = \Delta G^c + \Delta U_{se} + \Delta U_S \qquad \textbf{Equation 2.17}$$

Where ΔG^c is the change in chemical free energy (dependent on temperature and composition of the ZrO_2), ΔU_{se} is the strain energy associated with the transformed particle (for the case considered here $U_{se}^t = 0$ and $\Delta U_{se} = U_{se}^m$) and the surrounding matrix, and ΔU_S is the change in surface energy (associated with the interface between the inclusion and the matrix) (Lange, 1982). Thus, the transformability of the tetragonal ZrO_2 is influenced by temperature and composition (the chemical free energy), the constraining matrix (the strain energy) and the grain size (the surface energy). The condition for transformation to occur is given by **Equation 2.18**.

$$-\Delta G^c \geq \Delta U_{se} + \Delta U_S \qquad \textbf{Equation 2.18}$$

As this will satisfy the thermodynamic requirement $\Delta G_{t\to m} \leq 0$. To quantify the effect of each term, the analysis begins by considering the case of an unconstrained grain, i.e. a grain that is not embedded in a matrix. For this case $\Delta U_{se} = 0$, and ΔU_S is assumed to be negligible. Therefore:

$$\Delta G_{t\to m} = \Delta G^c \qquad \textbf{Equation 2.19}$$

The chemical free energy term, ΔG^c, can be expressed as a function of test temperature, T and transformational entropy change, ΔS (Becher & Swain, 1992) (Kelly & Denry, 2008):

$$\Delta G^c = \Delta S(T_0 - T) \qquad \textbf{Equation 2.20}$$

ΔS has been found to have a value of -3.2J/mol.K for temperatures below 100°C (Becher & Swain, 1992). T_0 is the temperature at which an unconstrained, pure tetragonal grain begins to transform to the monoclinic phase. For a pure, unconstrained ZrO_2 grain, when $T > T_o$, the grain will be tetragonal. When $T < T_o$, the tetragonal grain will transform to the monoclinic phase.

2.2.4.2. The Effect of Alloying

The temperature at which the transformation will occur can be reduced by the addition of dopants. Certain dopants (Y_2O_3, Fe_2O_3, Ga_2O_3 and CeO_2 (Li, et al., 1994)) lower the

unconstrained chemical free energy change of the tetragonal phase relative to the monoclinic phase (Becher & Swain, 1992), i.e. ΔG^c decreases. Yttria-stabilised zirconia is the most studied and used system (Li, et al., 1993). The ZrO_2-rich portion of the ZrO_2 – Y_2O_3 system's phase diagram is given in **Figure 2.30**.

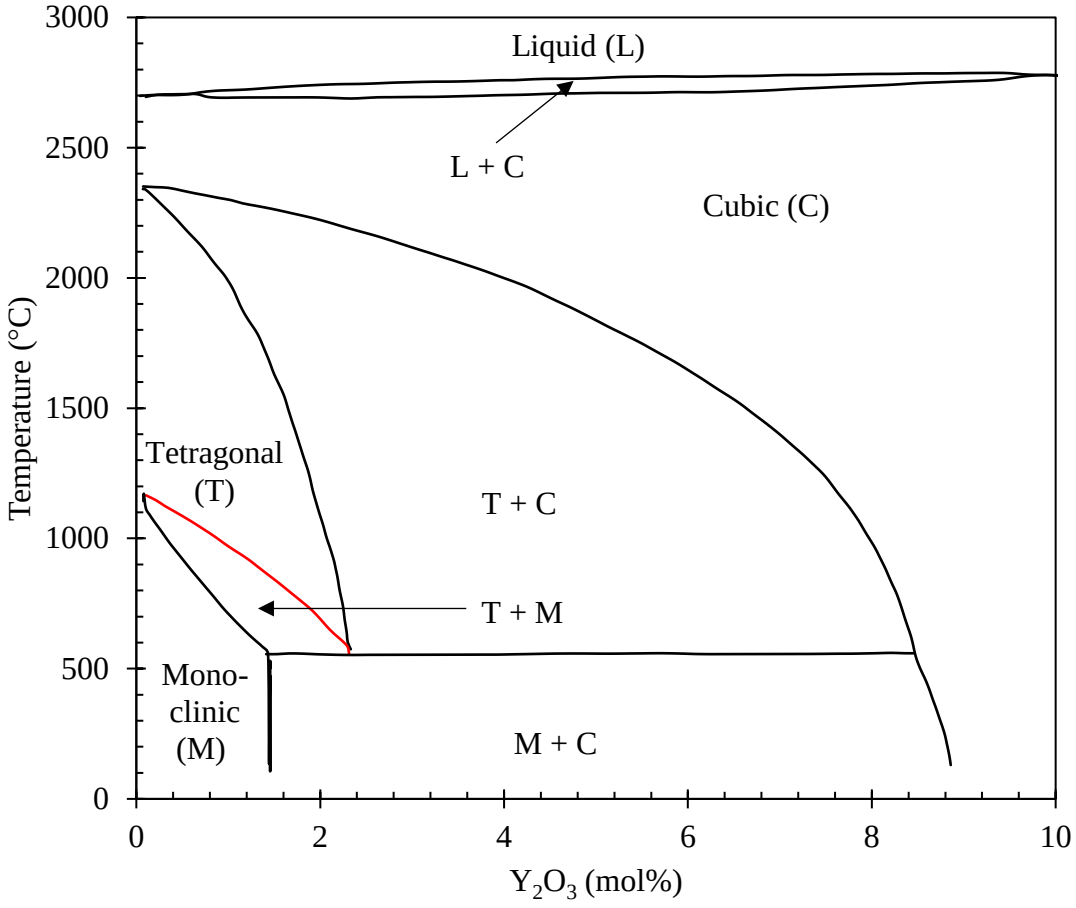


Figure 2.30: The ZrO_2 – Y_2O_3 phase diagram depicting the ZrO_2 rich side (Scott, 1975).

Figure 2.30 illustrates that the addition of Y_2O_3 causes a decrease in the temperature of the boundary between the tetragonal phase (T) and the monoclinic + tetragonal phase (M+T) fields (drawn in red). The addition of Y_2O_3 lowers the minimum temperature at which the tetragonal phase is thermodynamically stable. **Figure 2.30** also shows that the tetragonal phase is not the thermodynamically stable phase at room temperature for any composition. However, thermodynamically metastable tetragonal ZrO_2 can be retained to room temperature if there is insufficient energy to overcome the activation energy barrier of transformation (Basu, 2005).

H. G. Scott (1975) showed that when Y_2O_3 is added to ZrO_2, rapid quenching from high temperatures will allow for metastable phases to form. Samples in the range of 0 to 1.5mol%

Y_2O_3 were monoclinic when quenched, in the range of 3 to 5.5mol%, the samples were tetragonal and >6.5mol% the samples were cubic. In-between those ranges (1.5 to 3mol% and 5.5 to 6.5mol%) the samples contained a mix of the respective phases (Scott, 1975).

The tetragonal and cubic phases that form as a result of the Y_2O_3 doping have slight differences to the pure phases. Due to the ionic mismatch between the Zr^{4+} and Y^{3+} cations, oxygen vacancies form to compensate for the charge. This can be expressed using Kröger-Vink notation, **Equation 2.21** (Basu, 2005):

$$Y_2O_3 \xrightarrow{ZrO_2} 2Y'_{Zr} + 3O_O^X + V_{\ddot{O}} \qquad \textbf{Equation 2.21}$$

Where Y'_{Zr} is the yttrium atom occupying a zirconium lattice position, O_O^X is an oxygen atom occupying an oxygen lattice position, and $V_{\ddot{O}}$ is a vacancy occupying an oxygen lattice position (Basu, 2005). There is an oxygen vacancy for every Y_2O_3 formula unit.

The oxygen vacancies are located near the Zr atoms, not the Y atoms. Thus, the vacancies cause the formation of ZrO_7 polyhedra from ZrO_8 polyhedra. The Y atoms maintain eightfold coordination (YO_8) at all doping compositions. The Zr coordination number decreases from nearly 8 to 7 as the Y_2O_3 concentration increases from 3 to 20mol% (Li, et al., 1993) (Li, et al., 1994).

The distortion of both the Zr and Y atoms' local environment generally increases as the Y_2O_3 content is increased. This occurs to accommodate the increasing number of ZrO_7 polyhedra, which are not features of the tetragonal or cubic structures. As such, the stabilised phases are tetragonal or cubic only for the average overall structure. The global symmetry is not manifested in the local environment (Li, et al., 1993). The generation of the oxygen vacancies is believed to be the primary reason for the stabilisation of the high temperature phases to lower temperatures (Basu, 2005). As the transformation temperature is reduced by the alloy additions (Lange, 1982), T_o decreases to T_A, **Equation 2.22**.

$$\Delta G^c = \Delta S(T_A - T) \qquad \textbf{Equation 2.22}$$

This reduction causes a decrease in the ΔG^c term from **Equation 2.17**.

2.2.4.3. The Effect of the Constraining Matrix

Zirconia grains embedded in a matrix can remain tetragonal at temperatures below T_A. This is because of the strain energy, ΔU_{se}. The strain energy relates to the resistance of the matrix to

the volume and shape change of the grain during transformation (Becher & Swain, 1992) (Kelly & Denry, 2008). The change in energy may now be calculated as:

$$\Delta G_{t\rightarrow m} = \Delta G^{c} + \Delta U_{se} \qquad \textbf{Equation 2.23}$$

Thus, the requirement for transformation is:

$$-\Delta G^{c} > \Delta U_{se} \qquad \textbf{Equation 2.24}$$

The addition of this strain energy means that the transformation will now occur at a lower temperature than in the unconstrained case. The magnitude of the strain energy has been found to depend on the elastic properties of the transformed grain and the matrix, the grain shape, and the transformation strain (Lange, 1982). The strain energy can be expressed as (Lange, 1982):

$$U_{se}^{m} = \frac{1}{2}\sigma_{ij}^{I}\varepsilon_{ij}^{t} \qquad \textbf{Equation 2.25}$$

Where σ_{ij}^{I} defines the uniform stress state within the transformed inclusion, and ε_{ij}^{t} is the "stress-free" transformation strain, given by **Equation 2.15**. If it is assumed that the transformation only involves an isotropic volume expansion, i.e. $\varepsilon_{ij}^{t} = \frac{1}{3}\frac{\Delta V}{V}$, then for a spherical particle:

$$U_{se}^{m} = \frac{k}{6}\left(\frac{\Delta V}{V}\right)^{2} \qquad \textbf{Equation 2.26}$$

Where:

$$k = \frac{2E_1E_2}{(1+\upsilon_1)E_2 + 2(1-2\upsilon_2)E_1} \qquad \textbf{Equation 2.27}$$

and E_1 and E_2 and υ_1 and υ_2 are the Young's moduli and Poisson's ratios of the matrix (1) and transforming particle (2) respectively. **Equation 2.27** gives insight into the effect of the elastic properties of the constraining matrix. For a constraining matrix that has a large elastic modulus, the strain energy will also be large, therefore the transformation temperature will be low. The constrained transformation temperature is inversely proportional to the rigidity of the constraining matrix (Lange, 1982).

Equation 2.25 assumes that the initial tetragonal grain is free of residual stresses. However, due to the difference in thermal expansion coefficients of the matrix and the ZrO_2 grains,

cooling from the sintering temperature to room temperature will create residual stresses. When the residual stress state is accounted for, the strain energy becomes (Lange, 1982):

$$U_{se}^{m} = \frac{1}{2}\left(\sigma_{ij}^{I} \pm \sigma_{ij}^{r}\right)\left(\varepsilon_{ij}^{t} \pm \varepsilon_{ij}^{r}\right) \qquad \textbf{Equation 2.28}$$

Where σ_{ij}^{I} and ε_{ij}^{t} are the stresses and strains defined for the transformation from an unstressed tetragonal particle and σ_{ij}^{r} and ε_{ij}^{r} are the residual stresses and strains. The ± sign arises because the residual stresses and strains can have either the same sense (+) or the opposite sense (–) to the stresses and strains associated with the transformation. **Figure 2.31** illustrates the constrained transformation of a spherical tetragonal inclusion, where its initial state is stress-free (**Figure 2.31.a**) and under a residual stress of σ^{r} (**Figure 2.31.b**).

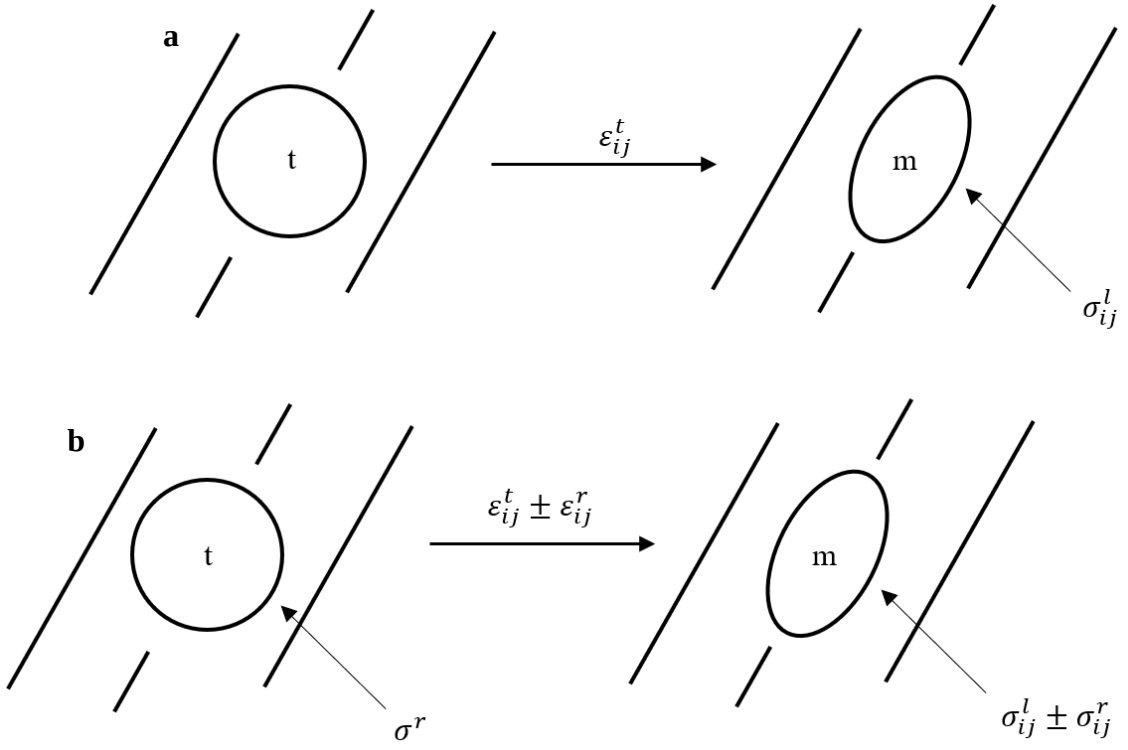


Figure 2.31: Constrained transformation where the initial state (**a**) is stress-free and (**b**) under a residual stress of σ^{r} (Lange, 1982).

Equation 2.28 shows that the residual stresses and strains can either increase or decrease the strain energy depending on their sense. If the transformation stresses are compressive and the residual stresses are tensile, the strain energy decreases. If both the transformational stress and the residual stresses are the same, the strain energy is amplified (Lange, 1982).

This shows that the transformation temperature of a tetragonal particle can be reduced by maximising the elastic properties (Young's modulus) of the constraining matrix and by ensuring that the residual strains have the same sense as the transformational strains. The latter can be achieved by using a material that has a higher thermal expansion coefficient than tetragonal-ZrO_2 for the matrix material (Lange, 1982).

2.2.4.4. The Effect of Grain Size

Hitherto the effect of grain size has been ignored. Experiments have shown that grain size is a significant factor in the retention of tetragonal-ZrO_2 (Lange, 1982). There is a critical grain size, below which tetragonal-ZrO_2 can be retained. The grain size effects the surface energy, ΔU_S, of the grains. By including this term, the change in energy is now given by **Equation 2.17** and the requirement for spontaneous transformation is given by **Equation 2.18**.

The analysis done by Lange (1982) considers the change in the surface energy, ΔU_S, per unit volume of a transformed spherical inclusion (a constrained particle). This can be expressed as **Equation 2.29**.

$$\Delta U_S = \frac{A_m\gamma_m - A_t\gamma_t}{V} = \frac{6(\gamma_m - \not{g}_s\gamma_t)}{D} \qquad \textbf{Equation 2.29}$$

Where A_m and A_t are the interfacial surface areas, γ_m and γ_t are the specific interfacial surface energies in the transformed and untransformed states, V is the transformed volume ($V = \pi D^3/6$), D is the diameter of the transformed inclusion and $\not{g}_s = A_t/A_m$. For the condition that $\Delta G_{t\rightarrow m} = 0$ and by substituting **Equation 2.29** into **Equation 2.18** and making the diameter of the transformed inclusion the subject, **Equation 2.30** is obtained:

$$D_c = \frac{6(\gamma_m - \not{g}_s\gamma_t)}{[-\Delta G^c - \Delta U_{se}]} \qquad \textbf{Equation 2.30}$$

Where D_c is the particle size at which the tetragonal to monoclinic transformation is in thermodynamic equilibrium. Therefore, when the particle size is greater than this critical value, $D > D_c$, the thermodynamics of the transformation are satisfied, $\Delta G_{t\rightarrow m} < 0$, and the transformation can proceed. This also means that if the particle size is less than D_c the transformation will not occur spontaneously, and the tetragonal particle will be retained (Lange, 1982).

2.2.4.5. Stress Induced Transformation

The preceding discussion explained how tetragonal grains can be stabilised to room temperature by controlling the temperature and composition (the chemical free energy), the constraining matrix (the strain energy) and the grain size (the surface energy). When the tetragonal grain is stabilised then $-\Delta G^c \leq \Delta U_{se} + \Delta U_S$, and $\Delta G_{t\rightarrow m} > 0$. Then, if an external stress is applied an extra term, ΔU_I, must be included in **Equation 17**:

$$\Delta G_{t\rightarrow m} = \Delta G^c + \Delta U_{se} + \Delta U_S - \Delta U_I \qquad \textbf{Equation 2.31}$$

The term ΔU_I is the interaction energy density due to the application of an external stress. This indicates that an applied stress can cause the transformation to occur if:

$$\Delta U_I \geq \Delta U_{se} + \Delta U_S + \Delta G^c \qquad \textbf{Equation 2.32}$$

As this will cause:

$$\Delta G_{t\rightarrow m} \leq 0 \qquad \textbf{Equation 2.33}$$

If this condition is met, the material will undergo transformation toughening. As the internal stresses and strains are accounted for in the ΔU_{se} term, the only contribution to ΔU_I is from the applied stress, then, ΔU_I can be defined in terms of the applied stress σ_a and the transformation dilatational strain ε^T (Kelly & Denry, 2008)

$$\Delta U_I = \sigma_a \times \varepsilon^T \qquad \textbf{Equation 2.34}$$

Therefore, a critical applied stress, σ_C^T, may be defined for which transformation will begin (when $\Delta U_I = \Delta U_{se} + \Delta U_S + \Delta G^c$):

$$\sigma_a = \sigma_C^T = \frac{\Delta U_{se} + \Delta U_S + \Delta G^c}{\varepsilon^T} \qquad \textbf{Equation 2.35}$$

By substituting the terms derived previously:

$$\sigma_C^T = \frac{\left(\frac{1}{2}\left(\sigma_{ij}^I \pm \sigma_{ij}^r\right)\left(\varepsilon_{ij}^t \pm \varepsilon_{ij}^r\right)\right) + \left(\frac{6(\gamma_m - \cancel{g}_s\gamma_t)}{D}\right) + \left(\Delta S_{t\rightarrow m}(T_A - T)\right)}{\varepsilon^T} \qquad \textbf{Equation 2.36}$$

From **Equation 2.36** it can be shown that the critical stress increases as the test temperature, T, increases, as $\Delta S_{t\rightarrow m}$ is negative. As the yttria content increases, causing T_A to decrease, the critical stress increases. Also, as grain size increases the critical stress decreases. It shows that

by maximising the rigidity of the constraining matrix, thereby increasing σ_{ij}^{I} and ε_{ij}^{t}, the critical stress is also maximised. Finally, it shows that by ensuring that the residual stress and strain, σ_{ij}^{r} and ε_{ij}^{r}, have the same sense as the transformation stress and strain, the critical stress is increased. This is done, according to Lange, (1982), by using a matrix material with a higher thermal coefficient of expansion than tetragonal ZrO_2. Therefore, the options available to tailor the conditions under which the transformation will occur are the temperature at which the material is expected to be used, the composition of the matrix material, the extent of Y_2O_3 doping, and the size of the ZrO_2 grains.

2.2.5. The Effect on Fracture Toughness

The fracture toughness of a brittle composite material, K_{Ic}, can be described by **Equation 2.37**.

$$K_{Ic} = K_0 + \Delta K_c \qquad \textbf{Equation 2.37}$$

K_0 is the matrix toughness and ΔK_c is the contribution to the fracture toughness of any crack shielding mechanisms (Hannink, et al., 2000). For dispersed zirconia ceramics, three mechanisms have been identified: transformation toughening, ΔK_{cT}, transformation-induced microcrack toughening, ΔK_{cM}, and crack deflection toughening, ΔK_{cD} (Hannink, et al., 2000). In general, the toughness contribution from transformation toughening (~15MPa.m$^{1/2}$) is greater than that from microcracking (~2 – 6MPa.m$^{1/2}$) or crack deflection (~2 – 4MPa.m$^{1/2}$) (Kelly & Denry, 2008).

2.2.5.1. Transformation Kinetics

As discussed in the crystallographic section, the tetragonal to monoclinic transformation is semi-reconstructive and induces shear strain. It consists of two major processes. First the Zr^{4+} ions transition from tetragonal lattice positions to monoclinic positions. This displacement causes the shear. The second stage is the migration of the oxygen ions to the oxygen sites (recall that the coordination number of the Zr^{4+} goes from 8 to 7 during the tetragonal to monoclinic transformation). It is suspected that the shear displacement of the Zr^{4+} ions is the rate-controlling factor for nucleation and longitudinal growth of monoclinic plates, and that the migration of O^{2-} ions is the rate-controlling factor for the lateral growth of the plates (Basu, 2005). From a kinetic perspective, the increase in the transformability of larger ZrO_2 grains can also be explained by the greater probability of a potent nuclei existing in a larger grain than in smaller grains (Kelly & Denry, 2008).

When the tetragonal to monoclinic transformation is caused by the tensile stress around a crack, the transformation involves the development of a transformation zone accompanying the crack tip, then after propagation, the crack wake. The size of this zone is another factor that effects the extent of toughening (Kelly & Denry, 2008). The toughening increment due to transformation toughening can be expressed as **Equation 2.38** (Kelly & Denry, 2008).

$$\Delta K_c = 0.22 \times E \times \varepsilon_{ij}^{T} \times f \times \frac{\sqrt{h}}{(1-\upsilon)} \qquad \textbf{Equation 2.38}$$

Where h is the transformation zone width, E is the local elastic modulus of the transformed material, f is the volume fraction of the transformable phase, υ is Poisson's ratio, and ε_{ij}^{T} is the dilatational strain.

Equation 2.38 shows that the incremental increase in the fracture toughness is controlled by the size of the transformation zone and the volume fraction of transformable tetragonal ZrO_2 grains (Basu, 2005). Therefore, the "transformability" of the tetragonal grains is vital. The incremental increase in fracture toughness is directly proportional to the fraction of zirconia grains that transform.

The enhanced fracture toughness caused by transformation toughening is only fully realised after sufficient crack growth. Initially ΔK_c is zero. As the crack grows, ΔK_c increases asymptotically. An increase in toughness during crack propagation has been termed Resistance (R) curve behaviour (Kelly & Denry, 2008) and is represented schematically in **Figure 2.32**.

This phenomenon can be described in three stages. The three stages are: the frontal, partial and extended stage (Basu, 2005). There is no contribution to toughness in the frontal stage ($\Delta K_c = 0$). It is assumed that the long-range strain field on the transforming particles is purely dilatational (Basu, 2005). As the crack propagates, crack tip shielding begins to occur when the tetragonal phase transforms. This is in the partially developed zone. In the extended zone, the asymptotic maximum is reached as the maximum number of tetragonal grains have transformed to the monoclinic phase (Basu, 2005). As the crack grows to approximately 5h to 10h, the toughness reaches the plateau (Kelly & Denry, 2008).

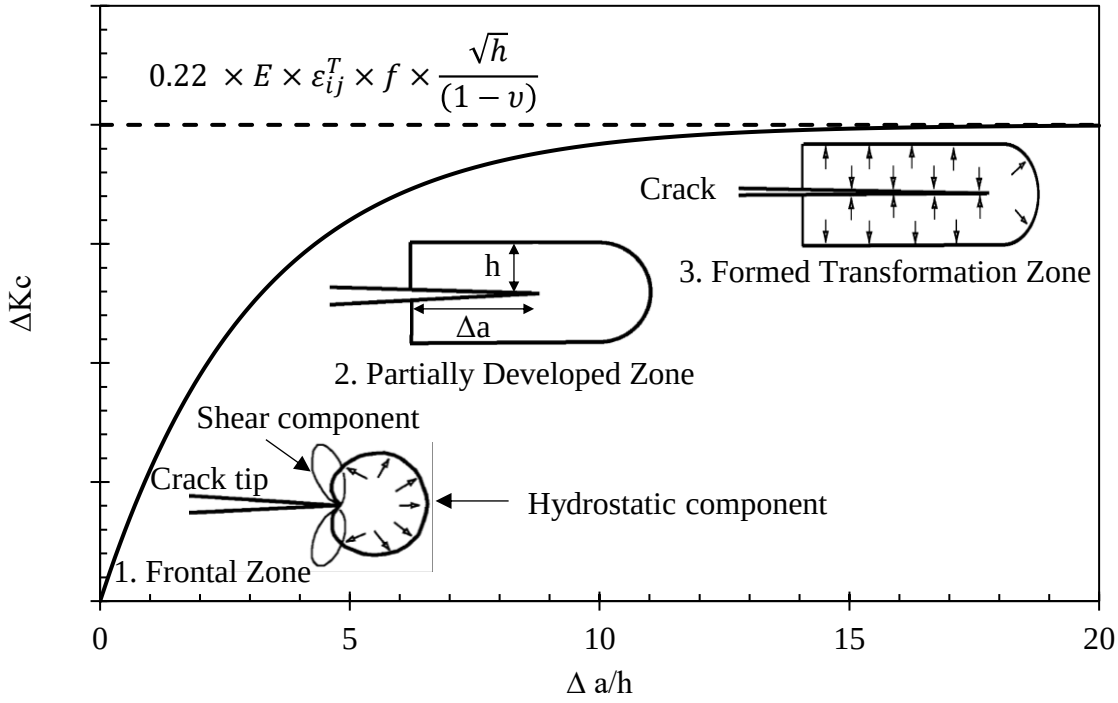


Figure 2.32: R-curve behaviour of a dispersed zirconia ceramic. Adapted from Kelly & Denry (2008).

In addition to the crack-tip shielding by the compressive dilatational stress engendered by transformation, other crack-tip shielding mechanisms have been identified. These mechanisms are a result of the transformed microstructure and include microcracking caused by the matrix material's response to the transformation strain and crack deflection caused by the difference in elastic modulus between the matrix and ZrO_2 inclusions (Kelly & Denry, 2008).

Due to the complex nature of fracture in zirconia toughened ceramics, many demonstrate non-linear and non-elastic yielding prior to failure. There are both elastic (reversible) and plastic components (irreversible) in the deformation mechanisms. The irreversible component is associated with the microcracking and the reversible component with the transformation (Kelly & Denry, 2008). The nonlinear failure is accounted for by both the stress-induced transformation and the microcracking (Kelly & Denry, 2008).

This analysis results in two important implications regarding transformation toughened ceramics: (1) actual stresses of failure can be lower than the value calculated by linear elastic analysis by up to 40%, and (2) these materials are unusually damage tolerant for ceramics. The strengths of specimens that have Vickers-indented surfaces have been observed to be equal to specimens with polished-surfaces (Kelly & Denry, 2008).

2.2.6. Production of Spinel-ZrO_2 composites

Ganesh & Ferreira, (2009) sintered $MgAl_2O_4$ – ZrO_2 composites with partially stabilised ZrO_2 contents between 0 – 20wt.% ZrO_2. Dried granules were uni-axially pressed at a pressure of 200MPa then sintered at 1500 – 1650^oC for 2 hours. **Table 2.6** shows the results for the samples sintered at 1600^oC, for 2 hours.

Table 2.6: Mechanical properties of sintered $MgAl_2O_4$ – ZrO_2 composites (Ganesh & Ferreira, 2009).

ZrO_2 content (wt.%)	**Bulk Density (kg/m^3)**	**Relative Density (%)**	**Fracture Toughness ($MPa.m^{1/2}$)**	**Hardness (Hv)**	**Linear Shrinkage (%)**
0	3410 ±17	95.20	2.50 ± 03	406.42 ± 9	17.8
5	3570 ± 18	96.43	2.51 ± 02	1220.64 ±14	18.4
15	3630 ± 12	91.99	2.53 ± 02	1257.14 ± 11	18.1
20	3750 ± 13	92.18	3.45 ± 03	1314.60 ± 13	18.3

Ganesh & Ferreira (2009) noted that small additions of ZrO_2 improved the sinterability of the ceramic to a maximum, thereafter further additions decreased it. This was deduced from the relative density. Their results indicated that irrespective of the sintered density, the partially stabilised zirconia increased the fracture toughness and hardness of the $MgAl_2O_4$ spinel. They attributed the improved fracture toughness to stress-induced tetragonal to monoclinic phase transformation toughening, microcrack toughening and crack deflection (Ganesh & Ferreira, 2009).

Mohan & Sarkar (2016) compacted stoichiometric mixtures of Al_2O_3 and MgO powder under a uniaxial pressure of 150MPa and then fired these compacts in the temperature range 1200° - 1600°C. The effect of the addition of ZrO_2 (the ZrO_2 was not stabilised with Y_2O_3) up to 2wt.% was investigated.

The addition of 0.5wt.% ZrO_2 improved the relative density of the spinel at high temperatures (>1500^oC) but decreased it at lower temperatures (<1500^oC). Greater amounts of ZrO_2 were found to reduce the density of the ceramic, which was attributed to the increase in micro-cracking (Mohan & Sarkar, 2016).

The incorporation of ZrO_2 was found to improve the spinel formation reaction between Al_2O_3 and MgO. The addition of ZrO_2 increased the temperature at which the shrinkage rate (due to sintering) overtook the expansion rate (due to the spinel formation reaction). SEM micrographs of the 2wt.% ceramic showed cracks, which they believed were caused by the tetragonal to monoclinic transformation. Lower ZrO_2 compositions showed pores, but not cracks.

The EDAX analysis found that the spinel grains in the 2wt.% sample did not contain any zirconium. The Zr^{4+} was found at the grain boundaries. Mohan & Sarkar (2016) concluded that the presence of the Zr^{4+} at the grain boundaries implied that the zirconia acted as a barrier for grain boundary migration and grain growth which led to a uniform and dense microstructure at higher temperatures.

Quenard et al. (2000) prepared $MgAl_2O_4 - xZrO_2$ ($1 \leq x \leq 30$) powder mixtures by the urea combustion route. The ZrO_2 powder in the mixture was not stabilised, however, due to its size, it was tetragonal at room temperature. The powders were either ball milled (BM) or attrition milled (A). The powder mixtures were uniaxially hot-pressed in graphite dies at 1500^oC.

When analysing the density data, they found no correlation between the amount of zirconia and the relative density. This result conflicts with Mohan & Sarkar, (2016) and Ganesh & Ferreira, (2009).

The more ZrO_2 present in the sample, the smaller the spinel grains were, for the ball milled samples. This led Quenard, et al.'s (2000) to conclude that the presence of ZrO_2 grains inhibited the growth of the spinel grains during hot pressing. However, this phenomenon was not clearly present in the attrition milled samples, where the presence of ZrO_2 had no or very little influence on the size of the spinel grains. This observation was dubious as they also reported difficulty in etching the surface of these samples, even after numerous attempts.

The average grain size of the ZrO_2 increased as the amount of ZrO_2 increased. This was due to an increase in the fraction of "large" grains which raised the average grain size. The large grains resulted from the coalescence of ZrO_2 at the grain boundaries (Quenard, et al., 2000). The phenomenon was more pronounced when the spinel grains were smaller. The mechanical properties of the samples fabricated by Quenard, et al. (2000) are shown in **Table 2.7**.

Table 2.7: The mechanical properties of the samples fabricated by Quenard, et al. (2000).

Specimen	Relative Density (%)	t-ZrO_2 Content (%)	ZrO_2 Average Grain Size (µm)	Fracture Toughness ($MPa.m^{1/2}$)	Vickers Hardness (Hv)
BM0	96.2	-	-	3.3	1444
BM1	96.5	100	-	3.0	1561
BM5	95.7	84	0.19	3.2	1584
BM10	98.3	89	0.25	3.0	1587
BM20	96.9	87	0.36	4.8	1559
BM30	96.7	48	0.44	6.6	1575
A0	95.5	-	-	2.3	1494
A1	95.7	100	-	2.8	1632
A5	96.6	88	0.35	3.1	1617
A10	95.8	89	0.37	3.4	1560
A20	96.4	60	0.42	4.0	1590
A30	94.8	19	0.44	6.6	1505

As the ZrO_2 content increased, the fraction of larger grains increased as well which leads to more grains that are large enough to undergo the tetragonal to monoclinic transformation upon cooling. After the average grain size exceeded 0.42µm, there was a large drop in the proportion of tetragonal-ZrO_2, **Figure 2.33**. Therefore, it would seem that the critical size for the ZrO_2 inclusions in the composite fabricated by Quenard, et al. (2000) was ~0.42µm. Thus, when the grain size increased beyond ~0.42µm, the change in surface energy was no longer great enough to stabilise the tetragonal phase.

The hardness for the ball milled samples increased with a small addition of ZrO_2 then stayed relatively constant for further additions. Quenard, et al. (2000) stated that particles at the grain junctions could minimize the matrix grain slide, even for low amount of ZrO_2, thus increasing hardness. For the attrition milled samples, after the initial increase in hardness, further additions reduced the hardness. This was suspected to be as a result of the increase in the density of microcracks. The increase in the density of microcracks was caused by the increase in the extent

of the tetragonal to monoclinic transformation during cooling for the samples with a greater ZrO_2 weight percent.

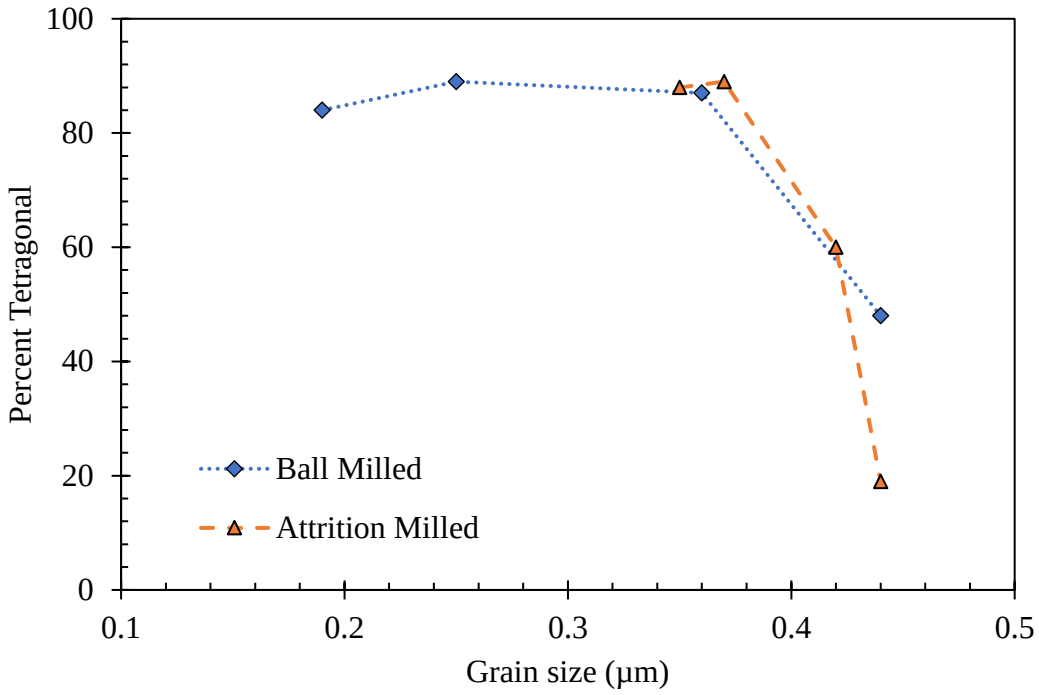


Figure 2.33: Retained tetragonal ZrO_2 as a function of grain size. Data from Quenard, et al. (2000).

The fracture toughness increased with increased additions of ZrO_2. What is noteworthy is that the fracture toughness continued to increase even though the proportion of tetragonal to monoclinic zirconia decreased. This observation suggests that multiple reinforcement mechanisms occur. Quenard, et al. (2000) stated that the presence of both monoclinic and tetragonal zirconia in the material pointed towards both the stress induced tetragonal to monoclinic transformation toughening and microcracking mechanisms being active simultaneously.

Besides hardness and fracture toughness, both Quenard et al. (2000) and Mohan & Sarkar (2016) measured the flexural strength. The flexural strengths measured by Mohan & Sarkar were particularly low, with the maximum strength being just under 100MPa, and the minimum just above 30MPa. The addition of ZrO_2 caused an increase in flexural strength up to 1.5wt.% ZrO_2, further additions caused a decrease in strength. Conversely Quenard et al. (2000) measured strengths as high as 578MPa, with the lowest strength reported of 234MPa. There

was a positive relation between the ZrO_2 additions and the flexural strength, unlike with Mohan & Sarkar (2016).

The substantial difference between the two studies could be because the strength of ceramic materials is greatly influenced by the largest flaw size present within the ceramic body. Which is significantly influenced by the quality of the starting powders and the fabrication route of the ceramic sample. Because of this, it is difficult to compare the measured flexural strengths between studies in which the production routes are not similar. However, both studies determined an improvement in the flexural strength by the addition of ZrO_2.

2.2.7. Production Insights Summary

The first requirement for the transformation toughening to be active is that the tetragonal-ZrO_2 is retained to room temperature. To ensure that this is the case, partially stabilized ZrO_2 should be used as this is already in the tetragonal phase. Furthermore, to prevent the generation of cubic-ZrO_2, the sintering temperature should be well below the C + S phase field temperature, **Figure 2.27**. This is possible with the use of the SPS, as the SPS furnace can simultaneously apply pressure and thermal energy. This reduces the required sintering temperature or time to achieve the same densification. Fine powders should also be used to stabilize the tetragonal phase and improve the mechanical properties of the composite materials. These strategies should ensure the retainment of tetragonal-ZrO_2 to room temperature.

Chapter 3: Methodology

3.1. Powder Preparation

3.1.1. Transparent Samples

The raw powders used to fabricate the transparent samples were alumina (Krahn Taimicron TM-DAR >99.99%) and magnesia (Baikowski M30CR >99.99%). The sintering aid was lithium fluoride (99.98% pure) obtained from Acros Organics. The particle size (d_{50}) of the MgO powder as per supplier specification was 1.4µm. The Al_2O_3 powder had a particle size range of 0.10~0.30µm according to the supplier. The maximum impurity levels given by the supplier for the alumina powder are shown in **Table 3.1**.

Table 3.1: Impurities within the Al_2O_3 powder.

Impurity	**Amount (ppm)**
Si	≤25
Fe	≤15
Na	≤10
K	≤5
Ca	≤5
Mg	≤5

The as supplied oxides were mixed in equal molar amounts (71.8wt.% Al_2O_3 and 28.2wt.% MgO) in a 250ml zirconium oxide milling jar (FRITCH). Absolute ethanol (MK CHEMICAL 99%) was used to make the slurry to encourage mixing and remove excess heat generated during milling. The LiF is hygroscopic and was therefore added to the slurry in a glove box under an argon atmosphere. The LiF was added at an amount of 1wt.%.

3.1.2. Dispersed Zirconia Ceramic (DZC) Samples

Spinel (Baikowski S30CR >99%) powder and 3mol% yttria-stabilised zirconia were used to make the composite samples. According to the suppliers, the spinel powder had a d_{50} of 0.15µm (**Table 3.2** lists the impurities), and the ZrO_2 powder had a d_{50} of 0.6µm. The as supplied oxides were mixed in several different ratios, **Table 3.3**. The powders were mixed in a 250ml

zirconium oxide milling jar together with absolute ethanol (MK CHEMICAL 99%) to form a slurry.

Table 3.2: Impurities within the $MgAl_2O_4$ powder.

Species	**Amount (ppm)**
Fe	4
Si	12
Na	7
Ca	4
K	27

Table 3.3: Composition of the mixtures.

Mixture	1	2	3	4	5	6
ZrO_2 (wt.%)	0	2	5	10	20	30
$MgAl_2O_4$ (wt.%)	100	98	95	90	80	70

3.1.3. Mixing, Sieving and Drying

Alumina milling balls were added to the powders at a mass ratio of 5:1 (balls : powder). The mixing of the powders was done with a planetary micro mill (FRITSCH pulverisette) for 9 hours and 46 minutes at 110rpm. The powder and milling balls were dried using a vertical rotary evaporator (EINS SCI E-RE-V). The water bath of the rotary evaporator was set to a temperature of 65°C and the rotation speed was 70rpm with a stop interval of 15s before reversing direction. The powders were dried using these settings for a duration of 50min. The dried powder and milling balls were then sieved through an 850- and a 125-micron screen (LABOTEC Test Sieve with stainless-steel frames and sieve surfaces) by a sieve shaker (Retsch AS 200). The undersize from the 125-micron screen was stored in a glass desiccator.

3.2. Sample Preparation

3.2.1. Sintering

The powders were sintered using a Spark Plasma Sintering Furnace (FCT HP-D5 Systeme GmbH). Sintering was performed under vacuum with an absolute gas pressure of ≈250Pa. The

heating stages of the process used a pulse time of 10ms with a pause of 5ms. A powder mass of 5 – 6g was used to produce samples with 20mm diameters and 5mm thicknesses. Samples were sintered in a graphite die set lined with graphite foil to protect the die. A carbon fibre blanket was secured around the graphite collar to reduce heat loss during sintering. A schematic diagram of the graphite die set is shown in **Figure 3.1**.

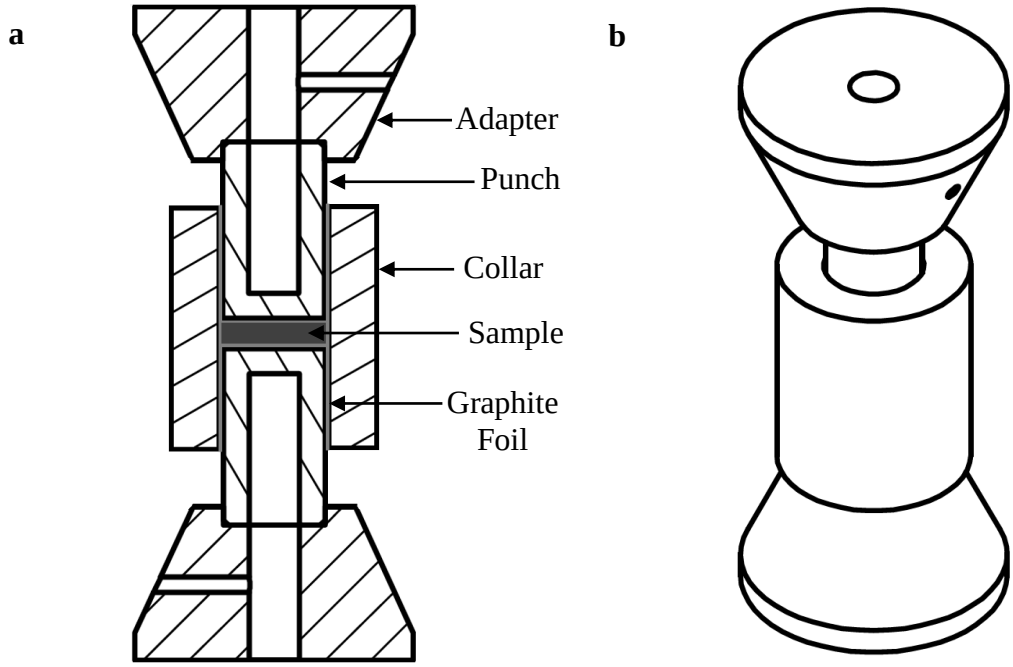
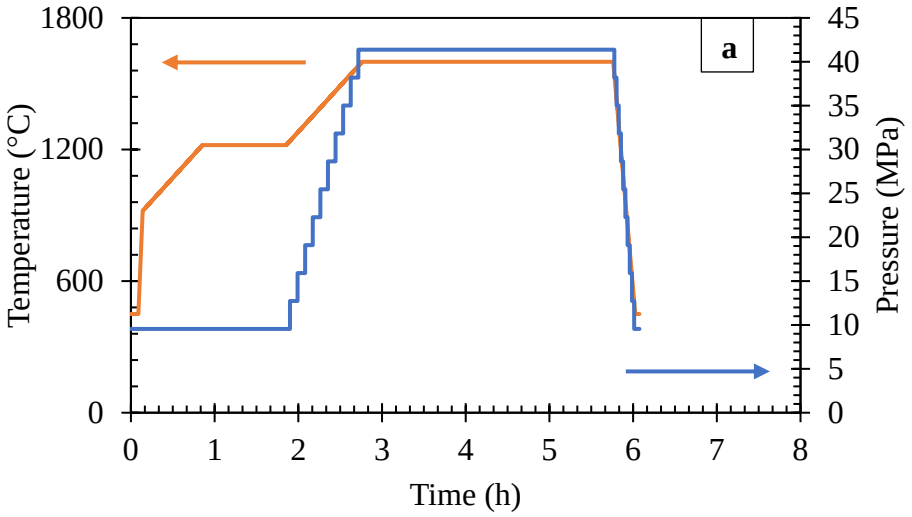
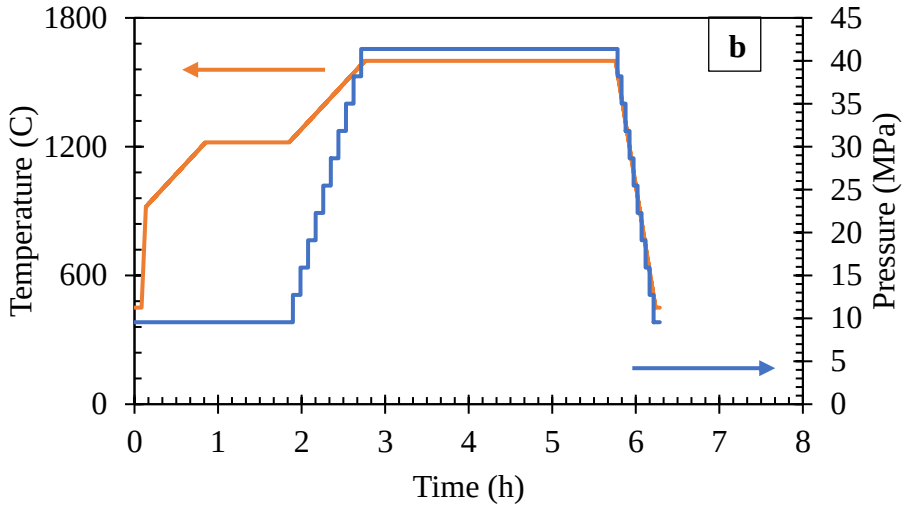
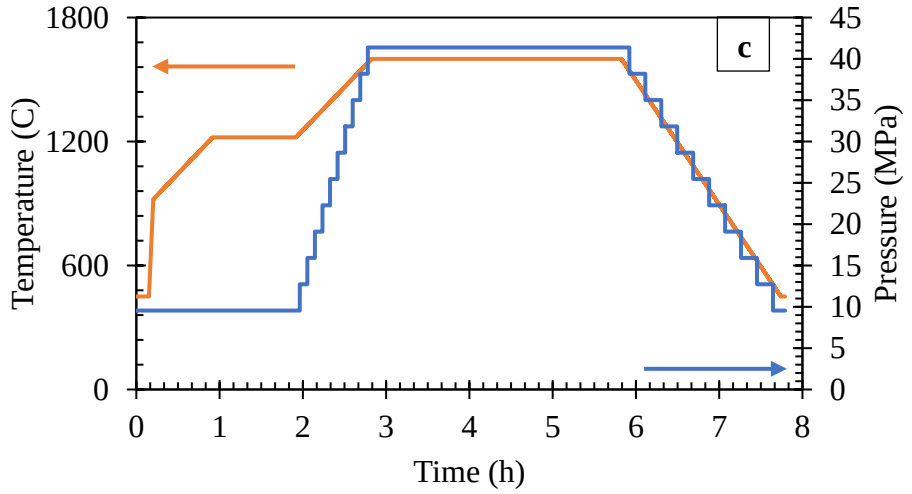


Figure 3.1: Schematic diagram of the die set's (**a**) cross section and (**b**) 3D projection. Credited to Rensburg (2018).

The sintering profiles for the transparent samples are shown in **Figures 3.2** and **3.3**. **Figure 3.2.a.** is the original sintering profile adapted from Esposito et. al, (2013). In **Figure 3.2.b** and **Figure 3.2.c** the cooling rate was reduced to 40°C/min and 10°C/min respectively. The table in the figures describes the sintering profile for the given graphs. In **Figure 3.3.a** the cooling rate was set to 40°C/min and the pressure was released five minutes before cooling began. In the last sintering profile, **Figure 3.3.b**, the sintering time was decreased from 3hrs to 1hr.

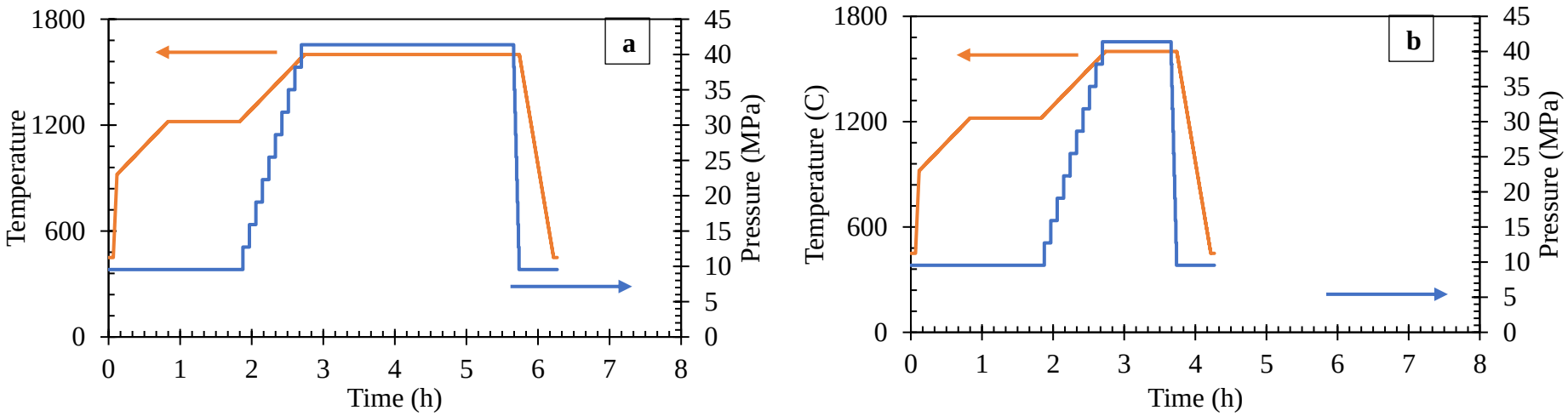






Temperature (˚C)	Pressure (MPa)	Duration (min)
RT to 450	0 to 10	5.33
450 to 920	10	3.10
920 to 1220	10	42.80
1220	10	60.14
1220 to 1600	10 to 40	54.33
1600	40	180.05
1600 to 450	40 to 10	16(**a**)/29(**b**)/115(**c**)
450 to RT	10	5

Figure 3.2: Heating profile (**a**) adapted from Esposito et al. (2013), (**b**) with a cooling rate of 40°C/min and, (**c**) with a cooling rate of 10°C/min.



Temperature (˚C)	Pressure (MPa)	Duration (min)
RT to 450	0 to 10	5
450 to 920	10	3
920 to 1220	10	43
1220	10	60
1220 to 1600	10 to 40	54
1600	40	175(**a**)/55(**b**)
1600	40 to 10	5
1600 to 450	10	29
450 to RT	10	5

Figure 3.3: Heating profile (**a**) where pressure is released before cooling and (**b**) where the sintering time is 1 hour.

Multiple samples were made for each of the sintering runs shown in **Figures 3.2** and **3.3**. This was to ensure that the results obtained were consistent. The naming convention used is given in **Table 3.4**. Samples produced using the sintering run depicted in **Figure 3.2.a** are referred to as Run 1, from **Figure 3.2.b** as Run 2 and so on. In addition to changing the sintering profiles, samples were also sintered without the LiF addition. These samples were sintered using sintering Run 4. Unless otherwise stated, samples sintered using Run 4 contain LiF. If the samples did not contain LiF it will be stated as Run 4 (no LiF).

Table 3.4: Naming convention for the sintering profiles used for the transparent samples.

Name of group	Heating profile	LiF addition (wt.%)
Run 1	**Figure 3.2.a**	1
Run 2	**Figure 3.2.b**	1
Run 3	**Figure 3.2.c**	1
Run 4	**Figure 3.3.a**	0 and 1
Run 5	**Figure 3.3.b**	1

The sintering profile for the DZC samples is given in **Figure 3.4** and **Table 3.5**. Ten samples were made for each ZrO_2 weight category.

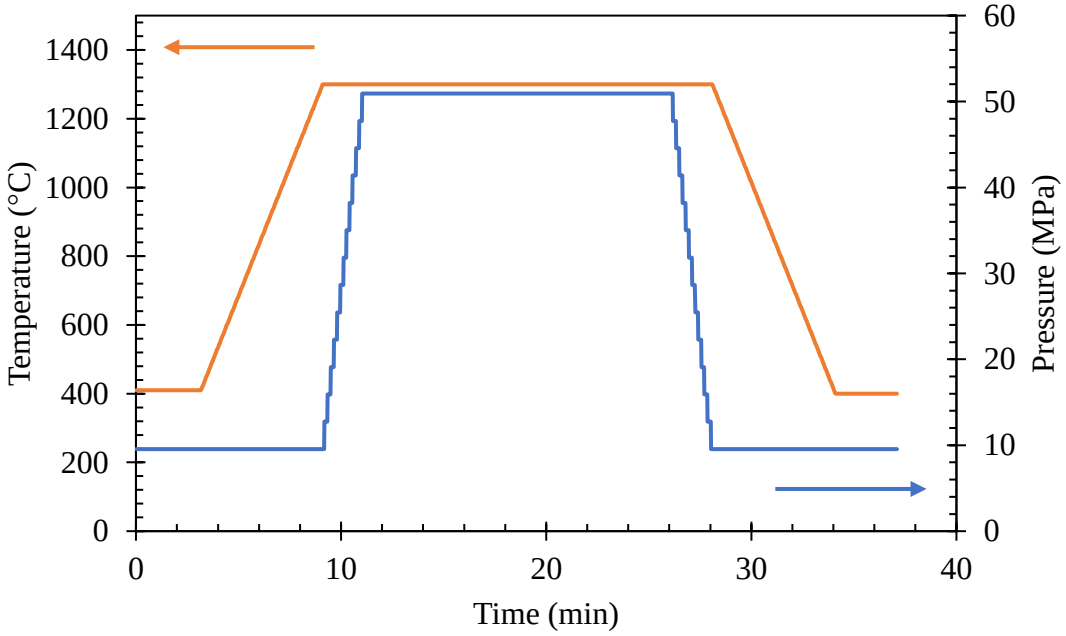


Figure 3.4: Heating profile for the dispersed zirconia samples.

Table 3.5: Sintering cycle for the dispersed zirconia ceramic samples.

Temperature (˚C)	Pressure (MPa)	Duration (min)	Heating Rate (°C/min)
RT to 400	0 to 10	3.2	125
400 to 1300	10	6.0	150
1300	10 to 50	2.0	20
1300	50	15	0
1300	50 to 10	2.0	20
1300 to 400	10	6	150
400 to RT	40 to 10	3.2	125

3.2.2. Polishing and Grinding

The sintered samples were ground and polished using a sample grinder/polisher (Leco Spectrum System 2000). The samples were sintered to 5mm thickness and were then ground down to 3mm thickness. The grinding was done using grinding disks with 80, 220, and 1200 grit (Struers MD Piano). The polishing was done using 6, 3, and 1-micron slurry (DiaPro Struers) on MD Allegro, MD Dac, and MD Nap polishing disks (Struers), respectively. Initially polishing was going to be done down to the 0.05-micron slurry for the transparent samples, however, this slurry preferentially removed material from the grain boundaries, which resulted in a lower resolution of the light passing through the samples.

3.3. Sample Analysis

3.3.1. Particle Size Analyser

Particle size analysis (PSA) was carried out using a Malvern Mastersizer 2000 to determine the size distribution of the as received powders. The d_{10}, d_{50} and d_{90} values (diameter of particles with cumulative fractions below 10, 50 and 90% respectively) were used to characterise the powders. The Malvern software analyses the scatter patterns produced as the powder particles pass in front of the laser beam and scatter the light. Using the Fraunhofer model, the diameters of the particles are calculated. Powders were each dispersed in an ultrasonic bath in order to break apart agglomerates and provide an accurate size analysis. Sodium hexameta-phosphate was added, to form a 1vol% solution with the distilled water, as a dispersant to prevent

agglomeration of the powders. The Al_2O_3, MgO, ZrO_2, and $MgAl_2O_4$ powders were analysed using the PSA.

3.3.2. Density Measurements

The method used to determine the density of the sintered samples was the Archimedes method. The samples wet and dry masses were measured using a Sartorius scale. The samples dry masses (W_{DA}) were measured after polishing. The samples were then boiled in distilled water for three hours, then their wet, submerged masses (W_{ws}) were measured. The density of each sample was then calculated using **Equation 3.1**.

$$TD = \frac{W_{DA} \times \rho_w}{W_{DA} - W_{ws}} \qquad \textbf{Equation 3.1}$$

Where TD is the density of the sample and ρ_w is the density of water. The temperature of the water was measured using a thermometer and the density of water was then acquired from a density table (Snelling, 2015) with the density of water as a function of temperature. The densities of all the sintered samples were measured using this method.

3.3.3. Spectrophotometry

The transmission test was done using a UV-Vis-NIR spectrophotometer (Aglient Technologies Cary 5000). The samples were placed at the far end of the sample holder, away from the detector, to ensure that minimal scattered light was detected. The transmittance of the transparent samples fabricated using Runs 1, 2, 4, 4 (no-LiF) and 5 were all measured.

3.3.4. XRD Analysis

X-Ray diffraction (XRD) analysis was performed using a Bruker D2 instrument to determine the phases and any impurities present in the starting powders and sintered samples. Sintered samples were cut through the centre of the disk then ground and polished to obtain a flat surface before analysis. Both the powders and sintered materials were subjected to the same scan parameters. The Co Kα radiation was generated at 10 mA and 30 kV to produce diffractograms over a range of 10 to 90° with a step size of 0.026 °2θ and a scan step time of 3.8 s. These were analysed using EVA© software (Bruker) in conjunction with the International Centre for Diffraction Data (ICDD) database (2019). The XRD analysis was conducted on the Al_2O_3, MgO, ZrO_2, and $MgAl_2O_4$ powders. A sintered sample from Run 4 of the transparent samples

was analysed using XRD analysis. A sample from each ZrO_2 weight category underwent XRD analysis for the DZC samples.

3.3.5. Scanning Electron Microscopy

A Carl Zeiss Sigma field emission gun scanning electron microscope (FEG-SEM) was used in the characterisation of the powders and the sintered samples. A small amount of powder was placed on a stub using graphite tape. Compressed air was blown over the powder adhering to the graphite tape to remove any loose powder before placing the sample into the SEM. This prevented contamination of the vacuum pumps attached to the SEM. Secondary electron images of the powders were captured allowing for the morphology and size of the various powders to be observed and measured and then compared to the PSA results and the sizes quoted by the supplier.

Sintered samples were cut and their cross-section polished. These samples were then thermally etched at 1200°C for 30min. The cross-section of the sample was coated with gold-palladium and carbon to allow the sample to be conductive under the SEM electron beam. Also, silver tape was used to connect the coated cross section to the aluminium stub to prevent charging while under the electron beam of the SEM. The microstructure of the etched surface and fractured surfaces were examined. Energy dispersive X-Ray analysis (EDX) was used in conjunction with SEM and XRD analysis to identify the phases present.

3.3.6. Optical Microscopy

Etched and coated samples were also analysed using an optical microscope (OLYMPUS GX41). The images acquired with the optical microscope and the SEM were used in conjunction with ImageJ software to measure grain size. The samples were coated not to enable conductivity but because they were transparent to visible light. The coating enabled the reflection of the visible light thus illuminating the surface analysed by the optical microscope.

3.3.7. Mechanical Properties

The mechanical properties of the transparent samples sintered using the run that resulted in the highest transmission were measured. The mechanical properties were determined for each ZrO_2 weight category for the DZC samples. The hardness indents were made using a Leco V-100-A2 Vickers hardness tester with a diamond indenter. A load of 49N (5kgf) was applied and

maintained for 30 seconds. A schematic of the indents and the measurements taken is shown in **Figure 3.5**.

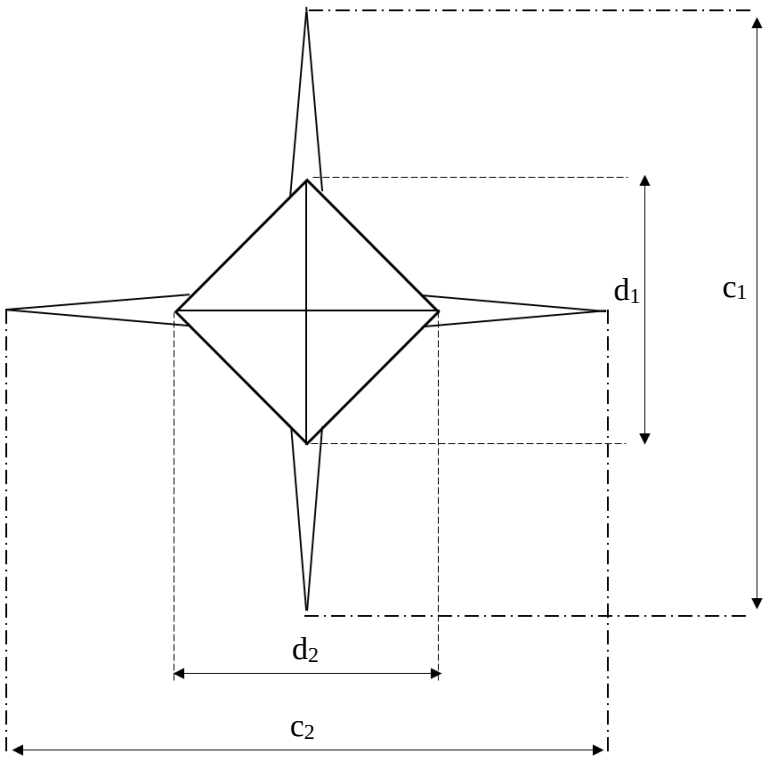


Figure 3.5: Schematic of an indent with the associated dimension measurements.

3.3.7.1. Hardness Test

The Vickers hardness value for each material was calculated using **Equation 3.2**.

$$HV = \frac{F}{A} \approx \frac{1.8544 \times F}{d^2} \qquad \textbf{Equation 3.239}$$

Where HV is the Vickers hardness number, F is the applied load (kg), A is the area of the indent, and d is the average length of the diagonals of the indent measured in millimeters.

3.3.7.2. Fracture Toughness

The indentation fracture toughness of the materials was calculated using **Equation 3.3**:

$$K_c = \xi_V^R \times \left(\frac{E}{H}\right)^{1/2} \times \left(\frac{P}{c_0^{3/2}}\right) \qquad \textbf{Equation 3.3}$$

Where K_c is the fracture toughness (Pa.m$^{0.5}$), ξ_V^R is a material-independent constant for Vickers-produced cracks with a value of ≈0.016 (Anstis, et al., 1980), E is the Young's Modulus (GPa), H is the Hardness (GPa), P is the applied load, and c_0 is the average crack length (m).

3.3.7.3. Biaxial Flexural Strength

The Ball on 3 Balls (B3B) test was used to determine the biaxial flexural strength. The DZC samples were ground to a thickness of ~3mm and polished using the 6µm diamond slurry on both faces. The transparent spinel samples had already been polished to a 1µm finish as they had previously undergone the transmittance test. As the transparent samples did not have the same surface finish as the DZC ceramics, it would be inappropriate to compare the biaxial flexural strengths between the two groups. A Tinius Olsen Universal Press was used to fracture the samples, along with the positioning aid and four balls. The setup for the B3B test is shown in **Figure 3.6**.

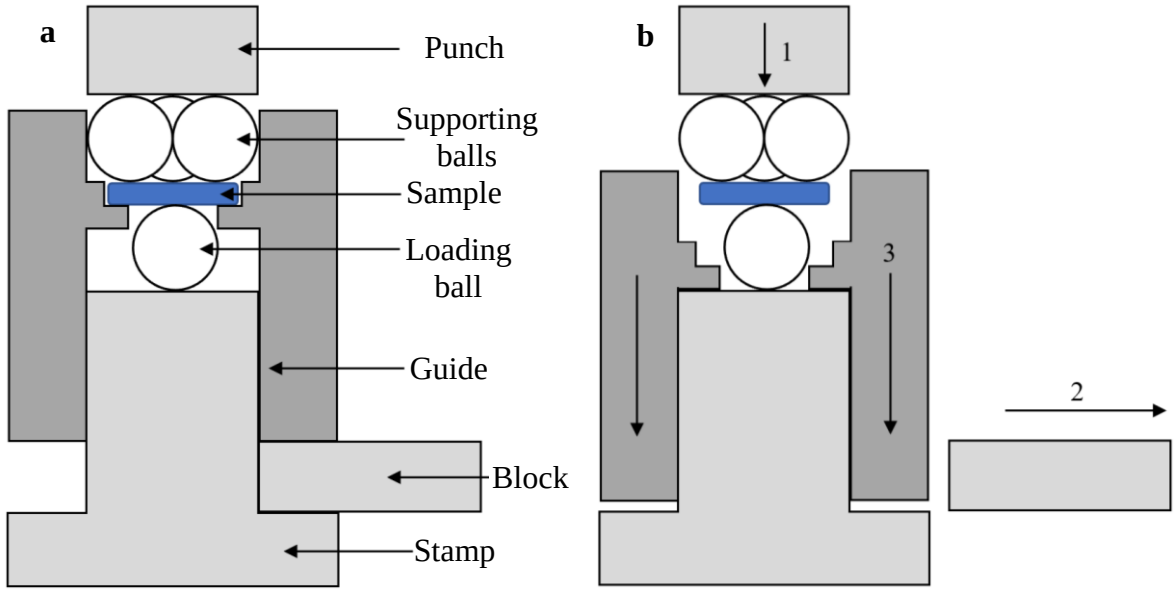


Figure 3.6: (**a**) Diagram of the B3B test set up and, (**b**) process to begin test. Adapted from (Harrer, et al., 2008).

The force as a function of displacement was measured by the Tinus Olsen press. The displacement rate was a constant 0.2mm/min for the duration of the pressing. A preload of ≈50N was applied before the block was removed (1). Once the block was removed (2) the guide was lowered (3) and the test began. The displacement continued to increase until fracture, at which point the maximum force was noted.

To calculate the maximum stress, σ_{max}, from the measured force, F, Borger, et al. (2002) modelled the system using a finite element method. As this is a complex system, the analytical solutions developed by others rely on assumptions that do not hold and therefore are not applicable in this work. The equation to calculate the maximum stress is given by **Equation 3.4**.

$$\sigma_{max} = f \times \frac{F}{t^2} \qquad \textbf{Equation 3.4}$$

Where f is a dimensionless factor and t is the thickness of the sample. Borger, et al. (2002) determined that f can be assumed to be independent of the applied force, the Young's modulus and the Poisson's ratio of the balls, and the Young's modulus of the sample. The independent variables that influence f are: $\frac{R_a}{R}$, $\frac{t}{R}$, and υ, where: R_a is the support radius, R is the radius of the disc, t is the thickness of the disk and υ is the Poisson's ratio of the disk material. If the balls all have the same radius then the support radius is given by **Equation 3.5** (Borger, et al., 2002).

$$R_a = \frac{2\sqrt{3}}{3} R_b \qquad \textbf{Equation 3.5}$$

Where R_b is the radius of the balls. The numerical expression determined by Borger, et al. (2002) to calculate the value of f is given by **Equation 3.6**.

$$f\left(\frac{t}{R}, \frac{R_a}{R}, \upsilon\right) = c_0 + \frac{\left(c_1 + c_2\frac{t}{R} + c_3\left(\frac{t}{R}\right)^2 + c_4\left(\frac{t}{R}\right)^3\right)}{1 + c_5\frac{t}{R}} \times \left(1 + c_6\frac{R_a}{R}\right) \qquad \textbf{Equation 3.6}$$

This equation gives the value of f as a function of R_a/R, t/R, and υ. The constants c_i are given in **Table 3.6.** The values for the constants were determined for three different Poisson's ratios by Borger, et al. (2002).

Table 3.6: Calculated values for the constants c_i used in **Equation 3.6** for three different Poisson's ratios (Borger, et al., 2002).

Constant	Poisson's Ratio		
	0.2	0.25	0.3
c_0	-12.354	-14.671	-17.346
c_1	15.549	17.988	20.774
c_2	489.20	567.22	622.62
c_3	-78.707	-80.945	-76.879
c_4	52.216	53.486	50.383
c_5	36.554	36.010	33.736
c_6	0.0820	0.0709	0.0613

For Poisson's ratios that are not equal to 0.2, 0.25, or 0.3. The data can be interpolated using **Equation 3.7**.

$$f\left(\frac{t}{R}, \frac{R_a}{R}, \upsilon\right) = \frac{\upsilon_2 - \upsilon}{\upsilon_2 - \upsilon_1} \times f\left(\frac{t}{R}, \frac{R_a}{R}, \upsilon_1\right) + \frac{\upsilon - \upsilon_1}{\upsilon_2 - \upsilon_1} \times f\left(\frac{t}{R}, \frac{R_a}{R}, \upsilon_2\right) \quad \textbf{Equation 3.7}$$

Equation 3.6 has been determined to be valid within the ranges provided in **Table 3.7**.

Table 3.7: Ranges determined by Borger, et al. (2002) to be valid for **Equation 3.6**.

Parameter	Evaluated Range
$\frac{R_a}{R}$	0.55 – 0.9
$\frac{t}{R}$	0.05 – 0.6
υ	0.20 – 0.3

Chapter 4: Results

4.1. Transparent Spinel

4.1.1. Powder Analysis

The particle size distributions of the starting powders are shown in **Figures 4.1** and **4.2**, and the characteristic sizes are given in **Table 4.1**. The MgO powder had a lognormal size distribution with a narrow peak, whereas the Al_2O_3 powder contained a few large agglomerates, **Figures 4.2.** and **4.3**. The d_{50} for the Al_2O_3 was 0.190µm and for the MgO it was 1.869µm. These values are both similar to the supplier specifications as indicated in **Section 3.1.1.** (**Transparent Samples**, **pp. 57**).

Table 4.1: Characteristic particle sizes for the MgO and Al_2O_3 powders.

Powder	**d_{10} (µm)**	**d_{50} (µm)**	**d_{90} (µm)**
Al_2O_3	0.118	0.190	2.583
MgO	1.069	1.869	3.434

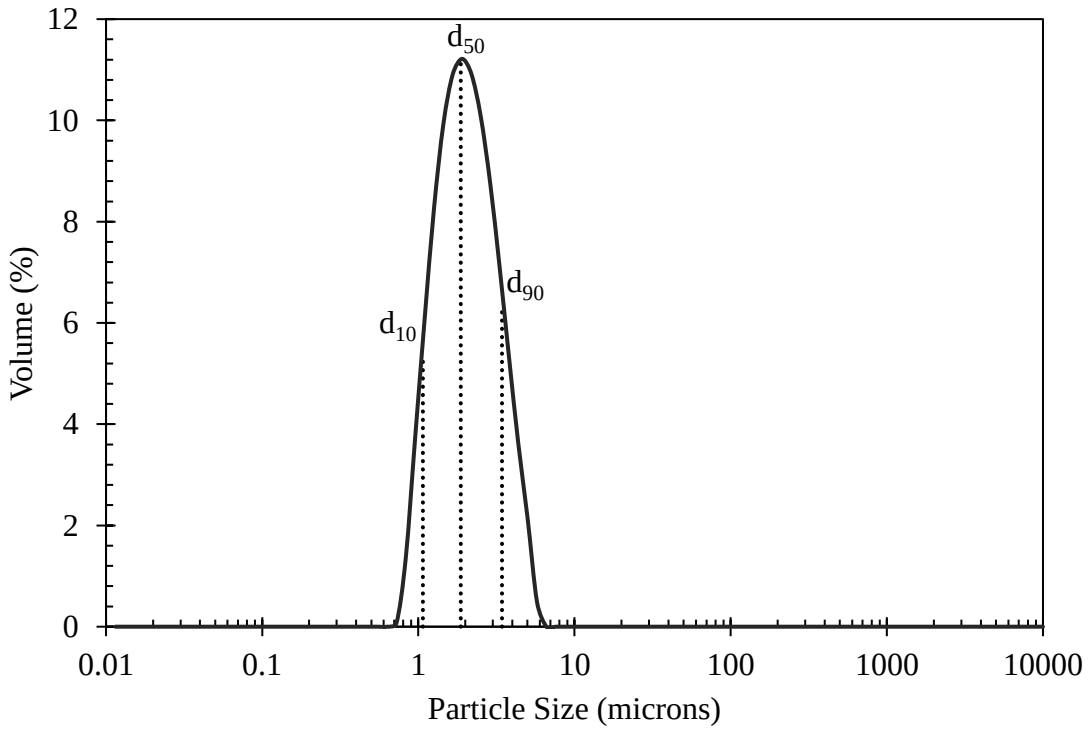


Figure 4.1: Particle size distribution for the MgO powder.

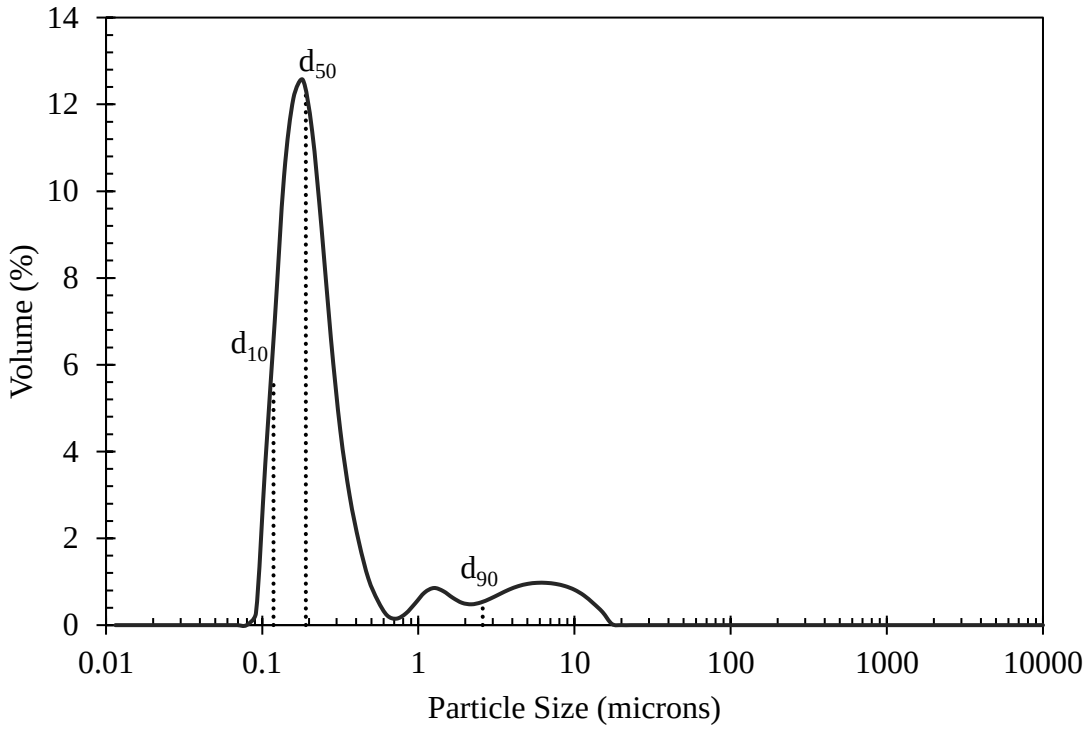


Figure 4.2: Particle size distribution for the Al_2O_3 powder.

Figures 4.3 and **4.4** show SEM images of an Al_2O_3 agglomerate and the MgO powder, respectively.

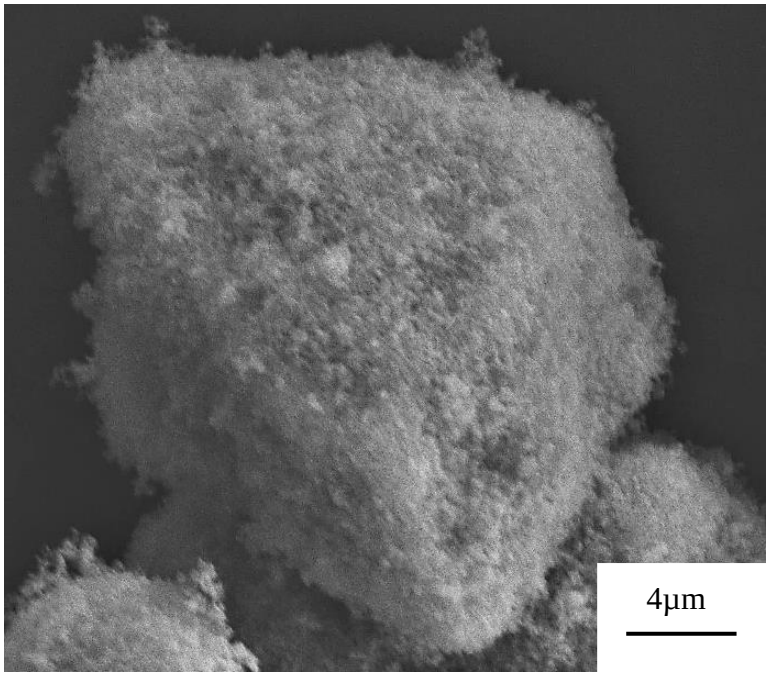


Figure 4.3: Secondary electron SEM image of a large Al_2O_3 agglomerate.

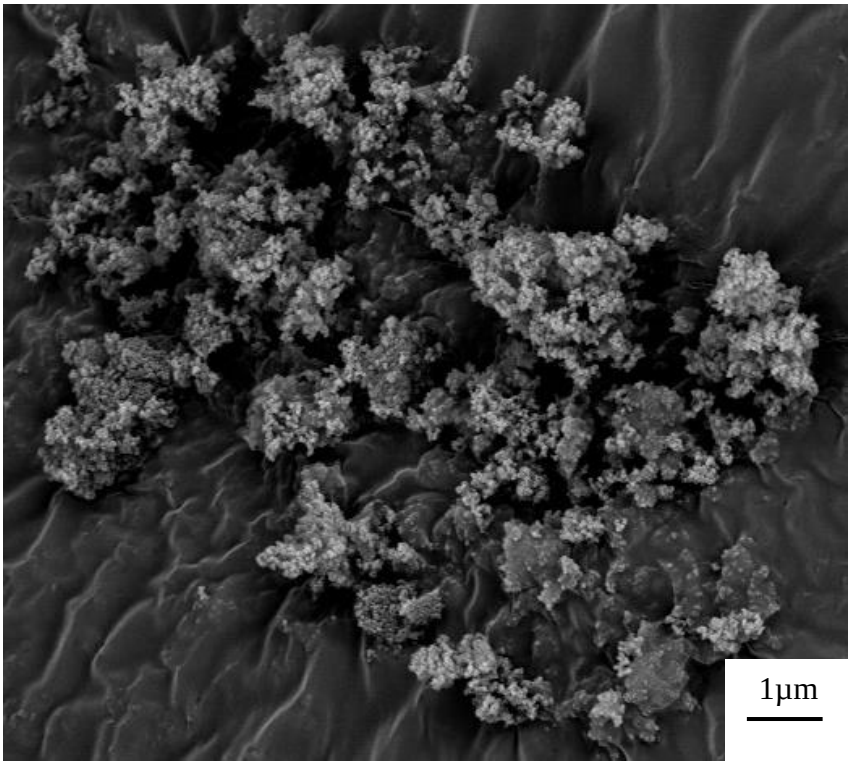


Figure 4.4: secondary electron SEM image of the MgO powder prior to milling.

The Al_2O_3 agglomerate looks 'flocculent like' and the MgO particles are irregularly shaped and hard to distinguish. **Figures 4.5** and **4.6** show the XRD spectra of the MgO and Al_2O_3 starting powders.

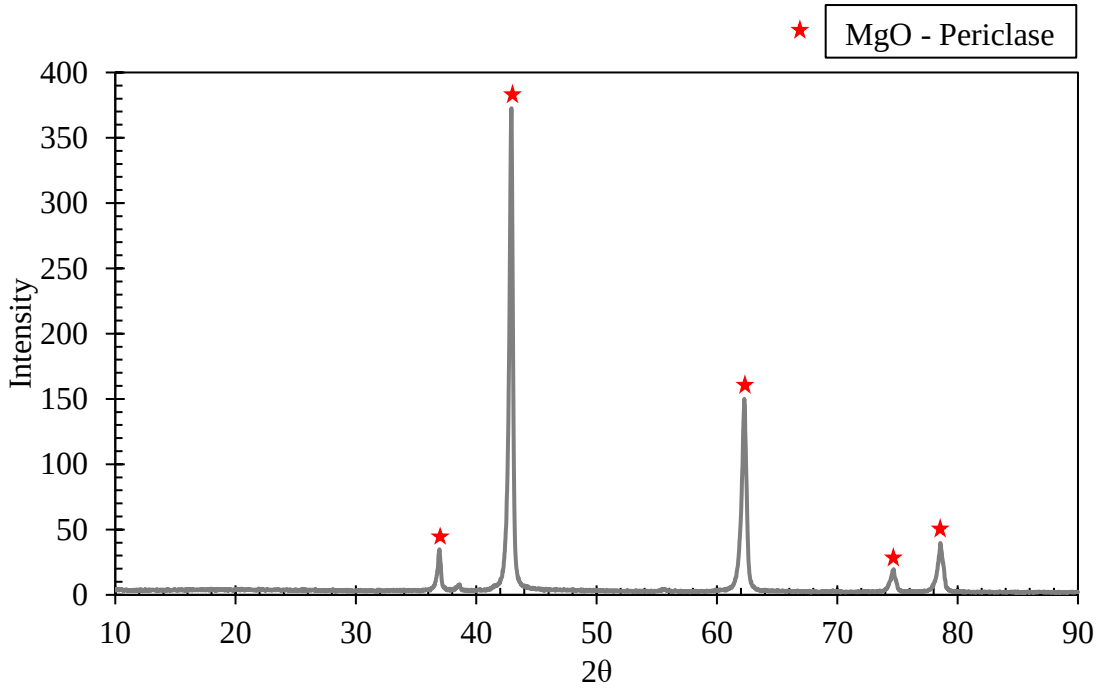


Figure 4.5: XRD spectra of the MgO powder.

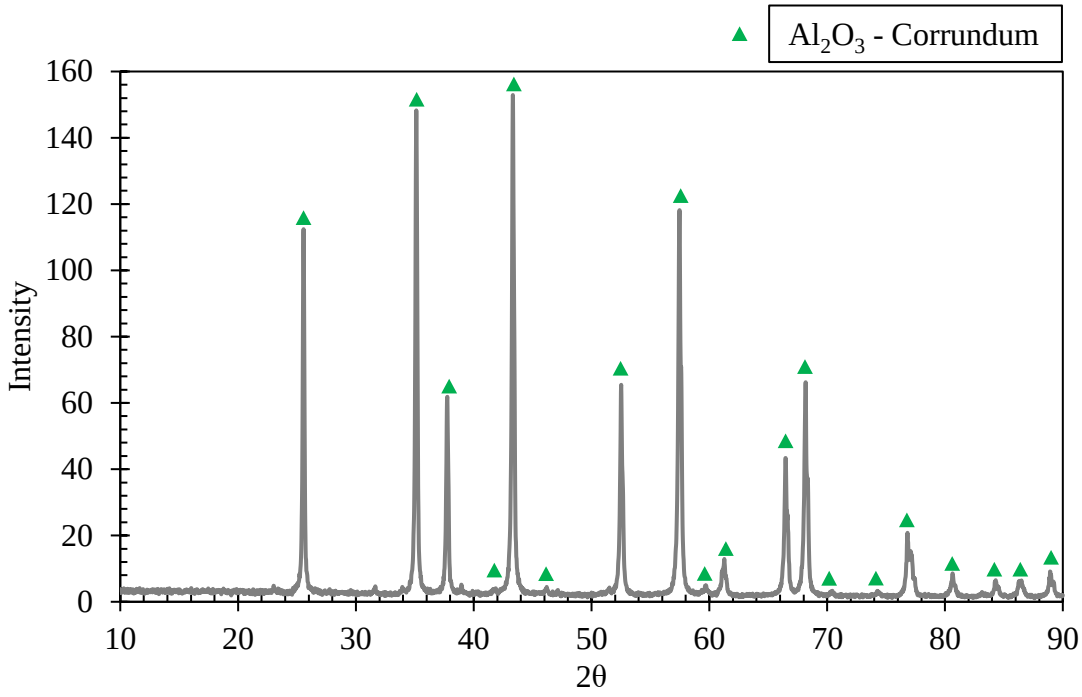


Figure 4.6: XRD spectra of the Al_2O_3 powder.

The peaks correspond to the XRD spectra from the International Centre for Diffraction Data (ICDD) database (2019) with the labels PDF: 01-074-4911 Periclase MgO and PDF 00-011-0661 α-Al_2O_3.

The Scherrer Equation was used to determine the mean crystallite size from the XRD data (Langford & Wilson, 1978). The XRD data was fitted using the sum of several Gaussian curves. The general equation for a Gaussian curve is shown by **Equation 4.1.**

$$f(x) = a \times e^{-\frac{(x-b)^2}{2c^2}} \qquad \textbf{Equation 4.1}$$

Where a is the peak hight, b is the peak position and c is the variance. **Figure 4.7** shows the sum of 5 Gaussian curves fitted to the XRD data of the MgO powder.

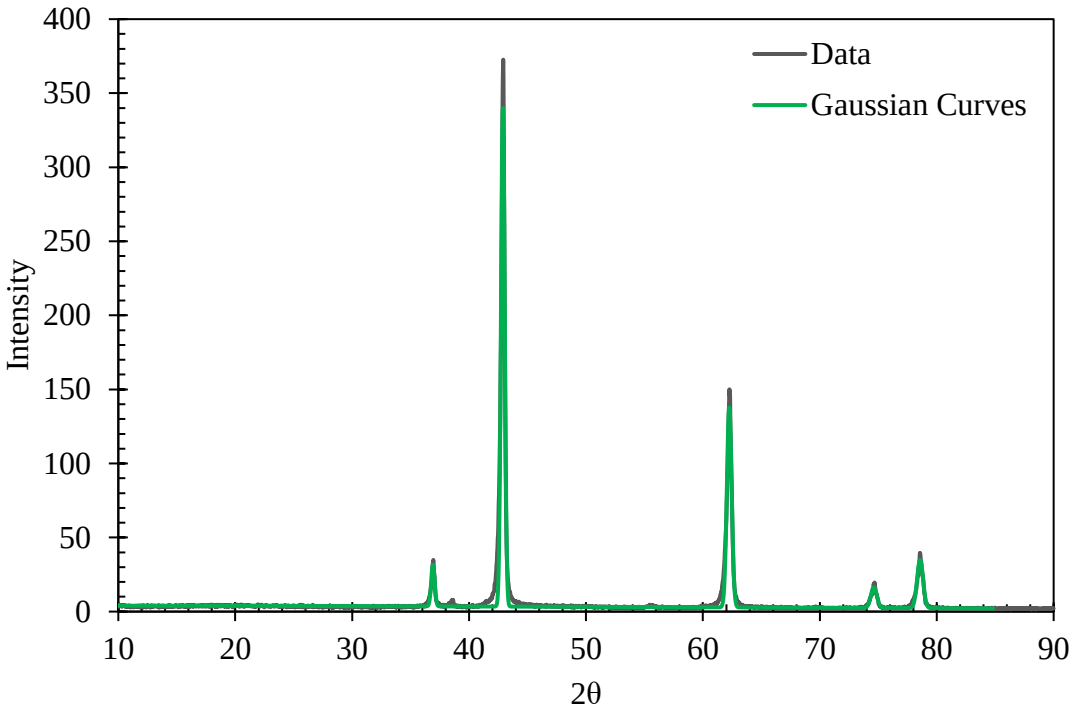


Figure 4.7: A Gaussian curve fitted to the XRD data of the MgO powder.

The Scherrer equation, **Equation 4.2**, was then used to determine the mean crystallite size using the values obtained from the fitted curves (Valerio & Morelhao, 2019).

$$\tau = \frac{K\lambda}{\beta \cos\theta} \qquad \textbf{Equation 4.2}$$

Where τ is the mean crystallite size, K is a dimensionless shape factor with a value of 0.92, θ is the Bragg angle of the peak and β is the full width half maximum of the peak which is given by **Equation 4.3.**

$$\beta = 2\sqrt{2\ln 2} \times c \qquad \textbf{Equation 4.3}$$

The term c is the variance in **Equation 4.1**. The calculated crystallite size for the MgO powder was 23nm and for the Al_2O_3 was 36nm. These values are orders of magnitude smaller than the particle sizes measured using the particle size analyser. An SEM micrograph of the mixed powders (after milling) is shown in **Figure 4.8**. The cubic particles are MgO and the rounded particles are Al_2O_3.

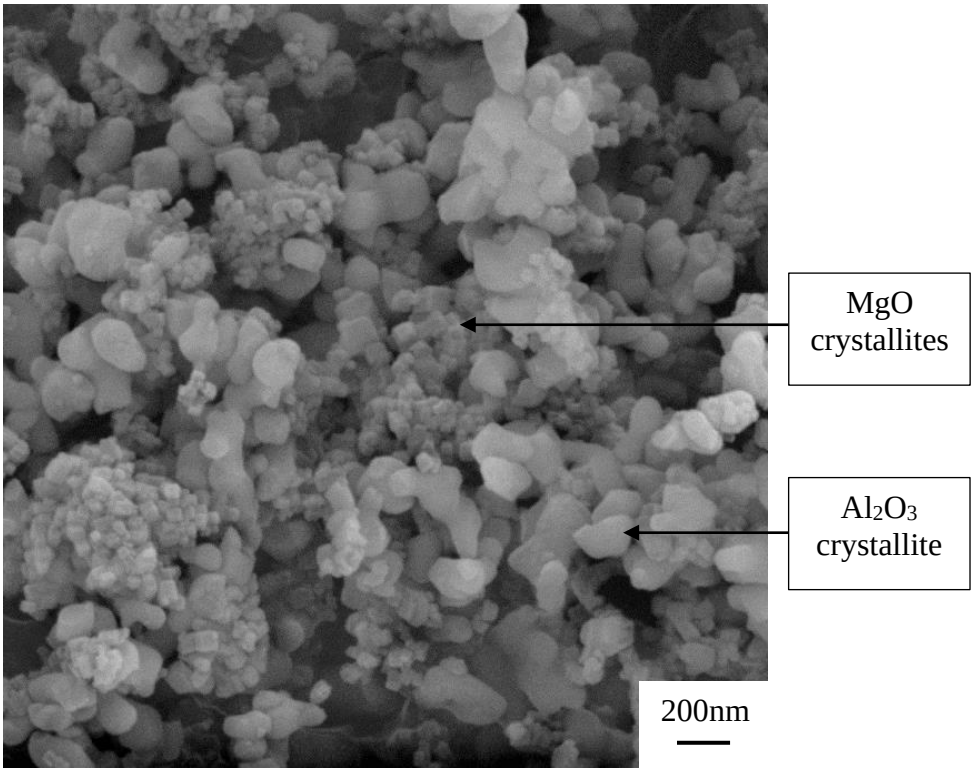


Figure 4.8: Secondary electron SEM image of the mixed Al_2O_3 and MgO after milling.

The SEM image in **Figure 4.8** corroborates the results from the Scherrer equation. The MgO crystallites (the cubic particles) are smaller than the Al_2O_3 crystallites (rounded particles). The SEM micrograph also shows that the powders were well mixed.

4.1.2. Sintering Results

Figure 4.9 shows the densification curve for Run 4 (**Section 3.2.1. Sintering, Figure 3.3.a pp. 61**). During the sintering cycle, the piston movement was recorded. These measurements have been plotted with the temperature and pressure versus time. The thermal expansion of the system was accounted for by doing the sintering run without any powder and measuring the piston displacement. The values recorded for the piston displacement that was caused by the thermal expansion of the system were then subtracted from the measured values when the powder was sintered. The resultant curves are shown in **Figure 4.9**. The linear shrinkage for the sample with the LiF was 54.75 ± 1.5% (Run 4), while for the sample without LiF it was 57.04 ± 1.28% (Run 4 no-LiF).

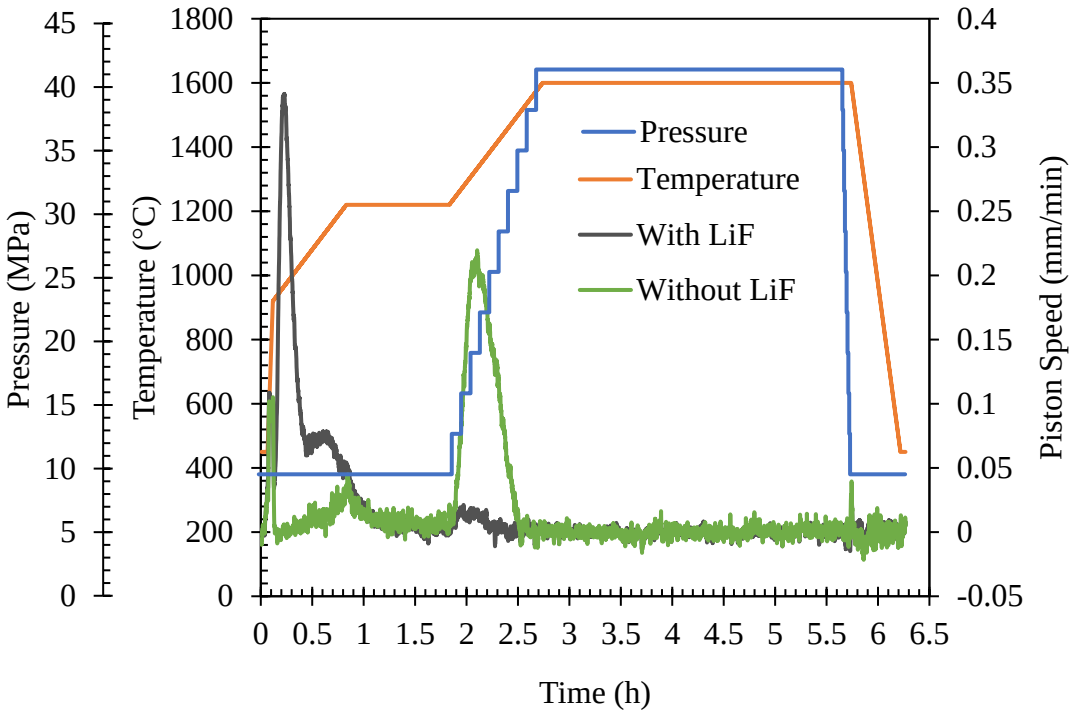


Figure 4.9: Piston movement during the sintering Run 4 with and without LiF additions.

In **Figure 4.9** it is shown that the sample sintered with LiF had a sudden onset of densification within the first hour and a half, and for the sample without LiF, there was a sudden onset of densification in the second hour and a half. The majority of the sintering occurred within the first three hours of the sintering cycle. As the first three hours were the same for all sintering cycles, the following results would be the same for all heating cycles described in **Section 3.2.1. Sintering Figure 3.2 and 3.3 pp. 60-61**.

Figure 4.10 shows the densification curve for the first hour and a half of Run 4. The pressure was held constant at 10MPa during this time. Initially both powders (with and without 1wt.% LiF) underwent densification as the temperature increased from room temperature to 900°C. When the sample with LiF, reached ≈ 925°C (m_1) the piston speed began to increase until it reached its peak at ≈ 965°C (M_1). After this, the piston speed went through a local minimum at ≈ 1060°C (m_2) which was followed by a local maximum at ≈ 1125°C (M_2). The sample without LiF had a minor peak as the temperature reached 1220°C (M_3).

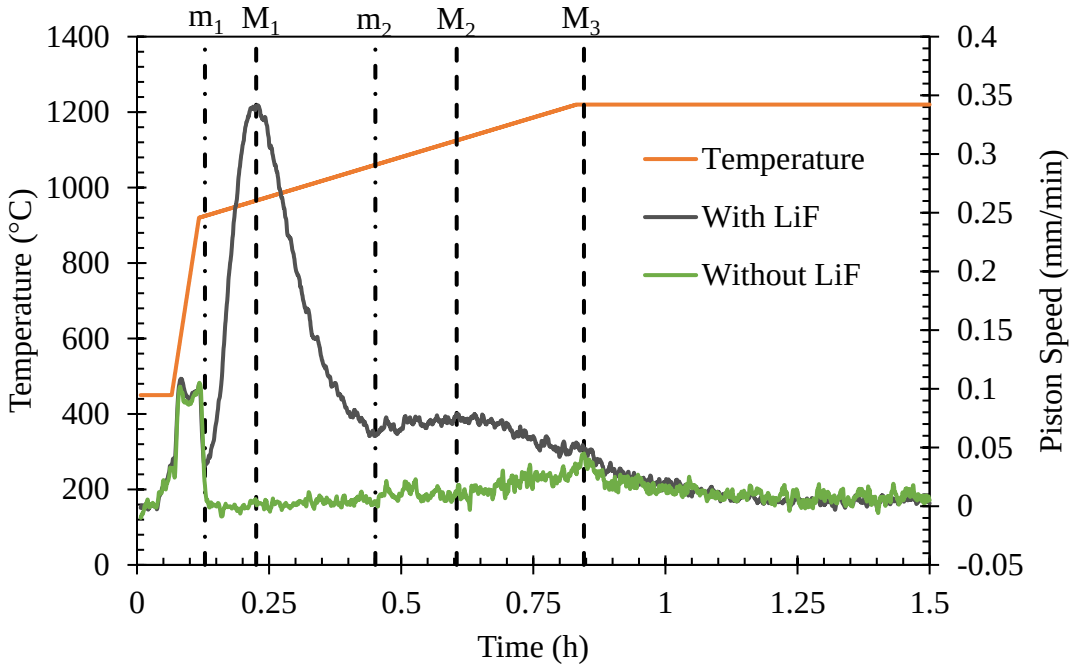


Figure 4.10: Densification curves of Run 4 for the first 1.5 hours.

In **Figure 4.11** the sintering curve is shown for the second hour and a half. During this time, the sample with LiF did not show any significant densification. The sample without the LiF however, peaked when the temperature and pressure reached 1333°C and 20MPa respectively (M_4).

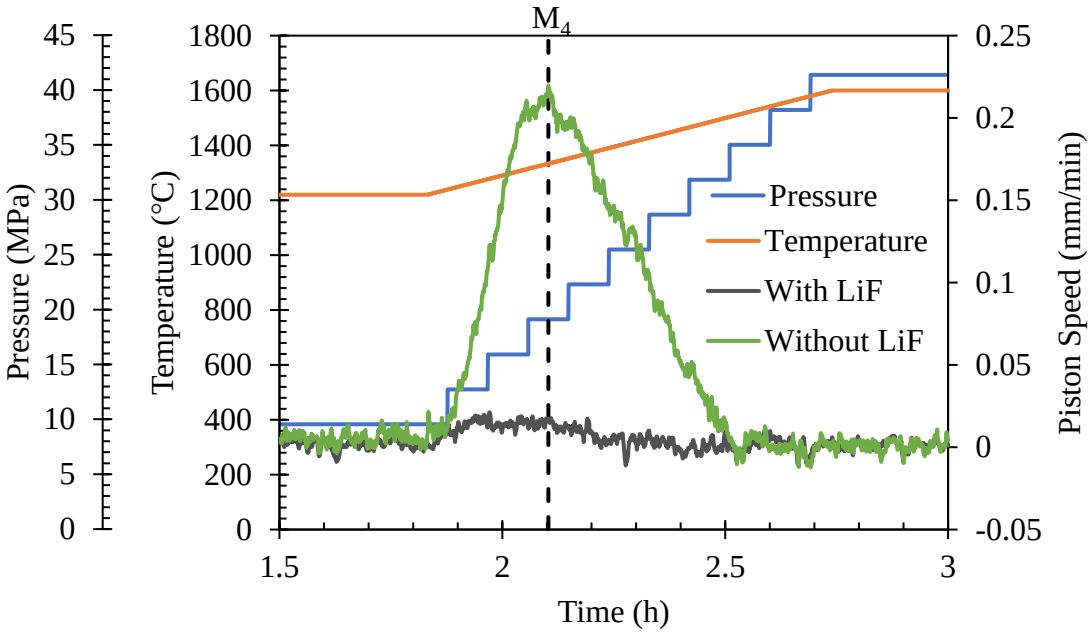


Figure 4.11: Densification curves of Run 4 from 1.5 to 3 hours.

4.1.3. XRD Analysis

The XRD spectra of the sintered sample (Run 4) indicates that the majority phase was spinel. The peaks correspond to PDF: 00-021-1152 $MgAl_2O_4$ spinel from the International Centre for Diffraction Data (ICDD) database (2019). No peaks for the individual phases of Al_2O_3 or MgO were detected, **Figure 4.12**.

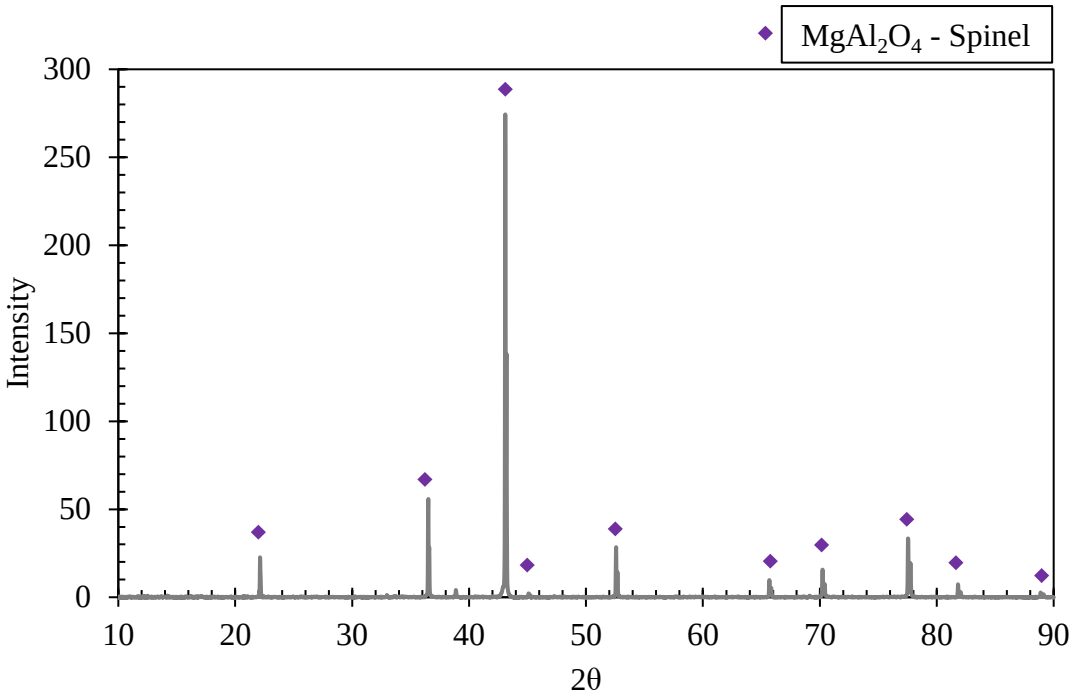


Figure 4.12: XRD spectra of the sintered sample (Run 4) showing peaks corresponding to $MgAl_2O_4$ spinel.

4.1.4. Transparency

In **Figure 4.13** the images of samples from each run that contained 1wt.% LiF are shown. The red circles superimposed on the image for Run 1 indicate the locations of small cracks. These cracks are less visible than the cracks that appeared for samples sintered in Runs 2 and 3. The sample for Run 3 was only translucent as the occurrence of the crack that ran through its body made grinding and polishing impossible without fracturing the sample. There were no cracks present in the samples sintered using Run 4 or 5.

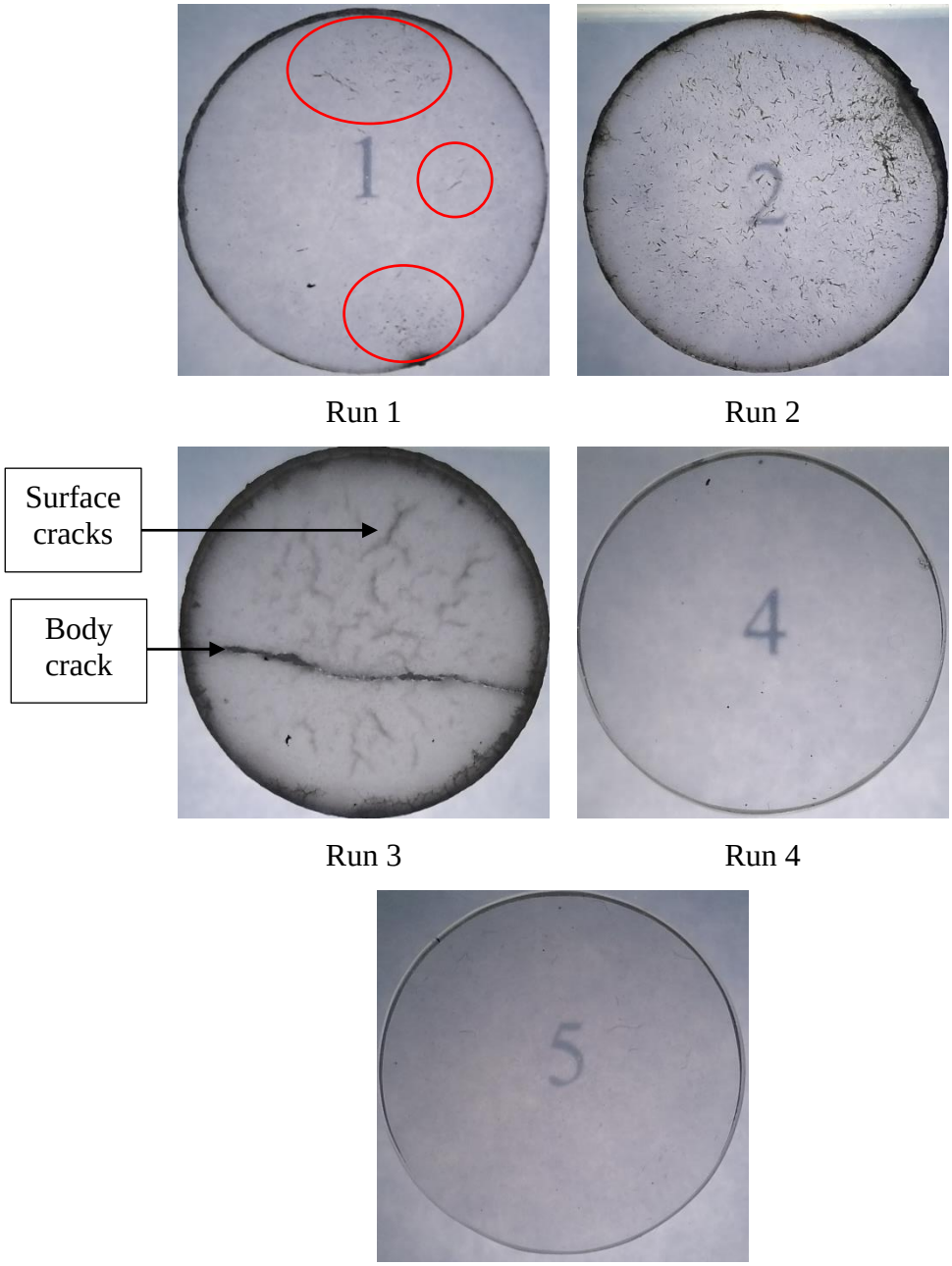
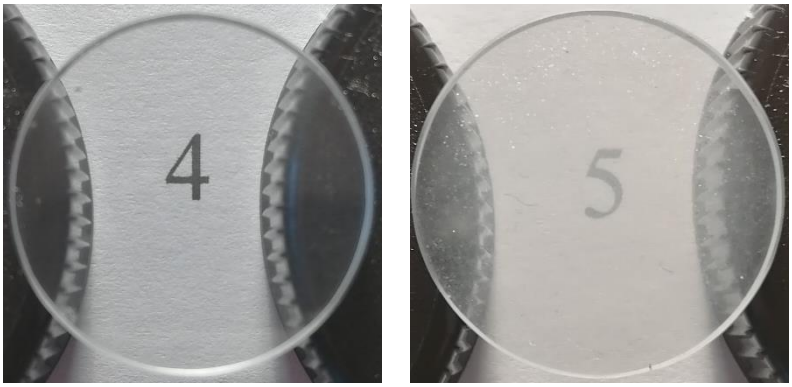


Figure 4.13: Images taken of the samples which were suspended 2cm above the paper showing the run number. The red circles in Run 1 enclose the locations at which surfaces cracks appeared.

In **Figure 4.14** it is shown that the samples produced using Run 5 were cloudy throughout the sample, whereas the samples produced by Run 4 were not.



Run 4 Run 5

Figure 4.14: Images of the suspended samples taken 1cm above the paper showing the run number.

In **Figure 4.15** images of the samples produced using Run 4 with and without the addition of LiF are shown. This highlighted the effect the addition of LiF had on the transparency of the sample.

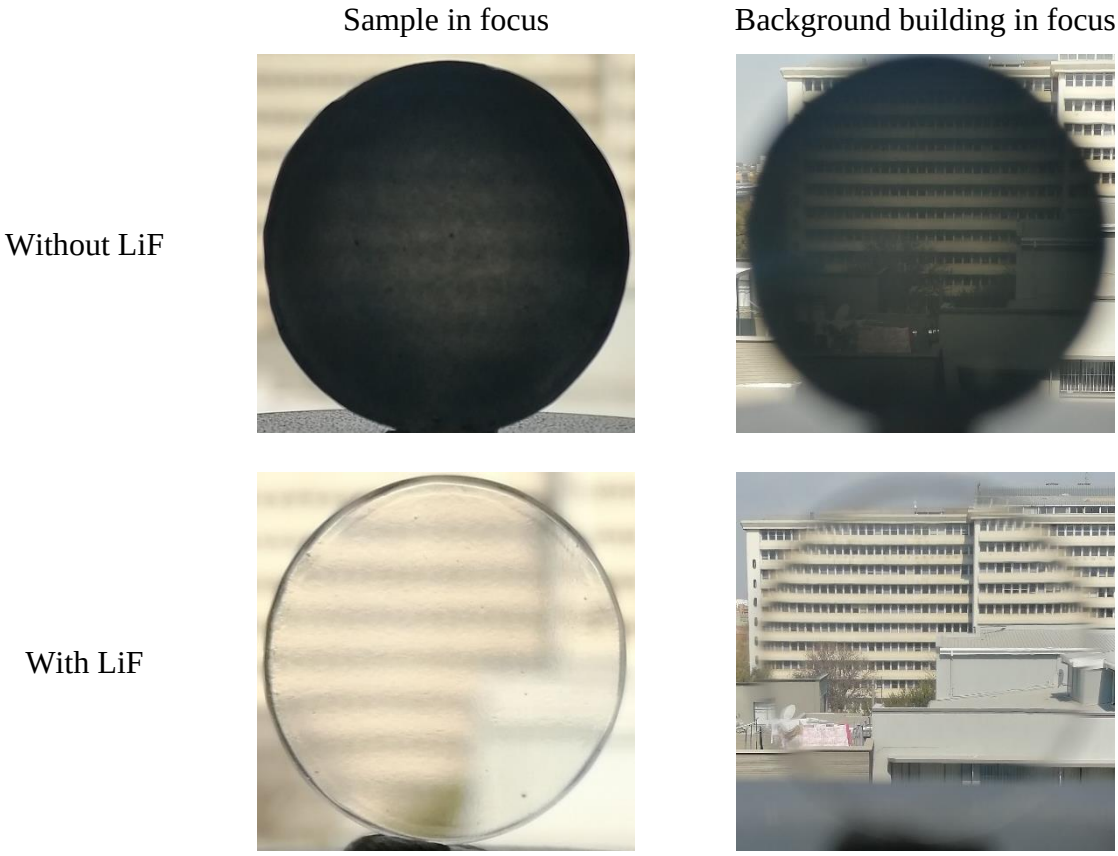


Figure 4.15: Images of the samples sintered using Run 4, with and without LiF.

The addition of 1wt.% LiF greatly increased the transmittance of the $MgAl_2O_4$ spinel. It removed the dark spots and haze and increased the clarity of the image, **Figure 4.15**. **Figure 4.16** shows the average transmission spectra for the different runs and **Table 4.2** gives the average transmission in the visible spectrum and the range. The data has been normalized to a sample thickness of 3.0mm using **Equation 4.4**. No data is given for the samples sintered using Run 3 as the body cracks made it impossible to grind and polish the samples.

$$T_{rel,2} = \left(T_{rel,1}\right)^{\frac{t_2}{t_1}} \qquad \textbf{Equation 4.4}$$

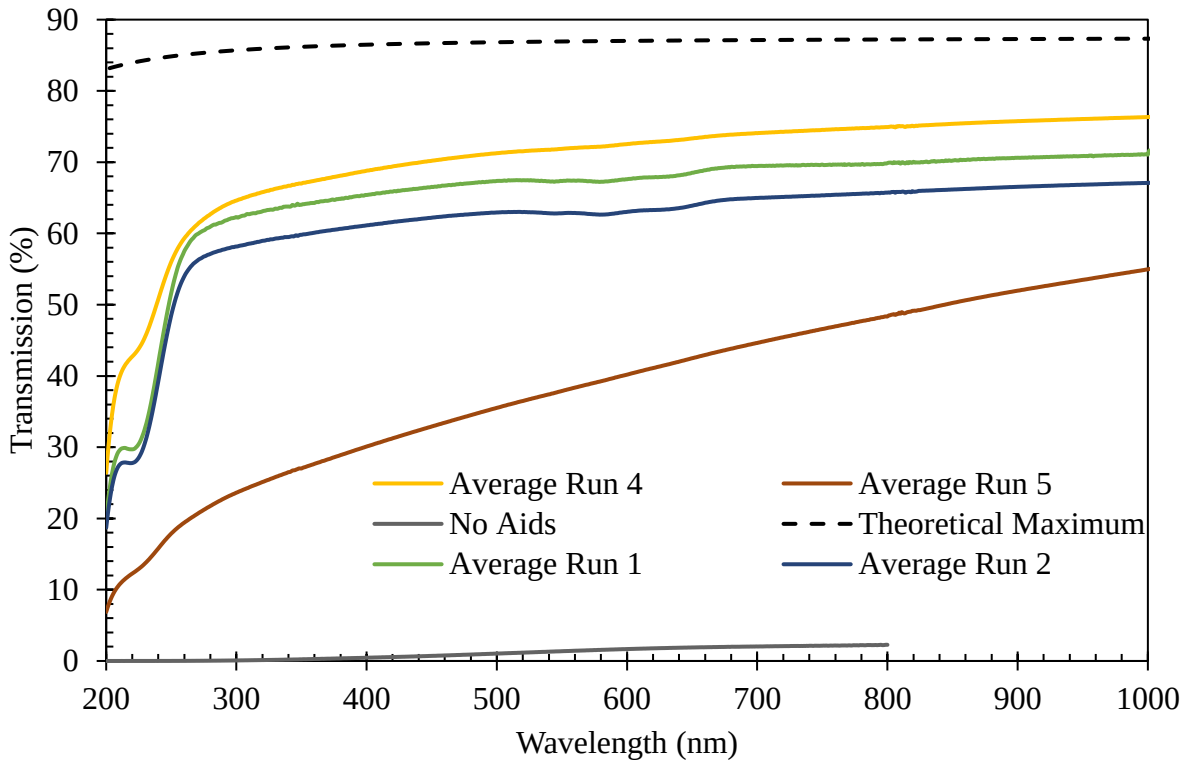


Figure 4.16: Transmission spectra normalized to 3cm thick and the theoretical maximum transmission (calculated in **Section 2.1.3. Transparency, pp. 17**).

Table 4.2: Average transmission in the visible range.

Sintering Run	**1**	**2**	**4 (LiF)**	**4 (no-LiF)**	**5**
Average Transmittance (%)	67.57	63.12	71.87	1.37	38.13
Range (%)	4.78	4.62	6.33	1.78	17.31

Figure 4.16 and **Table 4.2** show that Run 4 with the LiF had the highest transmission. The samples made with Run 4 without the LiF had the lowest transmission. Reducing the sintering time from 3hrs to 1hr (Run 4 to Run 5) resulted in two significant changes. The average transmission in the visible spectrum was reduced by ≈33%, **Table 4.2**. The other significant change was an increase the rate at which transmission decreased as wavelength decreased (the slope of the curve increased from 0.0176 to 0.0481%/nm within the visible spectrum in **Figure 4.16**).

4.1.5. Density

The average density of the sintered samples for each run are given in **Figure 4.17**. In **Figure 4.17.b**, it is shown that all sintering runs that contained LiF resulted in samples that were slightly less dense than the theoretical maximum density, even when the uncertainty in the measurements (depicted by the error bars) were considered. The ranking of densities corresponds to the ranking of transmittance, Run 4 had a higher density than Run 2, which had a higher density than Run 1, which had a higher density than Run 5. This ranking was the same for the average transmission given in **Table 4.2**. However, the uncertainty in the density measurements was greater than the difference between the average densities of the runs. Therefore, it cannot be stated with certainty that the density ranking was correct. The samples from sintering Run 3 could not be ground without inducing fracture (**Figure 4.13**). Therefore, the carbon from the graphite foil that adhered to the surfaces of the sample could not be totally removed. As such, the densities of these samples were not measured.

The average density for each sample of Run 4 is shown in **Figure 4.18**, and the density for characteristic samples of Run 4 (with LiF) are given in **Table 4.3**. Three of the thirteen samples (indicated by arrows) sintered using Run 4 have densities, that when the uncertainty was included could be fully dense. The remaining ten all have densities lower than the theoretical density. Therefore, the samples were expected to have residual porosity.

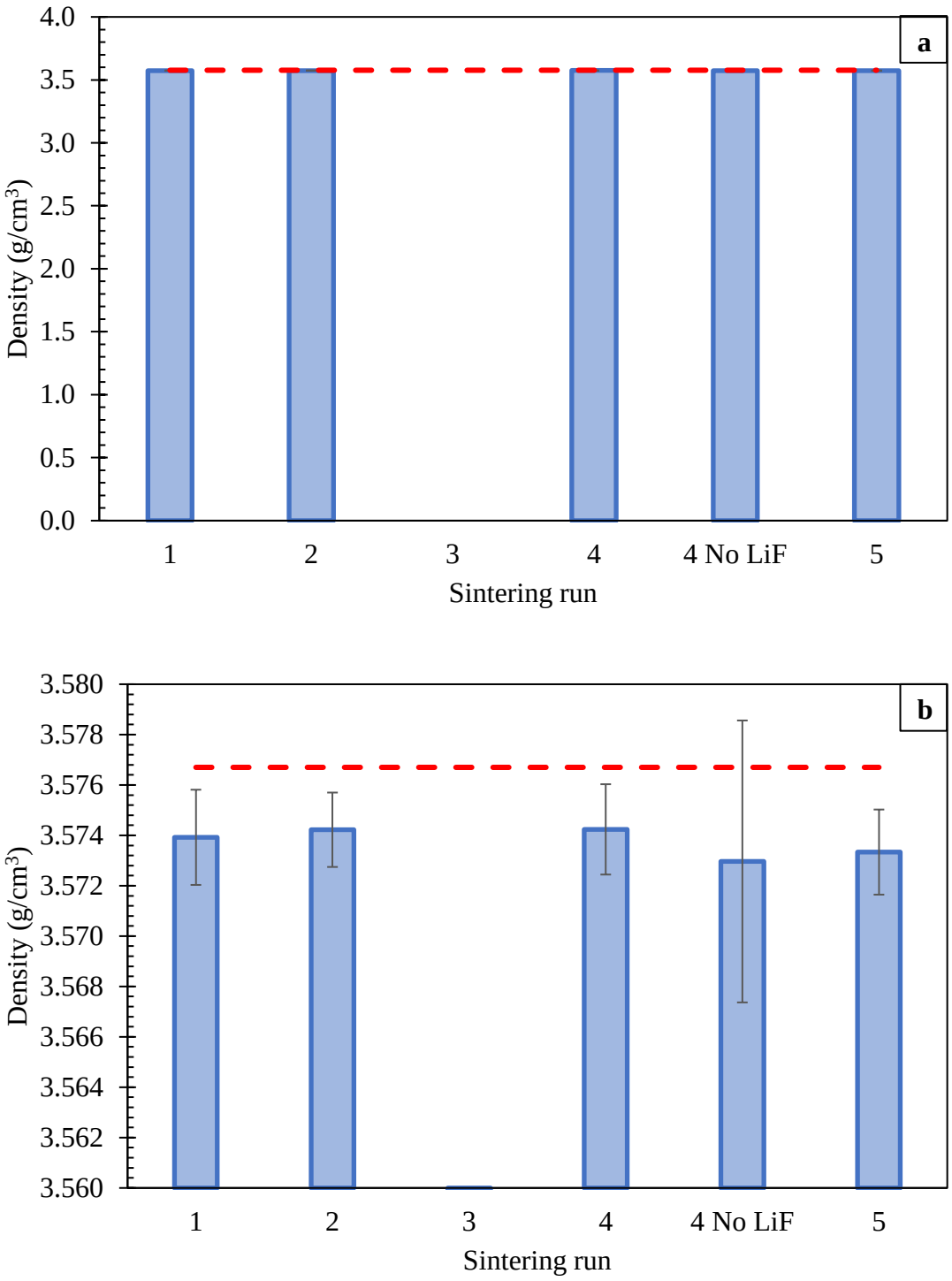


Figure 4.17: Average measured density of the sintered samples (**a**) with a standard y-axis (**b**) with a reduced y-axis range. The red line indicates the theoretical maximum density.

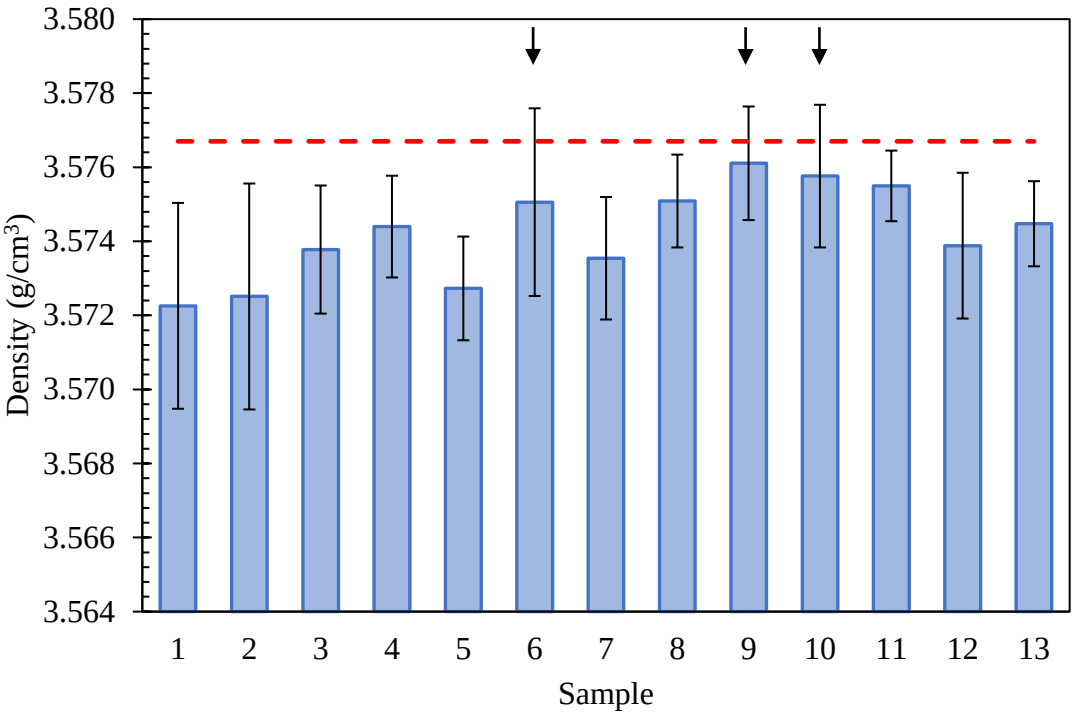


Figure 4.18: Densities of the sintered samples for Run 4 (with LiF).

Table 4.3: The average, minimum, and maximum densities of samples made using Run 4 (with LiF) (**Figure 4.18**).

	Minimum	**Average**	**Maximum**
Absolute Density (g/cm ^{3})	3.572 ± 0.003	3.574 ± 0.002	3.576 ± 0.002
Relative Density (%) *	99.88 ± 0.078	99.93 ±0.050	99.98 ± 0.043

* Based on a theoretical density of 3.5767g/cm^3.

4.1.6. Grain Structure

In **Figure 4.19** the thermally etched surface of a sample from Run 4 (with LiF) is shown.

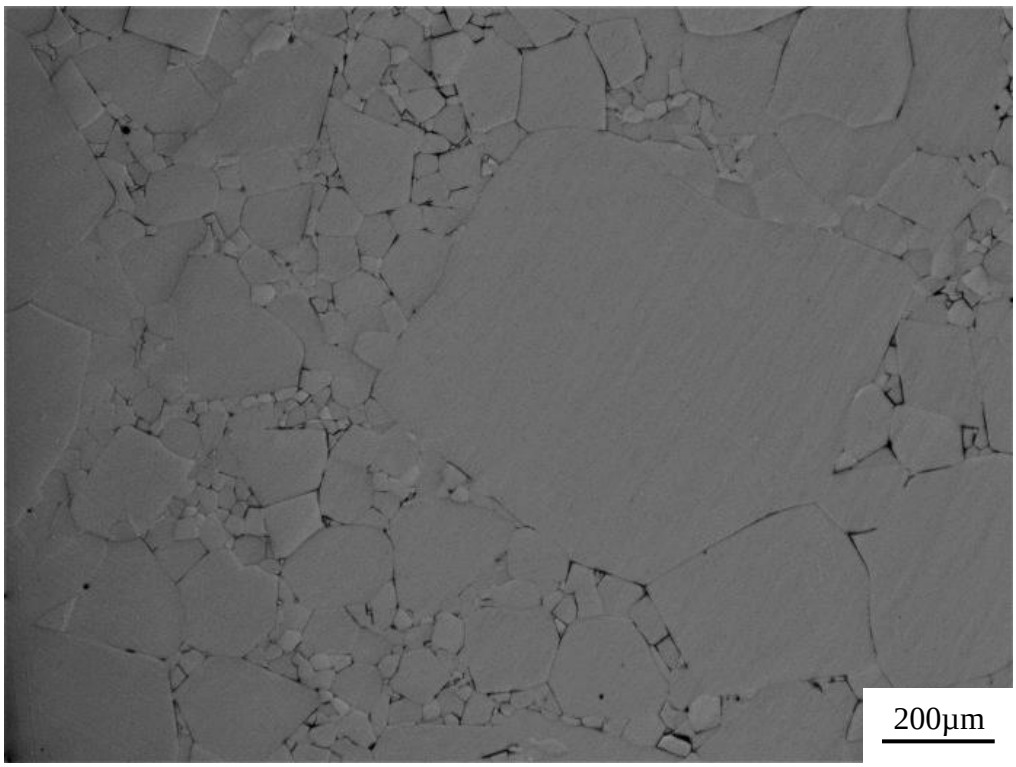


Figure 4.19: Etched image from an $MgAl_2O_4$ sample made using sintering Run 4 (with LiF).

The linear intercept method was used to calculate the average grain size using multiple micrographs. The average grain-size using this method was measured to be 96µm ± 34µm. This measurement alone was not enough to adequately quantify the microstructure as the grain size was not homogeneous. Thus, a frequency distribution was also determined. This was calculated by taking the average diameter of ≈750 grains, **Figure 4.20**. The obtained distribution had a similar shape to the distribution observed by Cohen, et al. (2018). Cohen, et al. (2018) consolidated spinel powder using an SPS, at 1400°C and 50MPa for 2 hours. The distribution shown in **Figure 4.20** for this work was skewed to larger grain sizes when compared to Cohen, et al. (2018).

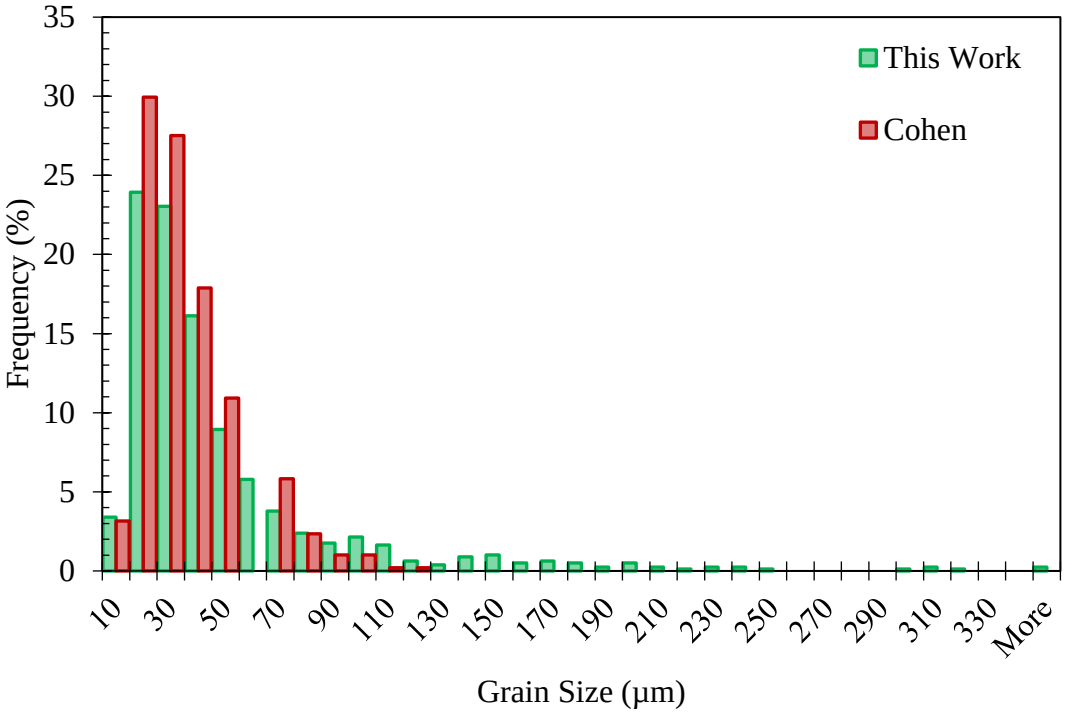


Figure 4.20: Measured grain size distribution of this work and that of (Cohen, et al., 2018).

When the natural-logarithm of the natural-logarithm of the grain size ($\ln(\ln(d_i))$) was plotted in a frequency distribution, **Figure 4.21**, it formed a normal distribution. Therefore, the grain size followed a log-lognormal distribution. This was unlike the starting powders which followed lognormal distributions. A normal distribution (Probability Density Function (PDF)) was fitted to the data and is represented by the red curve in the **Figure 4.21**. This was done by minimizing the sum of the absolute differences between the normal curve and the data for each size range. To minimize the absolute difference between the curve and the data, MS-Excel's "Solver" program was used, and the cells being varied were the mean and standard deviation of the normal distribution curve.

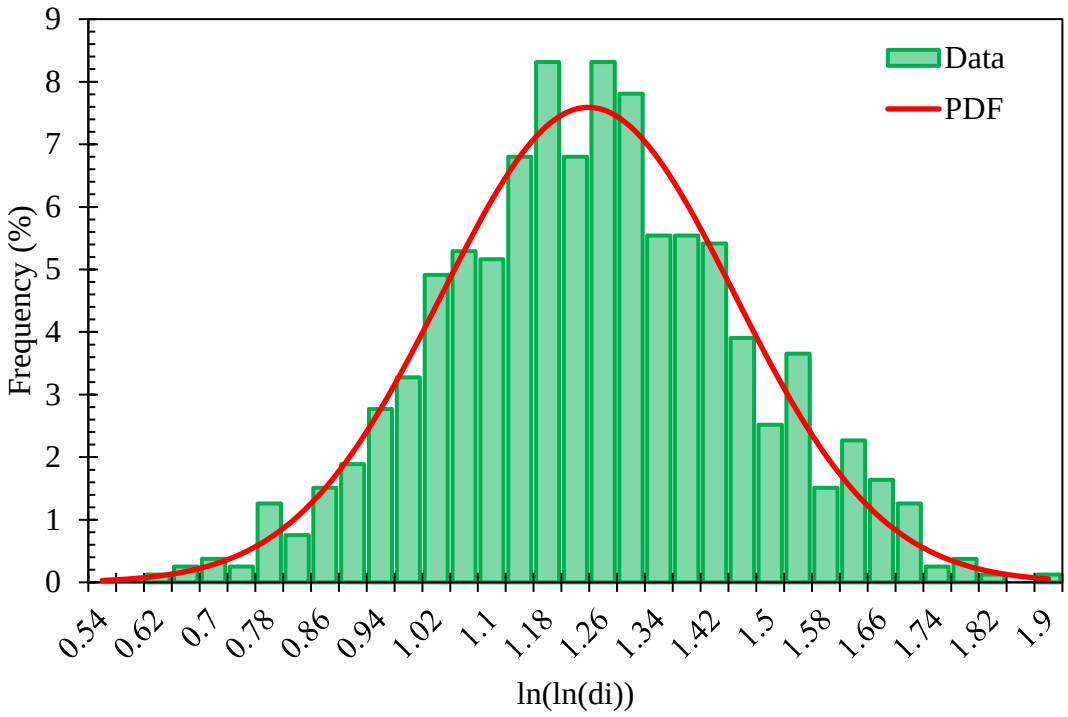


Figure 4.21: Normal distribution obtained by taking the natural logarithm of the natural logarithm of the grain size, $\ln(\ln(d_i))$.

The Shapiro-Wilk's test was used to test the distribution shown in **Figure 4.21** for normalcy. The Shapiro-Wilk test was chosen as it has been stated as the "best" test for normalcy (Ghasemi & Zahediasl, 2012).The null hypothesis of the Shapiro-Wilk test is that the data was taken from a normal distribution. The distribution plotted in **Figure 4.21** had a p-value >0.05 for the Shapiro-Wilk's test for normalcy. Therefore, there was not statistically significant evidence to reject the null hypothesis that the data was from a normal distribution.

The average diameter calculated from the frequency data was 45µm ± 45µm. The average diameter that Cohen, et al. (2018) measured was: 48.9µm ± 4.43µm. The standard deviation of the current work was much higher than Cohen, et al.'s (2018), however, this was expected as there was a greater spread of grain sizes, **Figure 4.20**. The Cumulative Density Function (CDF) of the best fit was plotted with the cumulative frequency data as a function of $\ln(\ln(d_i))$, **Figure 4.22**.

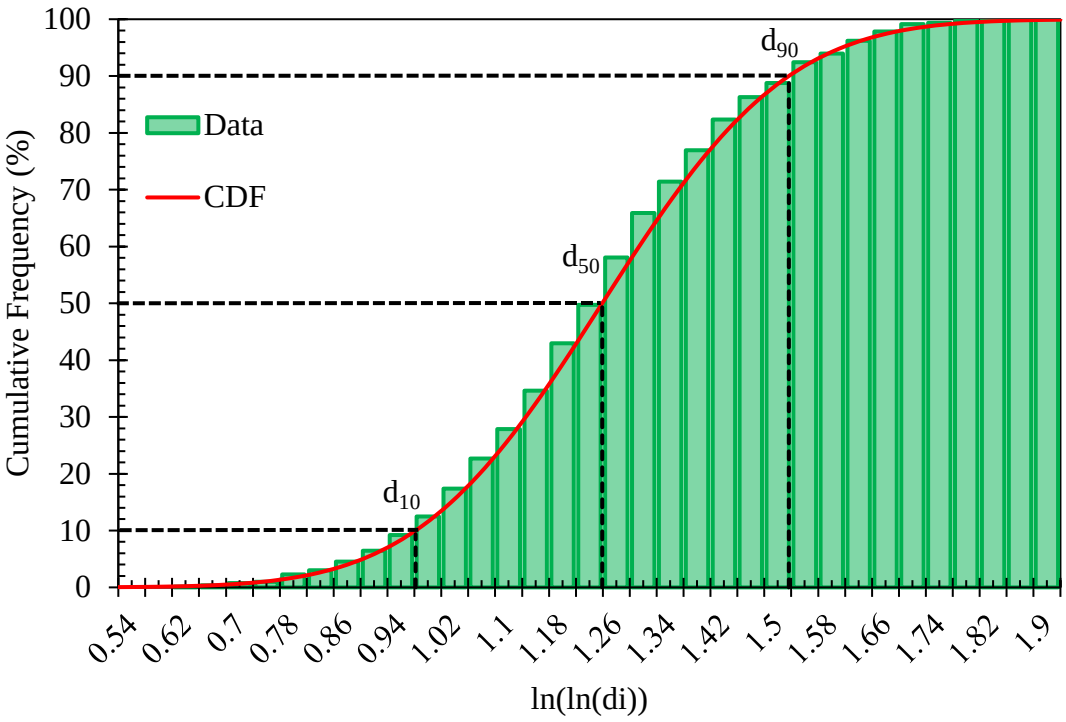


Figure 4.22: Plot of the cumulative density function and cumulative frequency data.

From **Figure 4.22** the d_{10}, d_{50}, and d_{90} could be determined for the grain sizes based on the fitted curve (CDF). The d_{10}, d_{50}, and d_{90} of the fitted curve (CDF) are given in **Table 4.4**.

Table 4.4:The d_{10}, d_{50}, and d_{90} of the fitted normal curve.

Percentile	Size (µm)
d_{10}	13.95
d_{50}	31.52
d_{90}	91.61

The d_{50} of the fitted curve (31.52µm) was smaller than the d_{50} calculated from the experimental data (45µm). This was because the mean of the log-lognormal curve was the geometric mean, while the mean of the data was the arithmetic mean. The geometric mean for the data was 32.25µm. Therefore, the curve fits the data well.

The calculated average grain size from the distribution was less than half the value measured by the linear intercept method. The measurement from both the distribution and the linear intercept method seem far smaller than what the micrograph in **Figure 4.19** shows. Therefore,

neither the linear intercept method nor measuring the average size of each grain produced a satisfactory value for the mean grain size. These methods could not accurately represent the grain-size of the heterogeneous microstructure. This occurred because the small grains, which contributed little to the area of the micrograph were weighted equally to the large grains in the determination of the average grain size. As the small grains were more numerous than the larger grains, **Figure 4.20**, the average was skewed towards the smaller grain size. To account for this, Rothman, et al. (2014) and Sokol, et al. (2014) gave the "Area Percentage" distribution. The "Area Percentage" distribution for this microstructure was estimated by assuming a cubic microstructure (for each grain, its largest and smallest diameter were multiplied to approximate its area) and this is shown in **Figure 4.23**.

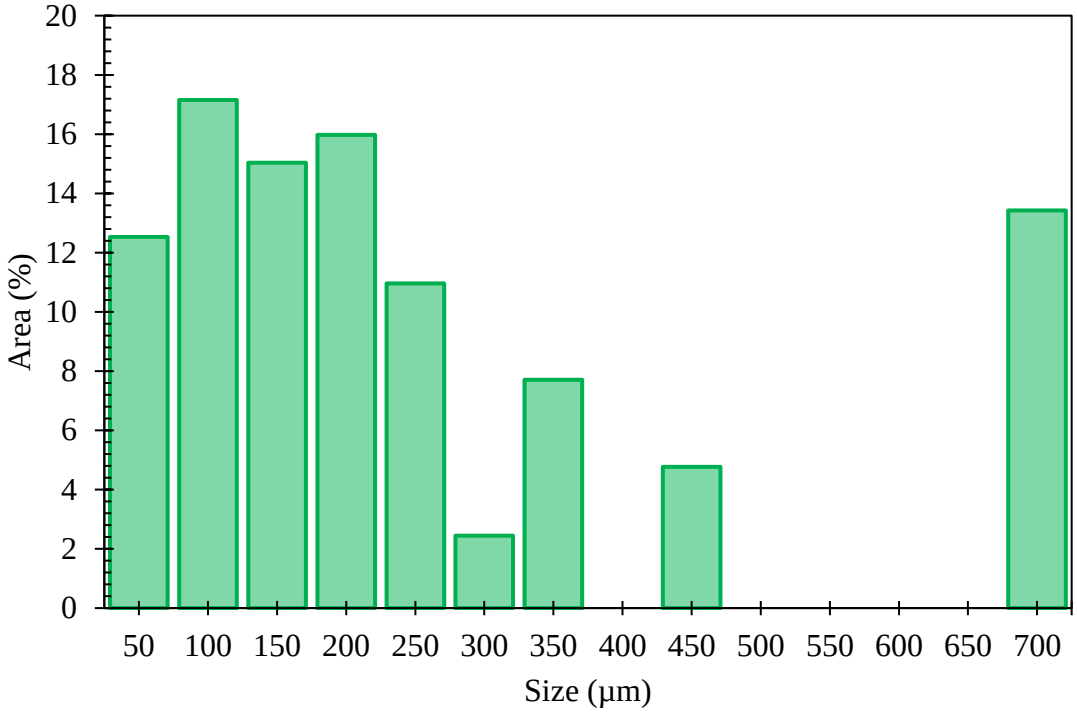


Figure 4.23: "Area Percent" distribution of the measured grains.

This distribution in **Figure 4.23** is bimodal. The small grains which individually contribute little to the total area, are numerous, thus form a peak in the distribution. The larger grains, which are far less numerous are, however so large that even a small number of them contribute a significant amount to the area. Approximately 67% of the grains (the grains <50 µm) contribute only ≈12.5% of the area. The "Area Percent" distribution seemed to better describe

the micrograph in **Figure 4.19**. The area-weighted grain-size was calculated using **Equation 4.5**.

$$\text{Weighted Area Diameter} = \frac{\sum_{i=1}^{n} A_i d_i}{A_T} \qquad \textbf{Equation 4.5}$$

Where A_i is the area of grain i, d_i is the diameter of grain i and A_T is the sum of the areas of all grains. The weighted standard deviation is given by **Equation 4.6**.

$$\text{Weighted standard devaition} = \sqrt{\frac{\sum_{i=1}^{n} A_i (d_i - d_a)^2}{\frac{(M-1)}{M} \sum_{i=1}^{n} A_i}} \qquad \textbf{Equation 4.6}$$

Where d_a is the weighted average diameter and M is the number of non-zero weights. The weighted area diameter was 236µm and the weighted standard deviation was 208µm. This value is much higher than the other two methods. However, this method accounts for the fact that even a small number of large grains can account for a large portion of the micrograph.

The weighted area diameter, 236µm ± 208µm, looks as though it has no practical use as the average value (236µm) is similar to the standard deviation (208µm), thus it would seem that the uncertainty in the measurement was as large as the actual measurement. However, this was not the case. The standard deviation was relatively high because the grain size varied over such a wide range, the largest grain had an average diameter of ≈698µm while the smallest grain had an average diameter of only ≈6.14µm. Therefore, the range of the grain sizes was ≈690µm. Thus, the standard deviation of 208µm does not imply that the uncertainty in the measurement was relatively high, just that the distribution of the grain sizes was wide. This accurately describes the microstructure depicted in the micrograph of **Figure 4.19**. It must be noted that the total area examined was ≈5mm^2, thus the sample size was small.

4.1.7. Mechanical Properties

The sample sintered using Run 4 (with LiF) had the best transmission, thus its mechanical properties were determined. The following section refers only to samples sintered using Run 4 with LiF.

The average fracture toughness was measured to be 1.56 MPa.m$^{-1/2}$ ± 0.26 MPa.m$^{-1/2}$ and the average hardness was 1245Hv ± 36Hv. These averages and standard deviations were calculated from data from multiple measurements on multiple samples. When the average fracture

toughness and hardness were calculated for each sample and that was used as the data set to calculate the standard deviation, the standard deviations were only 0.026MPa.m$^{-1/2}$ and 1.9Hv, respectively. Thus, the variance of mechanical properties was greater within each sample than between each sample. When using the area-weighted average grains size, the fracture toughness follows the data from other authors (Salem, 2013), **Figure 4.24**.

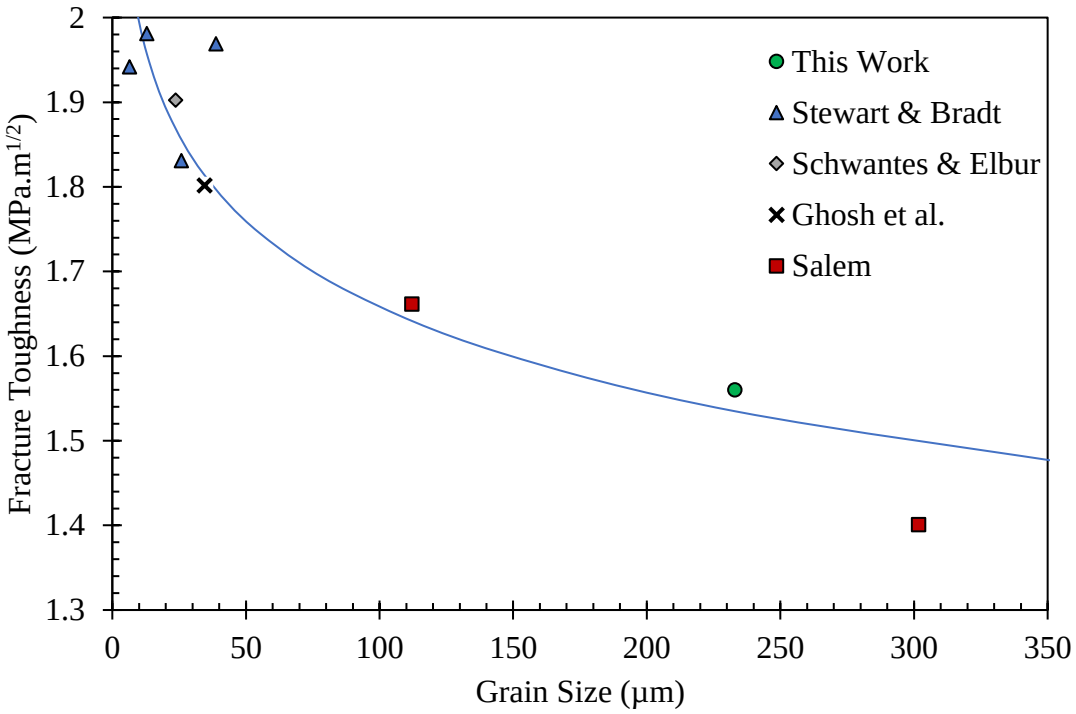


Figure 4.24: Fracture toughness as a function of grain size. Data from this work and that of other authors (Salem, 2013). The test methods for the above authors were single-edged precracked beam (Salem (2013)), controlled microflaw technique (Stewart & Bradt (1980) and Gosh et al. (1991)), and straight notched technique (Schwantes & Elbur (1983)).

Regrettably, the measurement for the fracture toughness was dubious. The brittle nature of spinel likely contributed to the damage originating from the indent. **Figure 4.25** shows a characteristic indent from which the hardness and fracture toughness values were determined. Superimposed on the image is a measurement of the length of a crack. There are many cracks surrounding the indent and they do not all originate from a corner of the indent. Spalling was also observed. Because there were many cracks, determining which cracks should be measured was difficult. This would likely prevent the attainment of consistent measurements.

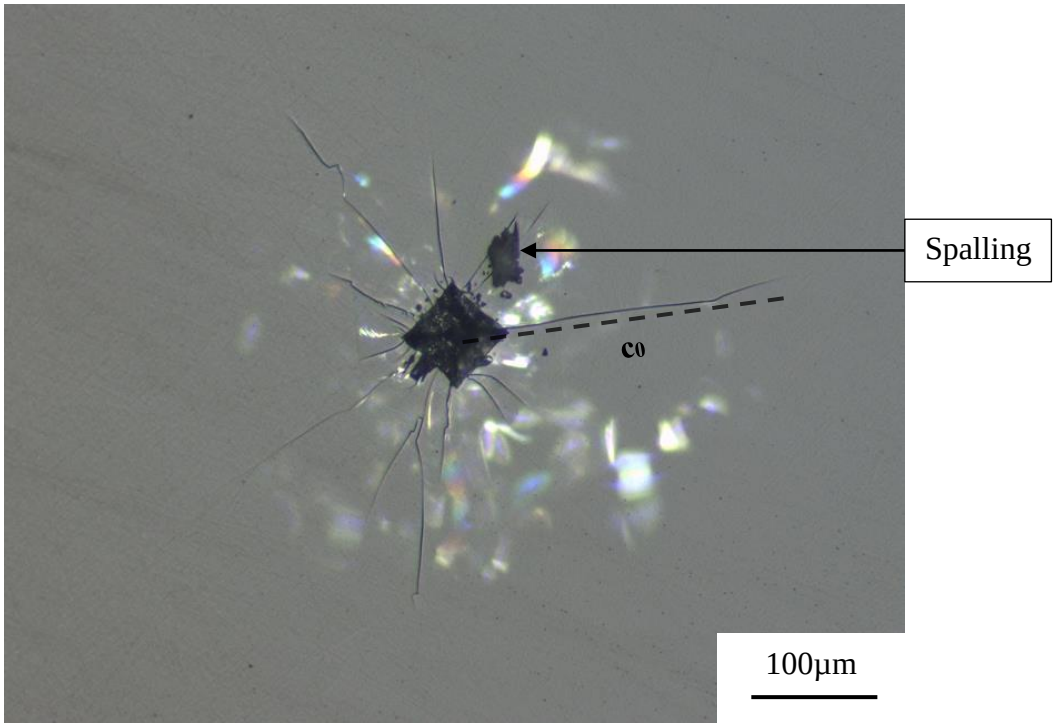


Figure 4.25: Characteristic indent of the transparent samples.

However, the indents were easily measured, thus the hardness values were more reliable. **Table 4.5** shows the measured hardness values of this work and of other authors. The hardness of these samples was slightly less than the reported values.

Table 4.5: Measured hardness of this work and of other authors.

Author	**Hardness (Hv)**
Rothman, et al. (2014)	1600 ± 28
Rothman, et al. (2013)	1450
Esposito, et al. (2013)	1420 ± 60
	1390 ± 60
Frage, et al. (2007)	1300 ± 50
This work	1245 ± 36

The biaxial flexural strength of the samples was also measured. An image of a sample fractured during the B3B test is shown in **Figure 4.26**. The fracture origin was in the centre of the sample and the cracks radiated outwards towards the periphery of the sample.

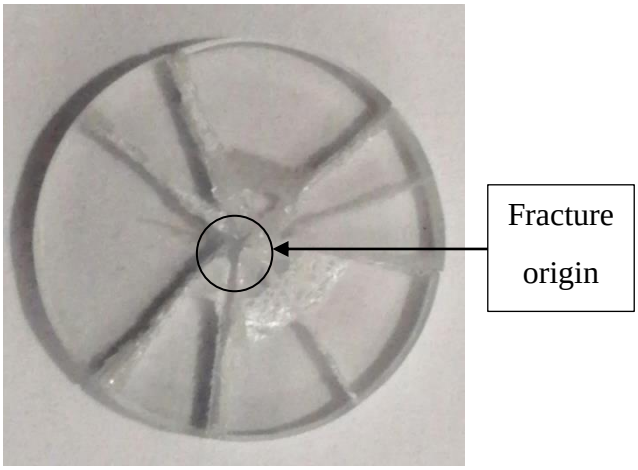


Figure 4.26: Sample fractured using the ball on 3 balls test.

A SEM micrograph of a fracture surface is shown in **Figure 4.27**. The location of the fracture origin is circled in black. The picture insert shows the location of the SEM image in **Figure 4.27** relative to the fractured sample. Progressively higher magnifications of the fracture origin are shown in **Figures 4.28** and **4.29**.

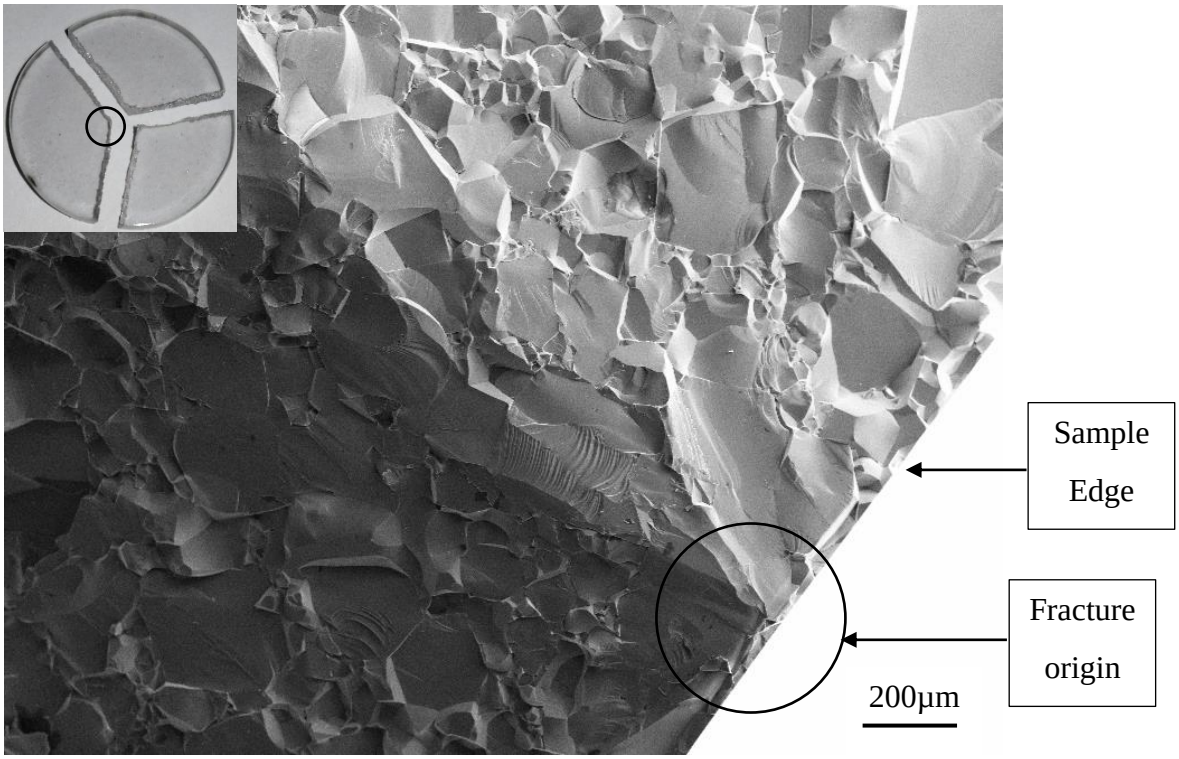


Figure 4.27: Secondary electron micrograph of the fracture origin.

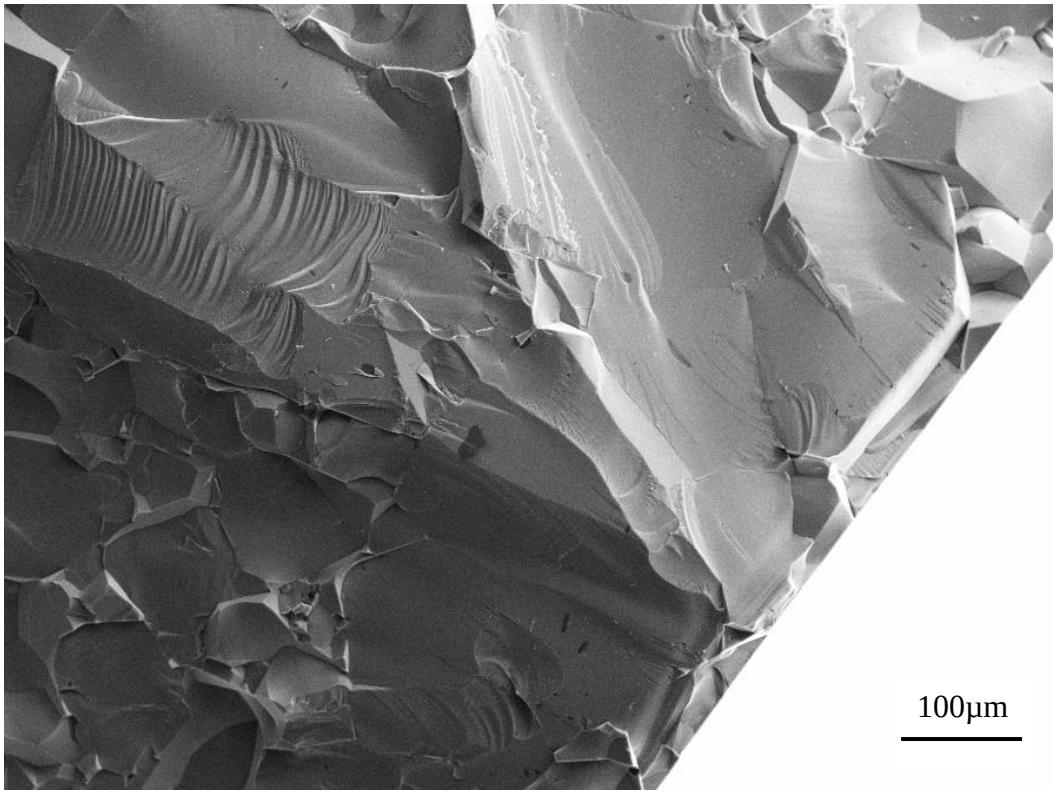


Figure 4.28: Secondary electron micrograph of the fracture origin.

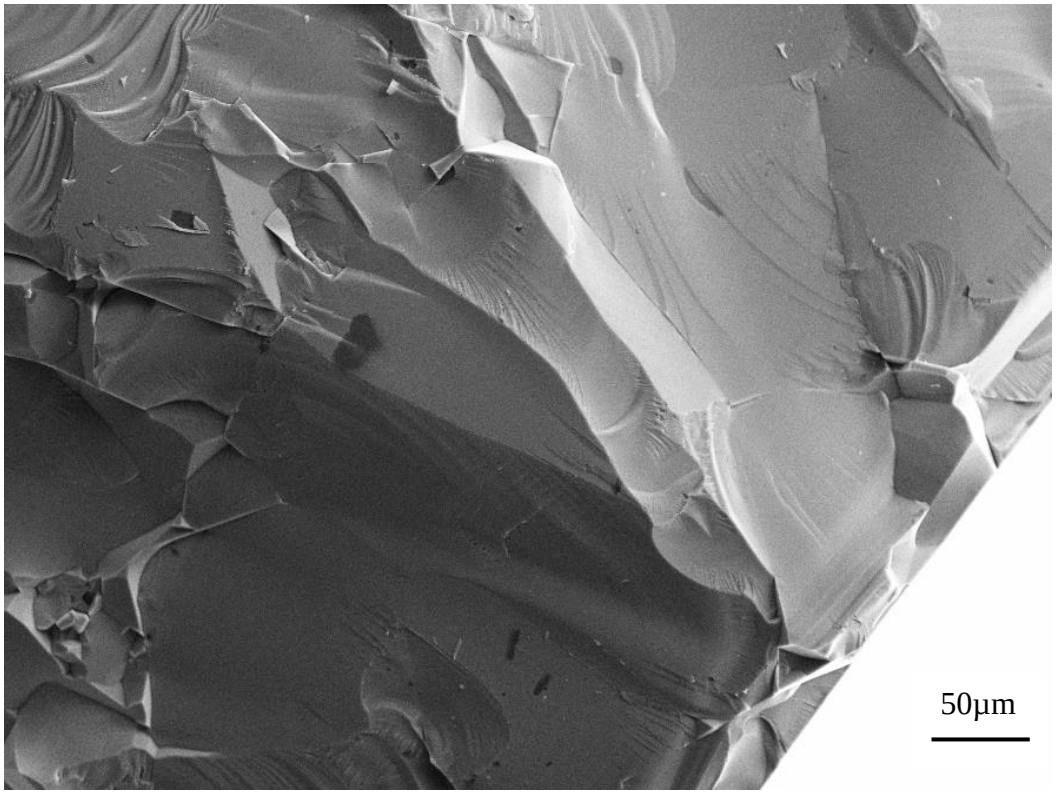


Figure 4.29: Secondary electron micrograph of the fracture origin.

To calculate the stress experienced by a sample undergoing the B3B test, the equations determined by Borger, et al. (2002) were used (**Section 3.3.7.3**. **Equations 3.4 to 3.7 pp. 67-69**). For these equations to be valid, Borger, et al. (2002) gave the limits to defined parameters. The parameters, experimental ranges/value and the allowable ranges are shown in **Table 4.6.**

Table 4.6: Experimental and allowable ranges for the parameters needed to calculate the stress for the B3B test.

Parameter	Experimental Range/Value	Allowable Range
$\frac{R_a}{R}$	0.73 – 0.75	0.55 – 0.90
$\frac{t}{R}$	0.29 – 0.31	0.05 – 0.60
υ	0.27	0.20 – 0.30

As the experimental values all fell within the allowable range, the equations determined by Borger, et al. (2002) could be used to calculate the stress. In **Figure 4.30**, the calculated stress as a function of piston extension is shown.

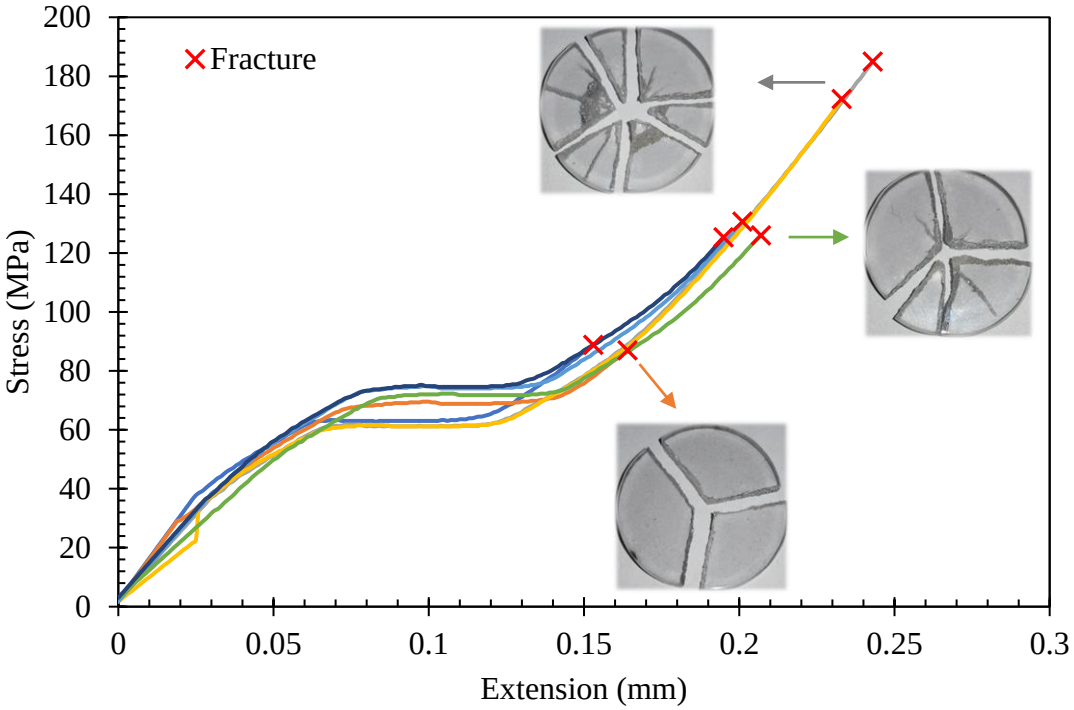


Figure 4.30: Stress as a function of extension for the ball on 3 balls test.

Samples that withstood a higher stress fractured into more pieces, as shown by the inserts in **Figure 4.30**. A correlation between the fracture stress and the number of pieces the sample broke into was also observed by Borger et al. (2001). Unfortunately, no author could be found that reported the stress extension curve. Also, when the extension was ≈0.07 to 0.13mm the stresses experienced by the samples were constant. To interpret the results of the fracture test the distribution given by **Equation 4.7** was used (Klein, 2009).

$$P(\sigma) = 1 - e^{\left[-\left(\frac{\sigma}{\sigma_N}\right)^m\right]} \qquad \textbf{Equation 4.7}$$

Where $P(\sigma)$ is the cumulative failure probability as a function of the applied tensile stress, m is the shape parameter or Weibull modulus and σ_N is the nominal strength which corresponds to a probability of failure of 63%. The experimental data was fitted to **Equation 4.7** by first linearizing **Equation 4.7** to **Equation 4.8**.

$$\ln\{-\ln[1 - P(\sigma)]\} = -m\ln(\sigma_N) + m\ln(\sigma) \qquad \textbf{Equation 4.8}$$

To determine the probability of failure for a given disk, the disks were ranked in ascending order with respect to the strength. Then the probabilities were assigned using **Equation 4.9** (Klein, 2009).

$$P_i = \frac{i - 0.5}{n} \qquad \textbf{Equation 4.9}$$

Where *i* is the disks ranking value ($i = 1, 2, 3, 4, \ldots, n$) and *n* is the number of specimens (Klein, 2009). In **Figure 4.31** the experimental data was fitted to **Equation 4.8**.

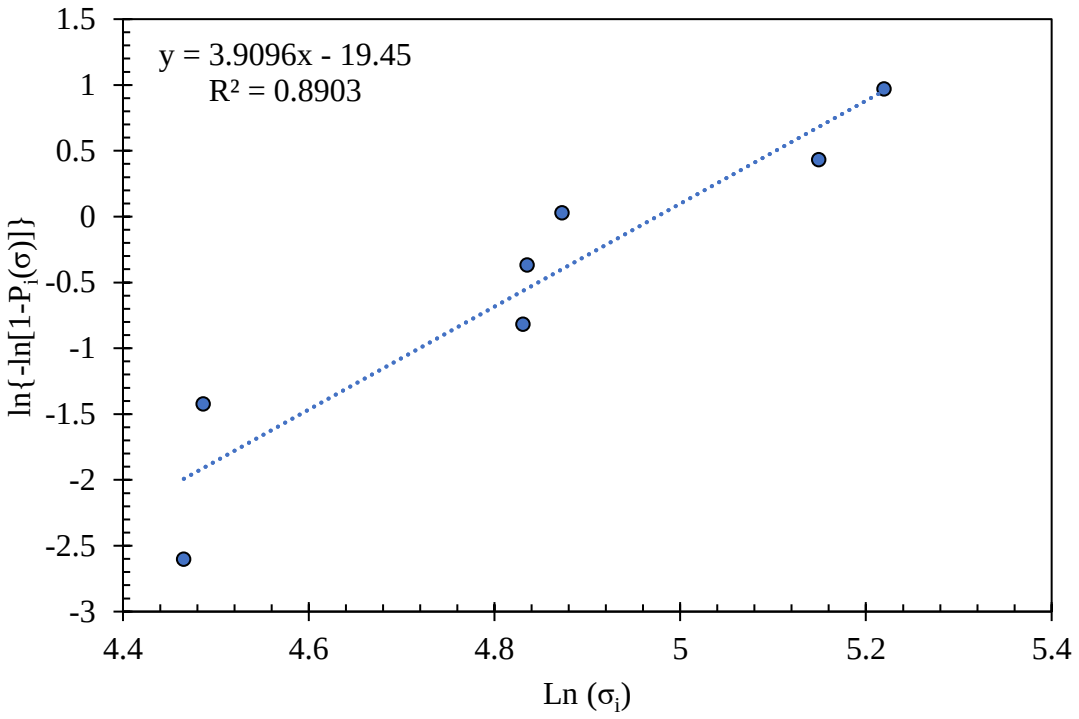


Figure 4.31: Experimental data fitted to **Equation 4.8**.

The nominal strength was 145MPa and the Weibull Modulus was 3.91. For comparison, Rothman, et al. (2014) measured a strength of 150 ± 20MPa for a spinel sample with a grain size of 40µm. As one of the potential uses of transparent spinel is to replace glass in transparent armour to reduce the armour's weight, the specific strength was also determined. The specific strength was determined by dividing the nominal strength by the average density. The specific strength was 40.5kN.m/kg.

SEM micrographs of the fracture surfaces are given in **Figures 4.32** to **4.39**. Transgranular fracture is shown by the cleavage steps while the intergranular fracture is shown by the grain boundaries. The fracture surfaces examined in the SEM show a mix of transgranular and intergranular fracture.

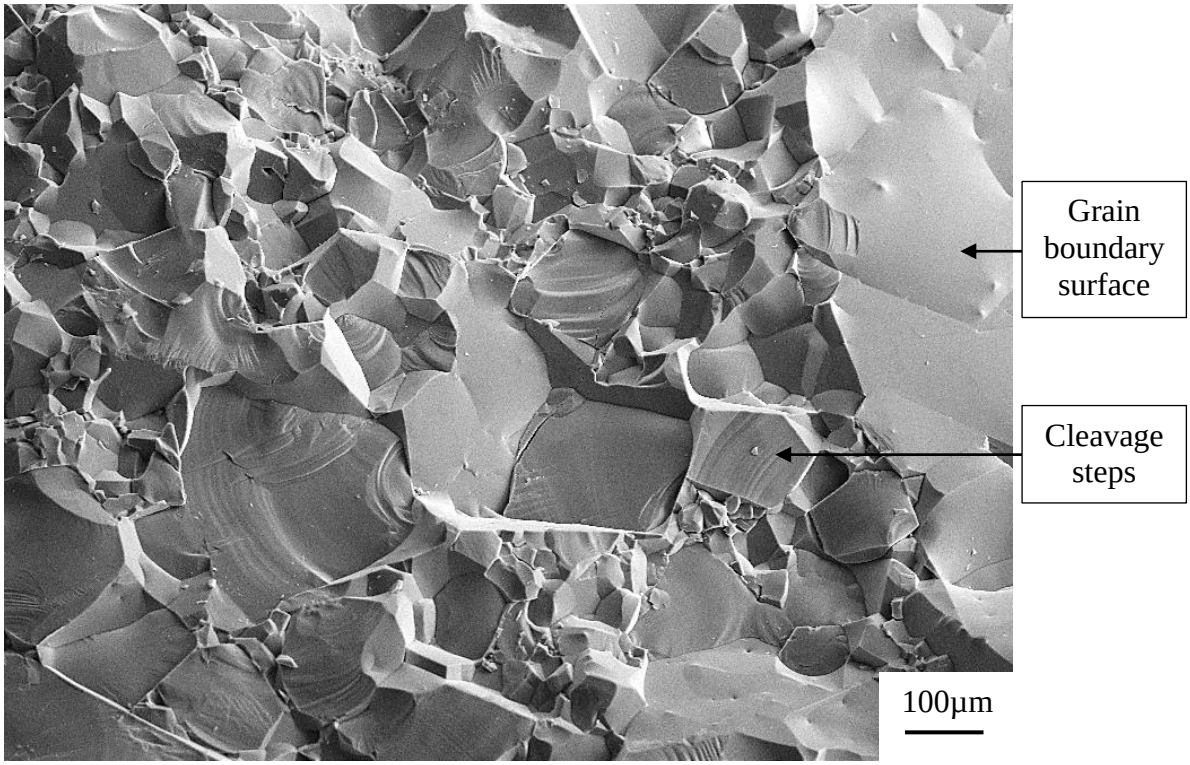


Figure 4.32: Low magnification SEM micrograph of the spinel's fracture surface.

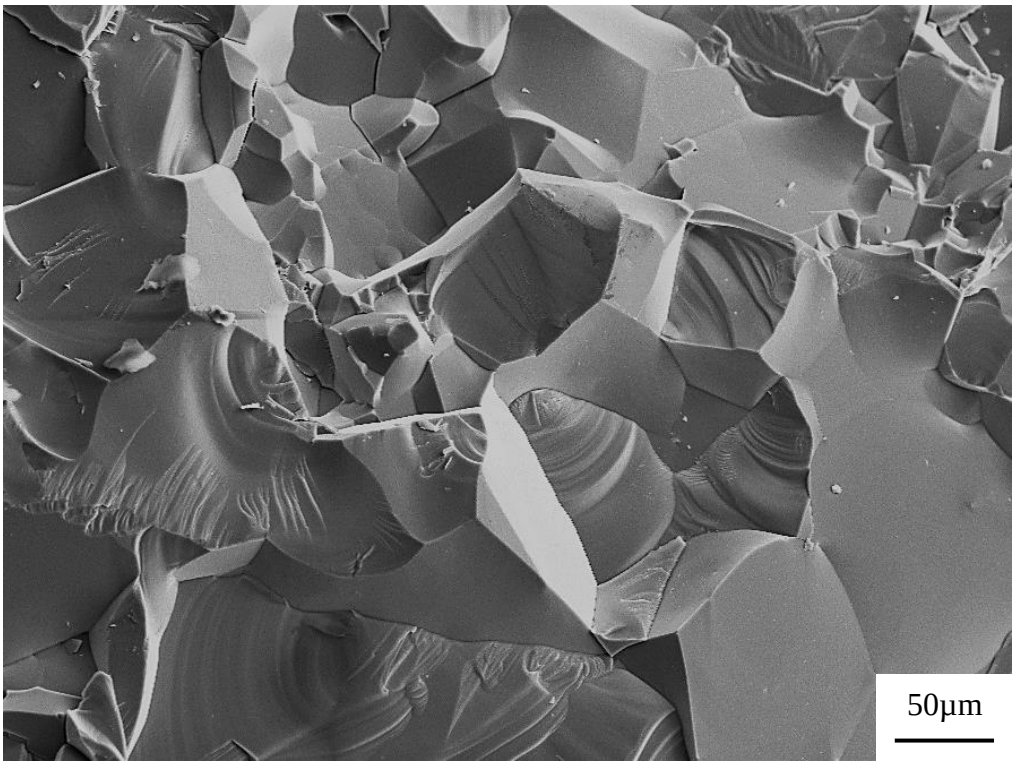


Figure 4.33: Medium magnification SEM micrograph of the spinel's fracture surface.

An EDS measurement was done over the entire fracture surface shown in **Figure 4.32** and the results are shown in **Table 4.7**. The amount of magnesium measured was slightly less than expected, whereas there was relatively more aluminium and oxygen than expected.

Table 4.7: EDS measurement on the fracture surface. The values contained in brackets indicate the theoretical value.

Element	**Mass Percent**	**Atomic Percent**
Oxygen	45.66 (44.98)	57.85 (57.14)
Magnesium	16.07 (17.09)	13.40 (14.29)
Aluminium	38.28 (37.93)	28.76 (28.57)

At high energy regions, such as triple points, non-uniform areas were found. These are shown in **Figures 4.34** to **4.36**. These non-uniform areas looked like damaged regions.

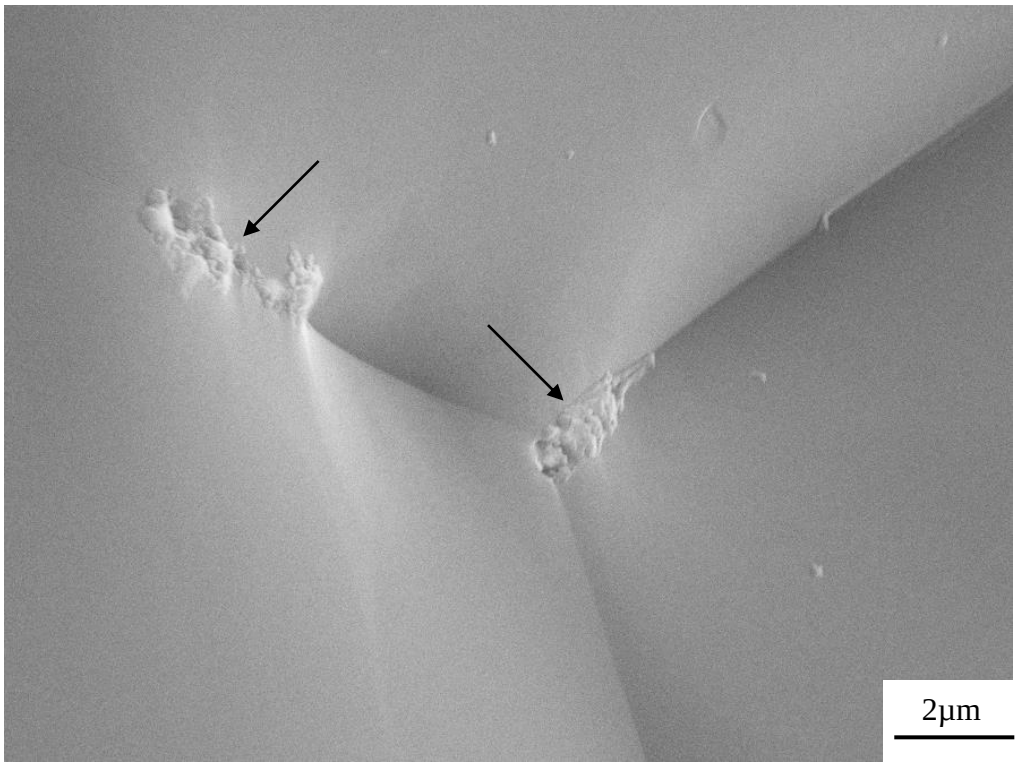


Figure 4.34: SEM micrograph of non-uniform areas found at a triple point and grain boundary.

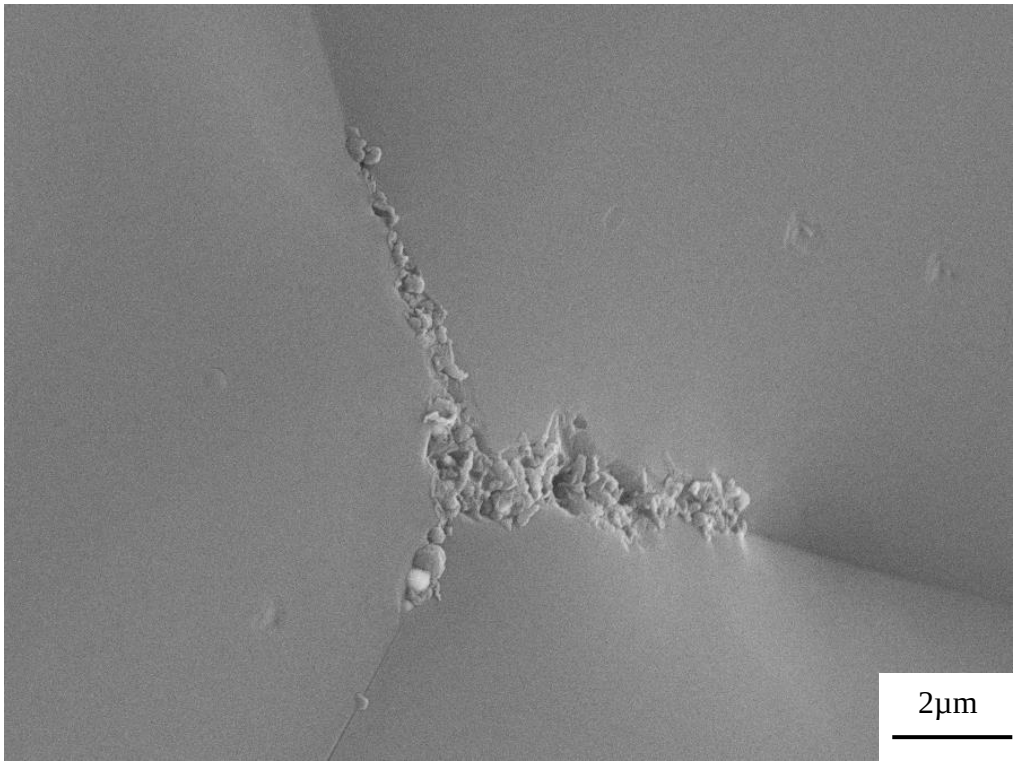


Figure 4.35: SEM micrograph of a non-uniform area found at a triple point.

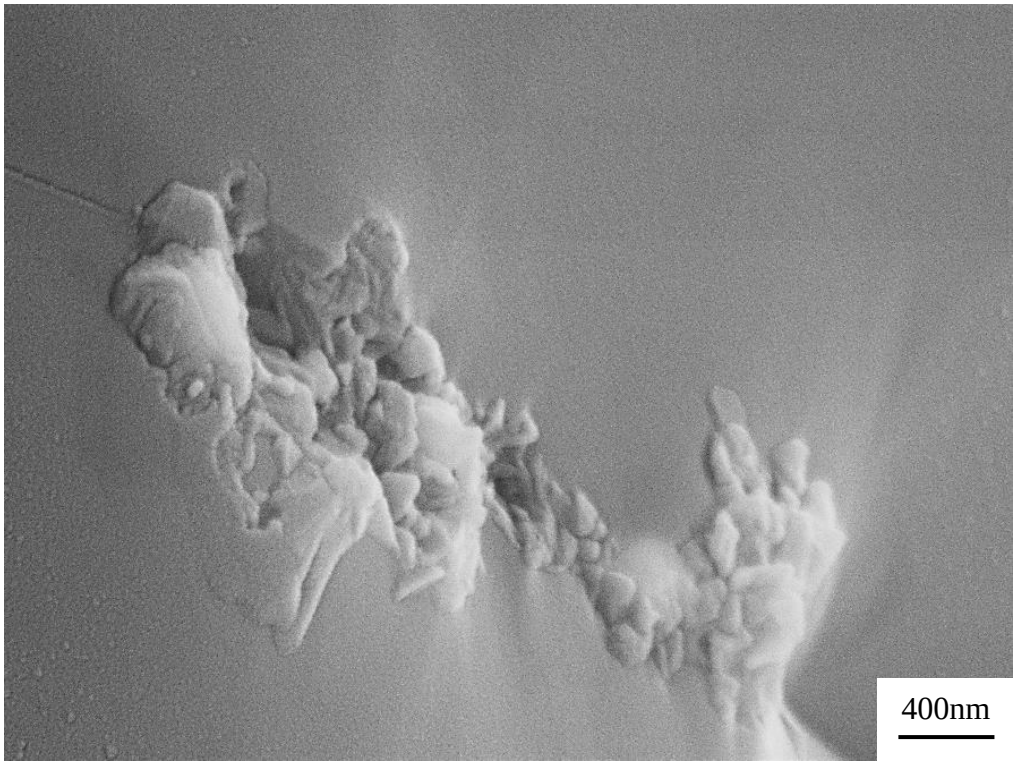


Figure 4.36: SEM micrograph of a non-uniform area found at a grain boundary.

An EDS analysis was conducted on the damaged region shown in **Figure 4.35** and the results are shown in **Table 4.8**. The relative amount of each element was very close to the theoretical amount for spinel.

Table 4.8: EDS analysis of the non-uniform area. The theoretical weight and atomic percent for spinel is shown in brackets.

Element	**Mass Percent**	**Atomic Percent**
Oxygen	44.81 (44.98)	56.97 (57.14)
Magnesium	17.29 (17.09)	14.46 (14.29)
Aluminium	37.9 (37.93)	28.57 (28.57)

In **Figures 4.37** to **4.39** images of pores are shown. The diameter of the pore in **Figure 4.37** was ≈6µm. The pores in **Figures 4.38** and **4.39** are smaller.

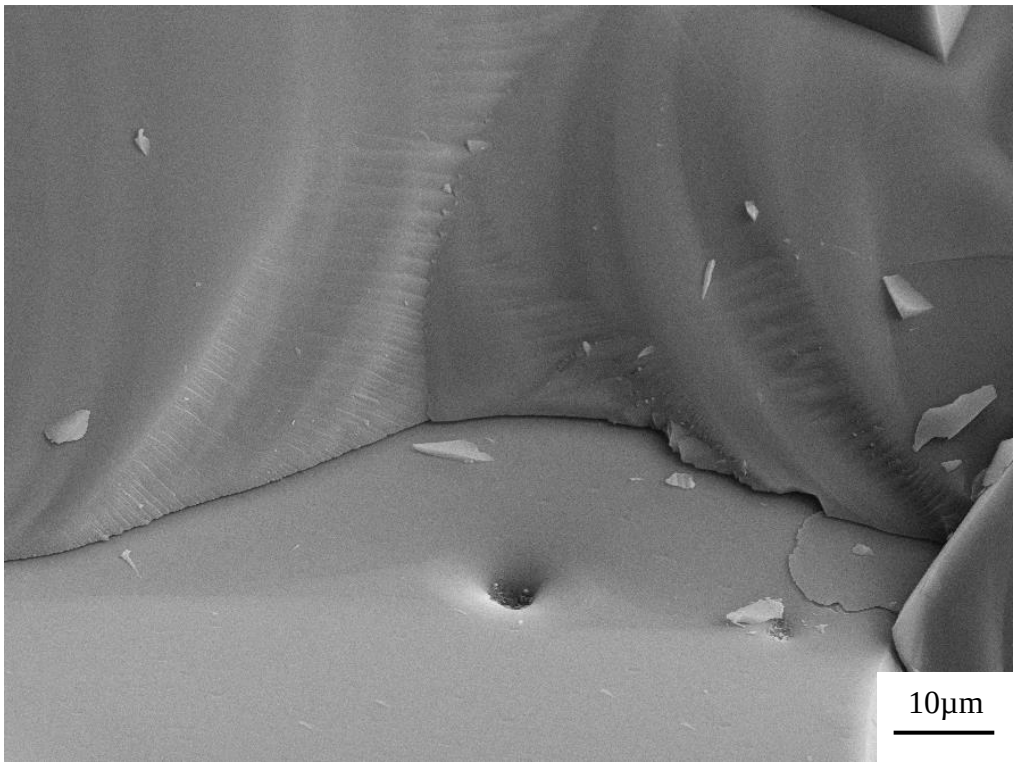


Figure 4.37: SEM micrograph of an occluded pore.

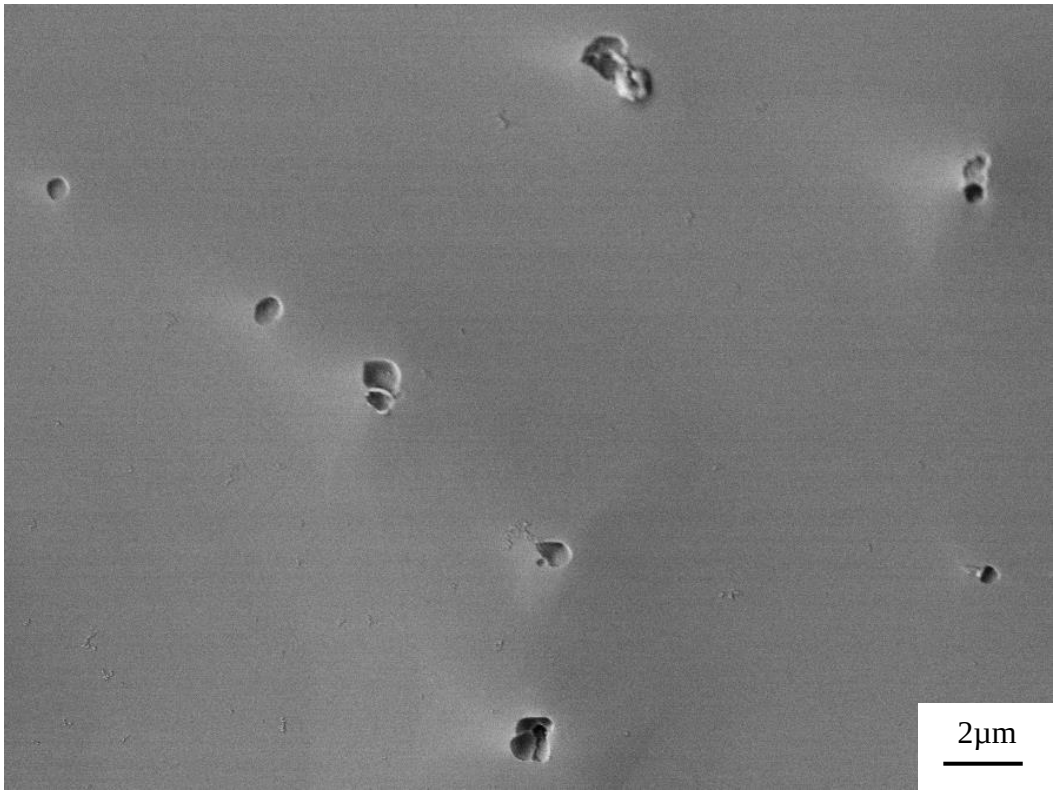


Figure 4.38*:* SEM micrograph of numerous pores on the surface of a grain.

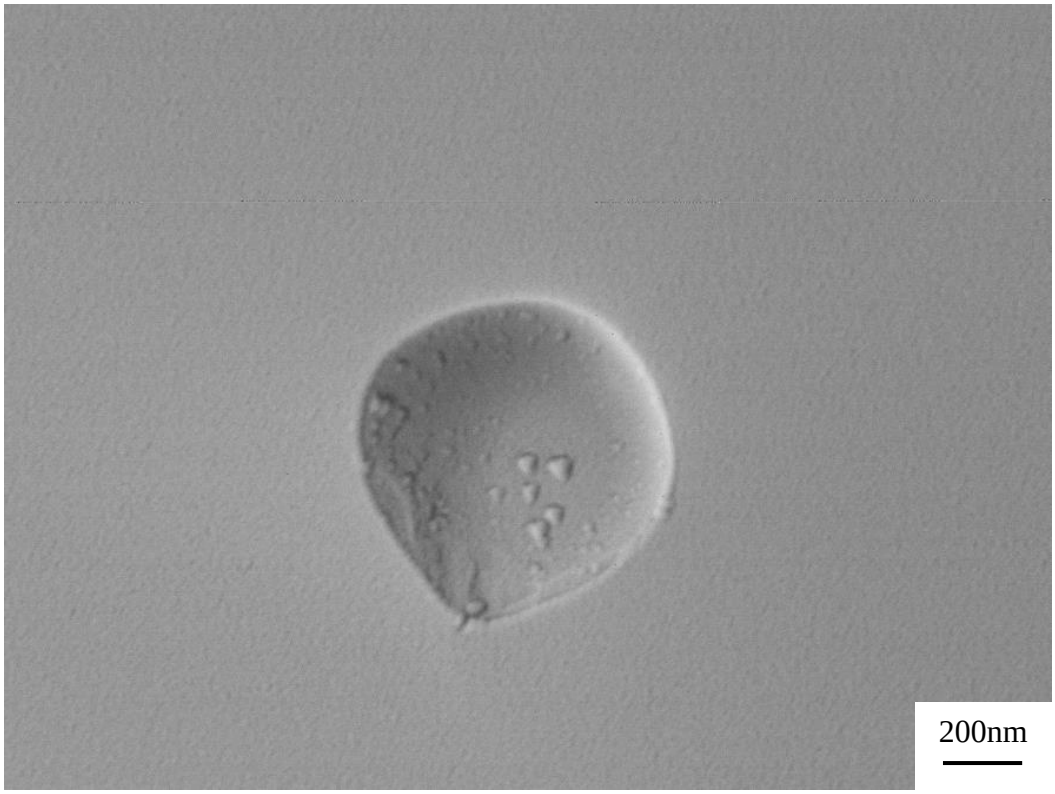


Figure 4.39: High magnification SEM micrograph of a pore.

4.2. Zirconia Dispersed Ceramics

4.2.1. Powder Analysis

The particle size distributions of the $MgAl_2O_4$ spinel powder and the ZrO_2 powder are given in **Figures 4.40** and **4.41**, respectively. The characteristic sizes for the particles are given in **Table 4.9**. Neither the spinel powder nor the ZrO_2 powder were distributed lognormally. Both powders particle size distributions were skewed to larger particle sizes. The spinel powder had smaller particles than the ZrO_2 powder. The mean particle sizes (d_{50}s) as quoted by the suppliers are given in brackets in **Table 4.9**.

Table 4.9: Characteristic sizes for the raw powders, the suppliers values are given in brackets.

Powder	**d_{10} (µm)**	**d_{50} (µm)**	**d_{90} (µm)**
Spinel	0.0758	0.199 (0.15)	1.020 (0.5)
ZrO_2	0.285	0.783 (0.6)	3.562

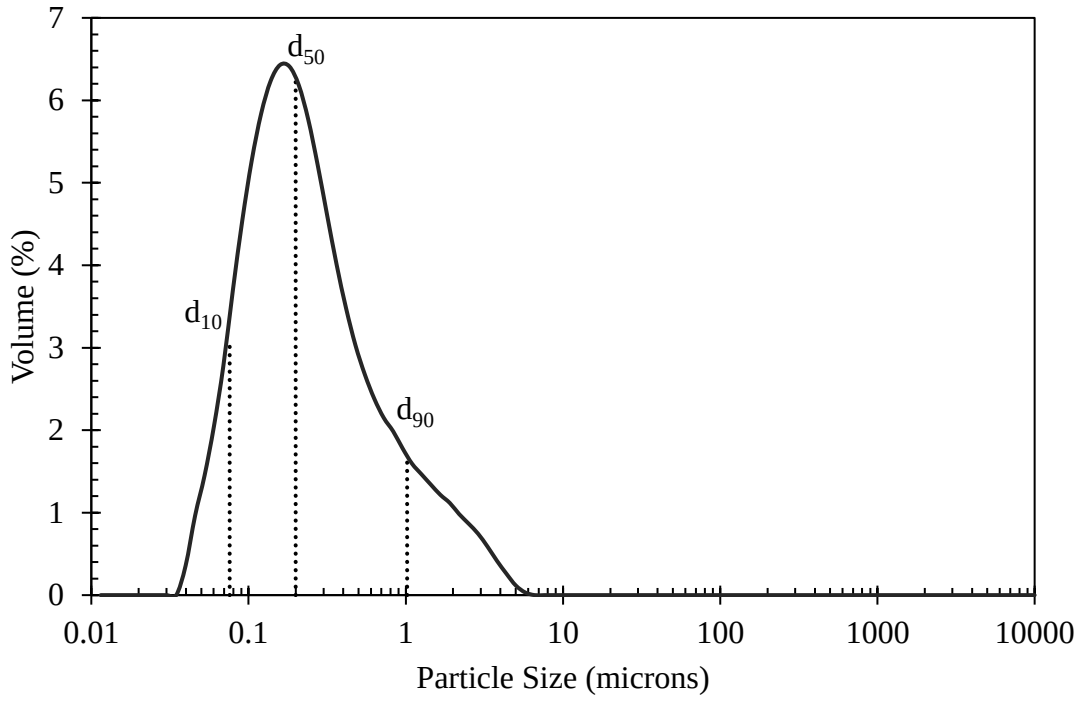


Figure 4.40: Particle size distribution for the spinel powder.

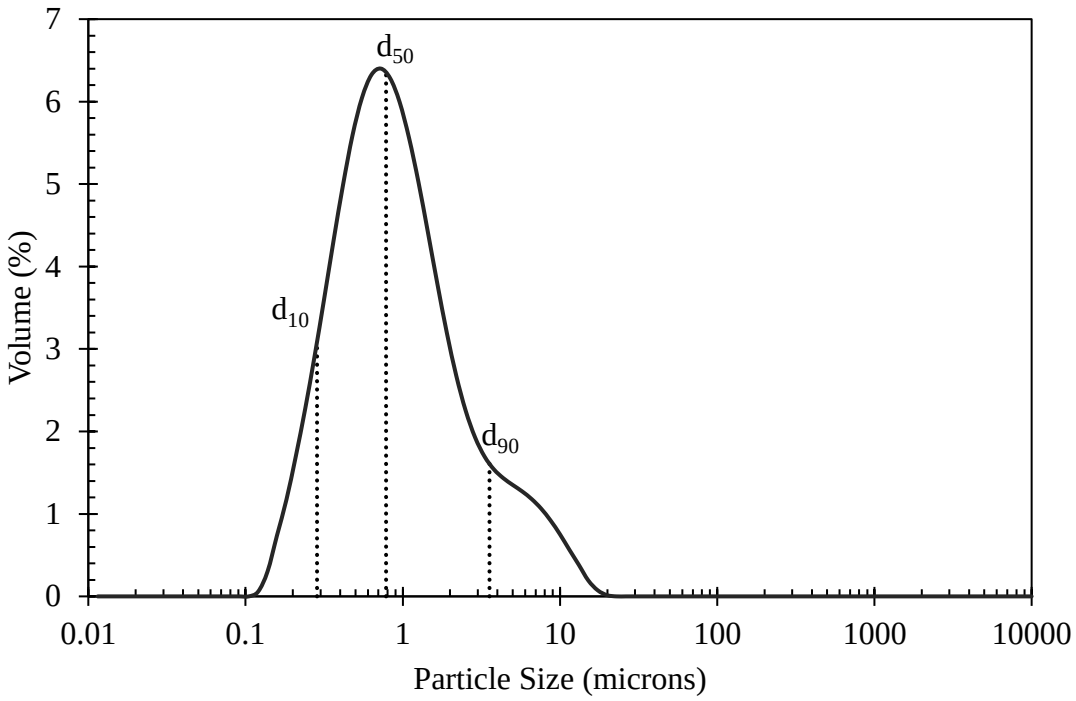


Figure 4.41: Particle size distribution for the ZrO_2 powder.

The XRD spectra for the $MgAl_2O_4$ powder and ZrO_2 powder are given in **Figures 4.42** and **4.43**, respectively.

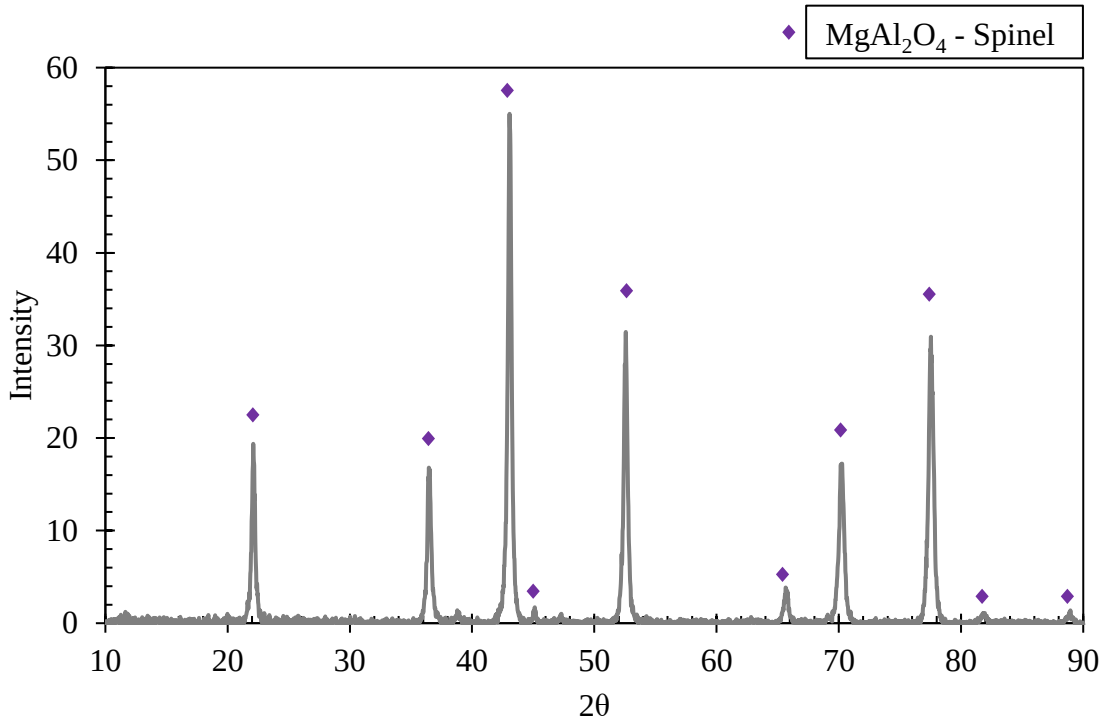


Figure 4.42: XRD spectra of the $MgAl_2O_4$ spinel powder.

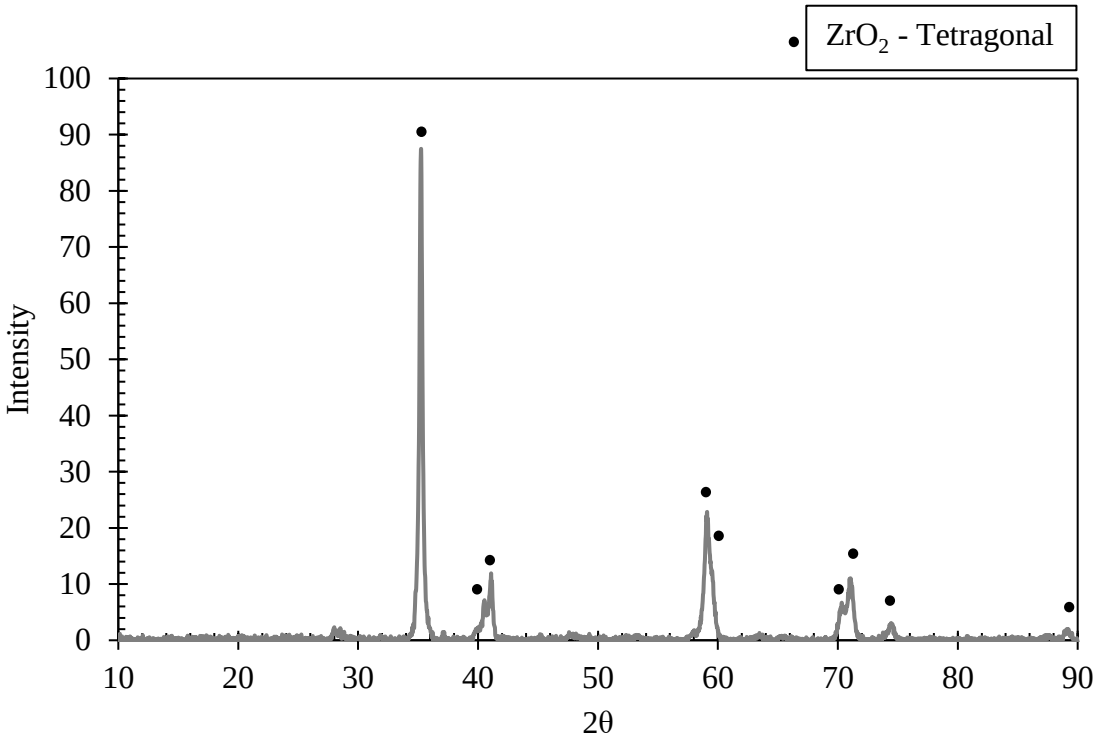


Figure 4. 43: XRD spectra of the tetragonal-ZrO_2 powder.

The peaks correspond to the spectra PDF: 00-021-1152 $MgAl_2O_4$ spinel and PDF: 01-079-1763 tetragonal-ZrO_2 from the International Centre for Diffraction Data (ICDD) database (2019). The Scherrer equation (**Equation 4.2. pp. 74**) was used to determine the mean crystallite size. For the spinel powder, the mean crystallite size was 25nm, and for the ZrO_2 powder it was 27nm. As with the powders used to fabricate the transparent samples, the mean crystallite size was orders of magnitude smaller than the measured particle size. SEM micrographs of the separate powders are shown in in **Figures 4.44** and **4.45**. The ZrO_2 particles are slightly smaller than the size determined by the particle size analysis. The larger ZrO_2 particles did not agglomerate to the same extent as the spinel powder. The SEM micrograph in **Figure 4.45** shows a relatively large spinel agglomerate. The individual particles that make up the agglomerate have a size similar to that determined by the Scherrer equation.

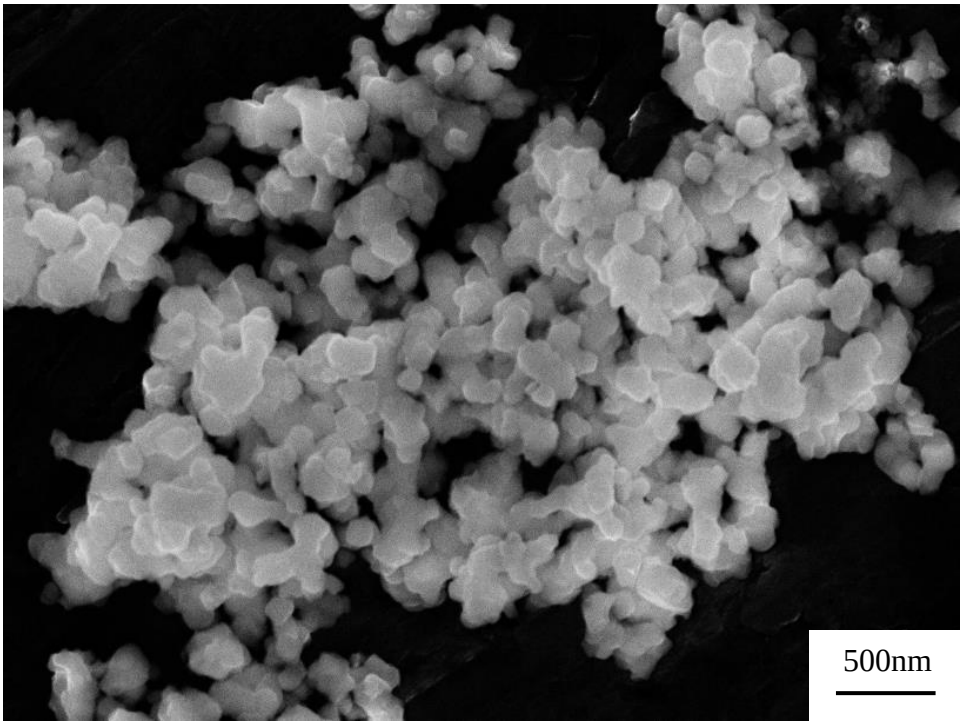


Figure 4.44: Immersion-lens SEM micrograph of the ZrO_2 powder.

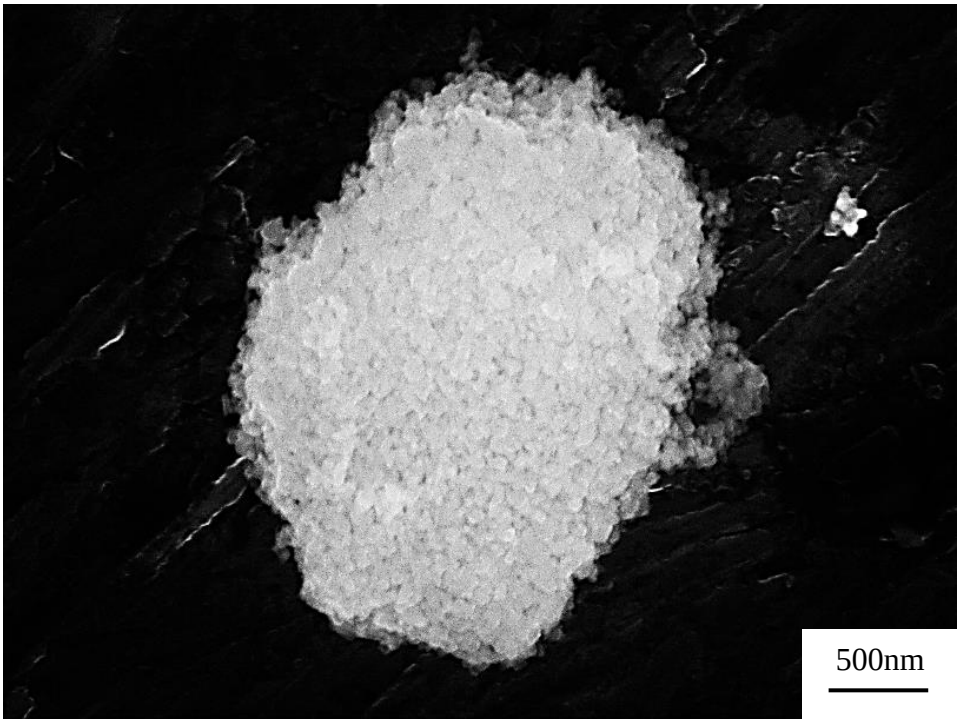
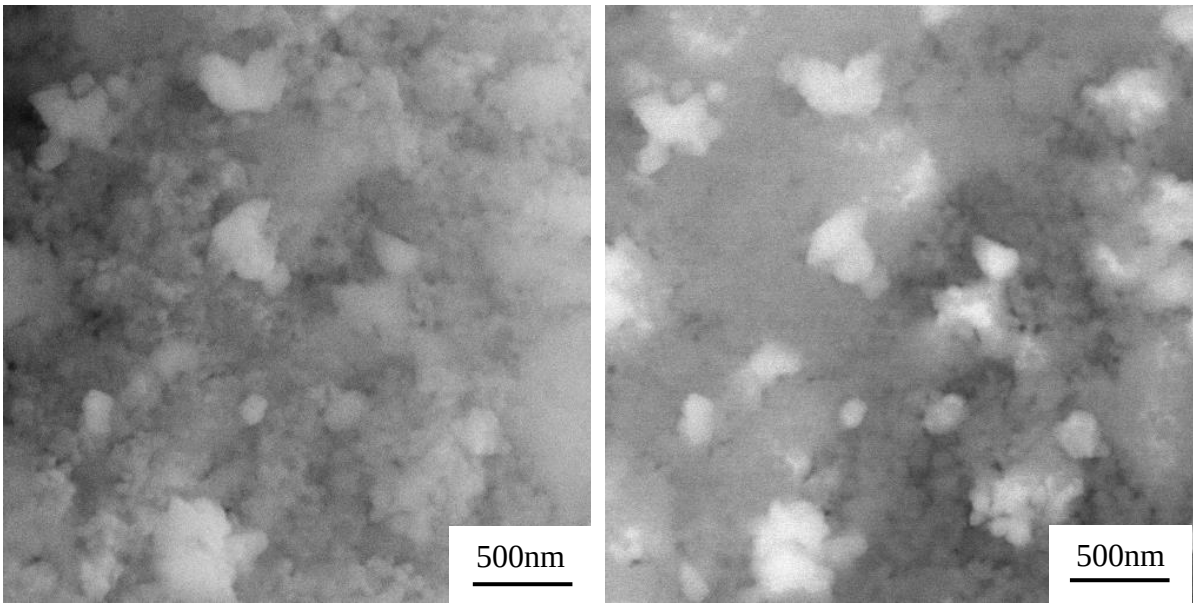


Figure 4.45: Immersion-lens SEM micrograph of the spinel powder.

SEM micrographs are shown of the mixed powder (30wt.% ZrO_2) using both the secondary electron and backscatter detector in **Figure 4.46**. The ZrO_2 particles are brighter in the

backscattered electron image and are larger than the spinel particles. A high magnification secondary electron image is shown in **Figure 4.47** of the 30wt.% ZrO_2 powder mixture.



Secondary electron image Backscattered electron image

Figure 4.46: Secondary and backscattered electron micrograph of the 30wt.% ZrO_2 mixed powder.

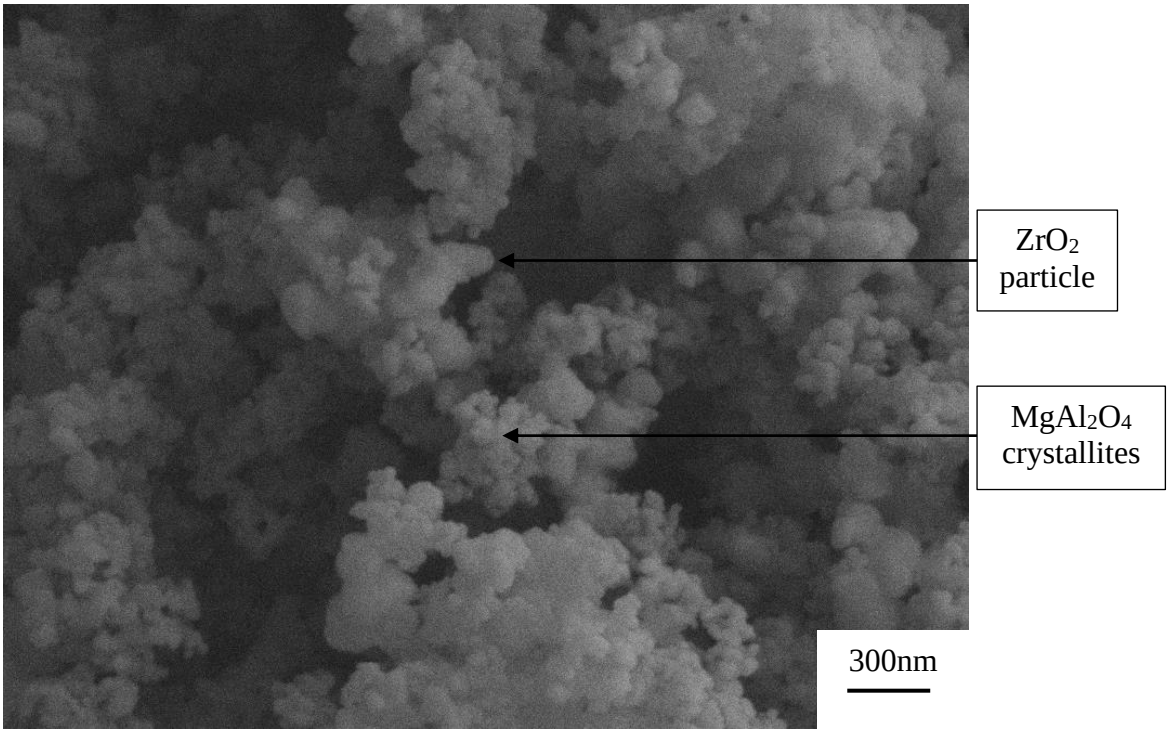


Figure 4.47: Secondary electron image of the 30wt.% ZrO_2 powder mixture.

4.2.2. Sintering Data

During the SPS sintering cycle the opposing pistons compress the sample. The average total piston movement for each ZrO_2 weight fraction was plotted in **Figure 4.48**, as well as the linear shrinkage for each composition. As the ZrO_2 content increased the linear shrinkage decreased. The error bars of the linear shrinkage are exaggerated due to the reduced scale of the secondary y-axis in **Figure 4.48**.

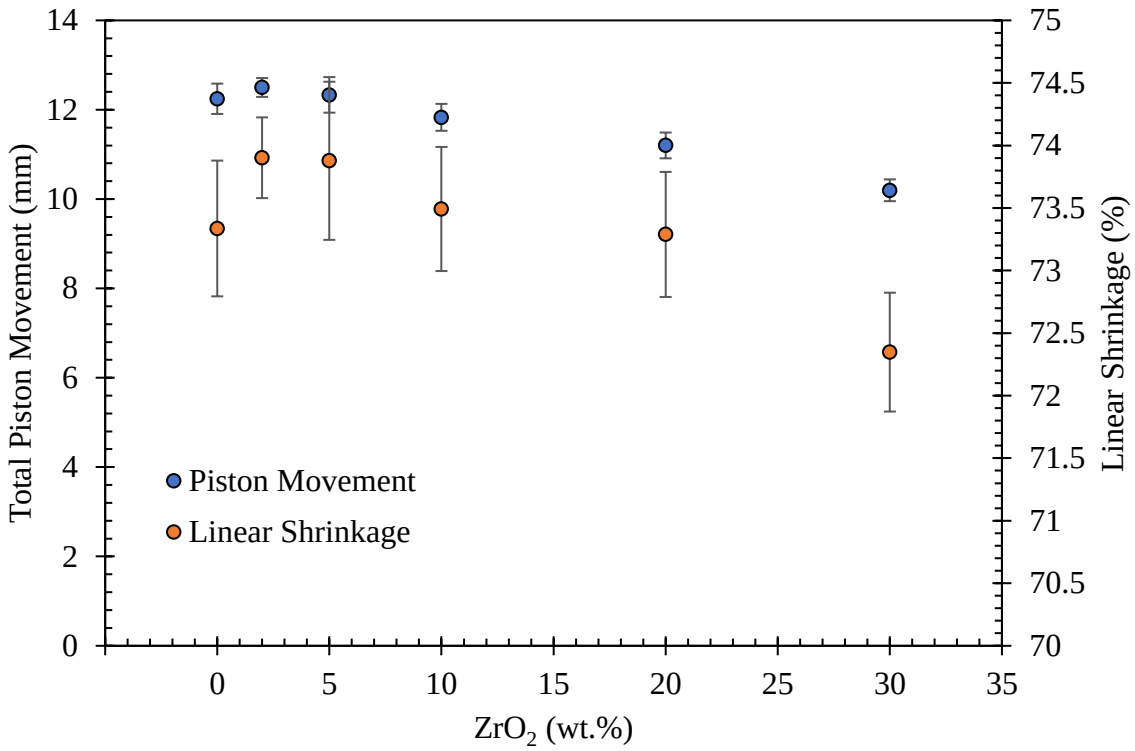


Figure 4.48: Total piston movement and linear shrinkage as a function of composition.

The total piston movement was not the same for each composition. Therefore, in-order to compare the piston speed, which would show the densification rate, the piston speed was calculated as a percentage of the total piston movement. This was plotted together with the pressure and temperature during each run as shown in **Figure 4.49**. Once again, the effects of the system's thermal expansion were deducted from the data by conducting sintering cycles without powder then subtracting these measurements from the measurements of the sintering cycles that had powder. The plot in **Figure 4.49.a** shows the piston speed for the entire run, while **Figure 4.49.b**. shows the piston speed between 5 and 15 minutes. The arrows indicate the changes caused by increasing the amount of ZrO_2 addition.

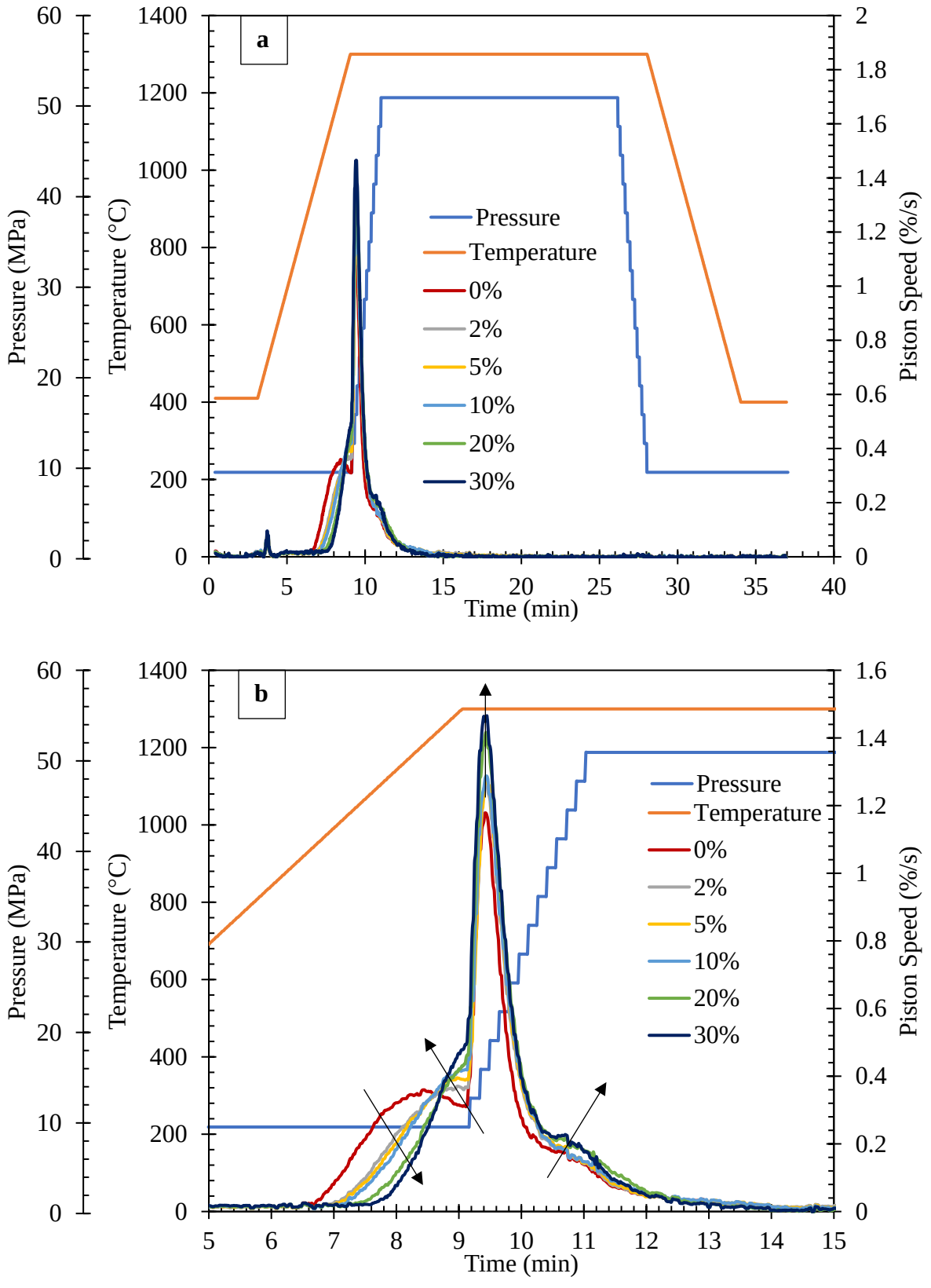


Figure 4.49: Relative piston speed during the SPS runs for each composition (**a**) for the entire run and (**b**) between 5 and 15 minutes (arrows show the change caused by increasing ZrO_2 weight percent)

4.2.3. Density

The average absolute density is given in **Figure 4.50**. The error bars indicate the sample standard deviation for each composition. As the ZrO_2 content increased, the density of the sintered samples also increased.

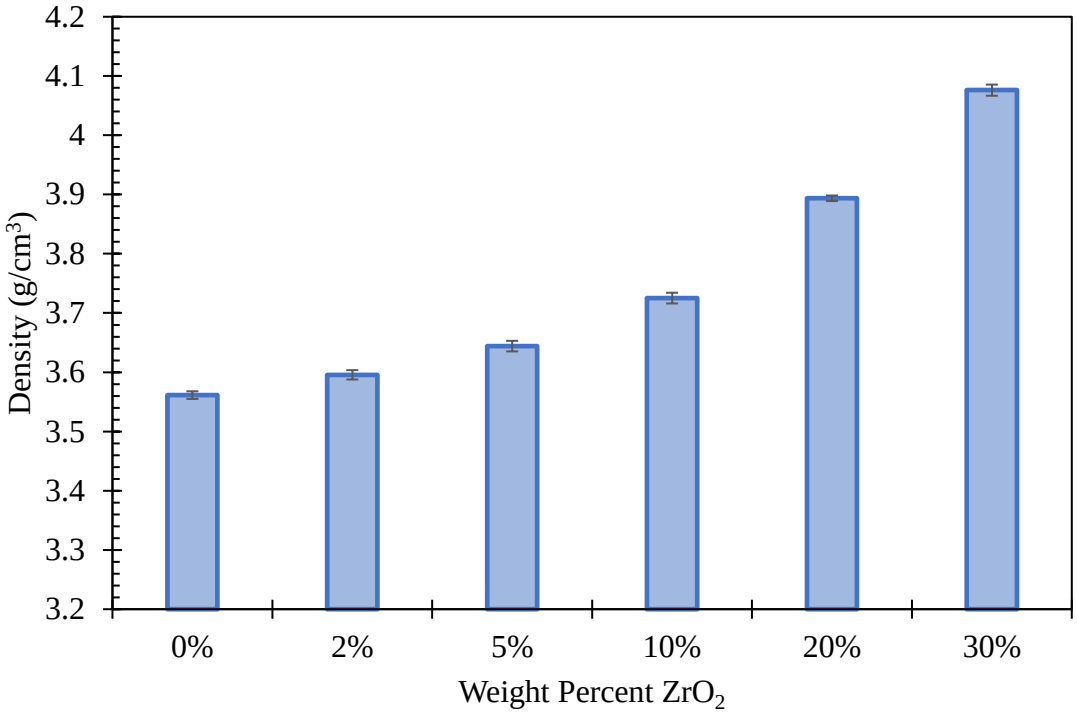


Figure 4.50: Average absolute density for each composition.

To calculate the relative density, the theoretical density for each ZrO_2 weight category was required. The "Rule of Mixtures" was used, **Equation 4.10**, to calculate the theoretical density for each ZrO_2 weight category.

$$\frac{1}{\rho_m} = \frac{x_s}{\rho_s} + \frac{x_z}{\rho_z} \qquad \textbf{Equation 4.10}$$

Where ρ is the theoretical density and x is the mass fraction of the mixture (m), spinel (s), and zirconia (z). **Figure 4.51** shows the relative density for each composition. The y-axis is extended past 100% to accommodate the error bars. The values for the theoretical densities of spinel and ZrO_2 are given in **Section 2.1.2. Spinel Crystallography pp. 12 and 2.2.1. ZrO_2 Crystallography pp. 33.**

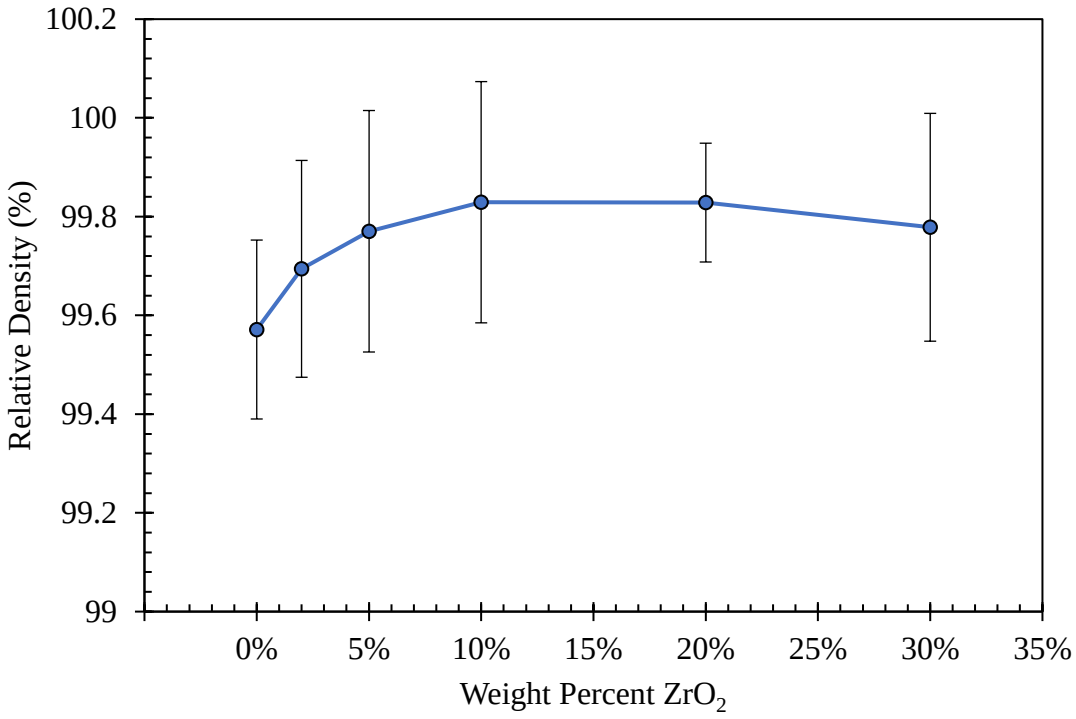


Figure 4.51: Average relative density for each composition.

The relative density increased as the ZrO_2 content increase to a point (10wt.%), then it slightly decreased. However, the uncertainties in the measurements were relatively large, thus, such a trend may not necessarily be correct.

4.2.4. XRD Analysis

The XRD spectra for the sintered composites are given in **Figure 4.52**. All peaks corresponded to either tetragonal-ZrO_2 or $MgAl_2O_4$ spinel. As the ZrO_2 content increased the peaks associated with ZrO_2 became more significant. The peaks used as a reference for the tetragonal-ZrO2 and the $MgAl_2O_4$ spinel were PDF: 01-079-1763 and PDF: 00-021-1152 respectively (from the International Centre for Diffraction Data (ICDD) database (2019)). No other significant peaks were present.

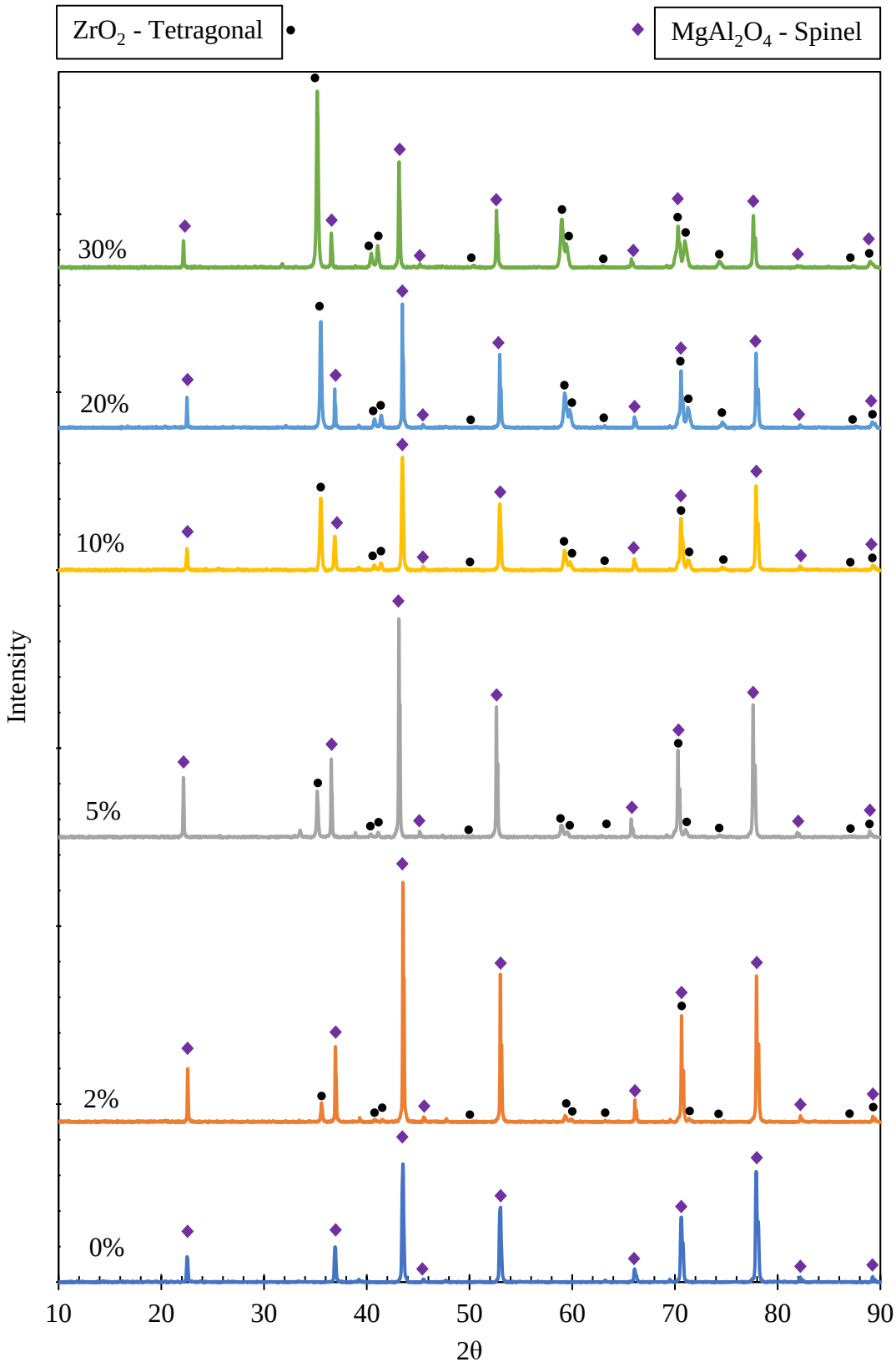


Figure 4.52: XRD spectra for the sintered composites.

4.2.5. EDS Analysis

In **Figure 4.53** the SEM micrographs of the etched sample surfaces using the backscatter detector are shown. As the ZrO_2 content increased, the number of white particles and the frequency of large particles increased.

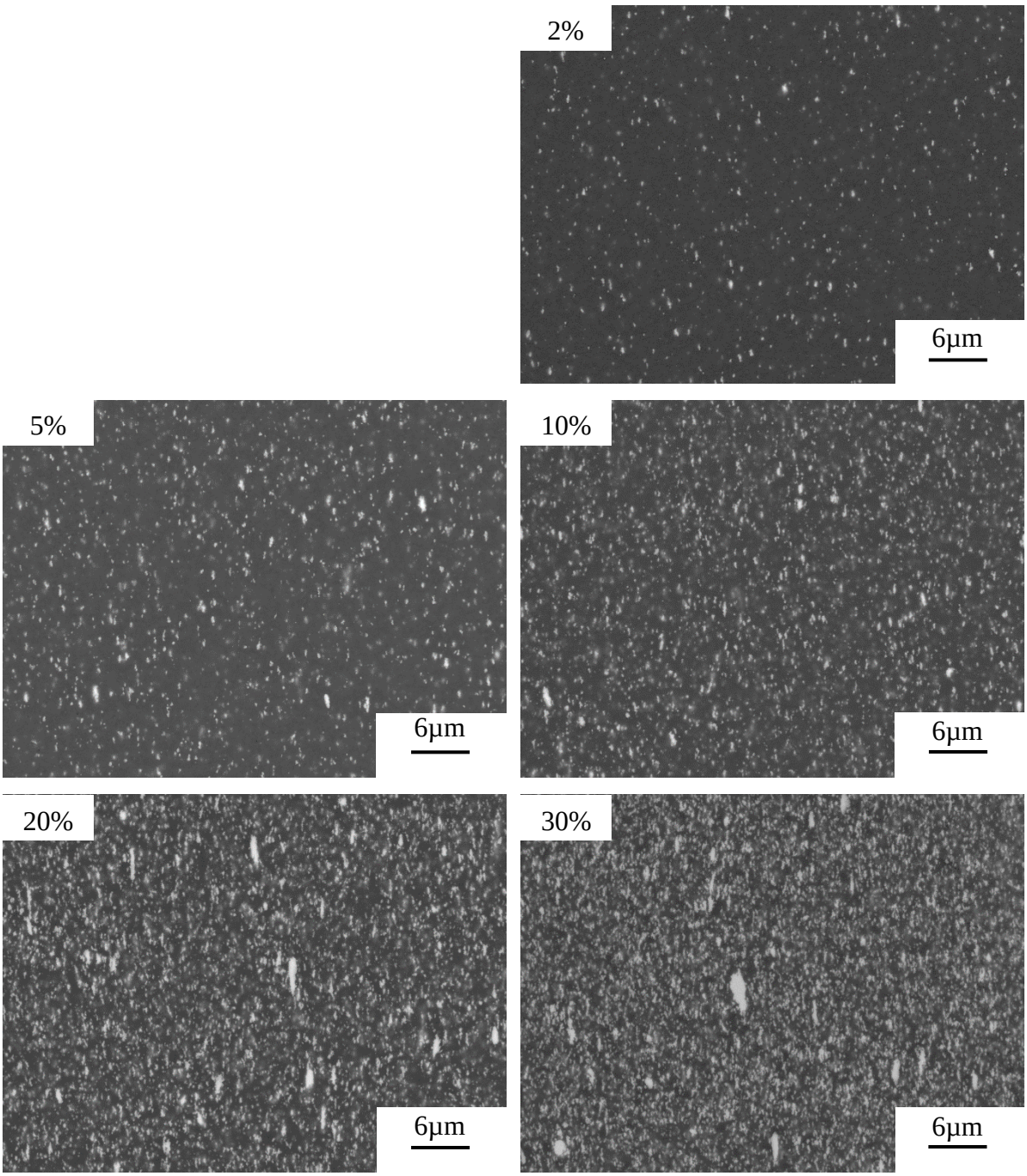


Figure 4.53: SEM micrographs of the etched surfaces using the backscatter detector (images taken at 5K magnification).

All EDS spectra were taken at an instrument setting of 5000 times magnification. The theoretical mass percentages of the elements based on the nominal compositions are given in **Table 4.10** and the mass percentages measured by the EDS are given in **Table 4.11**. The EDS spectra are given in the **Appendix Figures A1 to A6 pp. 192-194**.

Table 4.10: Theoretical mass percentages based on the nominal composition.

Nominal ZrO_2 (mass%)	**Elemental Mass (%)**				
	Mg	Al	O	Zr	Y
0	17.08	37.93	44.98	0.00	0.00
2	16.74	37.17	44.60	1.40	0.08
5	16.23	36.04	44.02	3.50	0.21
10	15.38	34.14	43.06	7.01	0.42
20	13.67	30.35	41.13	14.01	0.84
30	11.96	26.55	39.20	21.02	1.27

Table 4.11: Mass percent measured by the EDS.

Nominal ZrO_2 (mass%)	**Elemental Mass (%)**							
	Mg	Al	O	Zr	Y	Pd	Hf	Ca
0	16.4	38.4	45.2	-	-	-	-	-
2	16.1	37.3	44.6	1.4	-	0.6	-	-
5	15.6	36.1	45.0	2.8	-	0.6	-	-
10	14.7	33.8	44.8	6.1	-	0.6	-	-
20	13.0	29.5	43.5	12.5	0.7	0.5	0.3	0.1
30	10.9	25.0	43.6	18.2	0.9	0.6	0.5	0.3

The measured mass percent of the Mg, Al, Zr, and Y were used to calculate the ratio between ZrO_2 and $MgAl_2O_4$ within each mixture. The presence of yttrium was due to the fact that the zirconia was stabilised by 3mol% Y_2O_3. The calculated ZrO_2 mass% for each composite is given in **Table 4.12**. The ZrO_2 content calculated was slightly lower than expected, particularly for the 30 mass% ZrO_2 sample.

Table 4.12: Calculated ZrO_2 mass percent.

Nominal ZrO_2 (mass%)	**Calculated ZrO_2 (mass%)**	**Nominal ZrO_2 (vol.%)**	**Calculated ZrO_2 (vol.%)**
0	0	0	0
2	2.0	1.18	1.18
5	4.5	2.99	2.68
10	9.6	6.10	5.85
20	18.4	12.76	11.66
30	26.3	20.05	17.27

4.2.6. Grain Structure

From **Figures 4.54** to **4.56** backscattered SEM images with progressively higher magnifications of the etched sample surfaces are shown.

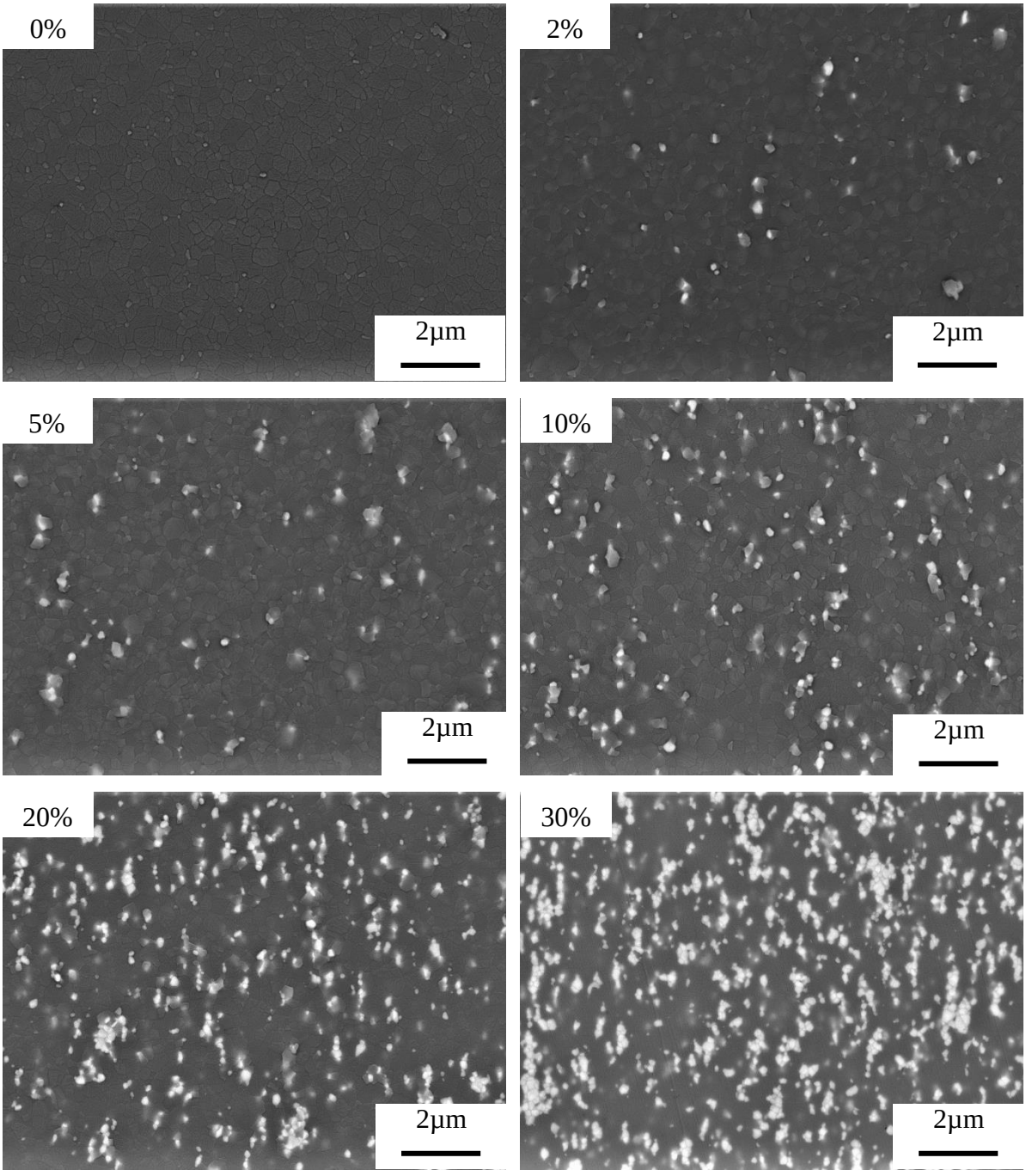


Figure 4.54: SEM micrographs of the etched surfaces using the backscatter detector (images taken at 20K magnification).

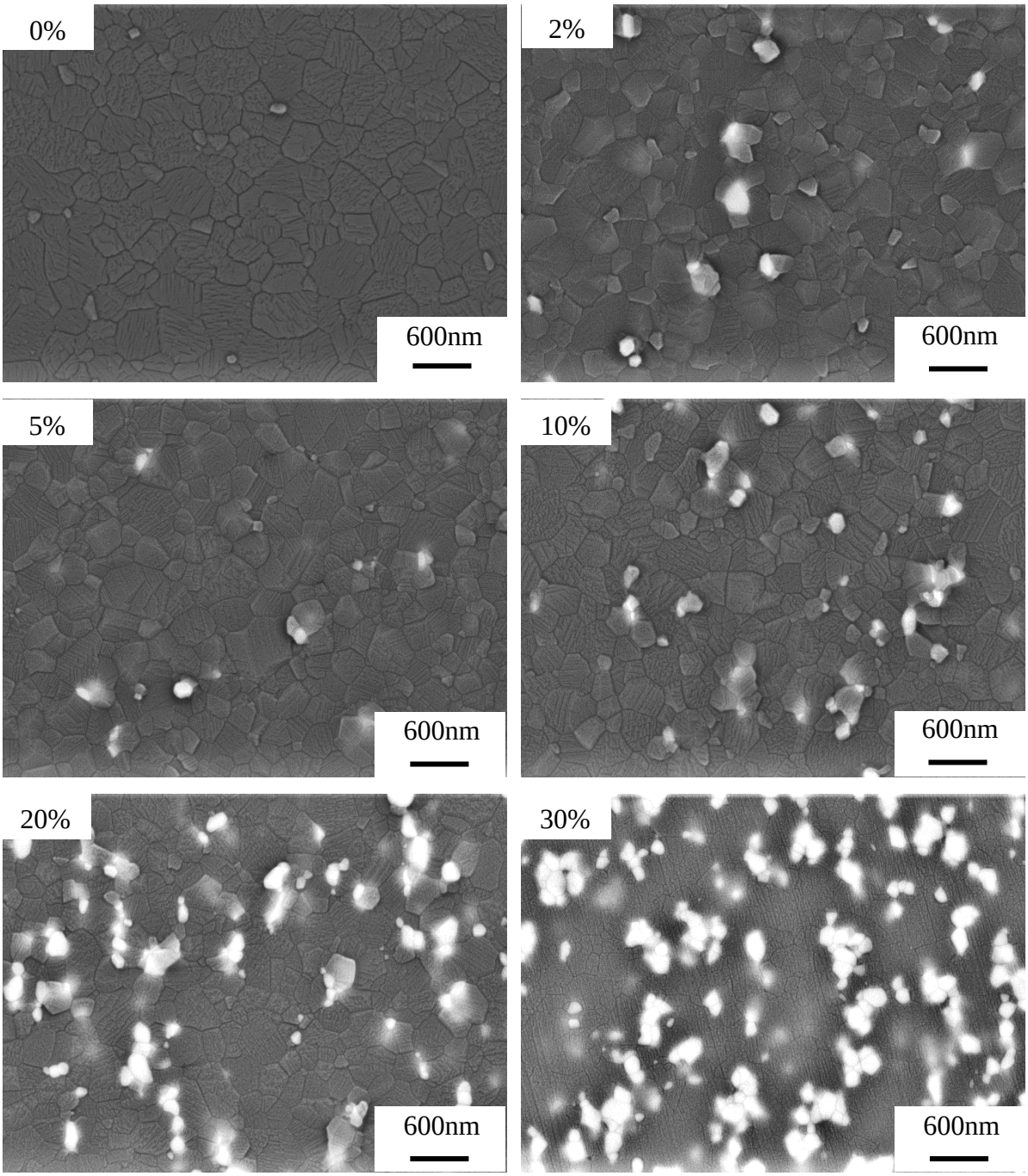


Figure 4.55: SEM micrographs of the etched surfaces using the backscatter detector (images taken at 50K magnification).

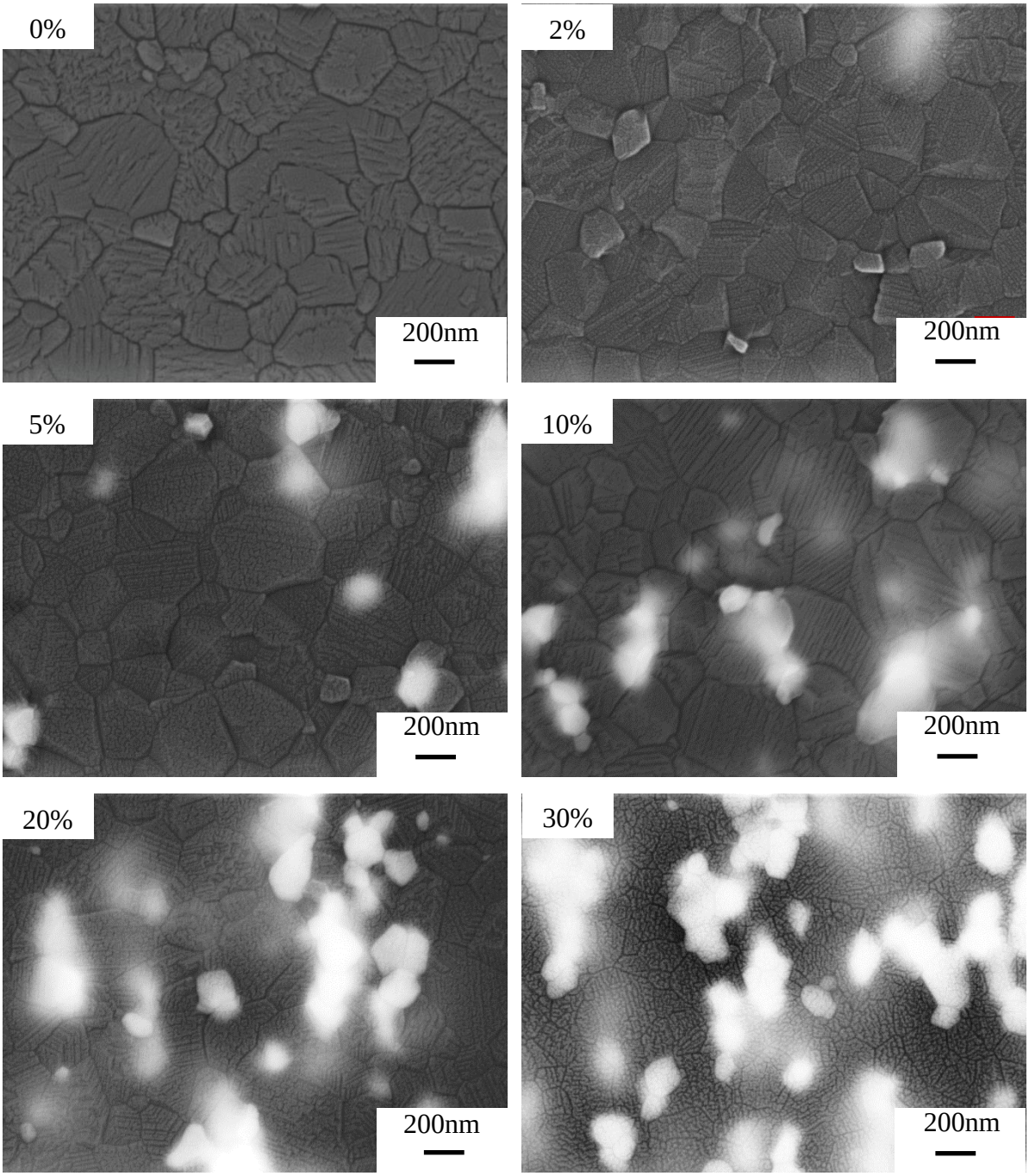


Figure 4.56: SEM micrographs of the etched surfaces using the backscatter detector (images taken at 100K magnification).

The linear intercept method was used to calculate the average grain size for each composition. Also, the grain size distributions were measured in the same way as was done for the transparent samples. The distributions are given in **Figures 4.57** to **4.61**. A lognormal distribution was fitted to the data and is represented by the red curves in **Figures 4.57** to **4.61**, labelled PDF for Probability Density Function. This was done by minimizing the sum of the absolute differences between the lognormal curve and the data for each size range. To minimize the difference between the curve and the data, MS-Excel's "Solver" program was used, and the cells being varied were the mean and standard deviation of the lognormal curve. The grain size distribution for the 30wt.% ZrO_2 is not included because the grains were not clearly distinguishable, **Figure 4.56,** thus they could not be accurately measured.

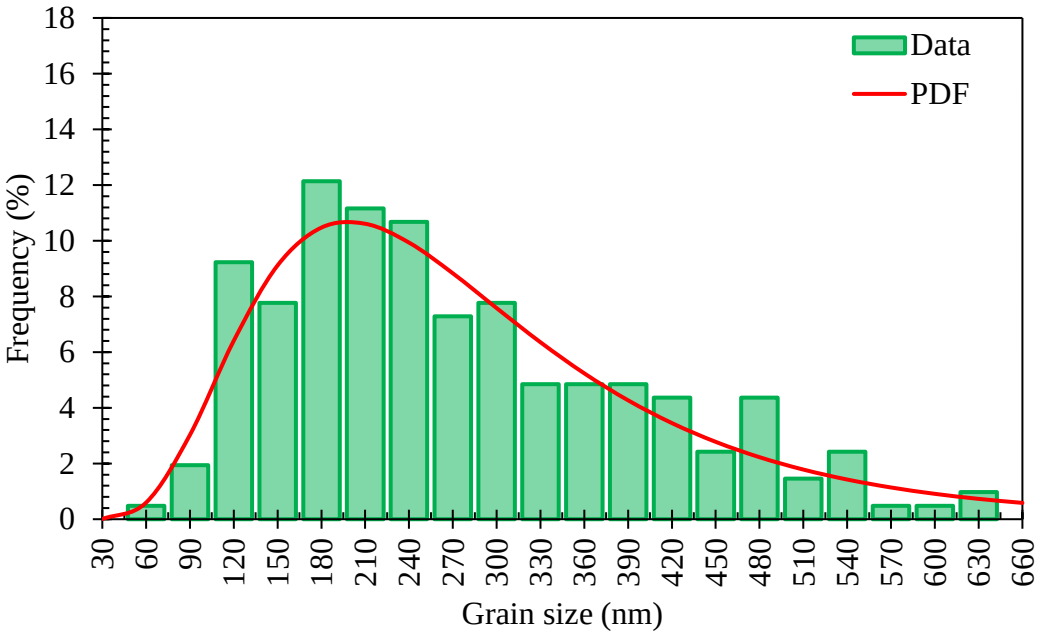


Figure 4.57: Grain Size distribution for the 0wt.% ZrO_2 sample.

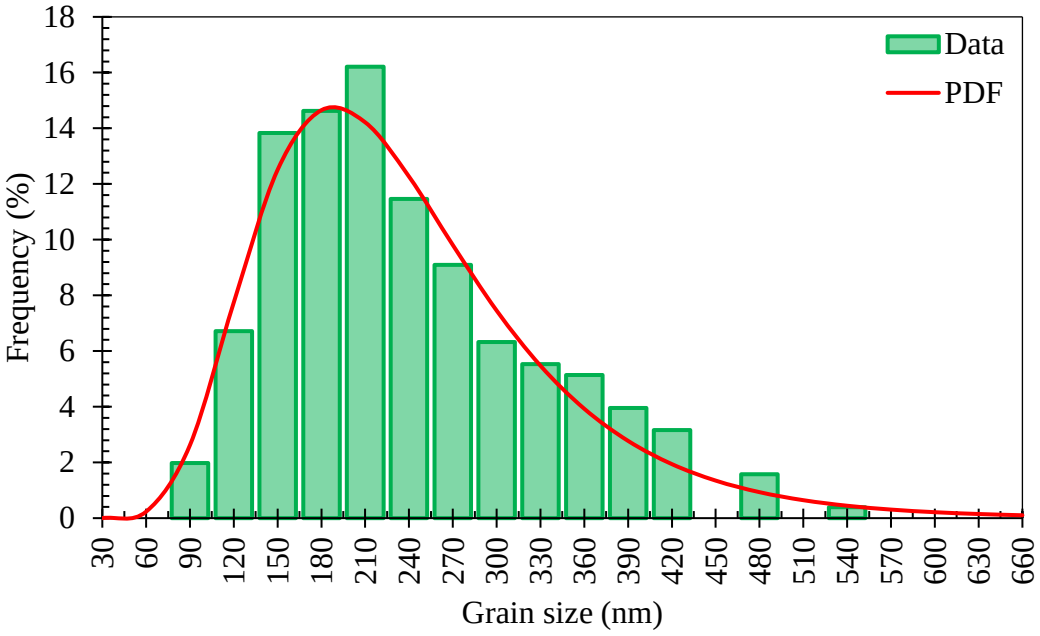


Figure 4.58: Grain Size distribution for the 2wt.% ZrO_2 sample.

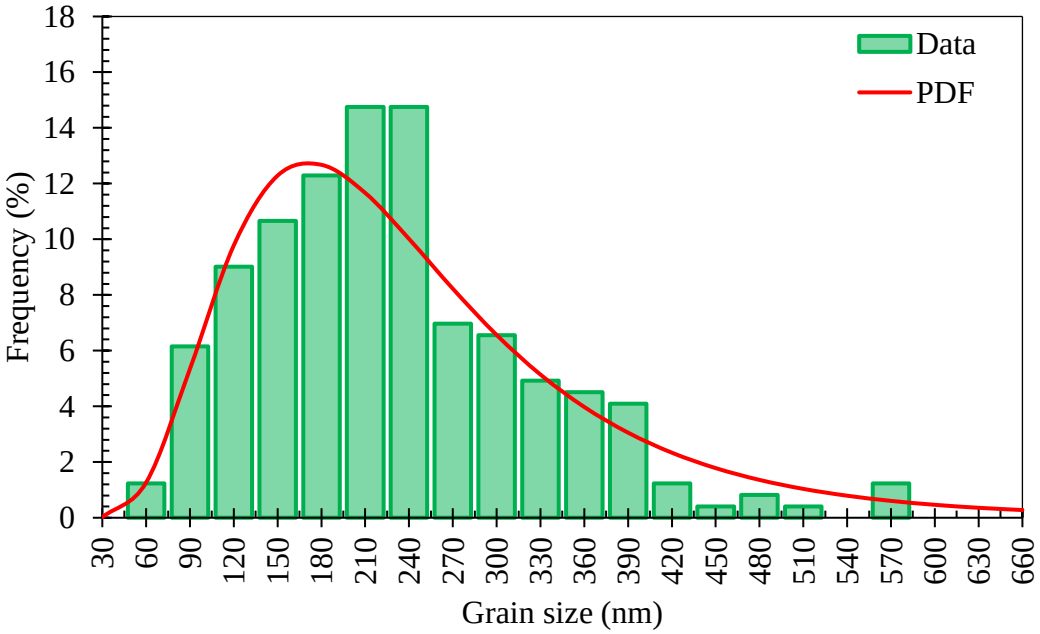


Figure 4.59: Grain Size distribution for the 5wt.% ZrO_2 sample.

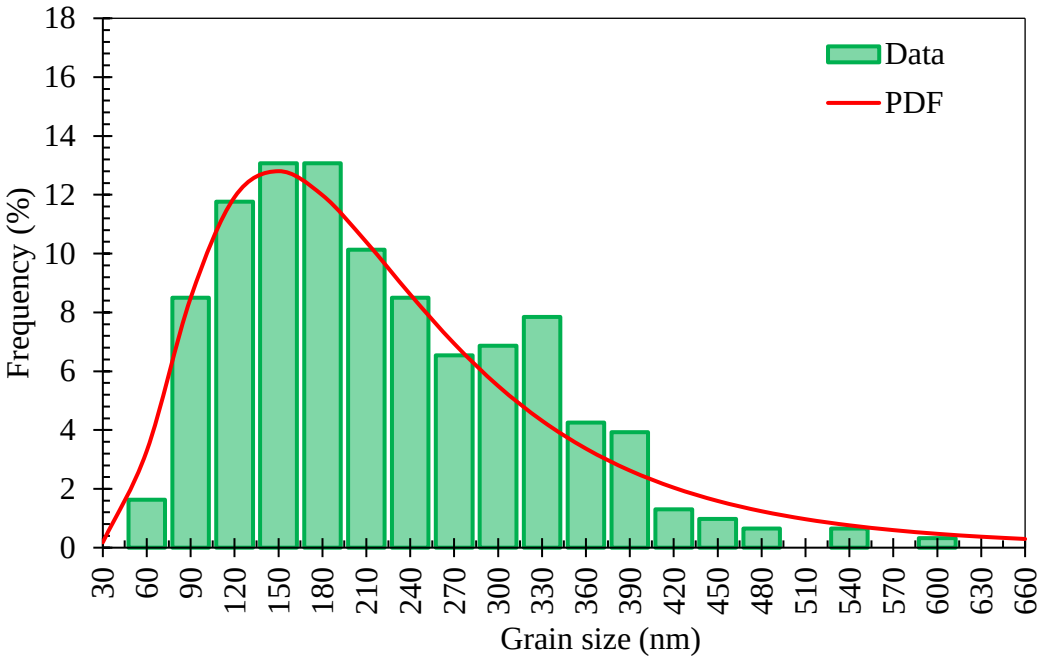


Figure 4.60: Grain Size distribution for the 10wt.% ZrO_2 sample.

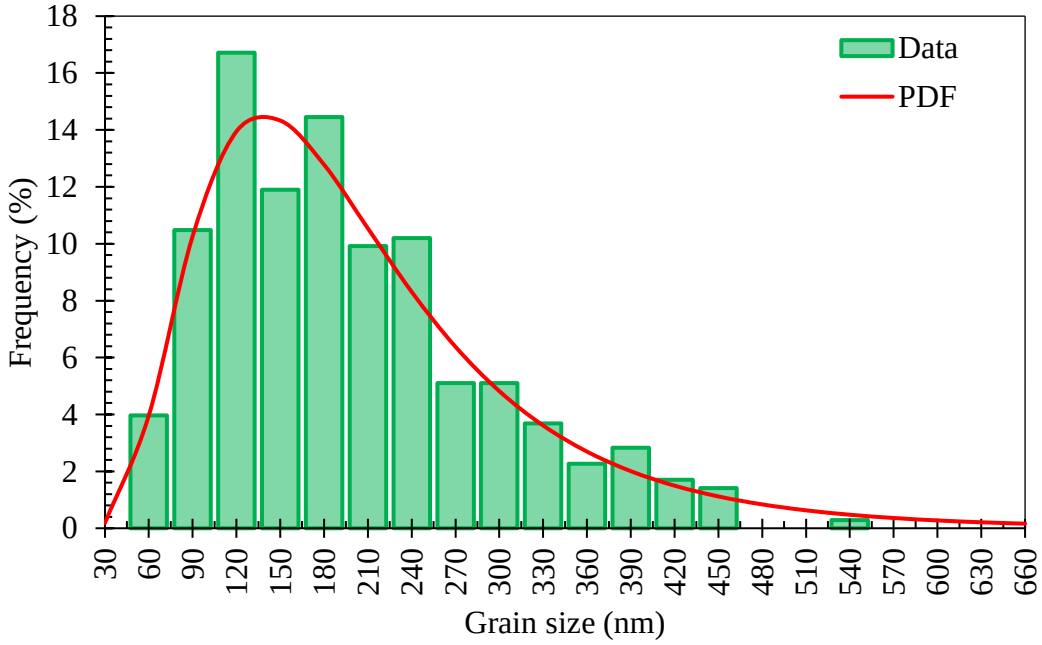


Figure 4.61: Grain Size distribution for the 20wt.% ZrO_2 sample.

A visual inspection of the curves in **Figures 4.57** to **4.61** indicate that they were a good fit to the data. **Table 4.13** shows the average grain size for each method.

Table 4.13: Average grain size for each method used to determine grain size.

Nominal Composition of ZrO_2 (wt.%)	Linear Intercept		Grain Distribution		Best Fit
	Average (nm)	Std Dev (nm)	Average (nm)	Std. Dev. (nm)	Mean (nm)
0	278	33	259	124	255
2	223	21	222	90	221
5	218	27	214	97	217
10	214	30	206	100	199
20	195	24	181	93	182

There was good agreement between the distribution data and the linear intercept method as well as the mean of the best fit curve. This was in contrast with the study of the transparent samples. **Table 4.13** shows that as the ZrO_2 content increased the average grain size decreased. **Figure 4.62** shows the best fit curves of the particle size distributions. The distribution from the 2% sample seems to be an outlier. The other compositions show that the addition of the ZrO_2 shifts the distribution to a smaller grain size.

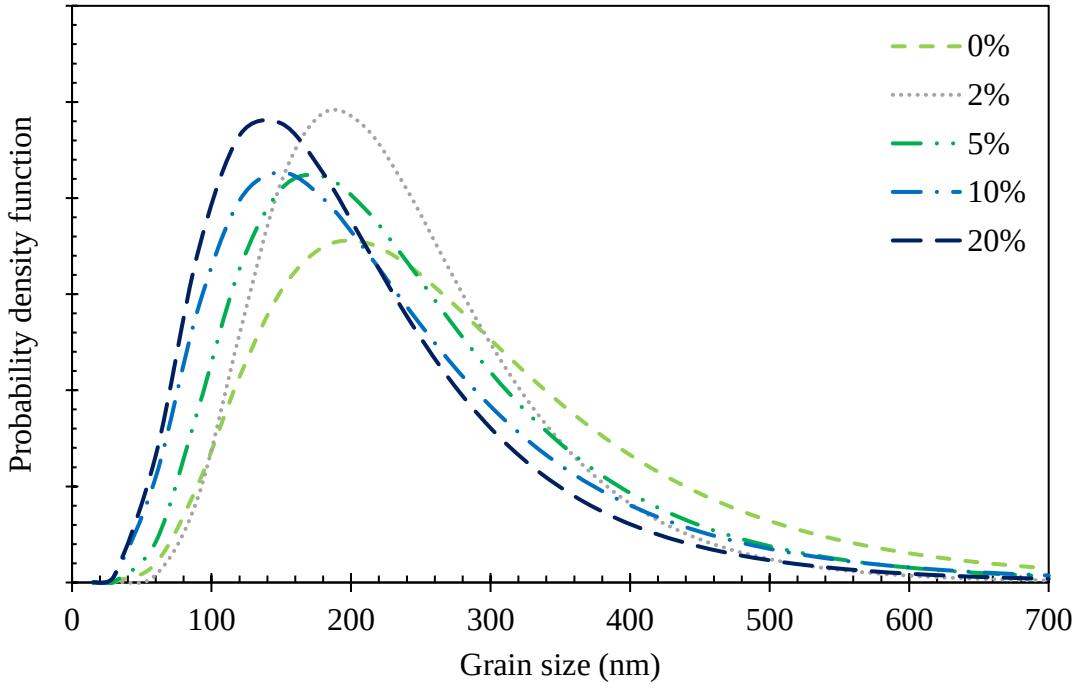


Figure 4.62: Plot of the best fit lognormal distributions at different ZrO_2 weight percent.

The natural logarithm of the grain sizes, $\ln(d_i)$, was calculated and plotted as well. A normal distribution probability density function with the same mean and standard deviation as the lognormal curve fits the data reasonably well, **Figures 4.63** to **4.67**. It should be noted that only the 0% and 2% ZrO_2 samples passed the Shapiro-Wilk test for normalcy. The other compositions had a p-value < 0.05. Therefore, there was significant statistical evidence to reject the null hypothesis of the test. The null hypothesis of the Shapiro-Wilk test is that the data was taken from a normal distribution. Thus, even though the probability density functions of the lognormal and normal distributions do seem to visually fit the data, they are not true representations of it. From **Figures 4.65** to **4.67** it can be seen what could be causing this deviation from normalcy for the 5, 10, and 20wt.% ZrO_2 samples. The data was skewed to the smaller grain sizes. This is shown near the "tail ends" of the distribution. The data on the smaller size of the mean was generally above the PDF, and after a certain value to the right of the mean, the data rapidly dropped below the PDF. This was reinforced by the skewness of the data which was -0.171, -0.099, -0.459, -0.279, -0.338 for the 0, 2, 5, 10, and 20wt.% ZrO_2 samples, respectively. The skewness of the data for the 0 and 2 wt.% ZrO_2 samples were less than the skewness for the 5, 10, and 20wt.% samples. Because of this asymmetry, the 5, 10, and 20wt.% samples did not pass the Shapiro-Wilk test.

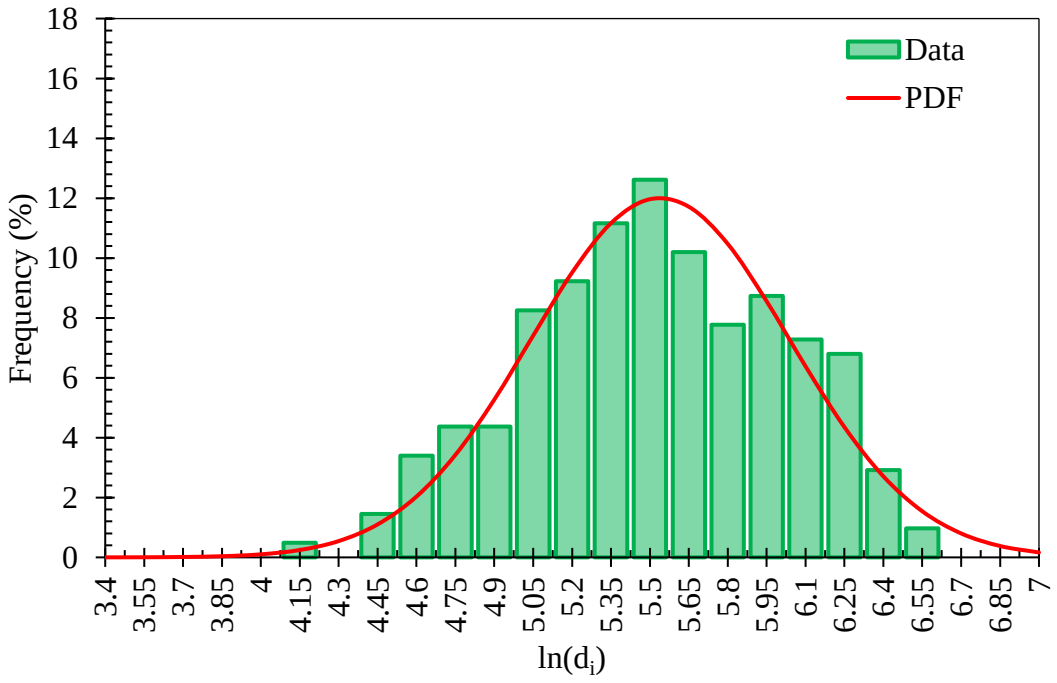


Figure 4.63: Distribution of the natural logarithm of the grain size for the 0wt.% ZrO_2 sample.

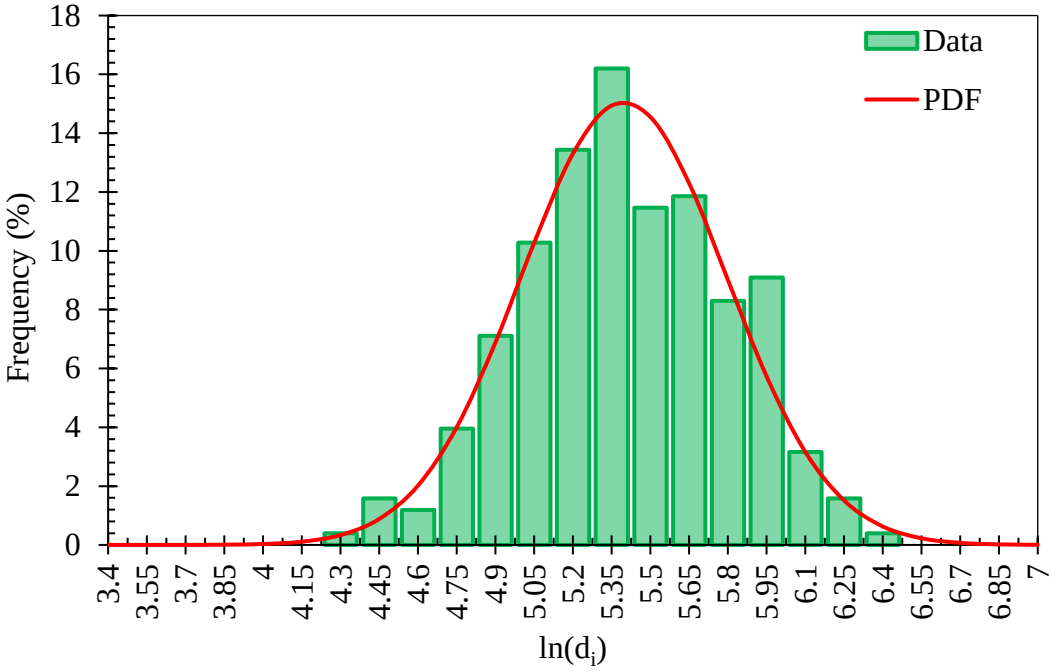


Figure 4.64: Distribution of the natural logarithm of the grain size for the 2wt.% ZrO_2 sample.

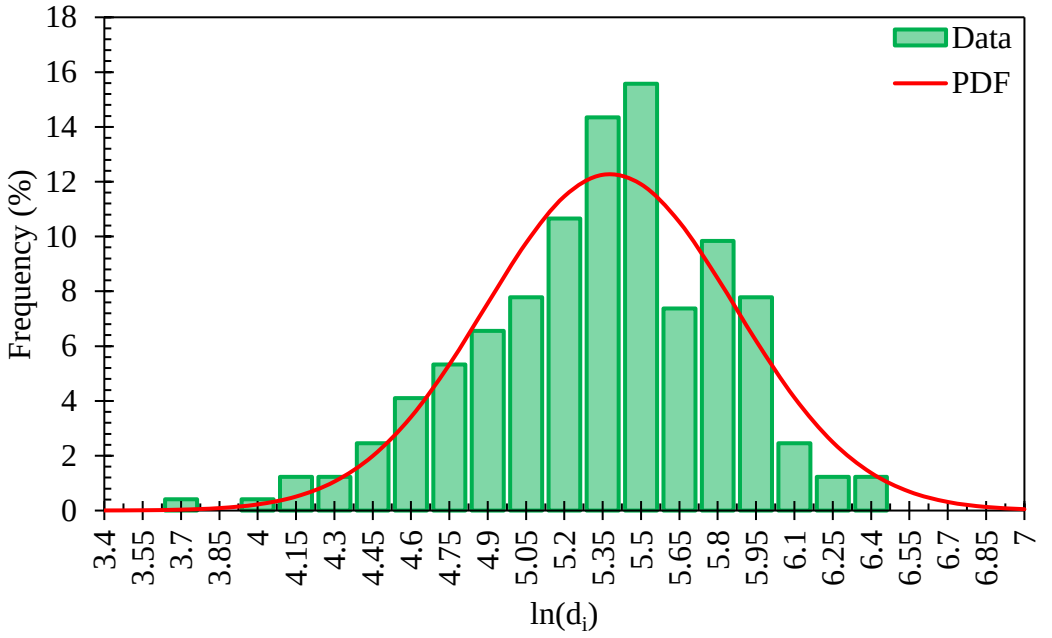


Figure 4.65: Distribution of the natural logarithm of the grain size for the 5wt.% ZrO_2 sample.

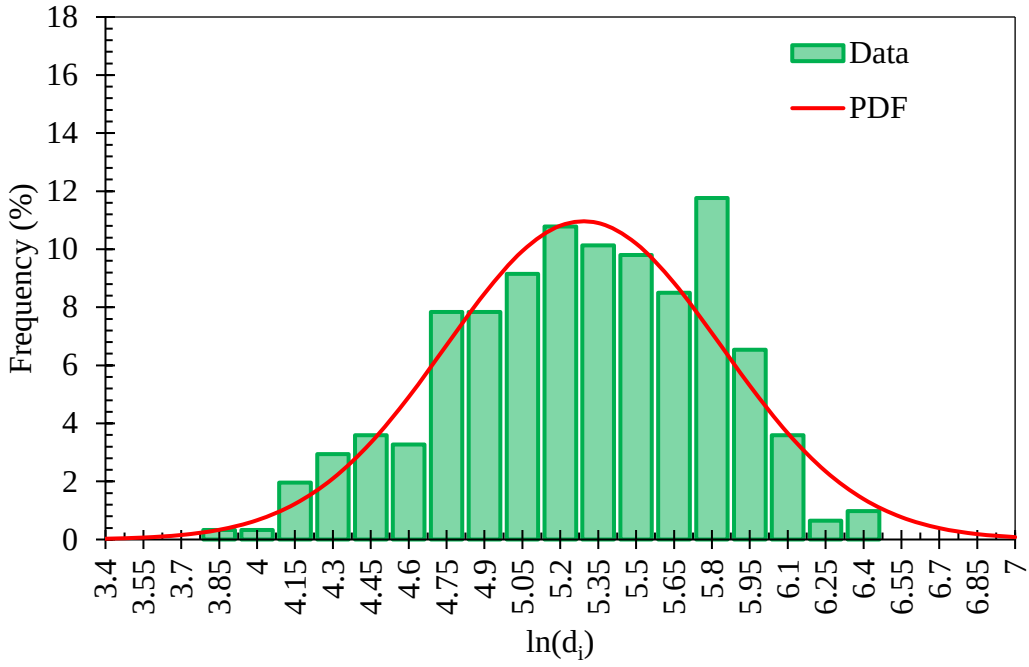


Figure 4.66: Distribution of the natural logarithm of the grain size for the 10wt.% ZrO_2 sample.

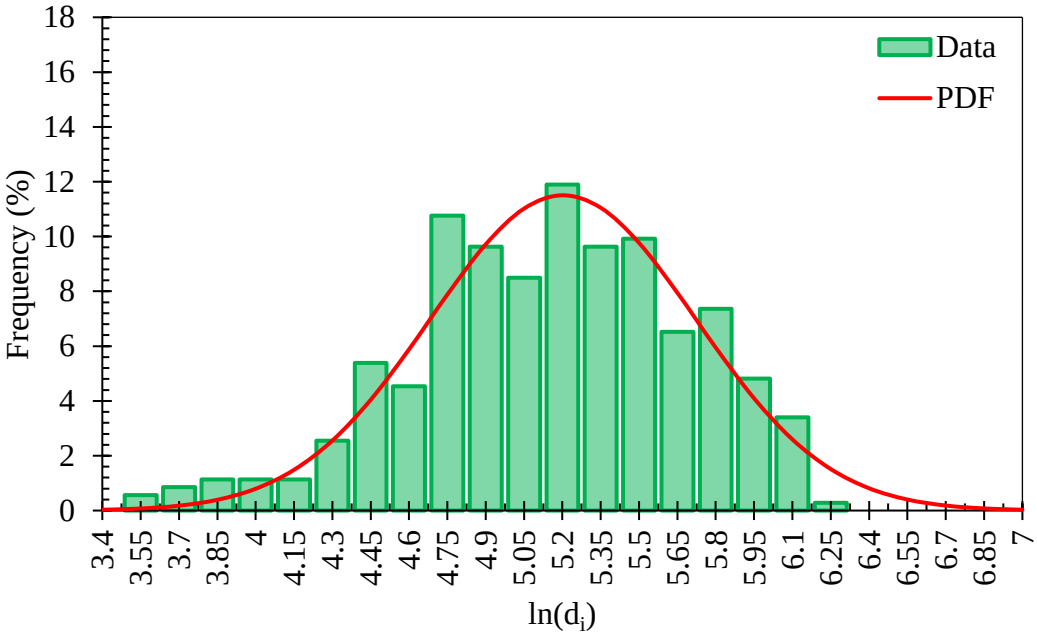


Figure 4.67: Distribution of the natural logarithm of the grain size for the 20wt.% ZrO_2 sample.

Figure 4.68 shows the mean grain size, from all the techniques used, as a function of ZrO_2 weight percent. The more ZrO_2 added, the smaller the measured mean grain size.

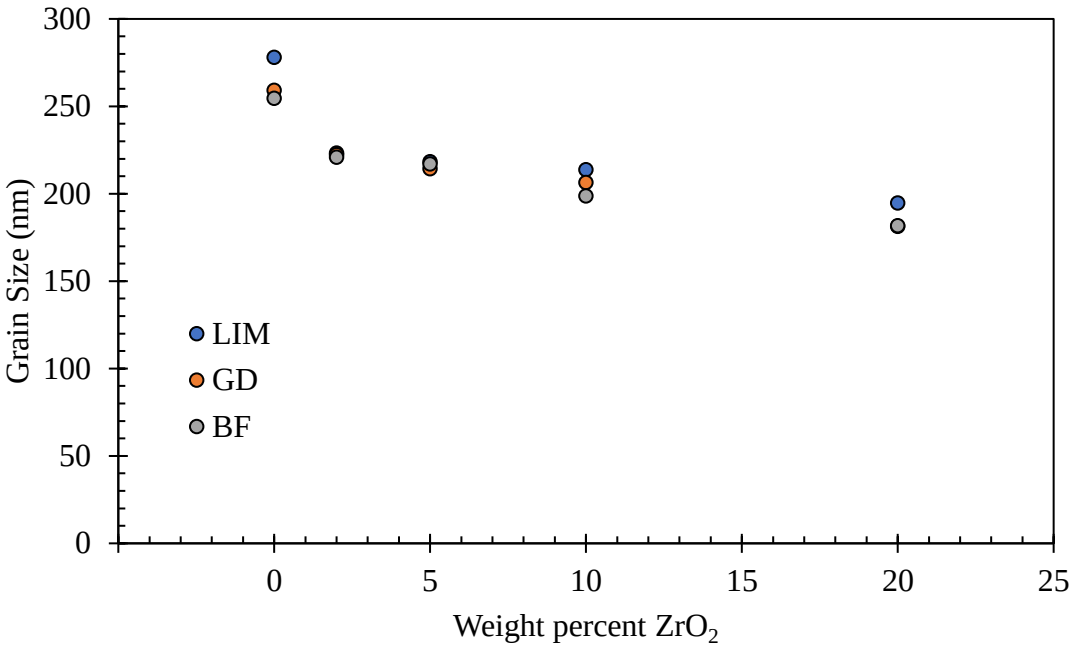


Figure 4.68: Mean grain size as a function of weight percent ZrO_2. Linear Intercept Method (LIM), Grain size Distribution (GD), Best Fit pdf (BF).

4.2.7. Mechanical Properties

To measure the fracture toughness of the composite samples by the indentation technique, their Young's Moduli needed to be estimated. The Youngs moduli of the composite samples were estimated using the Reuss (**Equation 4.11**) and Voigt (**Equation 4.12**) models for the lower and upper bounds, respectively.

$$E_c = \left(\frac{f}{E_p} + \frac{1-f}{E_m}\right)^{-1} \qquad \textbf{Equation 4.11}$$

And

$$E_c = fE_p + (1-f)E_m \qquad \textbf{Equation 4.12}$$

Where E_i is Young's modulus for the composite (c), particulate phase (p), and the matrix phase (m), and f is the volume fraction of the particulate phase. **Table 4.14** shows the calculated Young's moduli and the corresponding $MgAl_2O_4$ and ZrO_2 volumetric fractions based on the

nominal weight percent. The Young's modulus for $MgAl_2O_4$ was taken as 272 GPa (Harris & Turri, 2013) and for ZrO_2 it was 256 GPa (Exare, et al., 2016).

Table 4.14: Calculated upper and lower bounds of the Young's moduli for the composites.

Nominal ZrO_2 (wt.%)	**$MgAl_2O_4$ (vol. frac.)**	**ZrO_2 (vol. frac.)**	**Upper Bound (GPa)**	**Lower Bound (GPa)**
0	1	0	272.0	272.0
2	0.988	0.012	271.8	271.8
5	0.970	0.030	271.5	271.5
10	0.939	0.061	271.0	270.9
20	0.872	0.128	269.9	269.8
30	0.800	0.200	268.8	268.6

There was little difference between the upper and lower bounds of the Young's moduli. The average between the two was used in the calculation of fracture toughness. Unlike with the transparent samples, the indents on the composites were clearly visible, **Figures 4.69** and **4.70**. The cracks all radiated outward from the corner of the hardness indent as expected and no spalling or spurious cracks were observed.

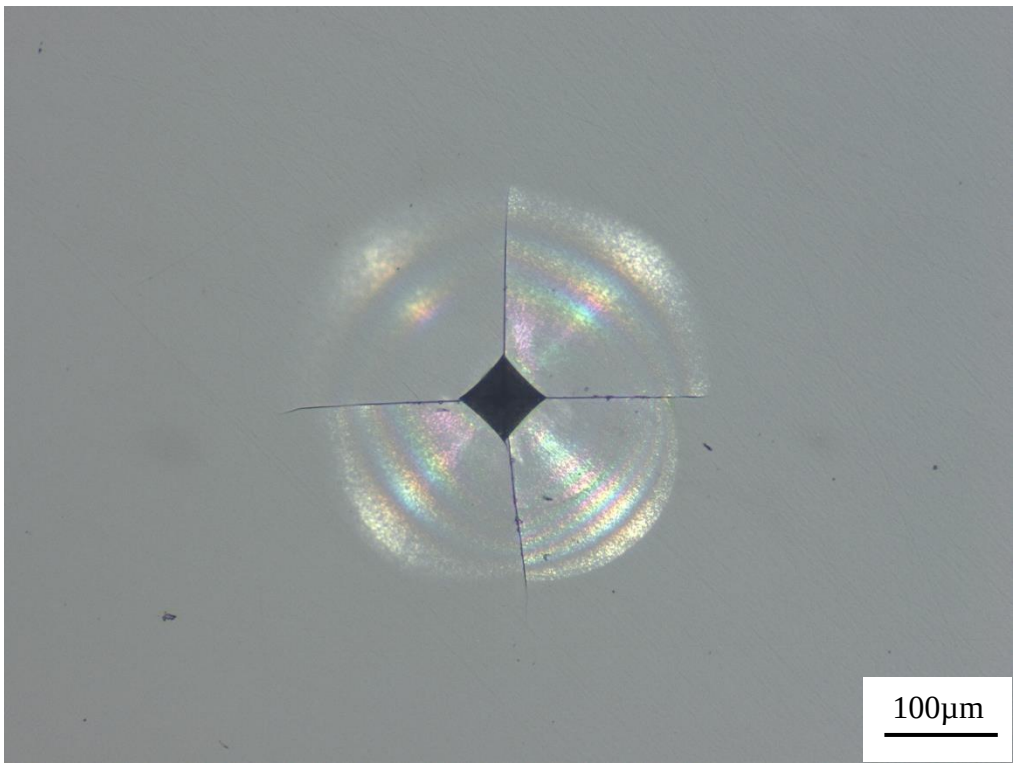


Figure 4.69: Characteristic Vickers indent on the 0wt.% ZrO_2 sample.

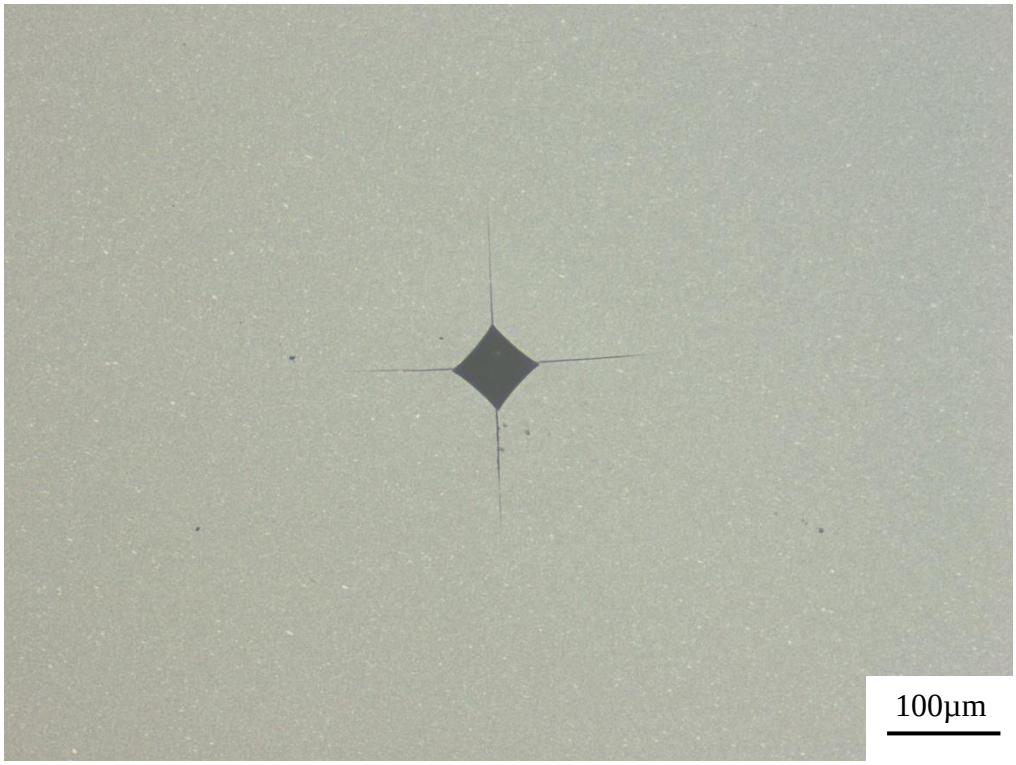


Figure 4.70: Characteristic Vickers indent on the 30wt.% ZrO_2 sample.

The measured hardness and fracture toughness of the ZrO_2 – $MgAl_2O_4$ composites are shown in **Table 4.15** and are plotted as a function of ZrO_2wt.%, **Figure 4.71**. The hardness and fracture toughness increased when the ZrO_2 content increased.

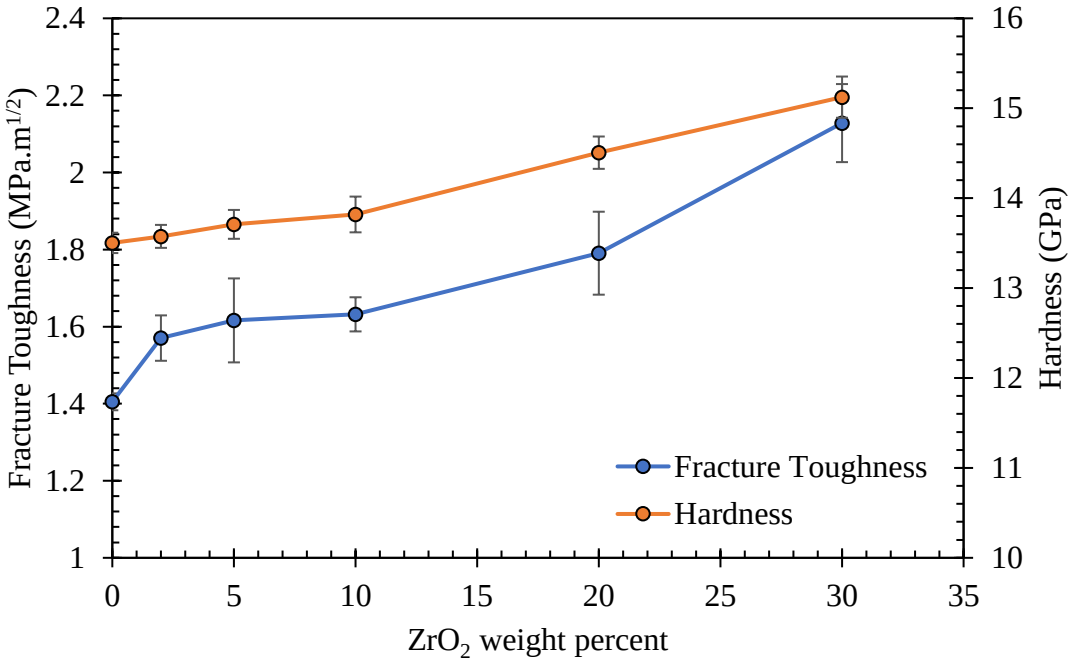


Figure 4.71: Hardness and fracture toughness as a function of the nominal ZrO_2 wt.%.

Table 4.15: The measured hardness and fracture toughness for the dispersed zirconia ceramics.

Nominal ZrO_2 (wt.%)	Hardness (GPa)	Fracture Toughness ($MPa.m^{1/2}$)
0	13.5 ± 0.11	1.40 ± 0.02
2	13.6 ± 0.13	1.57 ± 0.06
5	13.7 ± 0.16	1.62 ± 0.11
10	13.8 ± 0.20	1.63 ± 0.04
20	14.5 ± 0.18	1.79 ± 0.11
30	15.1 ± 0.23	2.13 ± 0.10

The ZrO_2 composite samples also underwent the B3B test. The fracture origin was once again on the surface of the sample, however, due to the catastrophic nature of the fractures, this could not be confirmed with the SEM for all samples. The fracture origin for a 30wt.% ZrO_2 sample is shown in **Figure 4.72**. The insert in the image shows where the SEM micrograph was taken.

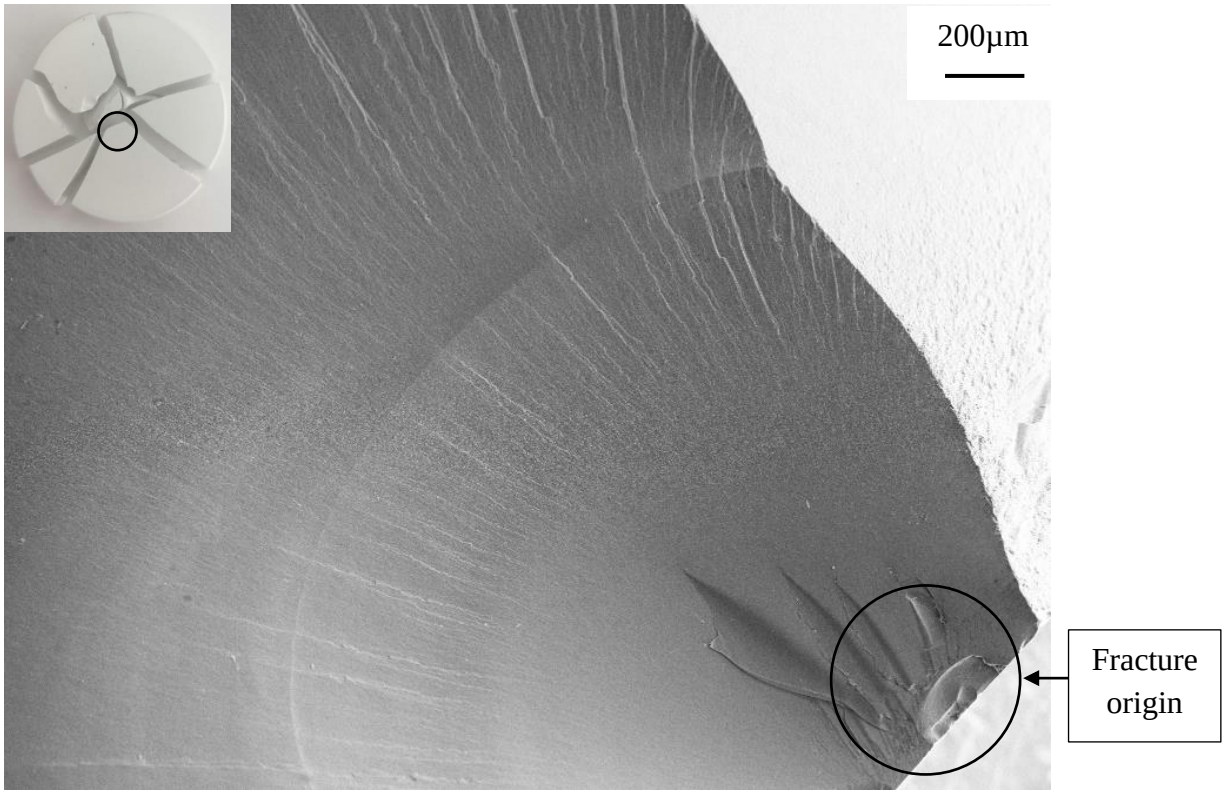


Figure 4.72: Secondary electron micrograph for the fracture origin for the 30wt.% ZrO_2 sample.

To calculate the stress that the sample was subjected to (**Equations 3.6** and **3.7 pp. 68-69**), the Poisson's Ratio was required. The Poisson's Ratio can be estimated for composite samples using **Equation 4.13** (Bourkas, et al., 2010).

$$\upsilon_c = \left(\frac{f}{\upsilon_p} + \frac{1-f}{\upsilon_m}\right)^{-1} \qquad \textbf{Equation 4.13}$$

Where υ_c, υ_p, υ_m, are the Poisson's ratio for the composite material (c), the particulate phase (p) and the matrix phase (m). f is the volume fraction of the particulate phase. The calculated Poisson's ratios are given in **Table 4.16**. The values used for the Poisson's ratios for the spinel and ZrO_2 were 0.27 (Harris & Turri, 2013) and 0.32 (Zhao, et al., 2011), respectively.

Table 4.16: Calculated Poisson's ratio for the dispersed zirconia ceramics.

Nominal ZrO_2 (wt.%)	**Poisson's Ratio**
0	0.27
2	0.270
5	0.271
10	0.272
20	0.273
30	0.276

In-order to utilise the equations developed by Borger, et al. (2002) (**Equations 3.6** and **3.7, pp. 68-69**), certain parameters derived from the samples had to fall within predetermined ranges. The range of the samples used in this work are given alongside the allowable range determined by Borger, et al. (2002) in **Table 4.17**.

Table 4.17: Experimental and allowable ranges for the parameters needed to calculate the stress for the B3B test for the ZrO_2 – $MgAl_2O_4$ composites.

Parameter	**Experimental Range/Value**	**Allowable Range**
$R_a/_R$	0.751	0.55 – 0.9
$t/_R$	0.327 – 0.337	0.05 – 0.6
υ	0.27 – 0.276	0.20 – 0.3

In **Figures 4.73** to **4.84** the results from the fracture test and Weibull analysis are shown. The same analysis was used as with the case for the transparent samples (**pp. 96**).

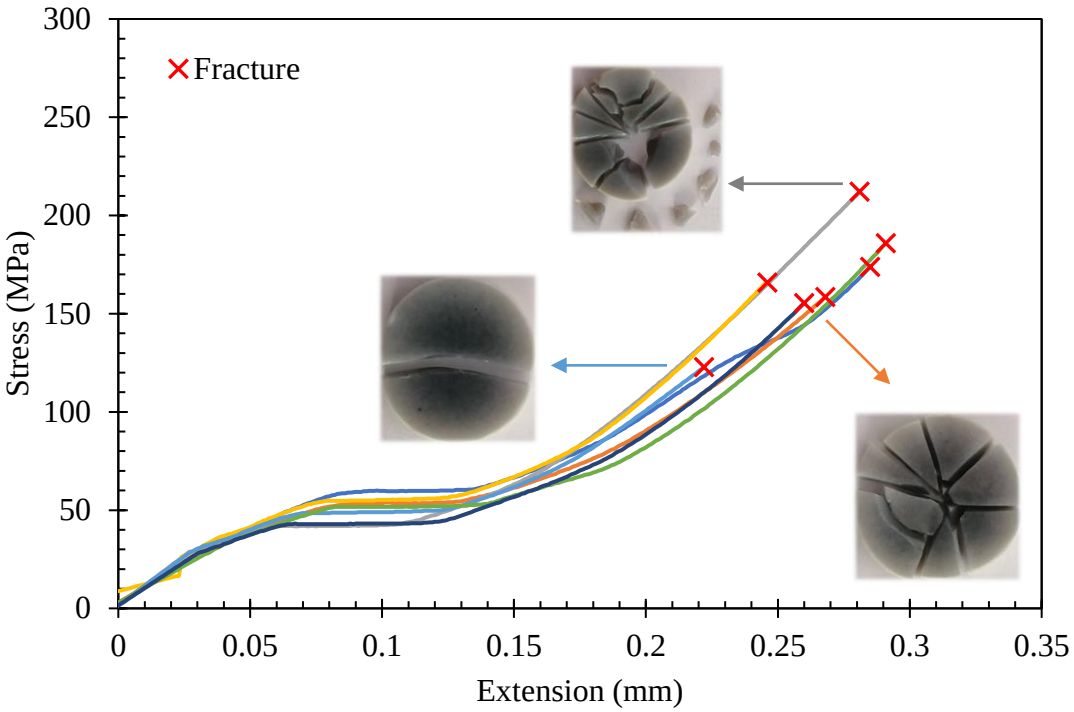


Figure 4.73: Fracture test results for the 0wt.% ZrO_2 samples.

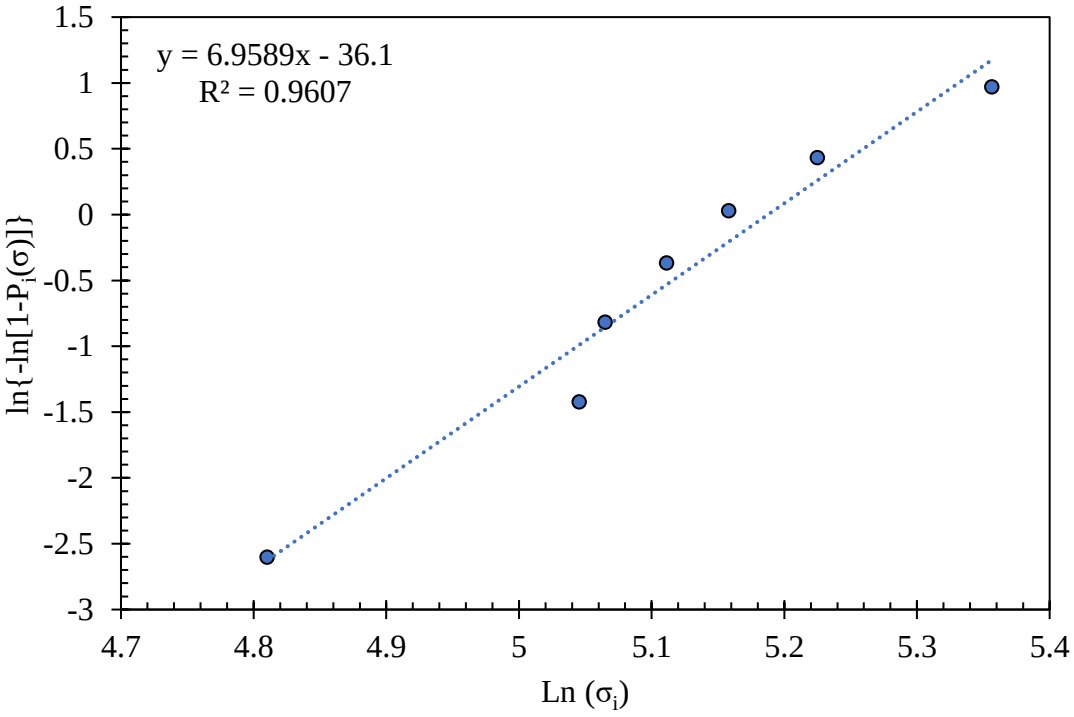


Figure 4.74: Weibull analysis for the 0wt.% ZrO_2 samples.

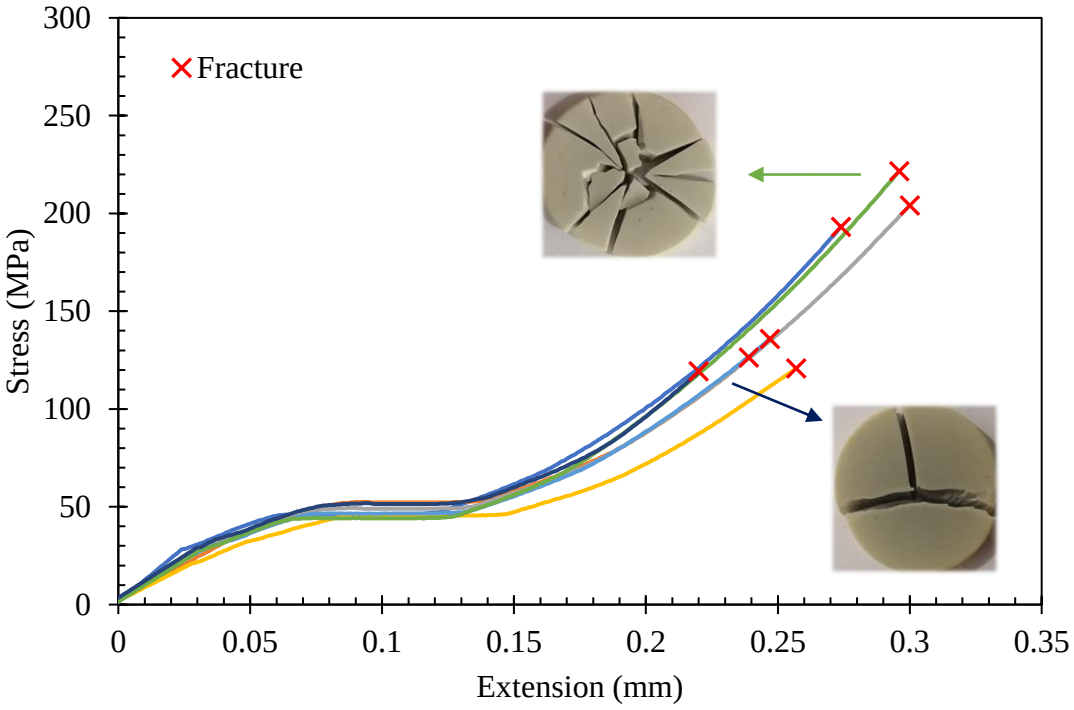


Figure 4.75: Fracture test results for the 2wt.% ZrO_2 samples.

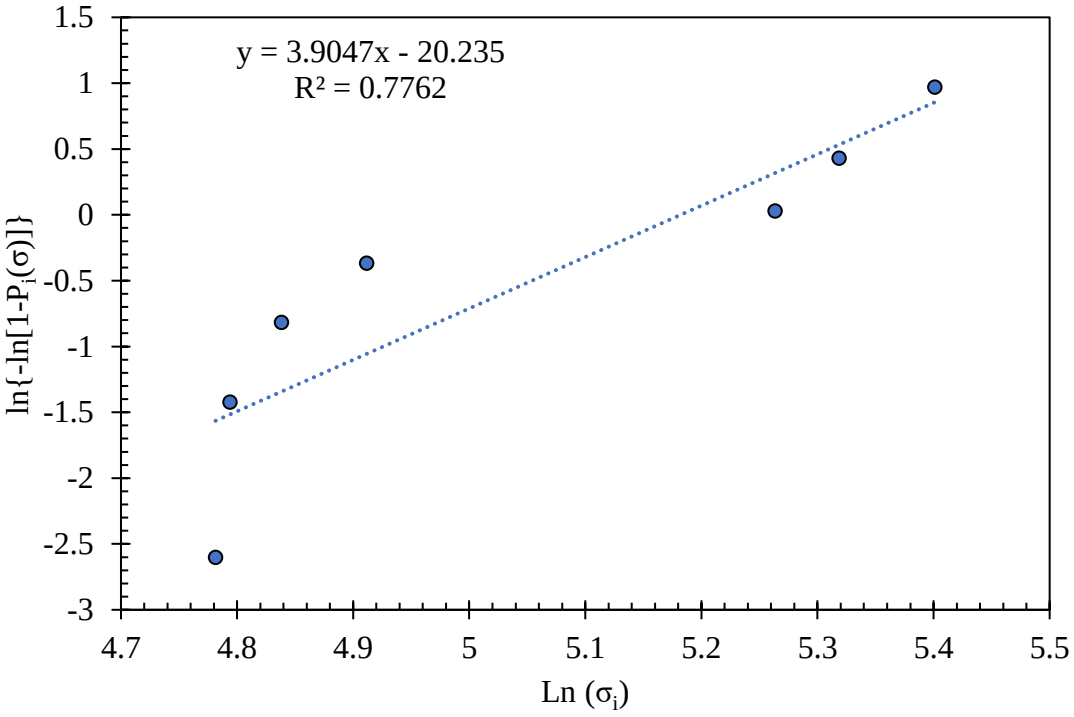


Figure 4.76: Weibull analysis for the 2wt.% ZrO_2 samples.

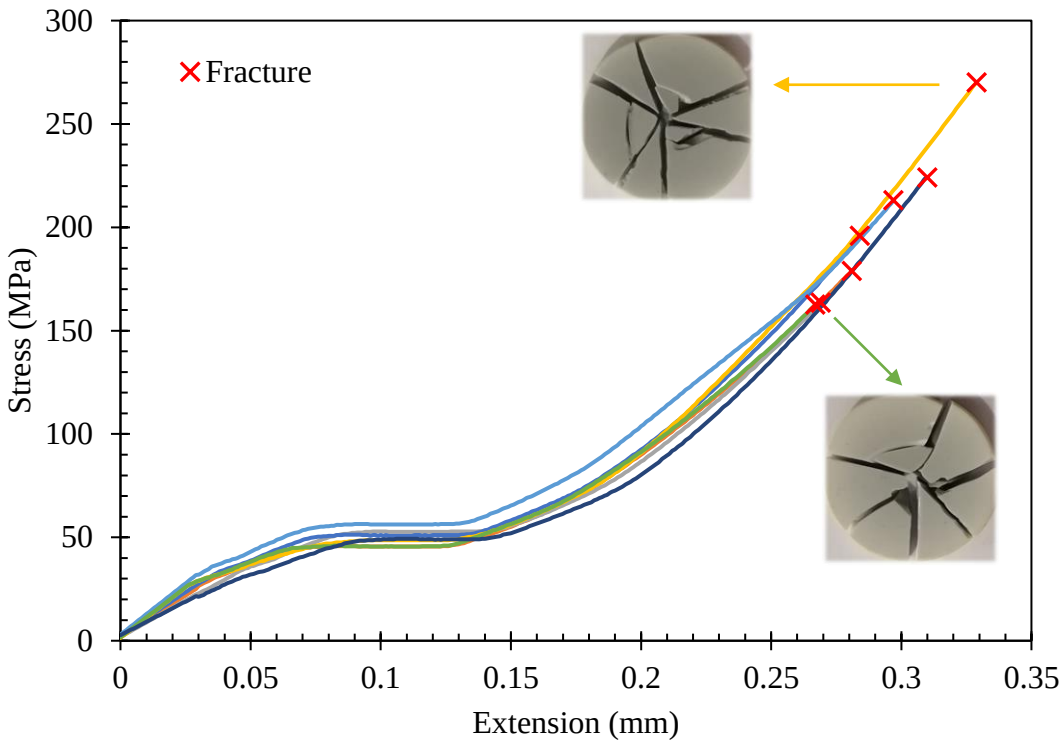


Figure 4.77: Fracture test results for the 5wt.% ZrO_2 samples.

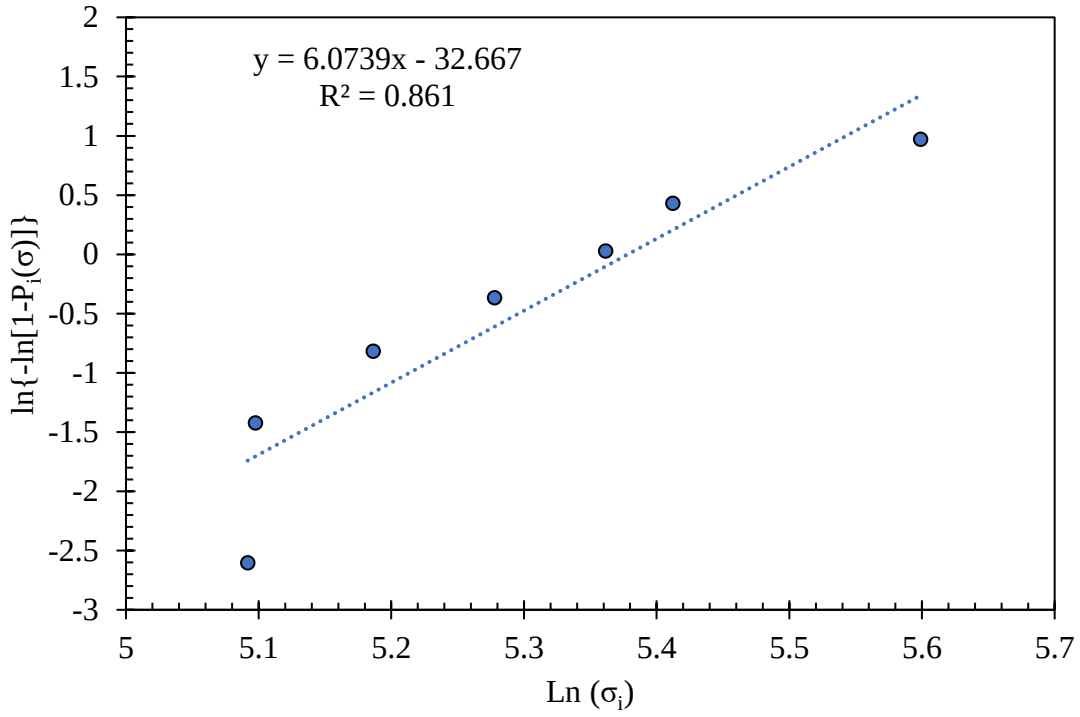


Figure 4.78: Weibull analysis for the 5wt.% ZrO_2 samples.

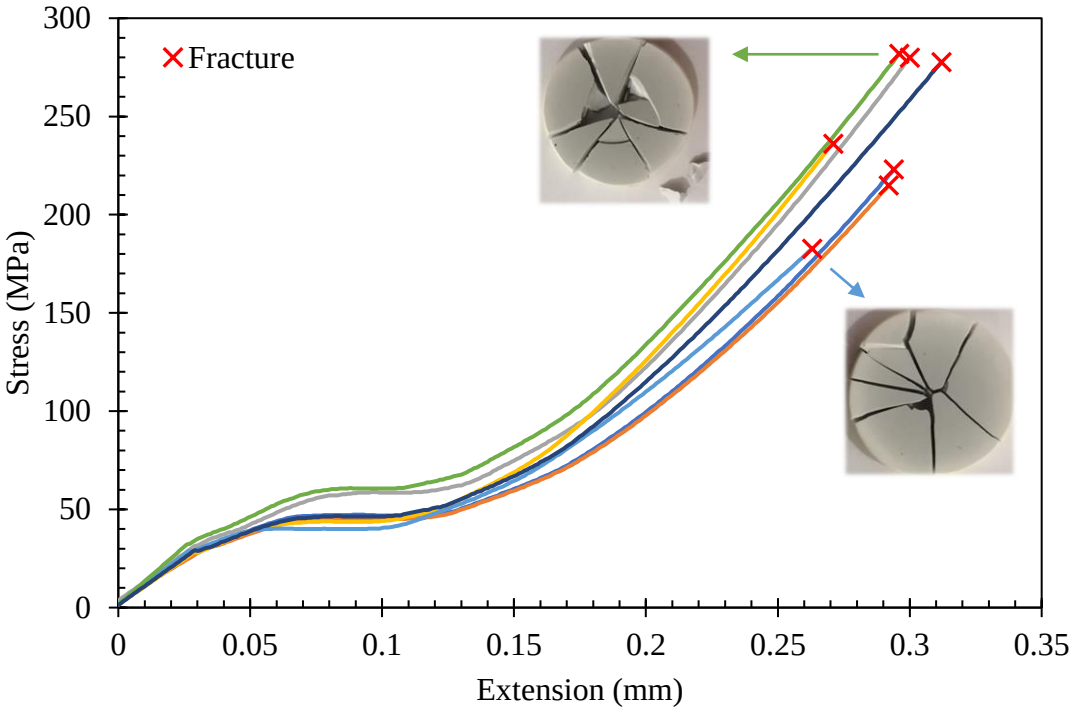


Figure 4.79: Fracture test results for the 10wt.% ZrO_2 samples.

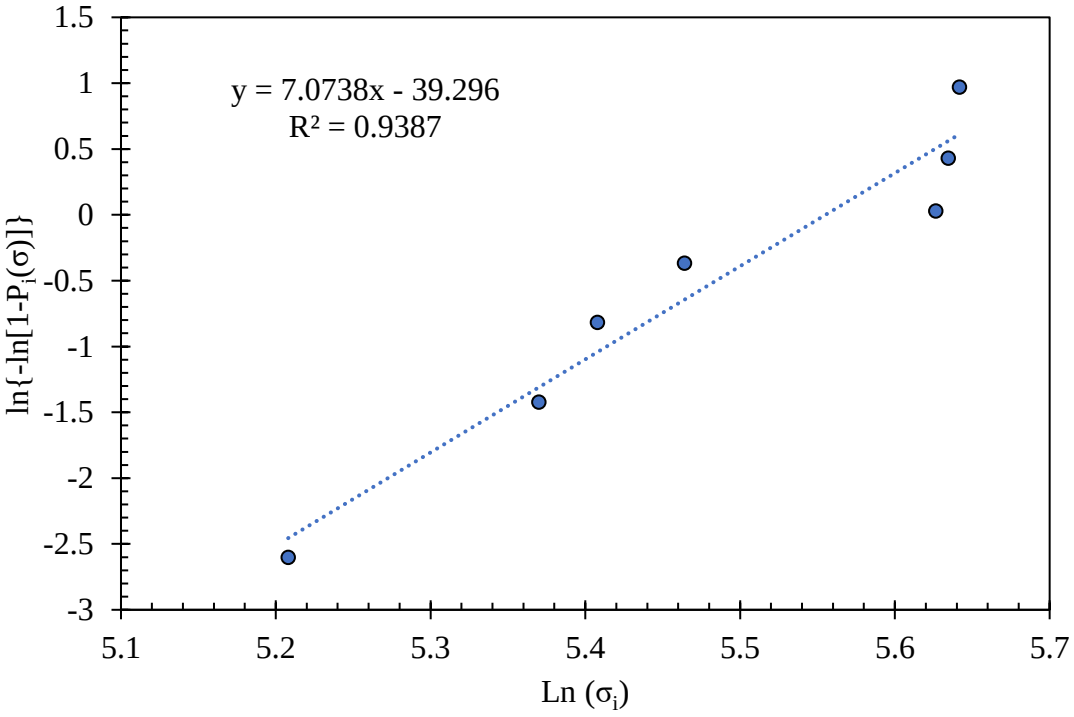


Figure 4.80: Weibull analysis for the 10wt.% ZrO_2 samples.

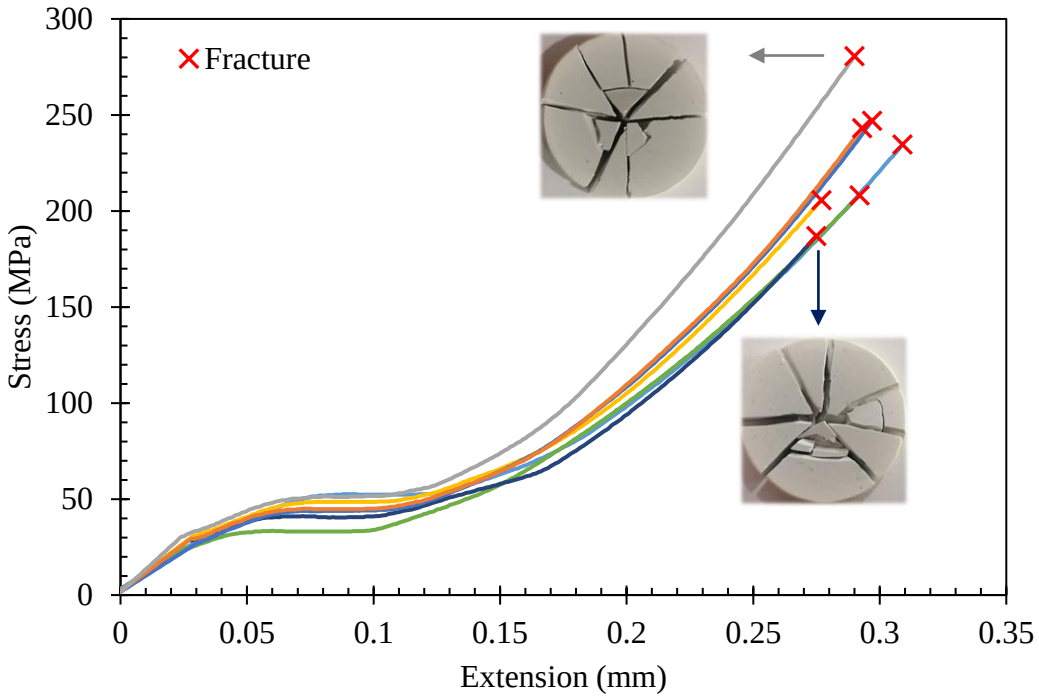


Figure 4.81: Fracture test results for the 20wt.% ZrO_2 samples.

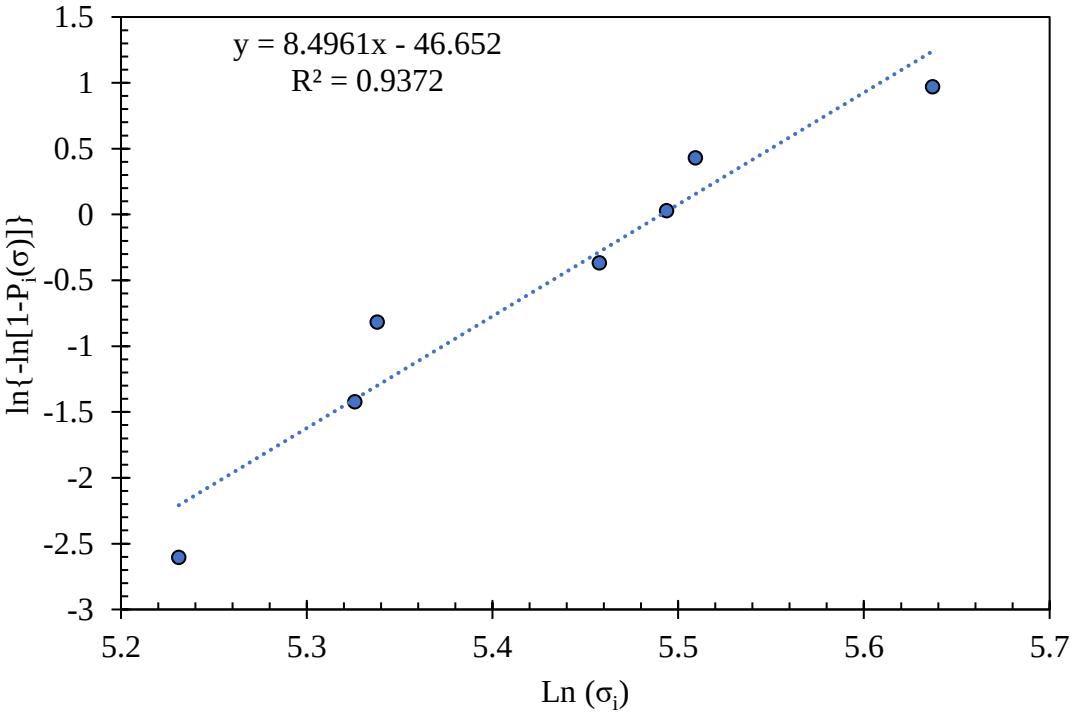


Figure 4.82: Weibull analysis for the 20wt.% ZrO_2 samples.

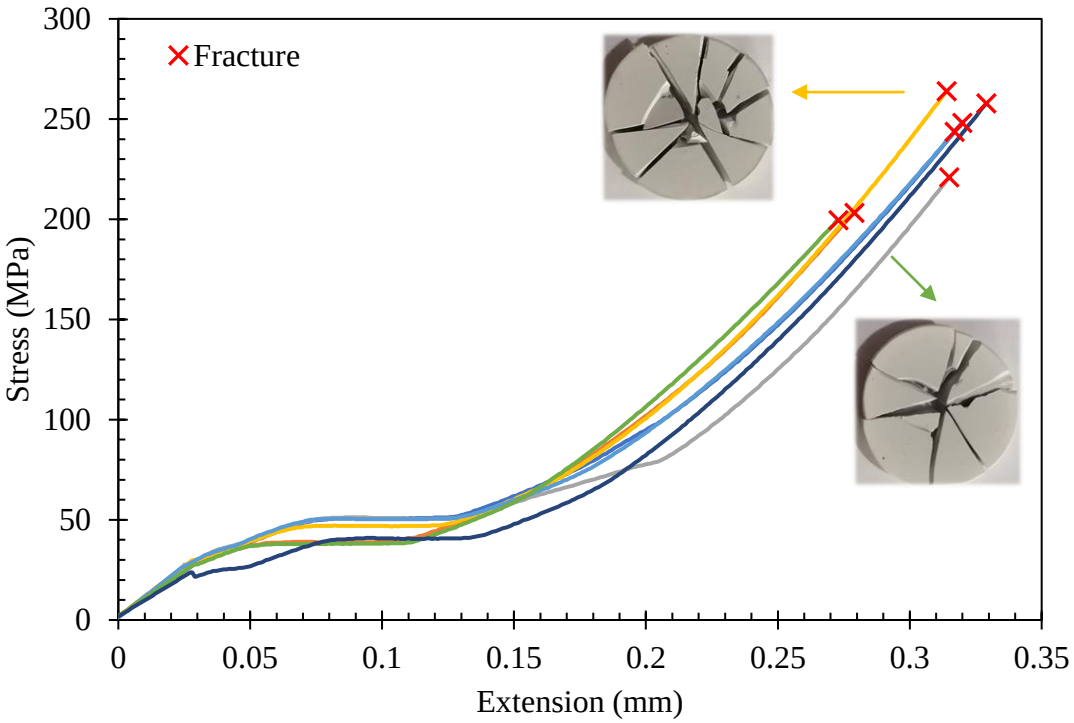


Figure 4.83: Fracture test results for the 30wt.% ZrO_2 samples.

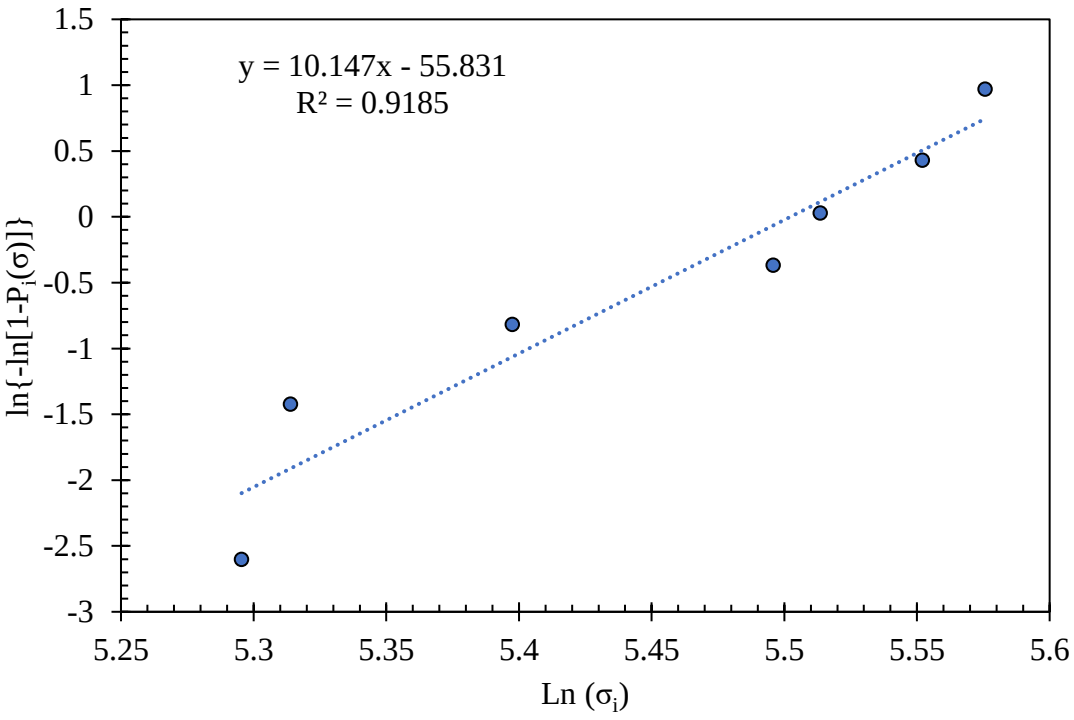


Figure 4.84: Weibull analysis for the 30wt.% ZrO_2 samples.

The Weibull moduli and nominal strengths are given in **Table 4.18**. The Weibull modulus initially decreased as the ZrO_2 wt.% went from 0% to 2%. Thereafter, further additions of ZrO_2 increased the Weibull modulus. The nominal strength increased as the ZrO_2 content increased up until 10wt.% ZrO_2, further addition caused a slight decrease in the strength after which it stayed relatively constant. The specific strength was calculated by dividing the nominal strength by the composites' average absolute density (**Figure 4.50**). This is plotted in **Figure 4.85**, along with the nominal strength as a function of ZrO_2 wt.%.

Table 4.18: Weibull modulus and the nominal strength for the composite samples.

ZrO_2 Content (wt.%)	**Weibull Modulus**	**Nominal Strength (MPa)**
30	10.15	245
20	8.50	242
10	7.07	259
5	6.07	217
2	3.90	178
0	6.96	179

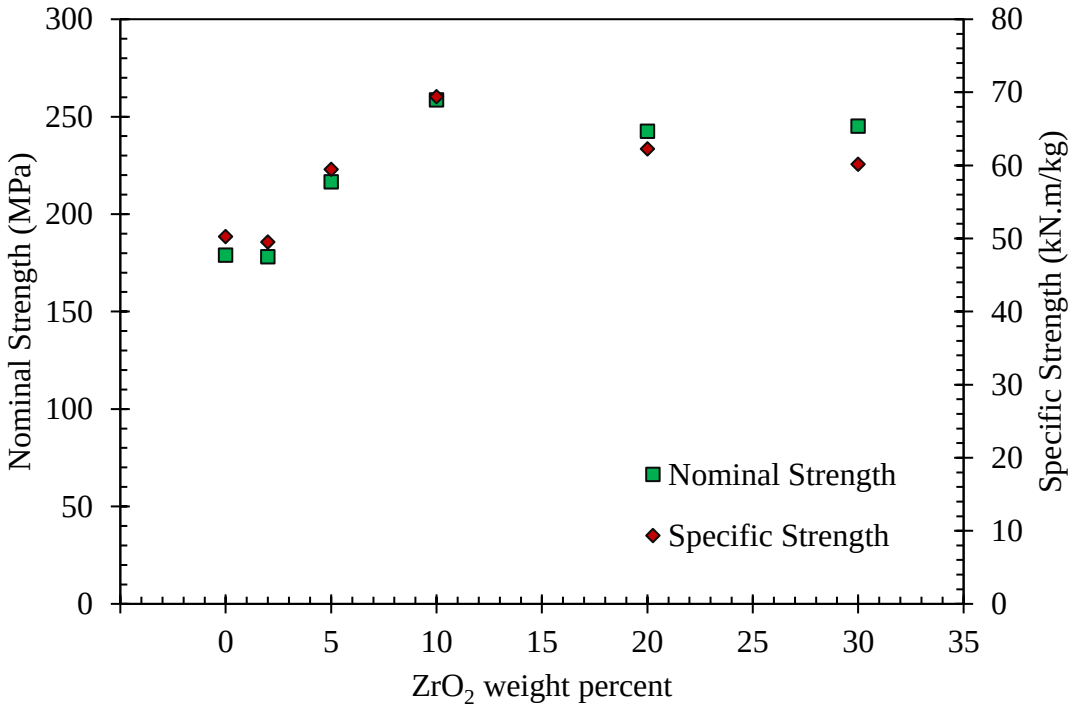


Figure 4.85: Strength of the composites as a function of ZrO_2 wt.%.

The fracture surfaces are shown in **Figure 4.86**. The fracture surface for the 0wt.% ZrO_2 shows transgranular fracture, whereas, the ceramics with the ZrO_2 show a mixture of both transgranular and intergranular fracture.

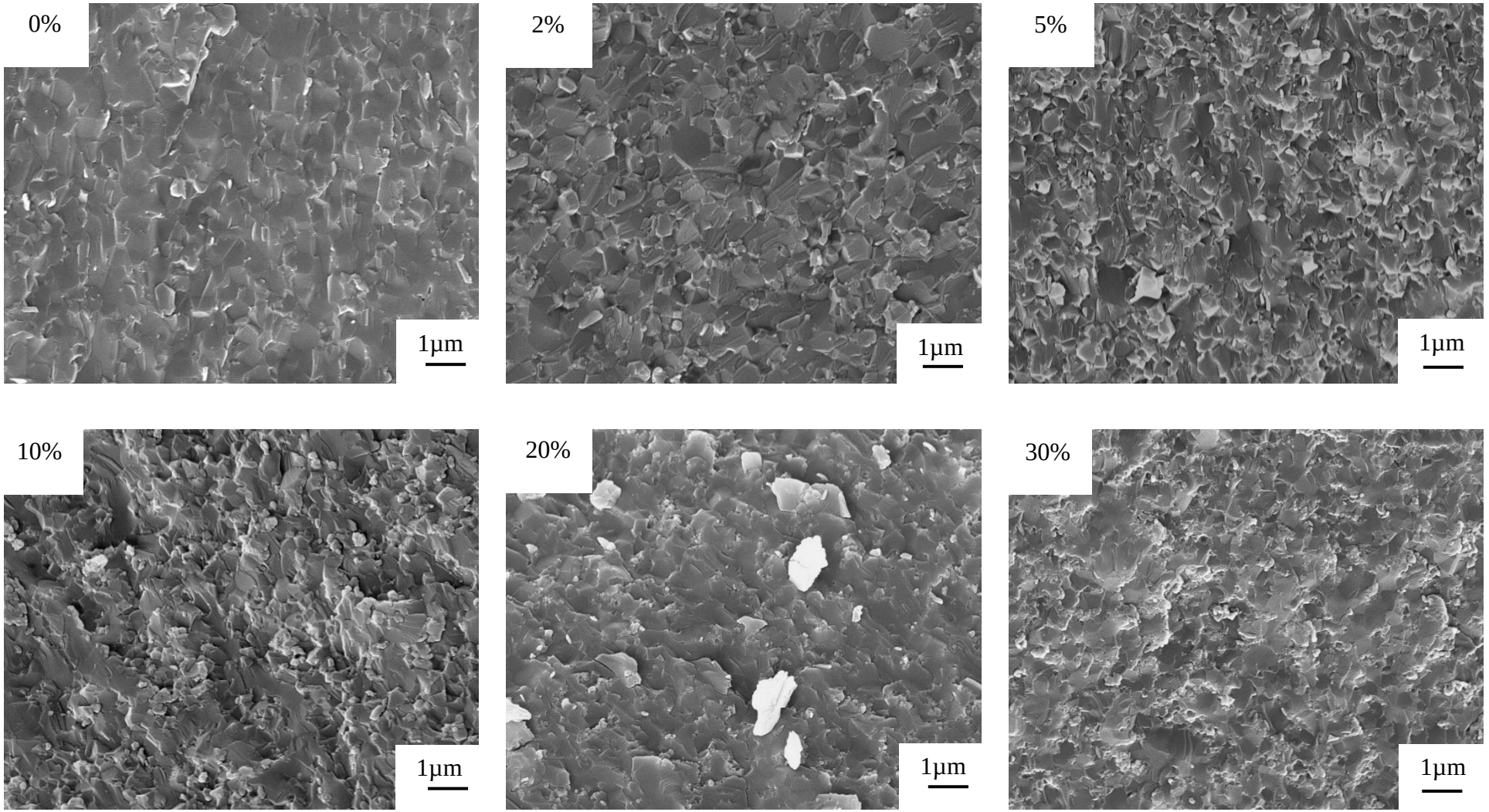


Figure 4.86: Immersion-lens SEM micrographs of the fracture surfaces.

Chapter 5: Discussion

5.1. Transparent Spinel

5.1.1. Powder Analysis

The mean particle sizes measured by the Particle Size Analyser (PSA) for the Al_2O_3 and the MgO powders were similar to the values given by the suppliers, **Table 5.1**.

Table 5.1: Particle size given by the suppliers and measured by the particle size analyser.

Mean particle size	Supplier	Particle size analysis
MgO (µm)	1.4	1.87
Al_2O_3 (µm)	0.1 to 0.3	0.19

The MgO particles were larger than the Al_2O_3 particles by an order of magnitude. The sizes obtained by the Scherrer equation (**Equation 4.2.**) used on the XRD data were orders of magnitude smaller than the values determined by the PSA. Also, the MgO was smaller (22nm) than the Al_2O_3 (35nm), which was the opposite order to the PSA measurements. These results seemed to contradict one another.

The PSA measured the size of the particles prior to milling and mixing. According to Staiger, et al. (2002), many powders that are found to have nanosized crystallites form agglomerates when in a dry state. As the PSA was done on the powders prior to milling, it was likely that agglomerates were present at during the PSA. These agglomerates did not break-up during the PSA despite the addition of sodium hexameta-phosphate, which was added to encourage dispersion, and the application of ultrasonic pulses. Balakrishnan, et al. (2010) has shown that the strength of agglomerates was inversely related to the crystallite size. Thus, the small crystallites of the powders enabled the agglomerates to resist break-up during the analysis. Also, the smaller MgO crystallites resulted in stronger, therefore, larger agglomerates than the Al_2O_3. It can be concluded that the PSA measured the size of the agglomerates not the crystallites. This also explains the morphology of the particles in **Figures 4.3** and **4.4**. The relatively large agglomerate in **Figure 4.3** was composed of crystallites that were ≈35nm in size. This gave it the flocculent appearance. Also, the particles were irregularly shaped in **Figure 4.4** as they consisted of a number of crystallites joined together.

As the Scherrer equation determines the mean size of the ordered domains (crystallites), the extent of agglomeration would not affect the measurement to the extent it did for the PSA. Individual crystallites are shown in **Figure 4.8**. The image in **Figure 4.8** was taken after milling and it shows that the agglomerates did break up as the powders are mixed on a scale smaller than the agglomerate sizes measured by the PSA. The MgO crystallites were small and cubic while the Al_2O_3 crystallites were relatively larger and more rounded. However, the crystallites were still not entirely separated, the MgO crystallites were still grouped together and so were the Al_2O_3 crystallites. These groupings could have been aggregates. The distinction between an agglomerate and an aggregate in this context will use the distinction that was stated by Balakrishnan, et al. (2010). An agglomerate is a collection of weakly bonded particles sticking together under van der Waals forces, whereas aggregates are constituted of crystallites which are bonded together by solid bridges of material. Therefore, for these powders, the crystallite size was not equal to the particle size. Rather the particle size was equal to the aggregate size, as this was the scale on which the powders were mixed. **Figure 5.1** shows the difference between a crystallite and an aggregate.

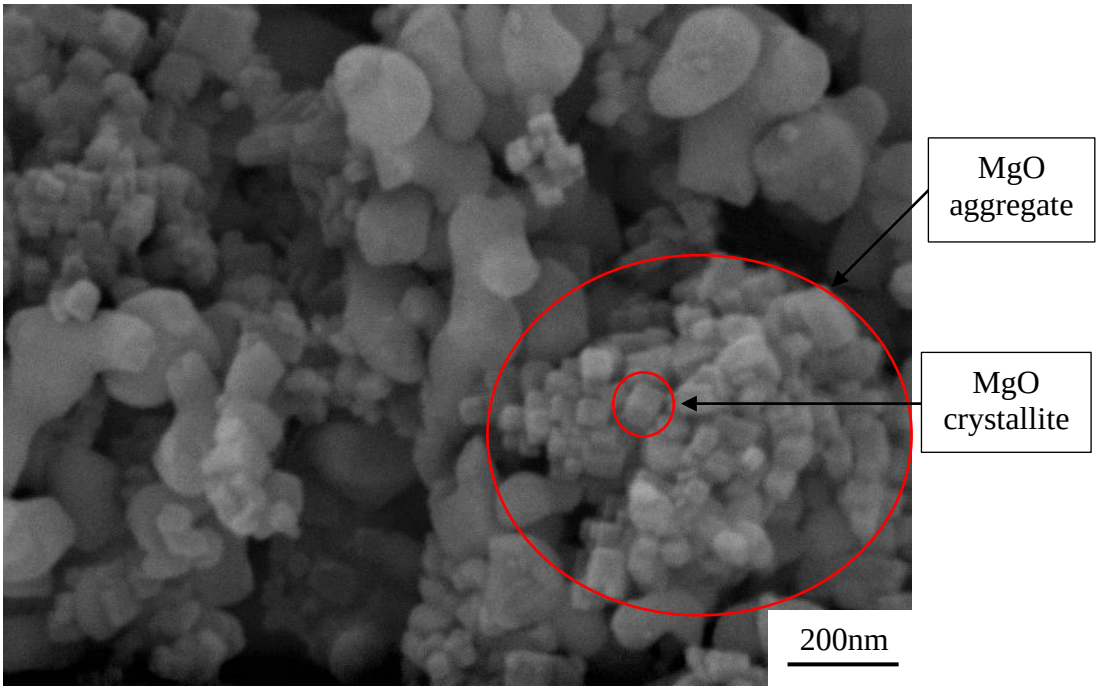


Figure 5.1: SEM micrograph of the mixed Al_2O_3 and MgO powder.

For these powders, several crystallites composed an aggregate, and several aggregates formed an agglomerate. The PSA measured the mean agglomerate size, and the Scherrer equation was used to determine the mean crystallite size. The aggregate size could not be determined as the

morphology of the aggregates made the boundaries between aggregates indistinct when examined in the SEM.

The EDS analysis showed that the only major elements in the Al_2O_3 powder were aluminium and oxygen and that the only major elements in the MgO were magnesium and oxygen. This was confirmed by the XRD which had peaks associated with only those of corundum (α-Al_2O_3) (**Figure 4.5**) and periclase (cubic-MgO) (**Figure 4.6**). Therefore, the powders that underwent sintering were pure, and well mixed. The sintered ceramic could then be classified as an advanced ceramic, the definition of which was given in **Section 1.1. Background, pp. 1**.

5.1.2. Sintering Cycle Analysis

Without the sintering aid LiF, the spinel formation reaction is governed by the counter-diffusion of the Al^{3+} and the Mg^{2+} ions through the oxygen lattice or the spinel phase (Aksel, 2004). The reaction is sufficiently modelled by the Jander solid-state reaction geometry, **Figure 5.2**.

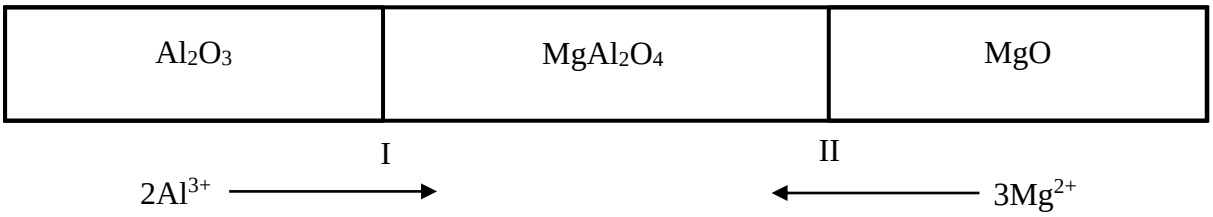


Figure 5.2: Reaction geometry of the spinel formation reaction (Aksel, 2004).

The reaction at the interface between the Al_2O_3 and the $MgAl_2O_4$ (I) is:

$$3Mg^{2+} + 4Al_2O_3 \rightarrow 3MgAl_2O_4 + 2Al^{3+} \qquad \textbf{Equation 5.1}$$

And the reaction at the interface between the $MgAl_2O_4$ and the MgO (II) is:

$$2Al^{3+} + 4MgO \rightarrow MgAl_2O_4 + 3Mg^{2+} \qquad \textbf{Equation 5.2}$$

This reaction mechanism given by Aksel (2004) shows that as more spinel forms, the diffusion distance required for the diffusing species increases. It is therefore difficult to fully react the Al_2O_3 and MgO, especially if the particle sizes are large. The samples without LiF (Run 4 no-LiF) had a minor densification peak at 1220°C, **Figure 4.10**. These samples also had a large densification peak within the second hour and a half of the sintering run, when the temperature was 1333°C and the pressure was 20MPa, **Figure 4.11**. This temperature was similar to the sintering temperature of 1300°C used by Morita, et al. in a number of experiments to fabricate

transparent spinel, (Morita, et al., 2008), (Morita, et al., 2015), (Morita, et al., 2018a), and (Morita, et al., 2018b). It was also similar to the temperature of 1300°C at which Aksel (2004) determined to be the optimum calcining temperature of a mixture of Al_2O_3 and MgO powder prior to sintering to $MgAl_2O_4$.

For the samples with LiF (Run 4), the sintering data shows that most of the densification occurred within the first hour and a half, **Figure 4.9** and **4.10**. There were two densification peaks that occurred within the sintering cycle, one began at 925°C and peaked at 965°C and the other began at 1060°C and peaked at 1125°C, **Figure 4.10**. Thus, the addition of LiF lowered the required temperature from 1333°C to 965°C and the pressure from 20MPa to 10MPa for appreciable densification.

This observation coincides with the literature as LiF has been observed to reduce the temperature of the spinel formation reaction, (Huang & Sun, 1997), (Rozenburg, et al., 2007), (Meir, et al., 2008), (Esposito, et al., 2013), and reduce the temperature at which spinel acquires full density, (Reimanis & Kleebe, 2007), (Rozenburg, et al., 2008), (Meir, et al., 2008), (Esposito, et al., 2015).

For the sample with the LiF, the temperature at which the first peak (M_1 in **Figure 4.10**) occurred was in agreement to the work done by Frage, et al. (2007). When Frage, et al. (2007) analysed the relative piston travel, they found that densification started at 950°C. The temperature at which densification began determined by both this work and Frage, et al. (2007) was slightly higher than that of Meir, et al. (2008), who detected a sudden increase in the densification of the samples containing LiF at ~870°C. Meir, et al. (2008) deduced that the cause of the peak was due to the melting of the LiF.

The temperature of the first peak (965°C) was appreciably higher than the melting temperature of LiF (848°C), therefore the reason given by Meir, et al. (2008) for the densification peak in their work was unlikely to be the case in this work. Rather, this work's results support the mechanism that Esposito, et al. (2013) adapted from Rozenburg, et al. (2007). The onset of the reaction between the LiF, MgO, and Al_2O_3 begins between 900° – 1000°C and can be written as **Equation 5.3** (Esposito, et al. (2013).

$$3LiF_{(l)} + MgO_{(s)} + Al_2O_{3\,(s)} \rightarrow LiF{:}MgF_{2\,(l)} + 2LiAlO_{2\,(s)} \qquad \textbf{Equation 5.3}$$

Thus, the addition of the LiF resulted in a liquid phase at the temperature of the first peak, either liquid LiF (as suggested by Meir, et al. (2008)) but more likely in this case the LiF:MgF_2 (as suggested by Esposito, et al (2013)). The liquid phase would have enhanced the densification rate through liquid phase sintering. The liquid phase penetrated the powdered compact and promoted the spinel formation reaction by mass transport which would have been more rapid than the solid-state diffusion shown in **Figure 5.2**. The increase in the rate of densification was manifested in the width of the densification peaks as well. The duration of the densification peak for the LiF containing sample was 0.32 hours (**Figure 4.10**), whereas the samples without the LiF had a duration of 0.63 hours (**Figure 4.11**), nearly twice as long.

Besides the formation of a liquid phase, the formation of the $LiAlO_2$ was also expected to have occurred, **Equation 5.3**. The $LiAlO_2$ would have assisted densification by the formation of oxygen vacancies (Rozenburg, et al., 2007). Rozenburg, et al. (2008) concluded that the rate-determining mechanism in spinel densification was oxygen lattice diffusion, which was also stated by Aksel (2004). The generation of the oxygen vacancies by the $LiAlO_2$ formation lowers the energy required for oxygen lattice diffusion, thereby enhancing spinel densification at lower temperatures (Rozenburg, et al., 2008). The cumulative effect of the discussed phenomena was a reduction in the activation energy for sintering spinel, which resulted in the lower temperature and pressure required for densification to begin.

The second peak (M_2 in **Figure 4.10**) coincided with the vaporisation of the liquid LiF and MgF_2 phases (LiF:MgF_2 in **Equation 5.3**) at 1050°C (Rozenburg, et al., 2007). This was further evidence that supported the occurrence of the reaction shown in **Equation 5.3**. Therefore, the results of this work, conformed with results observed in literature. The addition of LiF caused densification to occur at a lower temperature and pressure.

5.1.3. Sintered Sample Analysis

The XRD spectra of the sintered spinel (LiF-Run 4) had no peaks associated with Al_2O_3 or MgO, **Figure 4.12**. Only the peaks associated with $MgAl_2O_4$ spinel were present. This indicated that all the Al_2O_3 and MgO reacted fully to form $MgAl_2O_4$. This was reinforced by the density measurements, which showed that the samples had a density close to the theoretical maximum density of spinel, which is 3.576g/cm^3. The average density of the samples from Run 4 (with LiF) was 3.574 ± 0.002g/cm^3. For comparison, the density of a stoichiometric mixture of α-Al_2O_3 and cubic-MgO should be ≈3.85g/cm^3. The average density of the samples

was slightly lower than 3.576g/cm^3, which indicated that all Al_2O_3 and MgO reacted. If there was residual Al_2O_3 and MgO, the average density would have been higher than 3.576g/cm^3.

Figure 4.17 shows that porosity was unlikely the cause of the difference of transmission between the runs. All runs produced samples with similar densities, all the densities were within the range of the uncertainty in the measurements. Therefore, the substantial differences in transmission (**Figure 4.16** and **Table 4.2**) must be a result of other phenomena.

A visual examination of the samples fabricated using Runs 1, 2, and 3 showed that they had numerous internal cracks, **Figure 4.13**. These cracks did not manifest in the samples produced by Run 4 or 5. The cooling rate decreased from 73 to 40 to 10°C/min from Runs 1, 2, and 3. The reduction in cooling rate did not reduce the prevalence of the cracks. The extent of cracking seemed to increase. Therefore, it was deduced that these cracks were not the result of rapid inhomogeneous cooling. However, lowering the pressure applied by the pistons from 40MPa to 10MPa while the temperature was still at 1600°C did stop cracks from forming.

It was suspected that the cracks formed due to the generation of internal stress. The internal stresses are believed to be caused by the spinel formation reaction, which is associated with a volume increase of ~7.67%. Thus, the constrained expansion was believed to be the cause of the residual stresses. For Runs 1, 2, and 3, as the spinel cooled it became brittle, and the residual internal stresses caused cracks to develop. By releasing the pressure at a high temperature, the spinel could relax any internal stresses that arose from the expansion of the formation reaction while the spinel was still relatively plastic, therefore, preventing the formation of cracks. The formation of cracks resulted in a lower transmission of visible light for samples sintered using Runs 1 and 2, compared to Run 4 (with LiF), **Figure 4.16**.

The samples fabricated without LiF (Run 4 no-LiF) had dark spots and a dark grey hue (**Figure 4.15**). This is a common problem associated with samples sintered using an SPS furnace (Goldstein, 2012). This contamination was suspected to be carbon. The carbon of the dies could have reacted with residual oxygen within the furnace chamber, forming carbon oxides. These gaseous carbon oxides would then diffuse into the body of the spinel. This could occur by the reversible endothermic reaction **Equation 5.4**, where carbon would be deposited within the spinel.

$$2CO_{(g)} \leftrightarrow C_{(s)} + CO_{2_{(g)}} \qquad \textbf{Equation 5.4}$$

Alternately, carbon contamination could have also arisen by plasma induced carbon deposition originating from the graphitic dies (Meir, et al., 2008). The carbon contamination caused these samples (Run 4, no-LiF) to have the lowest transmission of visible light, **Figure 4.16**.

The addition of LiF prevented the excessive carbon contamination. This could be explained by the interaction between the LiF vapour and the residual carbon **Equation 5.5** (Meir, et al., 2008).

$$nLiF_{(g)} + nC_{(s)} \rightarrow nLi_{(s)} + (CF)n_{(g)} \uparrow \qquad \textbf{Equation 5.5}$$

The LiF vapour reacted with the deposited carbon and formed carbon monofluoride which then left the system as a gas. This reaction also explained why the graphitic dies corroded when they were not properly protected by the graphite foil, **Figure 3.1**. If the reaction shown in **Equation 5.5** did occur, then the lithium would remain within the sintered ceramic. This would be difficult to verify as EDS cannot detect lithium. The lithium would also be expected to incorporate into the spinel lattice by **Equation 5.6**. Therefore, XRD would also not be a suitable technique to detect the presence of lithium. A technique which may be able to detect the presence of lithium would be Secondary Ion Mass Spectroscopy (SIMS). However, this technique was beyond the scope of this work.

$$3Li \xrightarrow{Spinel} 2Li'_{Mg} + Li''_{Al} + 2V_O^{\cdot\cdot} \qquad \textbf{Equation 5.6}$$

The sample with the second lowest transmission was the sample sintered using Run 5, which had a sintering time of only 1 hour. The sample did not have any cracks or carbon contamination, but the shorter sintering time resulted in a cloudiness within the body of the sample, **Figure 4.14**. Cohen, et al. (2018) also observed this cloudiness. Cohen, et al. (2018) showed that the cloudiness can be removed by a post-sintering heat treatment, whereas the dark hues caused by carbon contamination cannot be removed.

The lower transmission achieved by Run 5 shows the importance of long sintering times to achieve good transparency, especially for single stage sintering processes. The need for a long sintering time necessitated the addition of LiF, without which there was excessive carbon contamination, **Figure 4.15**, and extremely low transmission. Therefore, the LiF was required to remove the carbon contamination that was caused by the graphitic environment in the SPS furnace especially due to the extremely long sintering cycles required, greater than 6 hours.

While Run 4 (with LiF) did have the highest transmission, it still did not achieve the theoretical maximum. **Figure 4.18** shows that many samples from Run 4 (with the LiF) had densities lower than the theoretical maximum even when considering the uncertainty in the density measurement. This could indicate that the samples sintered using Run 4 did not achieve the theoretical transmission because of insufficient densification. The presence of residual porosity was verified by the SEM, **Figure 4.37** to **4.39**. The presence of pores would reduce the transmission, however, pores could not be the only cause of the reduction in transmission. In **Figure 5.3.** the sintered samples (from Run 4 with LiF) have their densities plotted versus their average transmission in the visible spectrum. The coefficient of determination (R^2) for a linear fit was only 0.0515. Thus, the relationship between the density and transmittance of visible light for these samples was very weak at best.

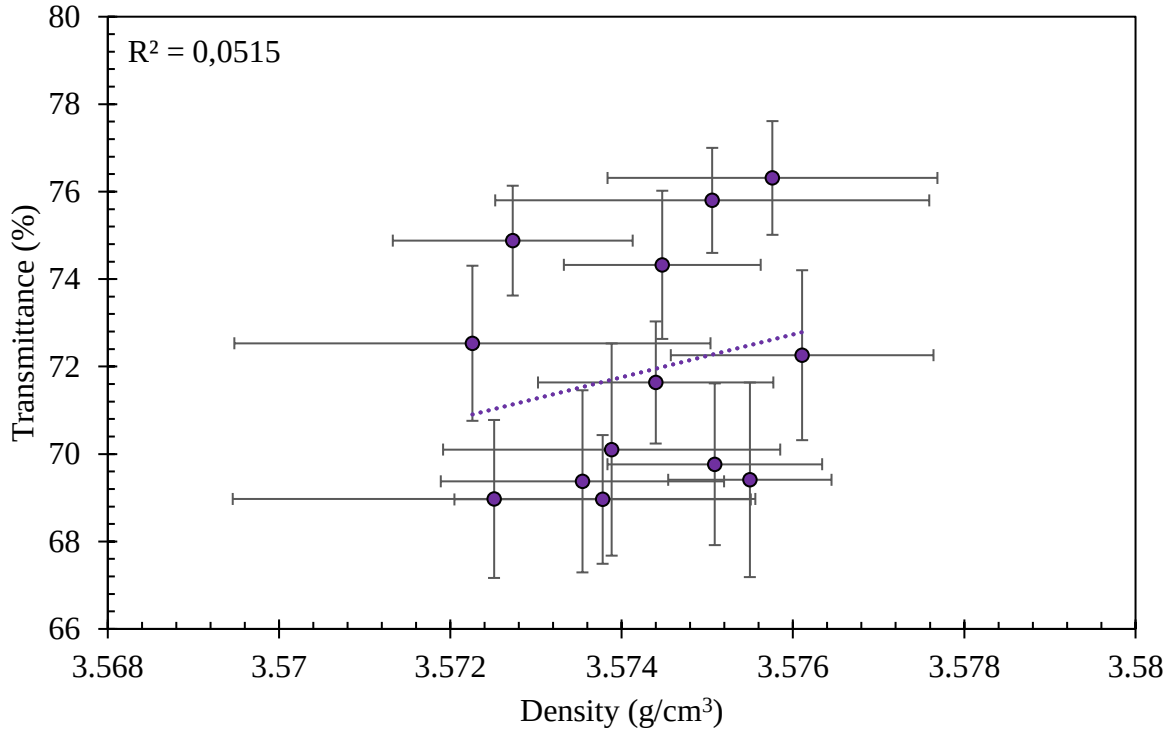


Figure 5.3: Average transmission as a function of density.

There are two potential scenarios that could explain this. Either the density was no longer the main cause of scatter and something else was also causing the reduction in transmission. Or the method of measuring density, the Archimedes principle, was not accurate enough at these levels of porosity.

The possibility that the Archimedes method used to measure density was not accurate enough is supported by the lengths of the error bars in **Figure 5.3**. The error bars for the data are of similar lengths to the distances between the points. This would conceal any trend that may be present. This explanation was further justified by the difference in transmission between the samples sintered using Run 4 and 5. The uncertainties of the density measurements for the samples sintered by Runs 4 and 5 were larger than the difference between the average densities, **Figure 4.17.b**. Therefore, the Archimedes method could not distinguish the densities of these two sample groups even though the difference in transmission was significant, **Figure 4.16** and **Table 4.2**. Therefore, at these extremely low porosity levels, a more precise measurement would be required.

However, there was also evidence that the porosity was not the sole reason for the reduction in transmission. **Figures 4.34** to **4.36** show non-uniform areas at high energy points (grain boundaries and triple points). The EDS measurements showed that these areas had the same atomic ratios as spinel **Table 4.8**, thus it is reasonable to assume they were spinel. However, due to their non-uniformity and rough morphology, these areas would not have a high inline transmission, they would scatter light. It was likely that these areas contributed to the reduction in transmission. This would explain why the transmission of visible light did not correlate well with the density measurements. The residual porosity, in conjunction with the non-uniform areas prevented the attainment of the theoretical transmission.

The formation of these non-uniform areas could be a result of the phenomena that caused the cracks in Runs 1, 2, and 3, just at a reduced magnitude. The areas appear to be regions of damage. This damage could have resulted from the increase in volume from the spinel formation reaction, which was expected to close pores. If the pores that were to be closed had a smaller volume than the volume expansion from the reaction, stresses would arise due to the constrained expansion. These stresses were the expected cause of the internal cracks that developed in the samples from Runs 1, 2, and 3. As the samples from Run 4 (with LiF) had a pressure regime that was expected to relax the stresses without causing significant damage, the cracks did not develop, but the stresses were still great enough to result in the minor damage that was present at the high energy points. Therefore, a potential solution to reduce the extent of these damaged areas could be to further increase the time that the ceramic is kept at top sintering temperature without the applied pressure.

When analysing the fracture surfaces at a low magnification, the EDS measurement showed that the atomic ratios for the magnesium, aluminium, and oxygen were not the same as the theoretical values, **Table 4.7**. Particularly, the magnesium was low, whereas the aluminium and oxygen were higher. The lower than expected magnesium could be a result of the formation of the LiF:MgF_2 liquid, **Equation 5.3**. The LiF:MgF_2 liquid phase was expected to begin vaporizing at ≈1050°C (Rozenburg, et al., 2008). If the liquid did vaporise then the magnesium could have escaped the system as a gaseous species (MgF_2), thus resulting in the magnesium deficiency measured by the EDS. However, this deficiency was not detected by the XRD measurement as the spinel structure can accommodate a range of ratios between MgO and Al_2O_3, **Figure 2.2** (**pp. 10**). Therefore, the spinel that was fabricated was non-stoichiometric and slightly Al_2O_3 rich. Spinel sintered in the presence of LiF has been observed to have a high aluminium content elsewhere, (Huang & Sun, 1997) (Rozenburg, et al., 2007).

5.1.4. Sintered Samples Microstructure

The microstructure of the samples produced using Run 4 with the LiF followed a log-lognormal distribution, **Figures 4.20** and **4.21**. This was confirmed by the Shapiro – Wilk's test for normalcy. This distribution of grain size resulted in an extremely wide range of grain sizes. The smallest measured grain size was ≈6µm, while the largest was ≈700µm. Thus, the grain sizes were distributed over two orders of magnitude. This resulted in a microstructure that could be considered heterogeneous, **Figure 4.19**. The log-lognormal grain size distribution was observed when considering the frequency of grain sizes, but it was bimodal when considering the area contribution of each size range, **Figure 4.23**. Due to the range of grain sizes, it was difficult to represent the grain size with a single number, and depending on the technique used, the grain size varied substantially. The linear intercept method measured a grain size of 96µm ± 34µm, the average grain size calculated from the frequency data gave a value of 45µm ± 45µm, the mean of the best fit normal distribution was 31.52µm, and the area weighted average was 236µm ± 208µm. Of all these values, the area weighted average seemed to represent the grain structure in **Figure 4.19** the best.

The standard deviation of the measurements was high (208µm is ≈90% of 236µm), however, this was not because the measurements were inaccurate or unreliable. The large value was a result of the wide range of grain sizes, which resulted in a very high standard deviation. This large variation could be considered to be a property of heterogeneous microstructures. The

standard deviation was relatively low for the linear intercept method compared to the other methods. This could be explained by the spatial distribution of the grains. If a number of grains with a large variation in size were spread out homogenously, lines cutting through the grains from multiple directions would still cut through a similar number of grains, leading to similar values for the average grain size. This would result in a low standard deviation between these values. However, when the grain sizes of individual grains are measured, the spatial distribution of the grains does not have an effect. Therefore, the standard deviation would be high as the spread of the grain sizes was high. This highlights a particular difficulty when trying to determine the grain size of a heterogeneous microstructure.

The heterogeneous microstructure of $MgAl_2O_4$ sintered in the presence of LiF has also been observed by Reimanis & Kleebe (2007), Rozenburg, et al. (2008), and Rothman, et al. (2014). The Li^+ cations that were incorporated into the spinel matrix formed oxygen vacancies, **Equation 5.6**. This lowered the energy for oxygen lattice diffusion, which enhanced the spinel grain growth (Rozenburg, et al., 2007). The spinel grains which incorporated the Li^+ cations grew at a faster rate than those grains which did not. This mechanism explains the observed microstructure, which consisted of very large grains and small grains in a bimodal distribution (when considering the area contributions of the grains).

The heterogeneity introduced into the microstructure by the LiF made the mean grain size less representative than for homogenous microstructures. The research is still lacking, however, there are contributions that focus on the role of grain size distribution on mechanical behaviour of heterogeneous materials (Berbenni, et al., 2007). Two arbitrary lognormal distributions with the same mean grain size are shown in **Figure 5.4**.

Even though these distributions clearly represent microstructures which are not identical, they would be treated as such if only the mean grain size was considered. This highlights the need to develop a better way to quantify heterogeneous microstructures when analysing the microstructure of LiF doped spinel. Too many authors only give the mean grain size, whilst completely leaving out any information about the grain size distribution when reporting on LiF doped spinel. Berbenni, et al. (2007) attempted to develop systematic methods of incorporating the grain size distribution into the analysis of the mechanical properties. Their work should be incorporated into future analyses of spinel sintered in the presence of LiF to give a clearer indication of the mean grain size and grain size distribution.

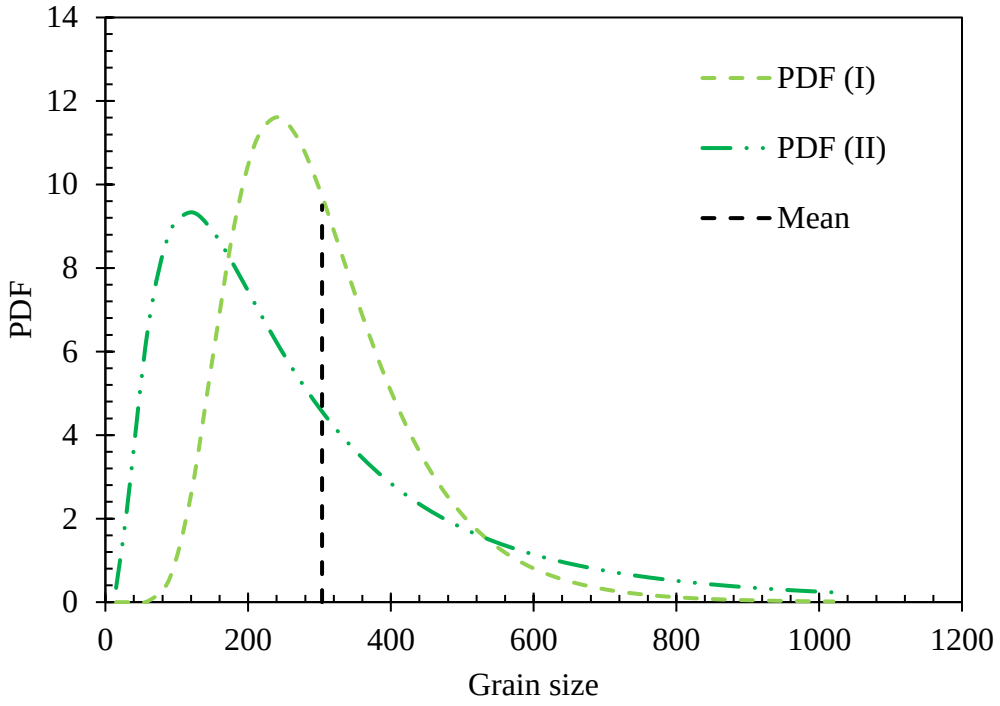


Figure 5.4: Arbitary lognormal distributions that have the same mean.

Rozenburg et al. (2008) suspected that including a lengthy step at low pressure and temperature increases the grain coarsening significantly. Rothman et al. (2014) observed that slower heating rates led to extensive grain growth when spinel was sintered in the presence of LiF. A long period of time at a relatively low temperature extends the time the LiF melt has to incorporate into the spinel, thus exacerbating the extent of non-uniform grain growth. The sintering run used (Run 4) had such a long period, **Figure 3.3.a** (**pp. 61**) LiF has a melting temperature of 848°C, and the second densification peak, M_2 in **Figure 4.10,** was expected to be the vaporisation of the liquid LiF which peaked at 1125°C. Taking these two temperatures as the limits at which liquid LiF would exist in the system means that the liquid LiF had ≈30min in contact with the spinel. Such a prolonged period of time likely contributed the grain growth for these samples.

5.1.5. Hardness and Fracture Toughness

The fracture toughness did seem to conform to the expected values, when compared to other authors, **Figure 4.24**. However, this result was uncertain as the indent had multiple cracks that did not originate from the corners of the indent. Spalling was also observed to have occurred, **Figure 4.25**. Such local disruptions are likely to affect the measured value of the fracture toughness (Anstis, et al., 1980). Thus, the value of the fracture toughness would need to be

verified by an alternative method to indentation fracture such as the single edge notched beam method (Wang & Atkinson, 2015).

The poor indent could be a result of the grain size relative to the crack length. The average crack length was 362 ± 50μm and the weighted average grain size was 236μm ± 208μm. Thus, the cracks were of the same order of magnitude as the grains. Anstis, et al. (1980) observed that when the grain size was similar to the crack length the indentation method for acquiring fracture toughness was not suitable.

The effect of a heterogeneous microstructure on a material's mechanical properties can be observed by looking at the standard deviation of the hardness and fracture toughness. Rothman, et al. (2014) measured the hardness on a single grain and on multiple grains of spinel and found a significant difference. This phenomenon manifests itself clearly when comparing the standard deviation of the hardness and fracture toughness between samples and within samples. The standard deviation was higher for the measurements taken within a single sample than the standard deviation of the average hardness between each sample. The reason for the greater standard deviation within single samples compared to between samples is shown in **Figure 5.5**. Due to the heterogenous microstructure, a Vickers indent could occur on a single large grain or multiple small grains. The grain size of the local environment could be very small or it could be essentially a single crystal. The difference in the local grain size caused the hardness to vary within a sample. However, after numerous indents, the average hardness values were similar which implied that the process consistently produced similar heterogenous samples.

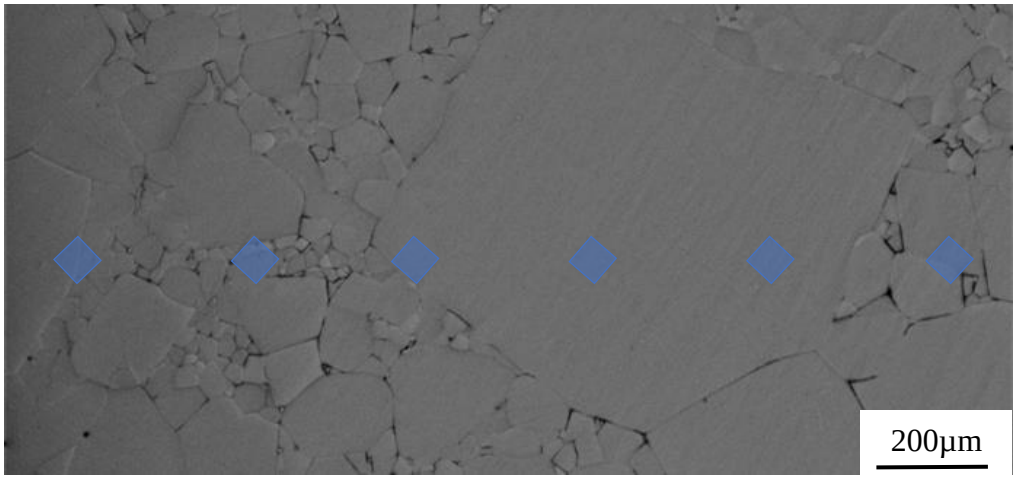


Figure 5.5: Microstructure of a Run 4 (with LiF) sample with diamond shapes representing hardness indents from **Figure 4.25** (the diamonds are to scale).

The average hardness of the samples from Run 4 was relatively low, 1245Hv ± 36Hv, compared to literature, **Table 4.5**. The addition of LiF had deleterious effects on the mechanical properties not just because it caused grain growth, but also because it caused inhomogeneous grain growth. This could adversely affect its application as transparent armour or space-craft window systems where consistency would be required. These are life sustaining components, thus it is critical that the materials produced be of the highest quality and easily reproducible.

While the LiF had a deleterious effect on the mechanical properties of the spinel, its pronounced benefit on the transmission of light cannot be ignored. The difference 1wt.% of LiF made on the transmission was an increase from 1.37 % to 71.87%, **Table 4.2**. The average transmittance for Run 4 (with LiF) was compared to the literature of single stage sintering in **Figure 5.6**. The fabrication route used in this work resulted in a relatively high transmission within the visible spectrum. This highlights the balance between the mechanical properties and the transmission of the spinel. The transmission was higher than the values found in literature, but this came at the expense of the mechanical properties which were lower than those reported in literature.

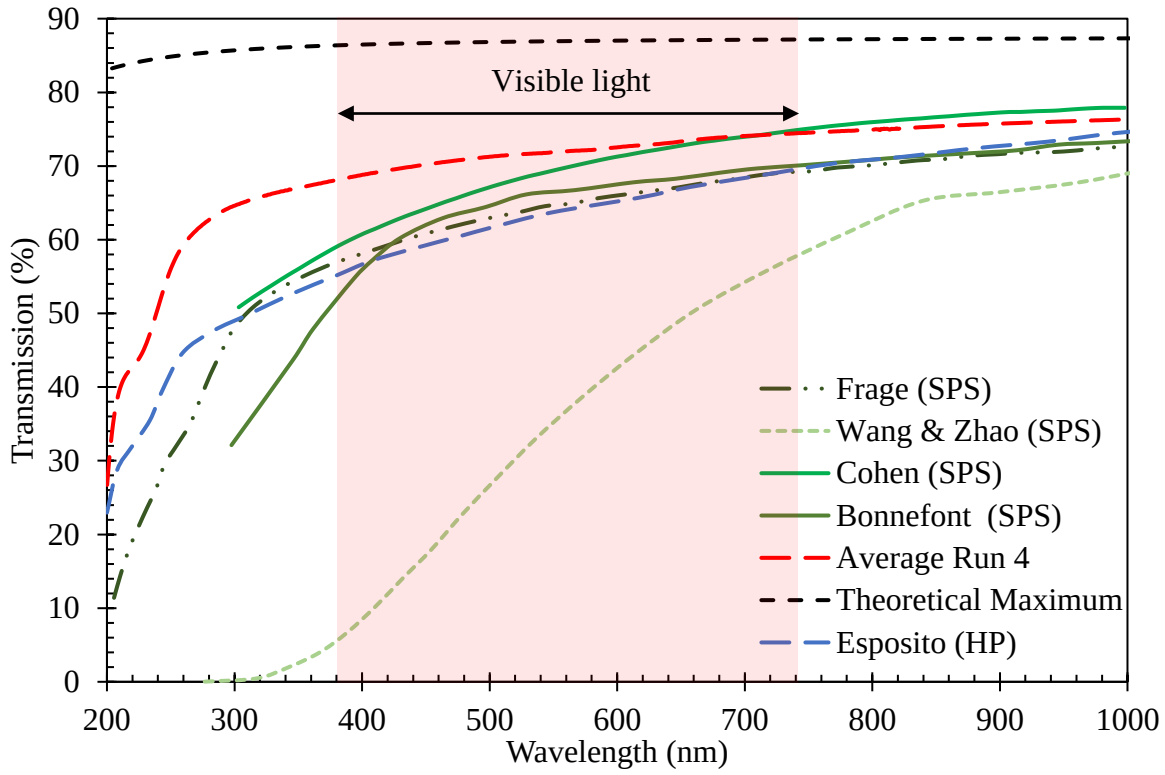


Figure 5.6: Average transmission for Run 4 compared to those found in literature for single-stage sintering. (Frage, et al., 2007), (Wang & Zhao, 2009), (Bonnefont, et al., 2012), (Esposito, et al., 2013), and (Cohen, et al., 2018).

5.1.6. Fracture Analysis

The fractures that occurred during the B3B test can be partially explained by the finite element analysis modelling done by Borger, et al. (2002). The samples fracture origin was in the centre of the disk, and the cracks propagated outward to the periphery **Figure 4.26**. This pattern follows the direction of maximum stress, **Figure 5.7**. In **Figure 5.7** the stresses were normalized as a percentage of the maximum stress.

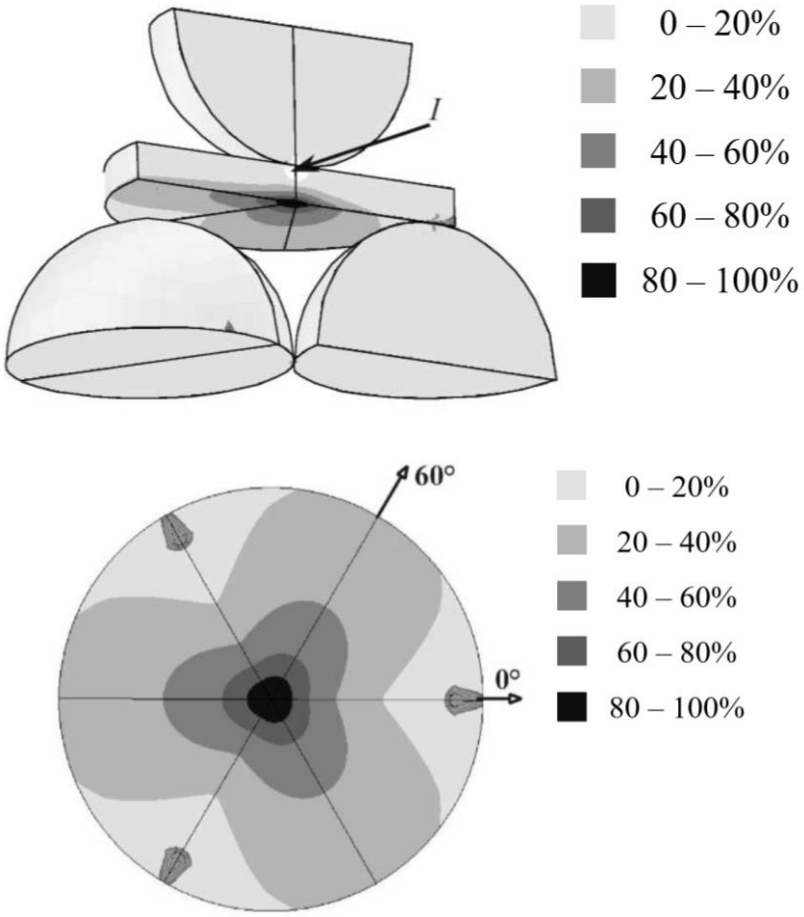


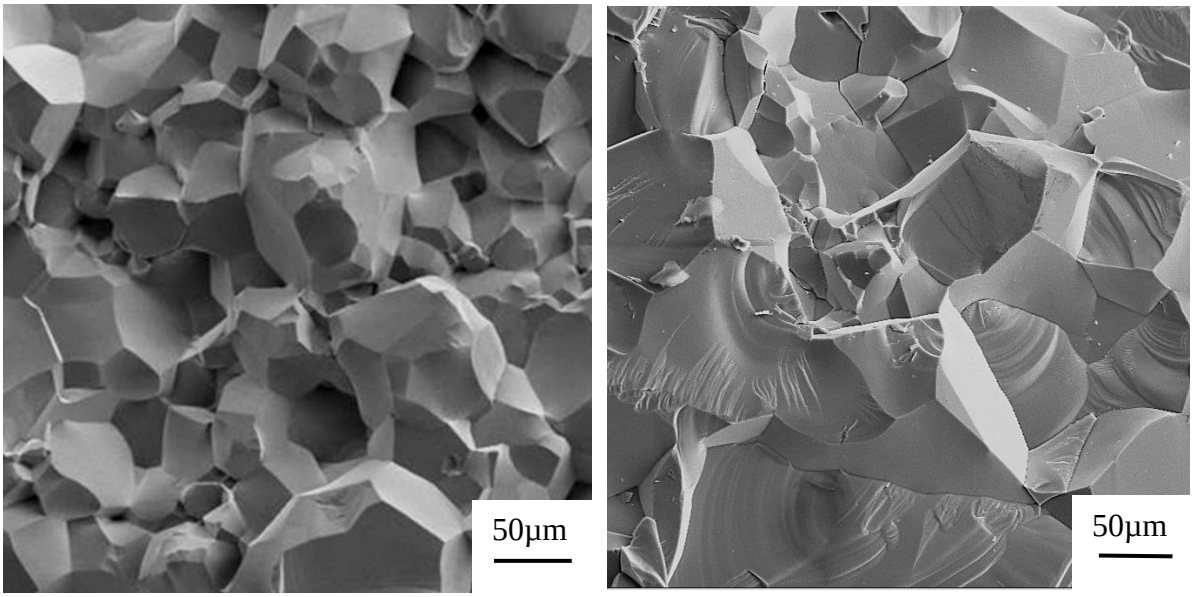
Figure 5.7: Finite element analysis depiciting the normalised tensile stress (Borger, et al., 2002).

According to Borger, et al. (2002), the surface opposite the loading ball should experience the highest tensile stress and the line of maximum stress from the centre to the periphery of the sample occurs in between the supporting balls (the 60° line, **Figure 5.7**). The origin of the fracture was confirmed to be at the surface of the sample, **Figures 4.27** to **4.29**, in agreement with the work done by Borger, et al. (2002). The fracture originated in the centre and spread

out following the lines of greatest tensile stress. The samples that survived to higher stresses fractured into more pieces, **Figure 4.30**. This would be the result of the release of a greater amount of stored elastic energy which would be associated with the greater stress.

The SEM images of the fracture surface, **Figure 4.32** and **4.33**, show the presence of both transgranular fracture and intergranular fracture. This was somewhat unexpected as the addition of LiF has been found to promote intergranular fracture, not transgranular fracture (Reimanis & Kleebe, 2007), (Salem, 2013), (Esposito, et al., 2015). It has been observed that most spinel lattice impurities segregate towards surfaces, such as grain boundaries (Goldstein, 2012), and that the LiF is active at the interface between the grains (Rozenburg, et al., 2007). Because of this and the presence of porosity at the grain boundaries, intergranular fracture is promoted (Salem, 2013). Thus, the extent of transgranular fracture in the samples produced in this work was surprising as it contradicted the observations and explanations found in literature.

Esposito, et al. (2015) fractured spinel samples that had 1wt.% LiF, but their samples were hot pressed not SPSed. Their samples were also sintered at 1600°C for 180min, with an intermediate soak time of 60min at 1220°C. An SEM image of the fracture surface of a sample fabricated by Esposito, et al. (2015) is shown side-by-side to an image of the fracture surface of a sample produced in this work (Run 4 with LiF) in **Figure 5.8.**



(Esposito, et al., 2015) This work

Figure 5.8: SEM micrographs of fracture surfaces of samples produced by Esposito, et al. (2015) and this work.

The extent of transgranular fracture in Esposito et al.'s sample was far less than this work. The occurrence of the transgranular fracture surfaces within the samples created in this work indicate that the grain boundaries are stronger than those in Esposito, et al. (2015). The cause of this discrepancy could be a result of the furnaces used to sinter the samples. Esposito, et al. (2015) used a hot press to consolidate the powders, whereas, an SPS furnace was used in this work. Sintering ceramic powders with an SPS furnace has been found to result in cleaner grain boundaries and reduced impurity segregation at grain boundaries (Munir, et al., 2006). Mizuguchi, et al. (2010) compared ZrB_2 samples sintered using a hot-press and an SPS furnace using transmission electron microscopy. There was a lower concentration of impurities at the grain boundaries of the SPSed samples than the hot-pressed samples. Mizuguchi, et al. (2010) suspected this was the result of electrical discharges generated between particles during the SPS process. Thus, the SPS process resulted in cleaner grain boundaries, which were subsequently stronger. This promoted transgranular fracture instead of intergranular fracture. Cleaner grain boundaries could also explain the greater transmission of the samples created in this work when compared to Esposito, et al. (2013), **Figure 5.6**. If impurities did not coalesce at grain boundaries, and stayed segregated, their interaction with light would be minimized.

5.1.7. Biaxial Flexural Strength

The Weibull modulus of the samples made from Run 4 with LiF was 3.91. This was low as the value of the Weibull modulus for many structural ceramics is around 10 (Petrovic, 1987). This indicates that the spread of the fracture stress for these samples was unusually high. Ceramic materials are sensitive to the largest flaw size present. If there was a wide spread of strength, it would imply that the process used to fabricate these ceramics resulted in a wide spread of flaw sizes. Not necessarily within a single sample, but between samples.

The low Weibull modulus was particularly deleterious because the sample sizes were relatively small, compared to its potential application as a window. If the size of the samples were increased, the probability of a sample containing a large flaw would also increase. Therefore, for a sample of larger windows, the nominal strength would likely be lower as the prevalence of large flaws would be greater in components with a larger volume (Danzer, et al., 2007).

The flaws could be pores or the damaged regions found at high energy areas. The pores that are present could have varied in size depending on the initial powder compact and the degree of pore coalescence. If the powder compact had relatively large aggregates or the extent of pore

coalescence was high, the resultant pores would be large. If the powder compact had a narrow size distribution and the extent of pore coalescence was low, the resultant pores would be more numerous but smaller. The other reason for the flaws could be the damaged regions, **Figures 4.34** to **4.36**. Depending on the local grain environment, the damaged area could be relatively large, if the local stresses were large, or if the relative geometry of the grains reduced the stress, the size of the damaged area could be small.

The inconsistent fracture stress which resulted from these flaws would preclude spinel as a viable substitute for glass as windows in spacecraft where consistency and predictability are paramount.

An analysis given by Amoros, et al. (2007) to describe the development of pores in porcelain tiles may be applicable to understand the process in LiF assisted spinel sintering. The addition of LiF resulted in the formation of a liquid phase. As the liquid phase began to form, it would likely surround the Al_2O_3, MgO and $MgAl_2O_4$ particles, liquid LiF has been found to have a low wetting angle with spinel (Meir, et al., 2008). This would result in a process-driving capillary pressure (P_c) at the contact points between particles. This capillary pressure would force the particles closer together, thus increasing shrinkage and lowering porosity, while also changing the pore size and shape (Amor´os, et al., 2007). As the porosity decreases, pores would begin to close. These occluded pores could trap the liquid phase. As, the temperature continued to increase, this liquid phase would vaporise and form a gas. The trapped gas would exert a pressure on the pore walls, (P_g). If the temperature was increased further, the pressure of the gas would exceed the capillary pressure and the pores would begin to grow, thus the porosity would start to increase (Amor´os, et al., 2007). Therefore, simply increasing the sintering temperature may not necessarily reduce the porosity. Such a mechanism seems to have occurred within these samples as the shape of the pore in **Figure 4.39** was semi-circular. The rounded shape appears to be from the exertion of isostatic pressure that would develop when entrapped gas was heated.

The porosity could potentially be reduced through better powder preparation. The powders used had very small crystallites, however, the presence of agglomerates and aggregates was confirmed. The milling did seem to break-up the soft agglomerates that were present in the powders, however, it did not completely remove the presence of aggregates, **Figure 4.8**.

Depending on the relative orientation of these aggregates, the attainment of full density may not be possible.

During the SPS process, there was a stage where a pseudo-green body was formed. When the sintering run began, the powder was first compressed by 3kN of force (this corresponded to 10MPa for the sample size used in this work). This pressing occurred for approximately 3 minutes. This powder compact could be thought of as a green body, thus, analysing literature relating to green bodies could provide certain insights.

To encourage sintering, the crystallites must be as small as possible, and so must the pores within the powdered compact. But, the distribution of pore size is arguably more important than the average size (Goldstein, 2012). A green body, with a small mean pore size but a wide distribution would have a lower sinterability than a green body with a slightly higher mean grain size but a narrower distribution. Due to the extremely low final porosity of the sintered spinel part for transparent applications, the most relevant pore size is the maximum, not the average pore size (Goldstein, 2012).

As shown in **Section 5.1.1. Powder Analysis**, the compact powders were collections of aggregates of various sizes and shapes. A minority of the particles were individual crystallites. Because of this, the ideal ordered arrangement for the particles, depicted in **Figure 5.9.a**, was unattainable. However, the arrangement shown in **Figure 5.9.b.** would be a realistic goal. The arrangement shown **in Figure 5.9.c.** would preclude the attainment of a fully sintered ceramic (Goldstein, 2012).

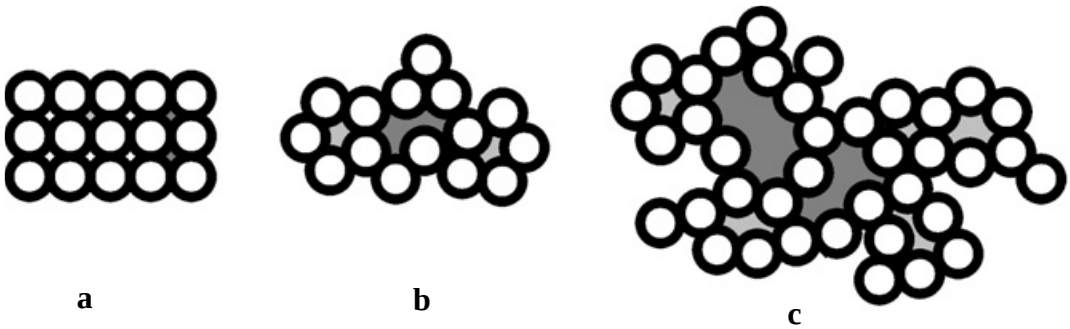


Figure 5.9: Schematic of the packing of crystallites (circles) in a powdered compact (**a**) the ideal case, (**b**) realistic goal and (**c**) poorly process powder (Goldstein, 2012).

The agglomerates were expected to break-up during the milling process, and not be present during the sintering process. However, after milling the slurry was dried using a rotary

evaporator. This drying process could result in partial re-agglomeration. Also, the SEM image **Figure 5.1** shows that aggregates were still present after the milling. Therefore, even though these powders did have exceedingly small crystallites (<50nm), the small crystallite size was likely underutilised, as the particle size would be represented by the aggregate size.

The presence of these aggregates would mean that the packing arrangement of the powders could be the arrangement shown in **Figure 5.9.b** or **5.9.c**, depending on the relative orientation of the irregularly shaped aggregates. This would have resulted in a random chance of a sample being well packed or poorly packed. This likely contributed to the low Weibull modulus calculated for the samples.

The milling could become more vigorous to break up the aggregates as these powders were relatively gently milled (only 110rpm), however, an issue with extended or vigorous comminution would be contamination. Thus, the milling equipment should ideally be fabricated from ultra-pure alumina, magnesia or spinel to prevent contamination which would lower transmission. Another issue that would need to be addressed is the re-agglomeration that occurs during the drying stage. The powders were screened through a 125µm sieve after drying, however, this is not nearly fine enough as the agglomerates measured by the PSA were <2µm. Dry manual crushing with a pestle and mortar prior to sintering may help reduce the prevalence of agglomerates but it also could lead to an increase in contamination.

The focus on powder processing should also ensure that occluded porosity is minimized. As the aggregates likely exhibited internal, variable size porosity, their presence likely resulted in the formation of occluded pores. Occluded pores are much more difficult to close than those present on grain boundaries (Goldstein, 2012). A schematic of a microstructure topography is shown in **Figure 5.10**. **Figure 5.10.a** is the ideal case, where the grains (squares) and pores (circles) are small, and the pores are attached to the grain boundaries. The configuration in **Figure 5.10.b** shows a sizeable fraction of large, occluded pores and large grains that is likely to result from the packing depicted in **Figure 5.9.c** (Goldstein, 2012).

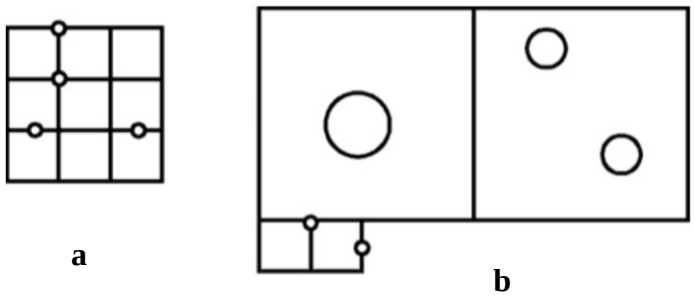


Figure 5 10: Schematic representation of the microstructure showing grains (squares) and pores (circles), (**a**) in the ideal case and (**b**) the case where full attainment of density is not posible (Goldstein, 2012).

The SEM micrograph, **Figure 4.37**, seems to show a large, occluded pore, thus more attention needs to be given to powder preparation for the elimination of residual porosity. Another indication that this process resulted in samples that had varied flaw sizes was the standard deviation of the transmission at a given wavelength. **Figure 5.11** shows the average transmission for samples produced using Run 4 (with LiF). The shaded area shows the range of one standard deviation above and below the average for the transmission at that wavelength. The production route was the same for each sample however, the transmission still varied over a noticeable range at a given wavelength. This was likely a result of the variation of flaw sizes between each sample.

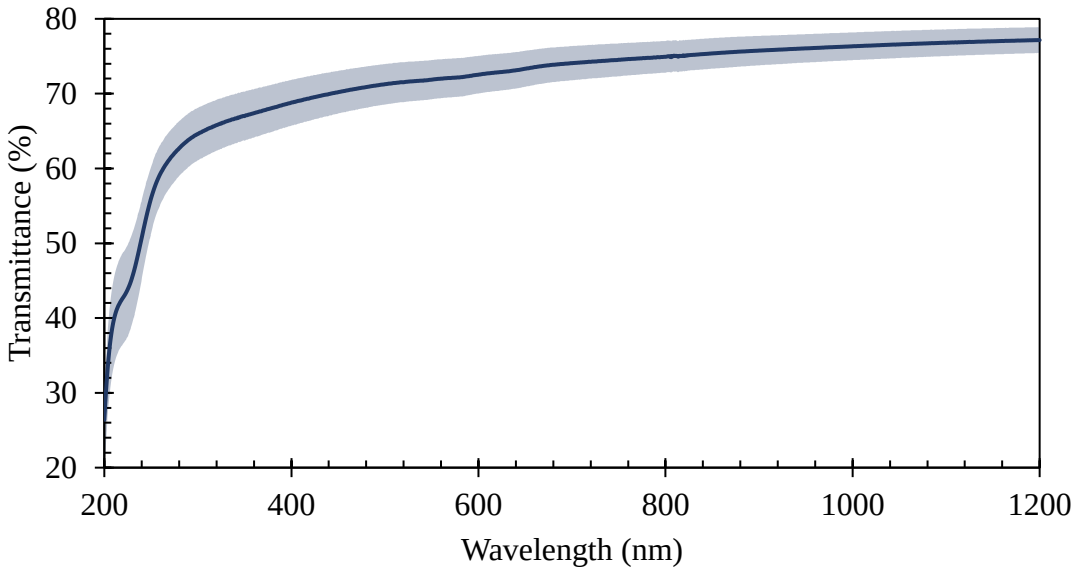


Figure 5.11: Average transmission for the samples produced using Run 4 (with LiF). The shaded region is one standard deviation above and below the average.

All these factors indicate why transparent spinel parts are difficult to manufacture. The extremely low levels of porosity and high levels of purity necessitate that every processing level must meet stringent quality control levels.

5.1.8. Comparison to Glass

As the potential use of transparent spinel is a replacement for glass, the mechanical properties of the spinel were compared to reported values for glass. The glasses used in this comparison were from Hand & Tadjiev (2010) who compared the mechanical properties of a number of glasses. The glasses chosen from Hand & Tadjiev's (2010) set for this comparison were the glasses with the highest hardness, highest fracture toughness, and the lowest and highest density, **Table 5.2**. The spinel had a density that was 29 to 49% higher than the glass, but the spinel had a fracture toughness that was 46 to 130% higher and a hardness that was 117 to 204% higher than the glass. Keep in mind that the spinel fabricated in this study had poorer mechanical properties than those measured in other literature.

Table 5.2: Mechanical properties of Glass (Hand & Tadjiev, 2010)

Property	**Density (g/cm^3)**	**Hardness (GPa)**	**Fracture Toughness ($MPa.m^{0.5}$)**
Highest Hardness	2.592	5.63 ± 0.11	0.68 ± 0.03
Highest Fracture Toughness	2.392	4.44 ± 0.08	1.07 ± 0.05
Highest density	2.769	4.02 ± 0.07	0.64 ± 0.01
Lowest density	2.392	4.44 ± 0.08	1.07 ± 0.05
Spinel (From this work)	3.574	12.21 ± 0.35	1.56 ± 0.26

It is difficult to determine the practical strength of glass. The theoretical strength of silica glass has been calculated to be approximately 24GPa (Kurkjian, et al., 2010). This value is two orders of magnitude higher than the measured value for the spinel samples of 145MPa. However, the practical strength of glass is far lower than its theoretical strength due to the presence of flaws and damage. Preston (1942) put it aptly, "The 'strength' that we find is simply the residual strength, and what we really measure is not how strong the glass is, but how nearly broken it is already." Thus, without strength data on the specific glass that the spinel would replace, any comparison to the strength of glass would simply be illustrative. Strength values for glass have

been reported in literature. Values found within literature report strengths of 50MPa (Klocek, 1991), 110MPa (Harris, 1999), and 115MPa (Klein, 2009), and Weibull moduli of 4 (Musikant, 1985) to 8.8 (Klein, 2009). The papers that reported the strength values did not report the density of the corresponding glass, therefore the specific strengths could not be determined and compared to that of spinel. However, the spinel did have a higher nominal strength than all the values reported for glass. The Weibull modulus of the spinel was lower than those values reported for glass.

The spinel had better mechanical properties than the values found for glass in literature, even though the spinel made in this work had mechanical properties that were lower than the values stipulated for spinel in literature. For this reason, less research should focus on improving the absolute value of spinel's mechanical properties. There are many studies which aim to fabricate spinel with nanosized grains or without the addition of LiF in the pursuit of improved mechanical properties, usually at a great cost to transmission. This, however, does not seem to address the most immediate hurdle preventing the commercialisation of spinel components. From this work, it seems that future efforts should focus on the improvement of the Weibull modulus, increasing the in-line transmission and the consistency of the transmission and reducing the cost of fabrication of spinel components. Such research should enable the economic viability of transparency spinel components.

5.2. Dispersed Zirconia Ceramics

5.2.1. Powder Analysis

The mean particle size, d_{50}, for the ZrO_2 powder was slightly larger than the supplier's specifications (0.783µm was measured, the supplier stated the size was 0.6µm). The characteristic sizes for the spinel powder from the supplier and the measured values are given in **Table 5.3**.

Table 5.3: Mean particle size for the spinel powder.

	d_{50} (µm)	**d_{90} (µm)**
Particle Size analyser	0.199	1.020
Supplier's specifications	0.15	0.5

The measured d_{50} for the spinel was also slightly larger than what the supplier specified. The measured d_{90} for the spinel powder was much larger than the supplier's specifications. The particle size distributions for both powders were not lognormally distributed. The data were skewed to the larger particle sizes. Therefore, it was concluded that there were agglomerates within the powders. The presence of agglomerates skewed the mean particle sizes to larger overall grain sizes. The presence of agglomerates also explains why the d_{90} for the spinel was much higher than what the supplier specified, **Table 5.3**. The value for the d_{90} would be more sensitive to the presence of agglomerates than the value for the d_{50}.

During the particle size analysis ultrasonic pulses were applied. Also, sodium hexameta-phosphate was added to encourage dispersion. Since the agglomerates were not broken up by the ultrasonic pulses or dispersed by the sodium hexameta-phosphate, it was concluded that the agglomerates were hard agglomerates.

As with the Al_2O_3 and MgO in the transparent samples, the Scherrer equation showed that the crystallite sizes were orders of magnitude smaller than the particle size. The crystallite size for the spinel powder was 25nm and for the ZrO_2 powder it was 27nm. The SEM micrographs of the powders, **Figures 4.44** and **4.45**, show that the ZrO_2 particles are larger than the spinel particles. The ZrO_2 particles shown in **Figure 4.44**, had a size of the same order of magnitude as the particle size analysis. The SEM micrograph of the spinel powder, **Figure 4.45**, shows a

large agglomerate made up of particles that have a size of the same order as calculated by the Scherrer equation.

The SEM micrograph of the mixed powder, **Figure 4.46**, highlights the difference in size between the ZrO_2 and spinel particles. The bright ZrO_2 particles look as if they are embedded in 'fluff' because the spinel particles are so fine.

The XRD spectra for the spinel powder only contained peaks associated with spinel, and the only peaks present in the XRD spectra for the ZrO_2 powder were associated with tetragonal ZrO_2. The EDS analysis for these powders detected only Zr, O, Mg, and Al (besides the coating elements Au and Pd). Therefore, the powders were pure, and the correct phases were present.

5.2.2. Sintering Cycle Analysis

The linear shrinkage decreased from ≈74% to ≈72% as the ZrO_2 content increased from 2 to 30%, **Figure 4.48**. Also, the sintering data shows that the addition of ZrO_2 increased the temperature at which densification began. The temperature at which densification began for the 0wt.%, 2wt.%, 5wt.%, 10wt.%, 20wt.%, and 30wt.% ZrO_2 composites were 940°C, 990°C, 1000°C, 1015°C, 1040°C, and 1080°C, respectively, **Figure 5.12**.

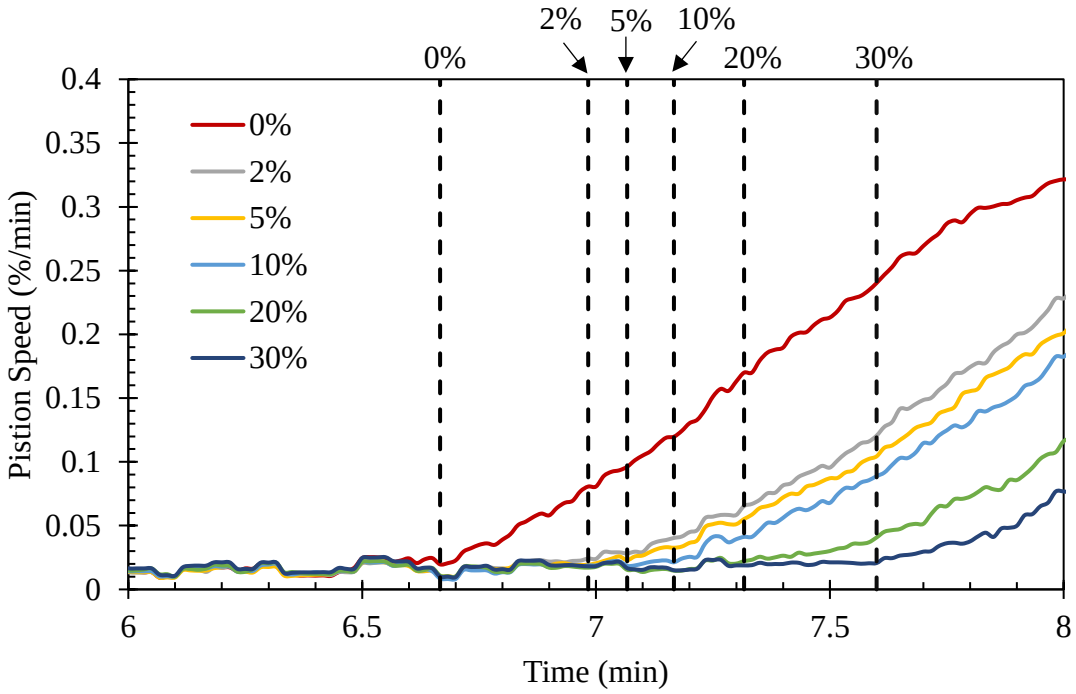


Figure 5.12: Initial increase in densification at different ZrO_2 weight percent, taken from **Figure 4.49**.

This was unexpected as this implies that pure spinel began densification when the temperature was 940°C but spinel in the presence of 30wt.% ZrO_2 only began densification at 1080°C. Therefore, the addition of the ZrO_2 caused the spinel to begin densification about 140°C higher than if no ZrO_2 were present. Even a small addition of ZrO_2 (2wt.%) led to a 50°C increase in the temperature at which densification began. Thus, the zirconia had an effect on the sintering of the spinel. This is shown in **Figure 5.13**. The piston speed for 30wt.% ZrO_2 was determined by adding the weighted sum of the piston speed for pure spinel and pure ZrO_2 (Shown in the **Appendix Figure A.7 pp.195**). This is compared to the measured data for the 30wt.% ZrO_2 in **Figure 5.13**.

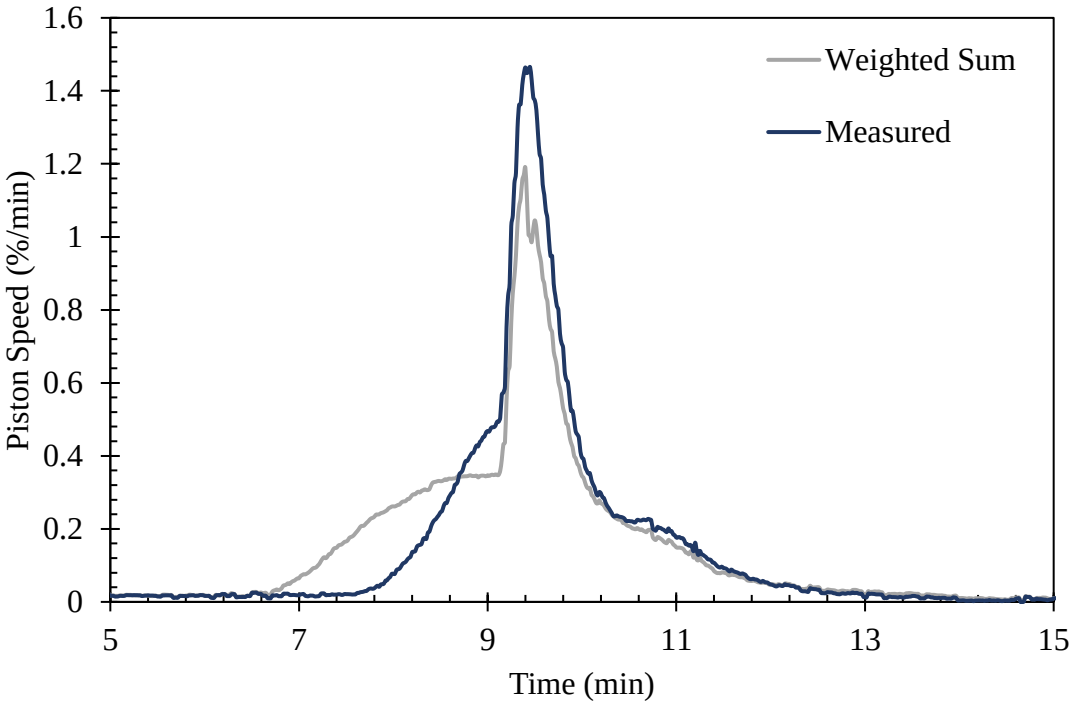


Figure 5.13: Relative piston speed during the SPS sintering cycle for the 30 wt.% ZrO_2. Both the measured speed and the calculated weighted sum speed are shown.

If the ZrO_2 had no effect on the sintering behaviour of the spinel, then the measured peak would have coincided with the weighted sum. These peaks did not overlap, therefore the sintering behaviour of the mixture of the ZrO_2 and $MgAl_2O_4$ was different to the sum of the individual components. Hence, the ZrO_2 must have interacted in some transient way with the spinel during the initial stages of the sintering cycle.

Another observed effect that the ZrO_2 had on the sintering of spinel was the increase in relative density as the ZrO_2 content increased from 0 to 10wt.%. Further additions of ZrO_2 led to a slight decrease in the relative density, **Figure 4.51**. Ganesh & Ferreira (2009) also noted that small additions of ZrO_2 to spinel improved the relative density of the ceramic, whereafter further additions decreased it. However, this conflicts with Quenard et al. (2000), who found no correlation between the amount of zirconia and the relative density.

Oddly, the relative density increased as the ZrO_2 content increased from 2 to 10wt.% but the linear shrinkage decreased in this ZrO_2 weight percent range. This indicated that the spinel powder was in a less dense state than the ZrO_2 powder. This was surprising as both the crystallite size and the mean particle size for the spinel were less than that of the ZrO_2. Therefore, the extent of agglomeration must have been higher in the spinel powder, which was what the SEM micrographs in **Figures 4.44** and **4.45** indicated. The extremely fine spinel powder tended to agglomerate to a greater degree than the ZrO_2 powder. The greater presence of the agglomerates lowered the packing efficiency of the spinel powder. Thus, even though the linear shrinkage of the pure spinel samples were greater than the 10wt.% ZrO_2 samples, their relative density was less.

5.2.3. Sintered Sample Analysis

The relative densities were close to unity, this indicated that the compositions of the samples were what was nominally stated. It follows that the majority of the ZrO_2 was still in the tetragonal phase. If it had transformed to the less dense monoclinic phase the densities would be lower. Not only because of the lower density of the monoclinic phase but also because of the microcracking which would result from the tetragonal to monoclinic transformation. Mohan & Sarkar, (2016) found that the formation of these cracks reduced density. As the relative densities were all >99.5%, the majority of ZrO_2 should be in the tetragonal phase. If it had been the case that 25% of the ZrO_2 transformed to the monoclinic phase upon cooling, the measured density of the 30wt.% ZrO_2 sample would be greater than its theoretical density. This would not be possible. Therefore, the density data indicated that the majority of the ZrO_2 was in the tetragonal phase.

The XRD spectra of the composites confirms what the density data showed. The XRD spectra had peaks that corresponded to the sum of the $MgAl_2O_4$ spinel spectra and the tetragonal-ZrO_2 spectra, **Figure 4.52**. Thus, the tetragonal-ZrO_2 was retained after sintering. The only two

phases present were $MgAl_2O_4$ spinel and tetragonal-ZrO_2. Therefore, whatever influence the ZrO_2 had on the sinterability of spinel did not result in a change in the phases.

In **Figure 4.53** backscattered images of an etched surface for the 2wt.%, 5wt.%, 10wt.%, 20wt.%, and 30wt.% ZrO_2 composites are shown. The ZrO_2 appears white as the Zr atoms have a higher atomic mass (91u for Zr compared to 24u for Mg and 27u for Al). The higher atomic mass enabled a greater number of electrons to be backscattered, thus increasing the brightness of ZrO_2 compared to $MgAl_2O_4$. The backscattered images show that the ZrO_2 was well dispersed in the composites, however, there are larger particles in the 20wt.% and 30wt.% composites.

The larger ZrO_2 particles found within the 20wt.% and 30wt.% composites were observed to be composed of a number of ZrO_2 grains. These particles are likely the result of agglomerated or aggregated crystallites that did not separate during milling. The presence of these agglomerates/aggregates was confirmed by the particle size analysis of the ZrO_2 powder.

The SEM micrographs of the etched surfaces show that the etched topography of the spinel grains changed as the ZrO_2 content increased, **Figure 4.56**. This was further evidence that the addition of ZrO_2 had a more pronounced effect on the spinel than simply being present in the microstructure. The grain boundaries were more resistant to the thermal etching, and as such became harder to distinguish. This issue was significant in the 30wt.% ZrO_2 shown in **Figure 4.56,** where the grain boundaries were indistinguishable from the topography of the spinel grains. Quenard, et al. (2000) also reported difficulty in chemically etching spinel which had similar additions of ZrO_2, even after numerous attempts.

The increased resistance to thermal etching and the increase in temperature required for densification to begin indicates that the addition of ZrO_2 to spinel improves its thermal properties. This would be a favourable property for spinel used in refractory applications.

5.2.4. Microstructure

Compared to the LiF-doped spinel, the grain structure of the composites was more homogeneous. Therefore, all the methods used to determine the average grain size produced similar values, **Table 4.13**. Also, the standard deviations are relatively lower than those for the transparent spinel, which was a further indication of a more homogeneous grain structure. Once

again, the standard deviations do not indicate the uncertainty in the measurements, rather the standard deviations are an indication of the distribution of grain sizes.

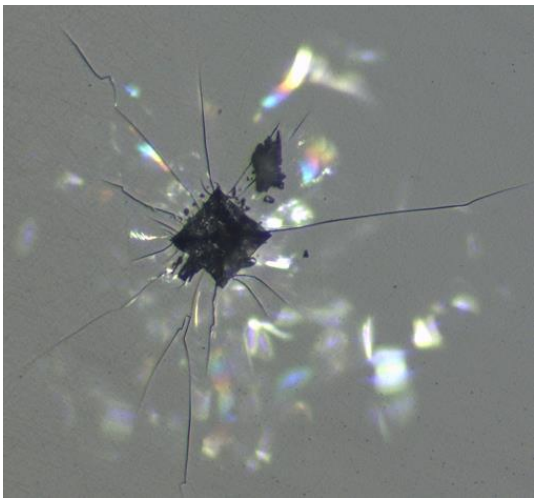
The mean grain size decreased as the ZrO_2 content increased, **Figure 4.68**. Quenard, et al. (2000) also found that the presence of ZrO_2 grains inhibited the growth of the spinel grains. By increasing the ZrO_2 content, the interfacial surface area shared between grains of the same composition was reduced, thus lowering the extent of diffusion and therefore grain growth. In pure spinel, all grains are surrounded by other spinel grains, thus the surface area for diffusion would be the same as the contact area of the grain. When ZrO_2 was added to the composite, the interfacial area between the spinel and ZrO_2 would not be applicable for diffusion, therefore the average surface area available for diffusion would be less than the contact area. This could explain why the addition of ZrO_2 decreased the average grain size of the composites.

However, this mechanism could not be the only reason for the decrease in grain size. If it were, the addition of 2wt.% ZrO_2 would not result in such a significant decrease in grain size, **Figure 4.68**. Mohan & Sarkar (2016) also observed a decrease in grain size as the ZrO_2 content increased. They concluded that the zirconia acted as a barrier for grain boundary migration by pinning the grain boundaries thereby reducing grain growth which led to a finer microstructure. Their mechanism was consistent with the results of this work. The decrease in average grain size was an unexpected but welcomed result, as this should improve the mechanical properties of the composite.

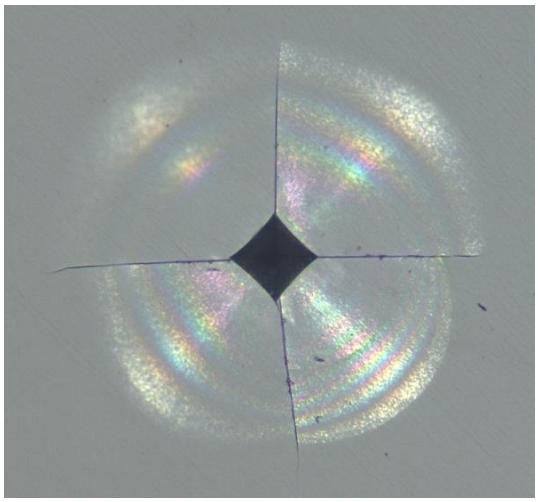
The suspicion that the large grain size of the transparent spinel resulted in spalling and numerous auxiliary cracks during indentation was confirmed, **Figure 5.14**. Both samples' indents shown in **Figure 5.14** were made on 100% spinel, however, the Grain Sizes (GS) differ by 3 orders of magnitude. The one sample was that of the transparent spinel, the other sample was that from the $MgAl_2O_4$ - ZrO_2 composites (0wt.% ZrO_2).

The indents on the spinel sample with a $GS \ll c_0$ (c_0 is the crack length) resulted in clear cracks, originating from the corners of the indent. Whereas, when the $GS \approx c_0$, there were multiple cracks and spalling occurred. This agrees with the work done by Anstis, et al. (1980), who observed that when the crack length was similar to the grain size, local disruptions occurred which likely impacted the measurement. Therefore, the fracture toughness measurements for the DZC can be assumed to be reliable, whereas the measurements for the

transparent spinel need to be authenticated by another method such as the single edge notched beam method (Wang & Atkinson, 2015).



Transparent spinel
Grain size ≈ 236µm



$MgAl_2O_4$ - ZrO_2 composites (0wt.% ZrO_2)
Grain size ≈ 0.264µm

Figure 5.14: Vickers indent on spinel samples.

As expected, the addition of ZrO_2 did improve the mechanical properties of the spinel. The hardness increased from 13.5GPa to 15.1GPa and the fracture toughness increased from 1.40MPa.$m^{0.5}$ to 2.13MPa.$m^{0.5}$. However, the increase in the fracture toughness of these composites was less than expected. In **Figures 5.15** and **5.16** the hardness and fracture toughness are compared to results found in literature. The grain sizes of the samples produced by Quenard, et al. (2000) are given in **Table 2.7 (pp. 55)**. Ganesh and Ferreira (2009) did not describe the grain size of their samples quantitatively.

The hardness of the samples was similar to those found in literature, **Figure 5.16**, but the fracture toughness was almost 3 times less than the value measured by other authors at 30wt.% ZrO_2, **Figure 5.15**. This would seem to indicate that the majority of the tetragonal-ZrO_2 grains did not transform to the monoclinic phase when in the presence of a tensile stress field ahead of a propagating crack i.e. transformation toughening did not occur to a substantial degree within these samples.

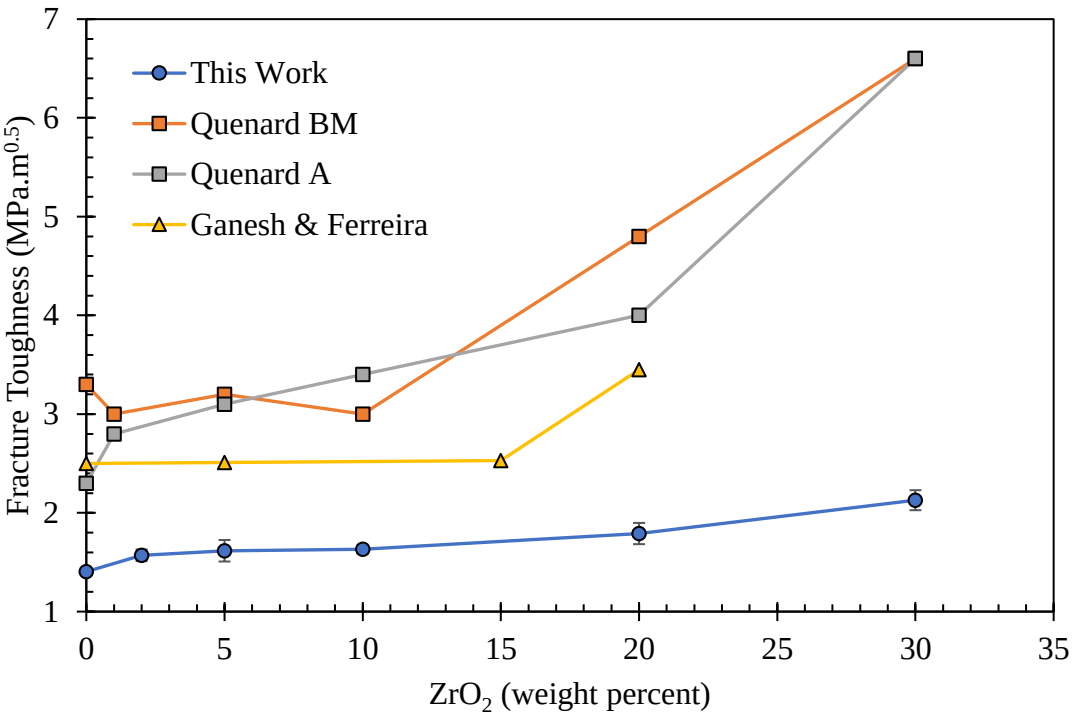


Figure 5.15: Fracture toughness as a function of ZrO_2 wt.% including data from Quenard, et al. (2000) and Ganesh & Ferreira, (2009).

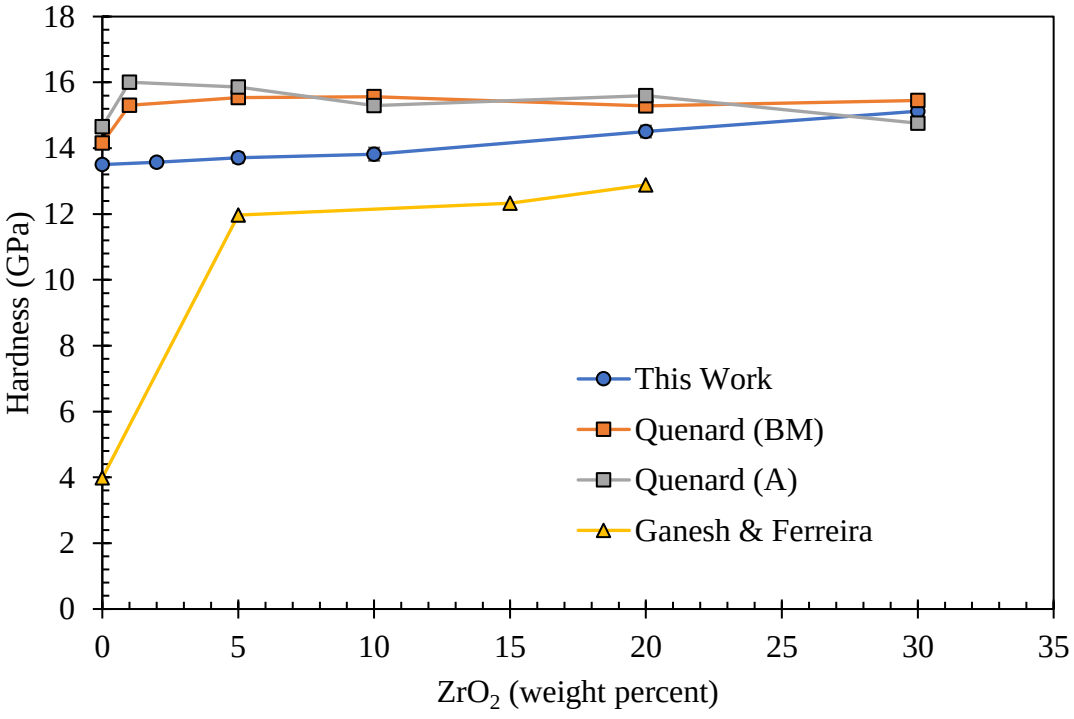


Figure 5.16: Hardness as a function of ZrO_2 wt. % including data from Quenard, et al. (2000) and Ganesh & Ferreira, (2009).

The reduction in grain size caused by the addition of the ZrO_2 to the spinel matrix would likely cause an increase in hardness and strength, as described by the Hall-Petch relation. However, the effect of grain refinement on the fracture toughness of ceramics is unfortunately not as straight forward. It has been observed that the fracture toughness for non-cubic ceramics has a maxima at a certain grain size (Rice, 1996). For cubic materials, such as spinel, the fracture toughness maxima is usually less pronounced, and in a few cases the fracture toughness decreases with an increase in grain size or no dependence on grain size is observed (Rice, 1996).

The ambiguity surrounding the effect of grain size on the fracture toughness of ceramics makes it difficult to assess the cause of the slight increase of the fracture toughness the addition of the ZrO_2 had on the spinel. It is unclear whether the grain refinement caused by the ZrO_2 could have caused the increase in fracture toughness of the composites or if a small fraction of relatively large ZrO_2 grains did transform. The fracture toughness of the samples for this work correlates well (R=0.9876) with the Hall-Petch relation, **Figure 5.17**. However, this was likely coincidental.

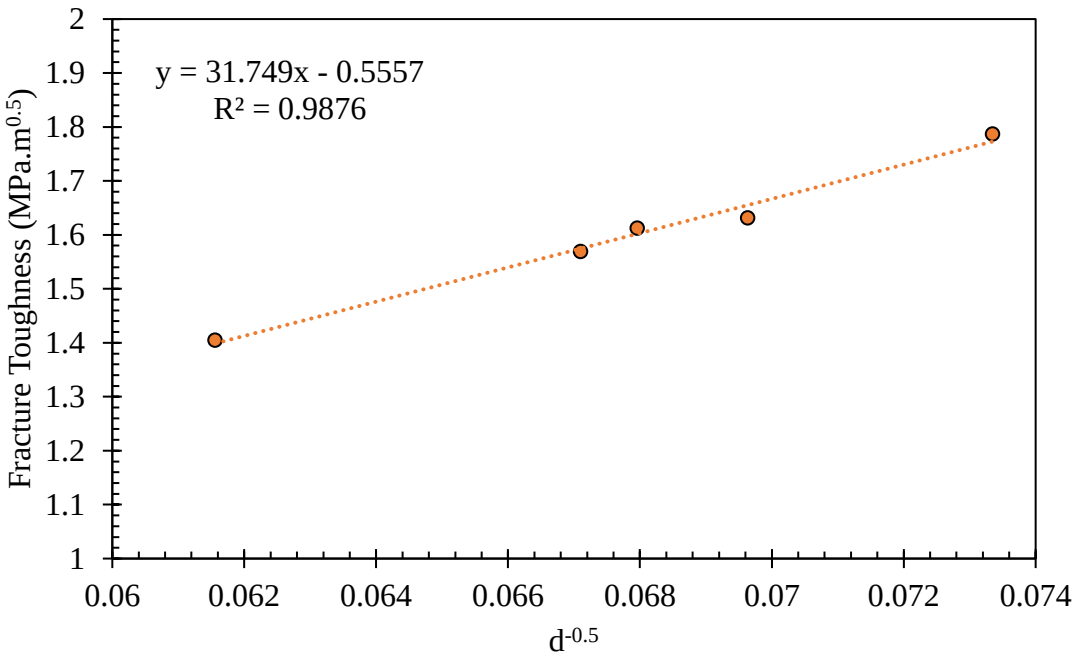


Figure 5.17: Fracture toughness as a function of $d^{-0.5}$, showing the fit to the Hall-Petch relation.

Regardless of which mechanism was dominant, the increase in fracture toughness was not as significant as expected. Therefore, a majority of the tetragonal zirconia grains were over stabilised. This observation is further supported by the fact that Quenard, et al. (2000) used undoped zirconia (which would encourage the transformation to the monoclinic phase) and achieved a much higher increase in fracture toughness, **Figure 5.15**.

For the transformation to not occur, the tetragonal-ZrO_2 must have been too stable. If the tetragonal-ZrO_2 was over stabilised, then the stress required to induce the transformation would be higher than the stress required to cause crack formation and propagation within the ceramic composite. Therefore, the composite would fail prior to the ZrO_2 transformation. The reason for this over stabilisation can be elucidated by **Equation 5.7**, which was derived in **Section 2.2.4.5. Stress Induced Transformation pp. 49**.

$$\sigma_C^T = \frac{\left(\frac{1}{2}\left(\sigma_{ij}^l \pm \sigma_{ij}^r\right)\left(\varepsilon_{ij}^t \pm \varepsilon_{ij}^r\right)\right) + \left(\frac{6(\gamma_m - \not{g}_s\gamma_t)}{D}\right) + \left(\Delta S_{t\rightarrow m}(T_A - T)\right)}{\varepsilon^T} \quad \textbf{Equation 5.7}$$

The required critical stress to cause the tetragonal to monoclinic transformation is increased by Y_2O_3 addition, grain size reduction and the elastic properties of the constraining matrix. The factors which stabilised the tetragonal-ZrO_2 (thus increasing the critical stress) in this work were the small grain sizes of ~220nm, the addition of 3mol% Y_2O_3 to the ZrO_2, and the higher Young's modulus of the $MgAl_2O_4$ than the ZrO_2. The factors that would have favoured the transformation (thus reducing the critical stress) were the lower thermal expansion coefficient of spinel compared to ZrO_2 and the room temperature testing. The combination of the stabilising factors must have outweighed the combination of the transformation favouring factors to such an extent that the resultant critical stress was too large for the ceramic composite to resist without fracturing.

As this research was aiming to assist in the development of better spinel refractories, this result was even more damning. At higher temperatures, the tetragonal phase is more stable than at lower temperatures. Therefore, had these ceramics been used as refractories, the high operating temperatures would further stabilise the tetragonal-ZrO_2. This would increase the required stress even more.

In order to ensure that the required stress is reached ahead of the crack-tip, the critical stress must be lowered to a value that is less than the stress required to cause a crack to propagate in

the spinel. This can be achieved by either reducing the Y_2O_3 additions or by increasing the size of the tetragonal grains. As finer grains lead to improved mechanical properties, the first step should be to reduce the Y_2O_3 content. If this still does not result in the transformation, then the ZrO_2 grains sizes should be increased.

The decrease in grain size caused by the zirconia addition does not fully explain the increase in hardness, **Figure 5.18**. The fit to the Hall-Perch relation was not particularly good, R=0.7447. The data does not follow a straight line as it should if the Hall-Petch relation was to be conformed to, **Figure 5.19**.

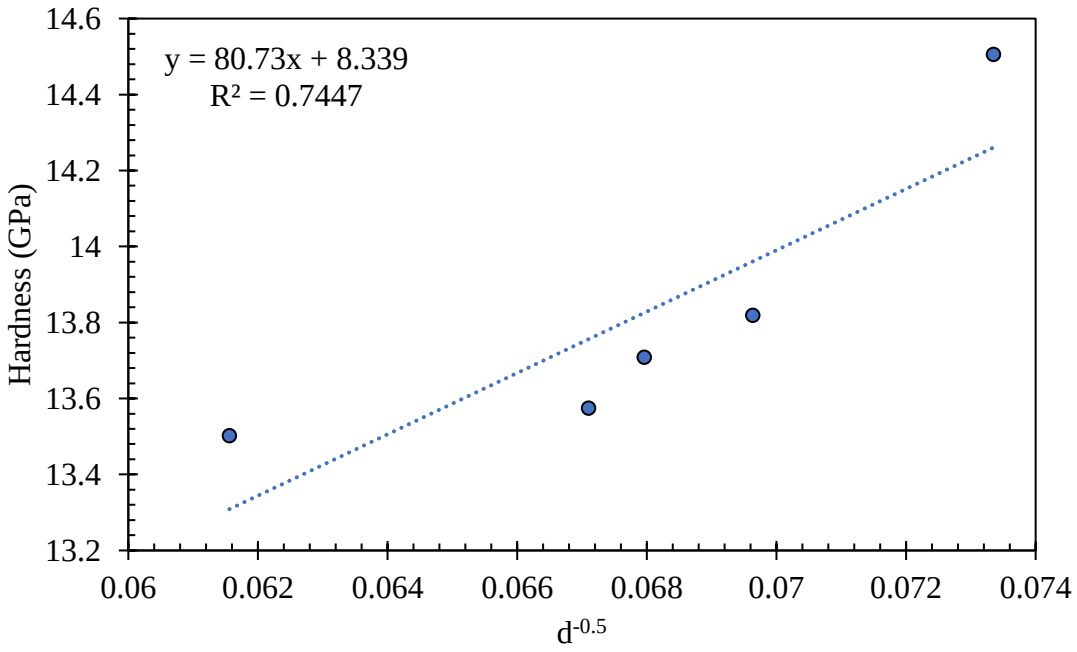


Figure 5.18: Hardness as a function of $d^{-0.5}$, showing the linear fit to the Hall-Petch relation.

As the Hall-Petch relation did not satisfactorily explain the increase in hardness, grain refinement could not have been the only strengthening mechanism that was present. Quenard, et al. (2000) stated that the increase in hardness could be explained by the presence of ZrO_2 particles at grain junctions. The ZrO_2 particles could minimize the matrix grain slide, even for low amounts of ZrO_2, thus increasing hardness. Another strengthen mechanism that was likely to occur was crack deflection. Crack deflection would be caused by the difference in elastic modulus between the spinel matrix and ZrO_2 inclusions (Kelly & Denry, 2008).

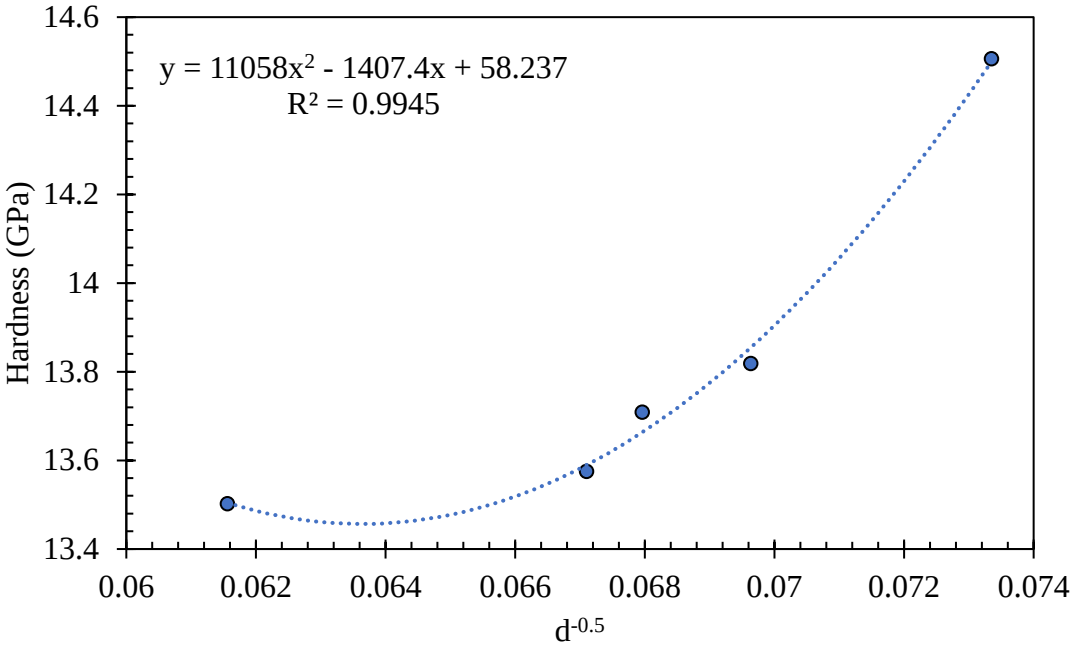


Figure 5.19: Hardness as a function of $d^{-0.5}$, showing a quadratic fit.

The addition of ZrO_2 also increased both the nominal strength and specific strength up to 10wt.% ZrO_2, further additions lowered the strength slightly, **Figure 4.85**. As with hardness, the nominal strength did not follow the Hall-Petch relation, **Figure 5.20**. Further indicating that multiple strengthening mechanisms were active.

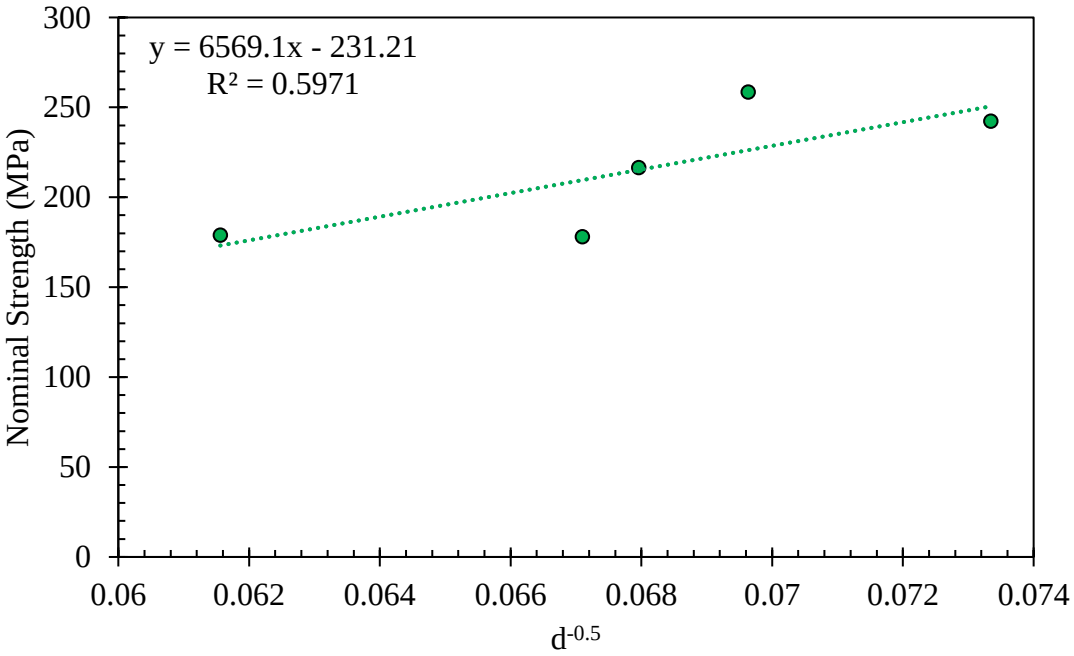


Figure 5.20: Strength as a function of $d^{-0.5}$, showing the linear fit to the Hall-Petch relation.

One surprising result was the effect the addition of the ZrO_2 had on the Weibull modulus of the ceramic materials. The Weibull modulus increased from 3.90 to 10.15 as the ZrO_2 wt.% increased from 2wt.% to 30wt.%, **Table 4.18**. However, the initial addition of ZrO_2 reduced the Weibull modulus from 6.96 (for the 0wt.% ZrO_2) to 3.90 (for the 2wt.% ZrO_2). The increase in the Weibull modulus could be explained if transformation toughening did occur. The process for making the DZC was the same for all samples regardless of the ZrO_2 wt.% additions. The only difference was the relative amount of each powder used.

It has been observed that using powders with a mix of relatively large particles and small particles may increase the density of the component, but it also increases the size of the flaws, even if the total flaw volume decreases (Amor´os, et al., 2007). This could explain the large decrease in Weibull moduli from the 0% to the 2%. The addition of the relatively large ZrO_2 particles caused an increase in the probability of large pores forming within the ceramic body. As a ceramic's strength is greatly influenced by the largest pore size, the greater probability of a large pore forming could cause a greater spread in strengths, thus a lower Weibull modulus.

Further additions of ZrO_2 led to the gradual increase of Weibull moduli even though the further addition of ZrO_2 should have led to a greater prevalence of larger flaws. This would indicate that a mechanism that would lower the spread of strength was active.

It has been shown that transformation toughened ceramics are more damage tolerant (Kelly & Denry, 2008). The strengths of specimens that have Vickers-indented surfaces have been observed to be equal to specimens with polished-surfaces (Kelly & Denry, 2008). If the zirconia toughened ceramics are more damage tolerant, their strengths are less sensitive to the size of the flaws within the ceramics body. Therefore, even though the distribution of flaw sizes within each weight category was likely similar, as the ZrO_2 content increased, the impact of the size of the flaws decreased because of the increase in damage tolerance associated with zirconia toughened ceramics. Thus, the spread of the fracture stresses narrowed, which led to an increase in the Weibull modulus.

The mechanical properties of the DZC were not consistent with any one toughening mechanism. This indicated that the effect of the addition of ZrO_2 on spinel was more complicated than was originally thought. It is likely that multiple strengthening mechanisms occurred simultaneously preventing a quantitative agreement to any single mechanism. However, what was clear, was that the addition of ZrO_2 did improve the mechanical properties

of spinel. The mechanisms that were likely to have occurred are grain refinement, transformation toughening (but not to the desired degree), and crack deflection (Kelly & Denry, 2008).

Chapter 6: Conclusions

6.1. Transparent Spinel

The fabrication of a transparent spinel disk using an SPS furnace and the sintering aid LiF in a single stage sintering process did achieve a transmission of visible light of ≈70%.

When using Al_2O_3 and MgO as starting materials in conjunction with a single stage sintering process the reactive sintering that results causes a volume expansion of 7.67%. This expansion caused the generation of internal stresses that led to the formation of cracks.

The residual porosity contributed to the decrease in transmission.

The addition of LiF and the long sintering times resulted in a heterogenous microstructure which could not easily be quantified.

The mechanical properties of the spinel fabricated in this work were inferior to those given in literature. However, the transmission was higher when compared to other single stage sintering processes.

Even though the mechanical properties were relatively low, they were still higher than the reported mechanical properties of glass. This indicates that spinel would be an appropriate substitute for glass.

The large spread of fracture strengths would preclude this material's use as a material for transparent armour or window systems in space craft due to its stochastic failure probability.

This work confirms that spinel does have the potential to replace fused silica windows once better fabrication techniques are developed that result in a more consistent product.

6.2. Dispersed Zirconia Ceramics

Tetragonal zirconia was retained to room temperature within the sintered ceramic. However, this zirconia was over-stabilised, thus the expected increase in fracture toughness was not realised.

There was an improvement in all measured mechanical properties by the addition of ZrO_2 up until 10wt.% ZrO_2. Further additions improved the hardness and fracture toughness, but the nominal strength decreased slightly.

Adding ZrO_2 improved the Weibull modulus of the samples. This indicated that there was a fraction of ZrO_2 grains that did undergo the tetragonal to monoclinic transformation. Ceramics that undergo transformation toughening are more damage tolerant.

No single strengthening mechanism could sufficiently explain the improvement in the various mechanical properties. Thus, it was inferred that numerous strengthening mechanisms occurred. The strengthening mechanisms that were identified were transformation toughening, grain refinement and crack deflection.

The addition of ZrO_2 did improve the hardness (from 13.5GPa to 15.1GPa), fracture toughness (from 1.40MPa.$m^{1/2}$ to 2.13MPa.$m^{1/2}$) and biaxial flexural strength (from 179MPa to a maximum of 259MPa at 10wt.% ZrO_2) of the spinel and, it also seems to improve the thermal stability of the spinel.

Chapter 7: Future Work

7.1. Transparent Spinel:

The extremely low level of porosity required coupled with the required purity necessitates that more advanced powder processing is done prior to sintering. The powder processing must be streamlined to ensure a uniform distribution of pore size, prevent re-agglomeration of the powders during the dry process, and reduce the prevalence of aggregates.

More attention should be given to quantifying the heterogenous grain structure that results from the addition of LiF. A majority of the literature simply gives the mean grain size when quantifying the microstructure, without regard for the distribution of the grain sizes.

The current sintering profile still needs adjustments. Based on the results of this work, a new sintering profile is suggested, **Figure 7.1**.

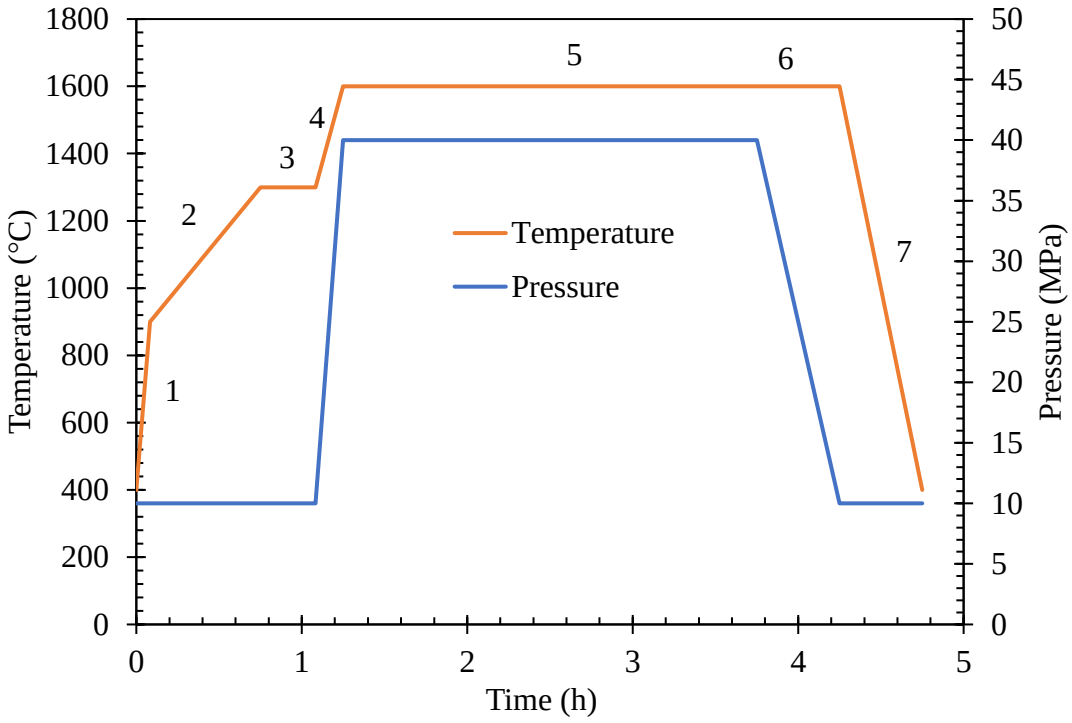


Figure 7.1: Potential sintering profile for transparent spinel for a spark plasma sintering furnace.

The temperature is rapidly increased to 900°C to melt the LiF (1). The heating rate reduces 40°C/min to give the LiF time interact with the powders (2). The temperature continues to

increase until 1300°C, where it is held for 20 minutes (3). This is to ensure all LiF has evaporated out of the system prior to the application of pressure. Then the temperature and pressure are increased to 1600°C and 40MPa (4). The sintering temperature will be held for 3 hours (5 + 6), but the pressure will only be held at 40MPa for 2.5 hours (5). The pressure is released 30 minutes prior to cooling to reduce the prevalence of the damaged areas (6). Then the temperature is cooled to room temperature (7).

7.2. Dispersed Zirconia Ceramic Composites

If the addition of ZrO_2 does improve the high temperature properties of spinel, it could be a vitally important discovery. Therefore, high temperature studies need to be conducted to determine if this phenomenon can be verified.

The numerous strengthening mechanisms that the ZrO_2 additions engender, add a layer of complexity to the system. A tool that might assist in the understanding of the $MgAl_2O_4 – ZrO_2$ system are artificial neural networks. If an artificial network can be 'trained' correctly, it could be able to determine which microstructures would enable the maximisation of the transformability of the ZrO_2 and thus the maximisation of the mechanical properties.

References

Agency for Toxic Substances & Disease Registry, 2013. *Chromium Toxicity What are the Physiologic Effects of Chromium Exposure?*. [Online] Available at: https://www.atsdr.cdc.gov/csem/csem.asp?csem=10&po=10 [Accessed 20 03 2020].

Akman, F., Khattari, Z., Kacal, M., Sayyed, M., Afaneh, F., 2019. The Radiation Shielding Features of Some Silicide, Boride and Oxide Types Ceramics. *Radiation Physics and Chemisty* , Volume 160, pp. 9-14.

Aksel, C., 2004. Spinel Formation, Reaction Conditions and Densification Properties of Magnesia-Spinel Composites. *Key Engineering Materials*, Volume 264-268, pp. 1071-1074.

Albers, A., Arslan, A. & Mitariu, M., 2005. Clutches Using Engineering Ceramics as Friction Material. *Materialwissenschaft und Werkstofftechnik,* 36(3), pp. 102-107.

Amor´os, J., Orts, M., Garc´ıa-Ten, J., Gozalbo, A., S´anchez, E., 2007. Effect of the Green Porous Texture on Porcelain Tile Properties. *Journal of the European Ceramic Society*, Issue 27, pp. 2295-2301.

Anstis, G. R., Chantikul, P., Lawn, B. R. & Marshall, a. D. B., 1980. A Critical Evaluation of Indentation Techniques for Measuring Fracture Toughness: I, Direct Crack Measurements. *Journal of the American Ceramic Society*, 64(9), pp. 533-538.

Astro Met Inc., n.d. *ZTA-96 Zirconia Toughened Alumina Ceramic.* [Online] Available at: https://www.astromet.com/zirconia-alumina-zta96.htm [Accessed 09 11 2020].

Balakrishnan, A., Pizette, P., Martin, C., Joshi, S., Saha, B., 2010. Effect of Particle Size in Aggregated and Agglomerated Ceramic Powders. *Acta Materialia,* 58(3), pp. 802-812.

Basu, B., 2005. Toughening of Yttria-Stabilised Tetragonal Zirconia Ceramics. *International Materials Review*, 50(4), pp. 239-256.

Becher, P. F. & Swain, M. V., 1992. Grain-Size-Dependent Transformation Behavior in Polycrstalline Tetragonal Zirconia. *Journal of the American Ceramic Society*, 75(3), pp. 493-502.

Benitez, T, Gomez, S., Oliveira, A., Travitzky, N., Hotza, D., 2017. Transparent Ceramic and Glass-Ceramic Materials for Armor Applications. *Ceramics International,* 43(16), pp. 13031-13046.

Berbenni, S., Favier, V. & Berveiller, M., 2007. Impact of the Grain Size Distribution on the Yield Stress of Heterogeneous Materials. *International Journal of Plasticity,* 23(1), pp. 114-142.

Bonnefont, G., Fantozzi, G., Trombert, S. & Bonneau, L., 2012. Fine-Grained Transparent MgAl2O4 Spinel Obtained by Spark Plasma Sintering of Commercially Available Nanopowders. *Ceramics International,* 38(1), pp. 131-140.

Borger, A., Supancic, P. & Danzer, R., 2002. The Ball on Three Balls Test for Strength Testing of Brittle Discs: Stress Distribution in the Disc. *Journal of the European Ceramic Society,* 22(9), pp. 1425-1436.

Bourkas, G., Prassianakis, I., Kytopoulos, V., Sideridis, E., Younis, C., 2010. Determination of Elastic Moduli of Particulate Composites by New Models and Comparison with Moduli Measured by Tension, Dynamic, and Ultrasonic Tests. *Hindawi: Advances in Materials Science and Engineering,* Volume 2010, pp. 1-13.

Cao, X. Q., Vassen, R. & Stoever, D., 2004. Ceramic Materials for Thermal Barrier Coatings. *Journal of the European Ceramic Society,* 24(1), pp. 1-10.

Ceylantekin, R. & Aksel, C., 2012. Improvements on the Mechanical Properties and Thermal Shock Behaviours of MgO-Spinel Composite Refractories by ZrO_2 Incorporation. *Ceramics International,* 38(2), pp. 995-1002.

Cohen, S., Ratzker, B., Sokol, Max., Kalabukhov, S., Frage, N., 2018. Polycrystalline Transparent Magnesium Aluminate Spinel Processed by a Combination of Spark Plasma Sintering (SPS) and Hot Isostatic Pressing (HIP). *Journal of the European Ceramic Society,* 38(15), pp. 5153-5159.

Danzer, R., Supancic, P., Pascual, J. & Lube, T., 2007. Fracture Statistics of Ceramics - Weibull Statistics and Deviations from Weibull Statistics. *Engineering Fracture Mechanics,* 74(18), pp. 2919-2932.

Denry, I. & Holloway, J. A., 2010 . Ceramics for Dental Applications: A Review. *Materials,* Volume 3, pp. 351-368.

Duwez, P., Brown, F. H. & Odell, F., 1951. The Zirconia-Yttria System. *Journal of the Electrochemical Society,* 98(9), pp. 356-362.

Esposito, L., Piancastelli, A. & Martelli, S., 2013. Production and Characterization of Transparent $MgAl_2O_4$ Prepared by Hot Pressing. *Journal of the European Ceramic Society,* 33(4), pp. 737-747.

Esposito, L., Piancastelli, A., Miceli, P. & Martelli, S., 2015. A Thermodynamic Approach to Obtaining Transparent Spinel ($MgAl_2O_4$) by Hot Pressing. *Journal of the European Ceramic Society* , 35(2), pp. 651-661.

Exare, C., Kiat, J. M., Guiblin, N. & Petricek, V., 2016. Mechanical Properties of ZTA: Correlation with Structural Properties and Influence of Ageing. *Hindawai: Journal of Ceramics,* pp. 1-7.

Fergus, J. W., 2010. Ceramic and Polymeric Solid Electrolytes for Lithium-ion Batteries. *Journal of Power Sources* , Volume 195, pp. 4554-4569.

Frage, N., Cohen, S., Meir, S., Kalabukhov, S., Dariel, M., 2007. Spark Plasma Sintering (SPS) of Transparent Magnesium-Aluminate Spinel. *Journal of Materials Science,* Volume 42, pp. 3273-3275.

Gallo, L., Boas, V., Rodrigues, A., Melo, F., Zanotto, E., 2019. Transparent Glass-Ceramics for Ballistic Protection: Materials and Challenges. *Journal of Materials Research and Technology,* 8(3), pp. 3357-3372.

Ganesh, I., 2013. A Review on Magnesium Aluminate (MgAl2O4) Spinel: Synthesis, Processing and Applications. *International MAterials Reviews* , 58(2), pp. 63-112.

Ganesh, I. & Ferreira, J., 2009. Synthesis and Characterization of $MgAl_2O_4$-ZrO_2 Composites. *Ceramics International,* 35(1), pp. 259-264.

Garvie, R. C., Hannink, R. H. & Pascoe, R. T., 1975. Ceramic Steel?. *Nature,* Volume 258, pp. 703-704.

Ghasemi, A. & Zahediasl, S., 2012. Normality Tests for Statistical Analysis: A Guide for Non-Statistians. *International Journal of Endocrinology & Metabolism,* 10(2), pp. 486-489.

Ghosh, A., White, K., Jenkins, M., Kobayashi, A., Bradt, C., 1991. Fracture Resistance of a Transparent Magnesium Aluminate Spinel. *Journal of the American Ceramic Society,* 74(7), pp. 1624-1630.

Goldstein, A., 2012. Correlation Between $MgAl_2O_4$ Spinel Structure, Processing Factors and Functional Properties of Transparent Parts (Progress Review). *Journal of the European Ceramic Society,* 32(11), pp. 2869-2886.

Goldstein, A. & Krell, A., 2016. Transparent Ceramics at 50: Progress Made and Further Prospects. *Journal of the American Ceramic Society,* 99(10), pp. 3173-3197.

Gooch, W. A., 2004. *An Overview of Ceramic Armor Applications.* Trenčín, U.S. Army Research Laboratory.

Graeve, O. A., 2008. Chapter 10: Zirconia. In: J. F. Shackelford & R. H. Doremus, eds. *Ceramic and Glass Materials: Structure, Properties and Processing.* New York: Springer , pp. 176-186.

Hallstedt, B., 1992. Thermodynamic Assessment of the System $MgO\text{-}Al_2O_3$. *Journal of the American Ceramic Society,* 75(6), pp. 1497-1507.

Hand, R. J. & Tadjiev, D. R., 2010. Mechanical Properties of Silicate Glasses as a Function of Composition. *Journal of Non-Crystalline Solids,* Volume 356, pp. 2417-2423.

Hannink, R. H. J., Kelly, P. M. & Muddle, B. C., 2000. Transformation Toughening in Zirconia-Containing Ceramics. *Journal of the American Ceramic Society,* 83(3), pp. 461-487.

Harrer, W., Danzer, R., Supancic, P. & Lube, T., 2008. *The Ball on Three Balls Test: Strength Testing of Specimens of Different Sizes and Geometries.*. Baden-Baden, European Ceramic Society.

Harris, D., 1999. *Materials for Infrared Windows and Domes: Properties and Performance.* Bellingham: SPIE Optical Engineering Press.

Harris, D. & Turri, G., 2013. Optical and Thermal Properties of Spinel with Revised (Increased) Absorption at 4 to 5μm Wavelengths and Comparison with Sapphire. *Optical Engineering* , 52(8), pp. 087113-1 - 087113-12.

Hosseini, S. M., 2008. Structural, Electronic and Optical Properties of Spinel $MgAl_2O_4$ Oxide. *Physica Status Solidi (b),* 245(12), pp. 2800-2807.

Huang, J.-L. & Sun, S.-Y., 1997. Investigation of High-Alumina Spinel: Effect of LiF and $CaCO_3$ Addition. *Journal of the American Ceramic Society,* 80(12), pp. 3237-3241.

Huijsmans, J. P. P., 2001. Ceramics in Solid Oxide Fuel Cells. *Solid State and Material Science* , Volume 5, pp. 317-323.

Insaco Inc., 2020. *Zirconia Toughened Alumina (ZTA).* [Online] Available at: https://www.insaco.com/materials/aluminum-oxides/alumina-zta [Accessed 09 11 2020].

Ishii, M., Hiraishi, J. & Yamanaka, T., 1982. Structure and Lattice Vibrations of Mg-Al Spinel Solid Solution. *Physics and Chemistry of Minerals,* Volume 8, pp. 64-68.

Kashii, N., Maekawa, H. & Hinatsu, Y., 1999. Dynamics of the Cation Mixing of $MgAl_2O_4$ and $ZnAl_2O_4$ Spinel. *Journal of the American Ceramic Society* , 82(7), pp. 1844-1848.

Kelly, J. R. & Denry, I., 2008. Stabilized Zirconia as a Structural Ceramic: An Overview. *Dental Materials,* 24(3), pp. 289-298.

Klein, C. A., 2009. Characteristic Strength, Weibull Modulus, and Failure Probability of Fused Silica Glass. *Optical Engineering,* 48(11), pp. 113401-1 - 113401-10.

Klocek, P., 1991. *Handbook of Infrared Optical Materials.* 1st ed. New York: Marcel Dekker.

Krell, A., Hutzler, T. & Klimke, J., 2009. Transmission Physics and Consequences for Materials Selection, Manufacturing, and Applications. *Journal of the European Ceramic Society,* 29(2), pp. 207-221.

Krell, A., Klimke, J. & Hutzler, T., 2009. Transparent Compact Ceramics: Inherent Physical Issues. *Optical Materials,* 31(8), pp. 1144-1150.

Kurkjian, C. R., Gupta, P. K. & Brow, R. K., 2010. The Strength of silicate Glasses: What Do We Know, What Do We Need to Know?. *International Journal of Applied Glass Science,* 1(1), pp. 27-37.

Lange, F. F., 1982. Transformation Toughening Part 1 SIze Effects Associated with the Thermodynamics of Constrained Transformations. *Journal of Materials Science,* Volume 17, pp. 225-234.

Langford, J. I. & Wilson, A. J. C., 1978. Scherrer after Sixty Years: A Survey and Some New Results in the Determination of Crystallite Size. *Journal of Applied Crystallography* , 11(2), pp. 102-113.

Li, P., Chen, I.-W. & Penner-Hahn, J. E., 1993. X-Ray-Absorption Studies of Zirconia Polymorphs. II. Effect of Y_2O_3 dopant on ZrO_2 Structure. *Physical Review B,* 48(14), pp. 10 074-10 081.

Li, P., Chen, I.-W. & Penner-Hahn, J. E., 1994. Effect of Dopants on Zirconia Stabilization - An X-Ray Absorption Study: 1, Trivalent Dopants. *Journal of the American Ceramic Society,* 77(1), pp. 118-128.

Maschio, R. D., Fabbri, B. & Fiori, C., 1988. Industrial Applications of Refractories Containing Magnesium Aluminate Spinel. *Industrial Ceramics,* 8(3), pp. 121-126.

Matizamhuka, W. R., 2018. Advanced Ceramics - The New Frontier in Modern-day Technology: Part 1. *The Journal of the Southern African Institute of MIning and Metallurgy,* 118(7), pp. 757-764.

McAllister Mills, 2020. *Molten Metal Filters.* [Online] Available at: https://www.mcallistermills.com/molten-metal-filters [Accessed 09 11 2020].

McEwan, N., Courtney, T., Parry, R. A. & Knupfer, P., 2011. Chromite - A Cost-Effective Refractory Raw Material for Refractories in Various Metallurgical Applications. *Southern African Institute of Mining and Metallurgy,* Volume 6, pp. 359-372.

McKittrick, J. & Kalonji, G., 1997. Non-stoichiometry and Defect Structures in Rapidly Solidified MgO-Al_2O_3-ZrO_2 Ternary Eutectics. *Materials Science and Engineering A,* 231(2), pp. 90-97.

Meir, S., Kalabukhov, S., Froumin, N., Dariel, M., Frage, N., 2008. Synthesis and Densification of Transparent Magnesium Aluminate Spinel by SPS Processing. *Journal of the American Ceramic Society*, 92(2), pp. 358-364.

Mizuguchi, T., Guo, S. & Kagawa, Y., 2010. Transmission Electron Microscopy Characterization of Spark Plasma Sintered ZrB_2 ceramic. *Ceramics International,* 36(3), pp. 943-946.

Mohan, S. K. & Sarkar, R., 2016. Effect of ZrO_2 addition on $MgAl_2O_4$ Spinel from Commercial Grade Oxide Reactants. *Ceramics International* , 42(8), pp. 10355-10365.

Morita, K., Kim, B. N., Hirage, K. & Yoshida, H., 2008. Fabrication of Transparent $MgAl_2O_4$ Spinel Polycrystal by Spark Plasma Sintering Processing. *Scripta Materialia,* 58(12), pp. 1114-1117.

Morita, K., Kim, B., Yoshida, H., Hiraga, K., Sakka, Y., 2015. Spectroscopic Study of the Discoloration of Transparent $MgAl_2O_4$ Spinel Fabricated by Spark-Plasma-Sintering (SPS) Processing. *Acta Materialia* , Volume 84, pp. 9-19.

Morita, K., Kim, B., Yoshida, H., Hiraga, K., Sakka, Y., 2018a. Distribution of Carbon Contamination in $MgAl_2O_4$ Spinel Occuring During Spark-Plasma-Sintering (SPS) Processing: I - Effect of heating Rate and Post-Annealing. *Journal of the European Ceramic Society* , 38(6), pp. 2588-2595.

Morita, K., Kim, B., Yoshida, H., Hiraga, K., Sakka, Y., 2018b. Distribution of Carbon Contamination in Oxide Ceramics Occuring During Spark-Plasma-Sintering (SPS) Processing: II - Effect of SPS and Loading Temperatures. *Journal of the European Ceramic Society,* 38(6), pp. 2596-2604.

Munir, Z. A., Anselmi-Tamburini, U. & Ohyanagi, M., 2006. The Effect of Electric Field and Pressure on the Synthesis and Consolidation of Materials: A review of the Spark Plasma Sintering Method. *Journal of Materials Science,* 41(3), pp. 763-777.

Musikant, S., 1985. *Optical Materials: An introduction to Selection and Application.* New York: Marcel Dekker.

Navias, L., 1961. Preparation and Properties of Spinel Made by Vapor Transport and Diffusion in the System $MgO\text{-}Al_2O_3$. *Journal of the American Ceramic Society* , 44(9), pp. 434-446.

Pavlyuchkov, D., Savinykh, G. & Fabrichnaya, O., 2014. Experimental Investigation and Thermodynamic Modeling of the ZrO_2-MgO-Al_2O_3 System. *Journal of the European Ceramic Society,* 34(5), pp. 1397-1408.

Petrescu, L., Petrescu, M., Ionita, V., Cazacu, E., Constantinescu, C., 2019. Magnetic Properties of Manganese-Zinc Soft Ferrite Ceramic for High Frequency Applications. *Materials,* Volume 3173, pp. 1-12.

Petrovic, J. J., 1987. Weibull Statistical Fracture Theory for the Fracture of Ceramics. *Metallurgical Transactions A,* 18(A), pp. 1829-1834.

Preston, F. W., 1942. The Mechanical Properties of Glass. *Journal of Applied Physics,* Volume 13, pp. 623-634.

Quenard, O., Laurent, C., Peigney, A. & Rousset, A., 2000. Zirconia-Spinel Composites. Part I: Synthesis of Powders and Dense Materials. *Materials Research Bulletin,* 35(12), pp. 1967-1977.

Quenard, O., Laurent, C., Peigney, A. & Rousset, A., 2000. Zirconia-Spinel Composites. Part II: Mechanical Properties. *Materials Research Bulletin ,* 35(12), pp. 1979-1987.

Reimanis, I. E. & Kleebe, H.-J., 2007. Reactions in the Sintering of $MgAl_2O_4$ Spinel Doped with LiF. *International Journal of Materials Research,* 98(12), pp. 1273-1278 .

Rensburg, M. J. v., 2018. *Graphite Die Set Drawing (20mm).* [Art] (University of the Witwatersrand).

Rice, R. W., 1996. Grain Size and Porosity Dependence of Ceramic Fracture Energy and Toughness at 22°C. *Journal of Materials Science ,* Volume 31, pp. 1969-1983.

Rothman, A., Kalabukhov, S., Sverdlov, N., Dariel, M., Frage, N., 2014. The Effect of Grain Size on the Mechanical and Optical Properties of Spark Plasma Sintering-Processed Magnesium Aluminate Spinel $MgAl_2O_4$. *International Journal of Applied Ceramic Technology* , 11(1), pp. 146-153.

Rozenburg, K., Reimanis, I. E., Kleebe, H.-J. & Cook, R. L., 2008. Sintering Kinetics of a $MgAl_2O_4$ Spinel Doped with LiF. *Journal of the AMerican Ceramic Society,* 91(2), pp. 444-450.

Rozenburg, K., Reimanis, I., Kleebe, H. & Cook, R. L., 2007. Chemical Interaction Between LiF and $MgAl_2O_4$ Spinel During Sintering. *Journal of the American Ceramic Society*, 90(7), pp. 2038-2042.

Ruff, O. & Ebert, F., 1929. Beiträge zur Keramik hochfeuerfester Stoffe. l. Die Formen des Zirkondioxyds. *Zeitschrift für anorganische und allgemeine Chemie,* 180(1), pp. 19-41.

Ruh, R. & Corfield, P. W. R., 1970. Crystal Structure of Monoclinic Hafnia and Comparison with Monoclinic Zirconia. *Journal of the American Ceramic Society* , 53(3), pp. 126-129.

Ruh, R., Garrett, H. J., Domagala, R. F. & Tallan, N. M., 1968. The System Zirconia-Hafnia. *Journal of the American Ceramic Society,* 51(1), pp. 23-27.

Salem, J. A., 2013. Transparent Armor Ceramics as Spacecraft Windows. *Journal of the American Ceramic Society,* 96(1), pp. 281-289.

Santos, H. & Costa, M., 2008. Evaluation of the Conversion Efficiency of Ceramic and Metallic Three Way Catalytic Converters. *Energy Conversion and Management* , Volume 49, pp. 291-300.

Sarkar, R., 2010. Refractory Applications of Magnesium Aluminate Spinel. *InterCeram: International Ceramic Review,* pp. 11-14.

Schwantes, S. & Elber, W., 1983. Slow Crack Growth in Spinel in Water. *NASA Technical Memorandum.*

Scott, H. G., 1975. Phase Relationships in the Zirconia-Yttria System. *Journal of Materials Science,* 10(9), pp. 1527-1535.

Sedel, L., 2000. Evolution of Alumina-on-Alumina Implants. *Clinical Orthopaedics and Related Research,* Volume 379, pp. 48-54.

Shevchenko, A. V., Gerasimyuk, G. I., Lopato, L. M. & Yusupova, S. G., 1993. Interactions in the System ZrO_2-$MgAl_2O_4$. *Inorganic Materials,* Volume 29, pp. 117-118.

Shin, H., Benali, A., Crabb, E., Jokisaari, A., Heinonen, O., 2018. Zirconia and Hafnia Polymorphs- Ground State Structural Properties from Diffusion Monte Carlo. *Physical Review Materials,* 7(2), pp. 075001-1 -14.

Sickafus, K. & Wills, J. M., 1999. Structure of Spinel. *Journal of the American Ceramic Society,* Volume 82, pp. 3270-3292.

Smart, L. E. & Moore, E. A., 2005. *Solid State Chemistry An Introduction.* 3rd ed. Boca Raton: Taylor & Francis Group.

Smith, D. K. & Newkirk, H. W., 1965. The Crystal Structure of Baddeleyite (Monoclinic ZrO_2) and its Relation to the Polymorphism of ZrO_2. *Acta Crystallographica,* Issue 18, pp. 983-991.

Snelling, C., 2015. *SI Metric.* [Online] Available at: https://www.simetric.co.uk/si_water.htm [Accessed 10 11 2020].

Sokol, M., Kalabukhov, S., Dariel, M. & Frage, N., 2014. High-Pressure Spark Plasma Sintering (SPS) of Transparent Polycrystalline Magnesium Aluminate Spinel (PMAS). *Journal of the European Ceramic Society,* 34(16), pp. 4305-4310.

Staiger, M., Bowen, P., Ketterer, J. & Bohonek, J., 2002. Particle Size Distribution Measurement and Assessment of Agglomeration of Commercial Nanosized Ceramic Particles. *Journal of Dispersion Science and Technology,* 23(5), pp. 619-630.

Stewart, R. L. & Bradt, R. C., 1980. Fracture of Polycrystalline $MgAl_2O_4$. *Journal of the American Ceramic Society* , pp. 619-623.

Straßburger, E., 2009. Ballisitc Testing of Transparent Armour Ceramics. *Journal of the European Ceramic Society* , 29(2), pp. 267-273.

Su, H. & Johnson, D. L., 1996. Master Sintering Curve: A Practical Approach to Sintering. *Journal of the American Ceramic Society* , 79(11), pp. 3211-3217.

Superior Technical Ceramics, 2020. *Zirconia Toughened Alumina (ZTA).* [Online] Available at: https://www.ceramics.net/ceramic-materials-solutions/zta [Accessed 09 11 2020].

Teufer, G., 1962. The Crystal Structure of Tetragonal ZrO_2. *Acta Crystallographica,* 15(11), p. 1187.

Thermansys, 2017. *Zirconia Toughened Alumina (ZTA) Crucibles.* [Online] Available at: https://www.tceramics.com/products/22_Zirconia-Toughened-Alumina-(ZTA)-Crucibles [Accessed 09 11 2020].

Trueblood & McCullough, 1959. The Crystal Structure of Baddeleyite (Monoclinic ZrO_2). *Acta Crystallographica,* Issue 12, pp. 507-511.

Valerio, A. & Morelhao, S. L., 2019. Usage of Scherrer's Formula in X-ray Diffraction Analysis of Size Distribution in Systems of Monocrystalline Nanoparticles. *University of Sao Paulo* , pp. 1-9.

VAMAS, 1993. *Classification of Advanced Technical Ceramics*, s.l.: The Versailles Project on Advanced Materials and Standards.

Vleugels, J., 2006. Fabrication, Wear and Performance of Ceramic Cutting Tools. *Advances in Science and Technology,* Volume 45, pp. 1776-1785.

Wang, C. & Zhao, Z., 2009. Transparent $MgAl_2O_4$ Ceramic Produced by Spark Plasma Sintering. *Scripta Materialia* , 61(2), pp. 193-196.

Wang, X. & Atkinson, A., 2015. On the Measure of Ceramic Fracture Toughness Using Single Edge Notched Beams. *Journal of the European Ceramic Society*, 35(13), pp. 3713-3720.

Yan, M. F., Rhodes, W. W. & Galiagher, P. K., 1988. Dopant Effects on the Superconductivity of $YBa_2Cu_3O_7$ Ceramics. *Journal of Applied Physics,* Volume 63, pp. 821-828.

Zhao, X.-S., Shang, S.-L., Liu, Z.-K. & Shen, J.-Y., 2011. Elastic Properties of Cubic, Tetragonal and Monoclinic ZrO_2 from First-Principles Calculations. *Journal of Nuclear Materials,* 415(1), pp. 13-17.

Appendix

The list of private companies that are within the emerging industry of space exploration is given in **Table A.1**.

Table A.1: Private Aerospace Companies

Bigelow Aerospace	Planet Labs
Blue Origin	Planetary Resources
Copenhagen Suborbital	Sierra Nevada Corporation
Deep Space Industries	Space Adventures
Golden Spike	SpaceX
Masten Space Systems	Swiss Space Systems
Moon Express	Virgin Galactic
NanoRacks	Xcore
Orbital Sciences	Zero2Infinity

A list of minerals that have the spinel structure are given in **Table A.2**.

Table A.2: Minerals with the spinel crystal structure (Maschio, et al., 1988).

Name	**Composition**
Spinel	$MgAl_2O_4$
Magnesioferrite	$MgFe_2O_4$
Franklinite	$ZnFe_2O_4$
Magnetite	$FeFe_2O_4$
Chromite	$FeCr_2O_4$
Hercynite	$FeAl_2O_4$
Gahnite	$ZnAl_2O_4$
Galaxite	$MnAl_2O_4$

The following figures show the EDS spectra for the $ZrO_2 – MgAl_2O_4$ composites. The presence of gold in the spectrum does not show up in the calculated weight percent as gold was used to coat the sample. It was automatically excluded by the program for the calculation of the relative weight precent.

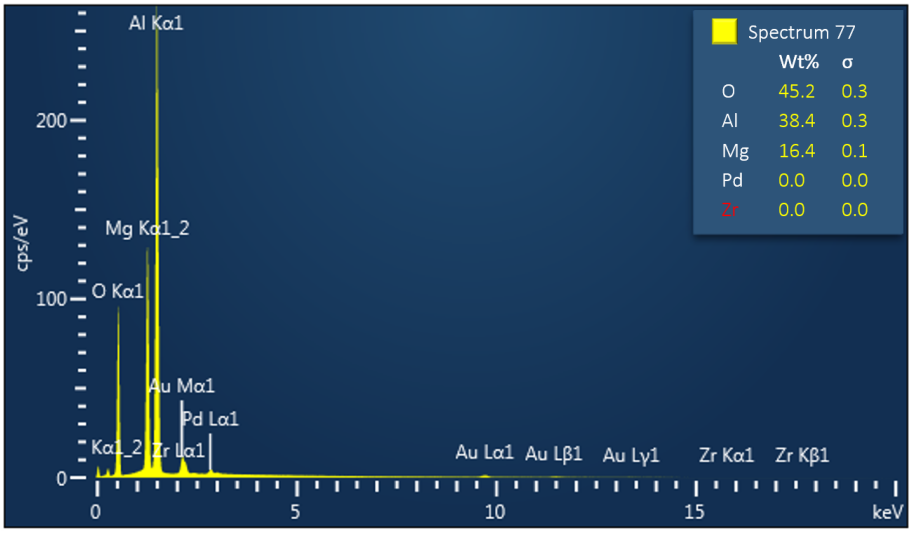


Figure A.1: EDS spectra for the 0wt.% ZrO_2 sample.

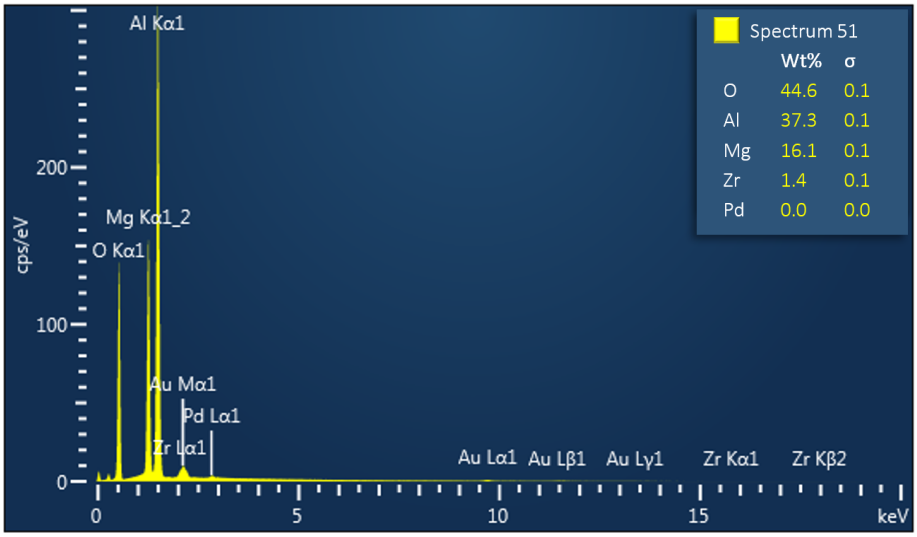


Figure A.2: EDS spectra for the 2wt.% ZrO_2 sample.

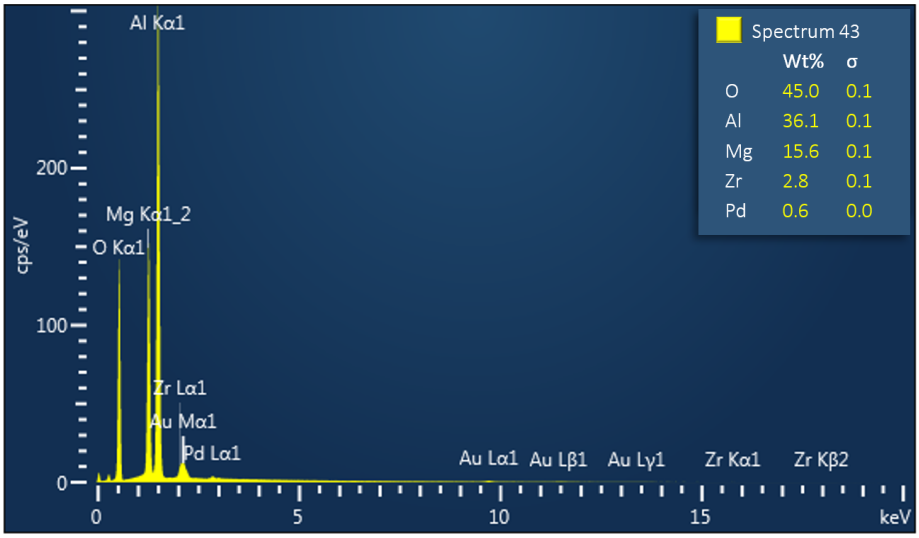


Figure A.3: EDS spectra for the 5wt.% ZrO_2 sample.

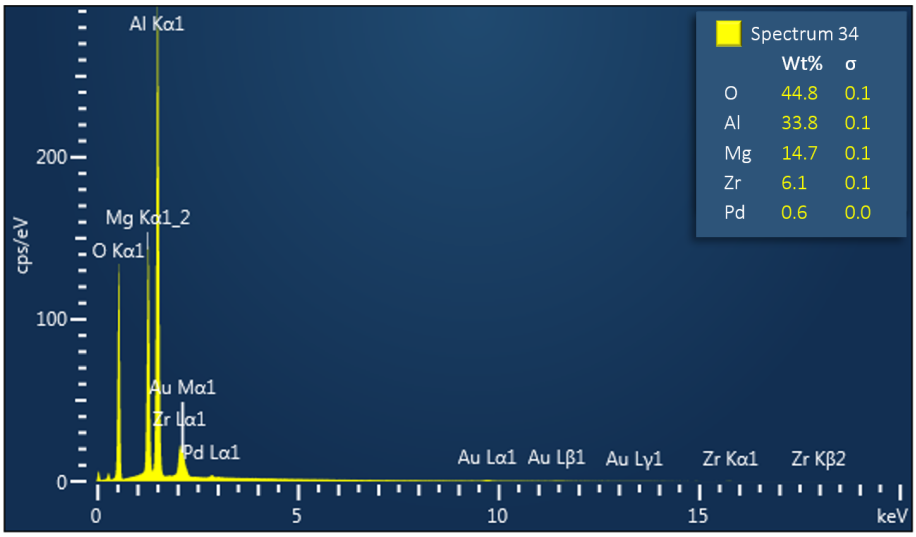


Figure A.4: EDS spectra for the 10wt.% ZrO_2 sample.

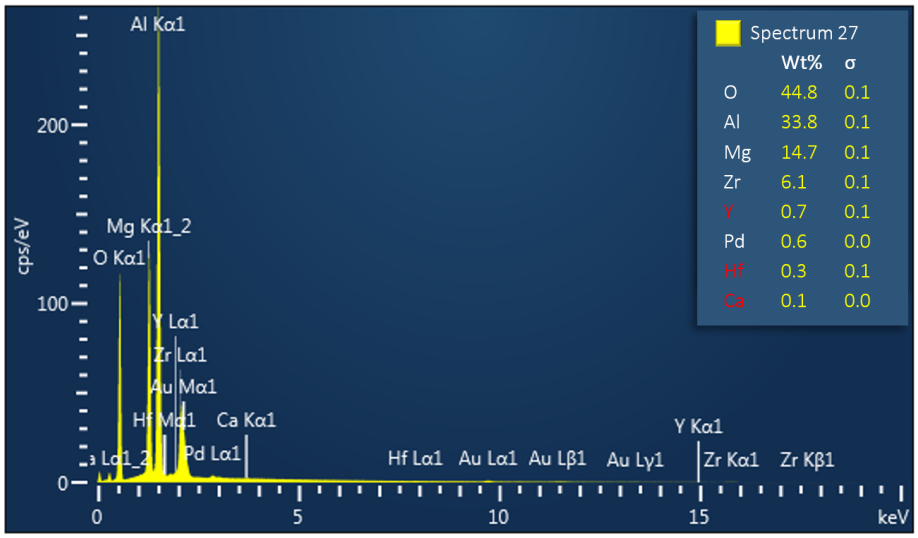


Figure A.5: EDS spectra for the 20wt.% ZrO_2 sample.

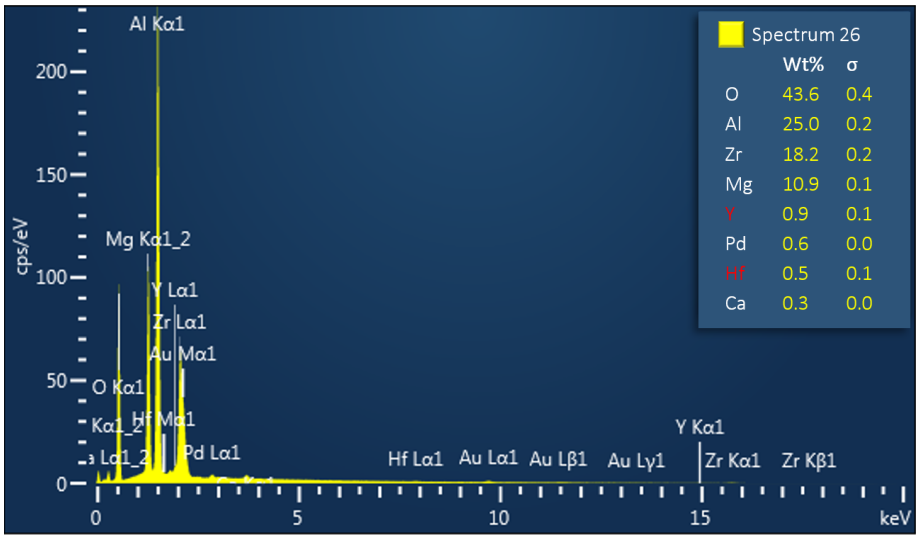


Figure A.6: EDS spectra for the 30wt.% ZrO_2 sample.

Figure A.7 shows the data used to calculate the weighted sum curve shown in **Figure 5.13**.

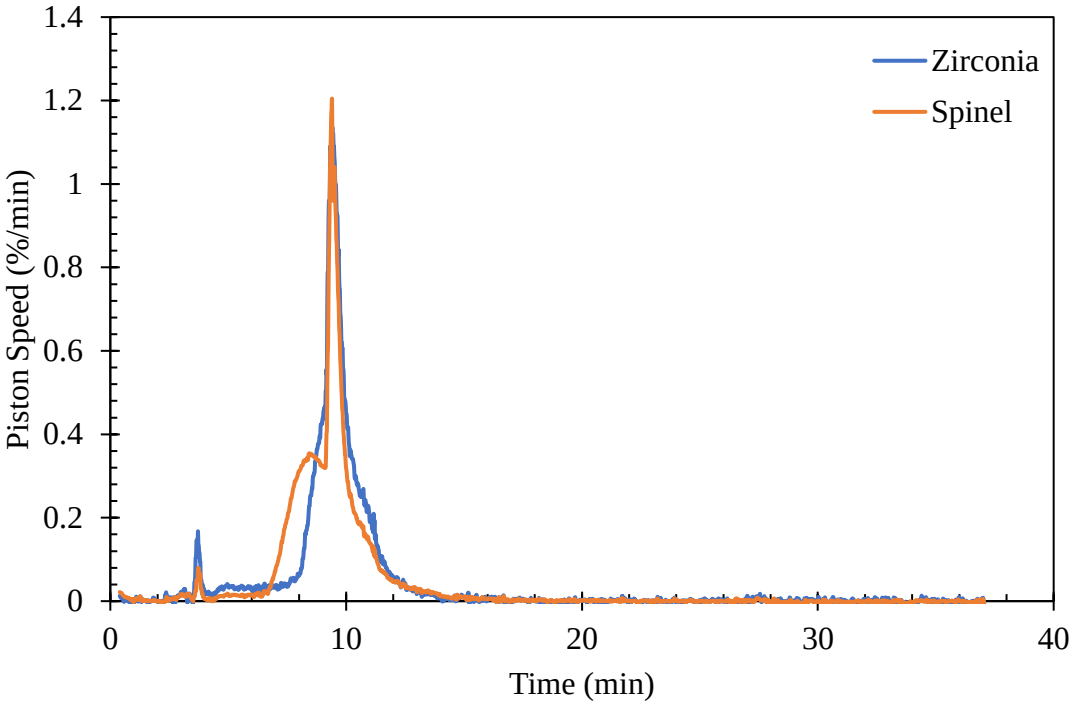


Figure A.7: Densification Curve for samples composed of 100% $MgAl_2O_4$ and 100% ZrO_2.